Universitat de València

Facultat de Química
Instituto de Ciencia Molecular (ICMol)

Nuevos materiales moleculares multifuncionales conmutables con transición de espín

Programa de Doctorado:
Programa de Doctorado en Química (RD99/2011)

Doctorando:
Manuel Meneses Sánchez

Tutor de la tesis:
Prof. Dr. José Antonio Real Cabezos

Directores de la tesis:
Prof. Dr. José Antonio Real Cabezos
Dr. Carlos Bartual Murgui

Julio, 2022

El Prof. Dr. **José Antonio Real Cabezos**, Catedrático del Departamento de Química Inorgánica de la Universitat de València, adscrito al Instituto de Ciencia Molecular (ICMol) y el Dr. **Carlos Bartual Murgui**, Investigador Doctor Senior adscrito al Instituto de Ciencia Molecular (ICMol),

CERTIFICA:

Que la presente Tesis Doctoral, titulada: **Nuevos materiales moleculares multifuncionales conmutable con transición de espín**, se ha realizado bajo la codirección de ambos en el Instituto de Ciencia Molecular (ICMol) en la Universitat de València por el Graduado en Química Manuel Meneses Sánchez, y autoriza su presentación para optar al grado de Doctor en Química por la Universitat de València.

En Paterna, a 4 de Julio de 2022.

Prof. Dr. José Antonio Real Cabezos
Director y tutor

Dr. Carlos Bartual Murgui
Director

AGRADECIMIENTOS

La presente Tesis Doctoral no habría podido realizarse si no hubiera sido gracias a la ayuda y apoyo de muchas personas durante toda esta etapa de mi vida.

Para empezar, me gustaría agradecer a mi director de tesis José Antonio Real y a Mª Carmen Muñoz, por toda la confianza y ayuda depositada en mí para permitirme desarrollar la tesis en su grupo de investigación. Gracias por vuestra dedicación y todo el conocimiento que me habéis transmitido durante todos estos años. También, gracias por esos pequeños descansos y charlas sobre otros temas de mucho interés, no solo científicos, de los cuales he aprendido muchas otras cosas. Igualmente, muchas gracias a Carlos Bartual, mi cotutor de la tesis, el cual, ha estado siempre ahí, ayudándome con todo lo que he necesitado.

Agradezco a todos los miembros del tribunal y a los evaluadores por acceder a valorar esta tesis Doctoral.

Me gustaría agradecer a todos los miembros del grupo de investigación *Switchable Molecular Materials* (*SMolMat*) de la Universitat de València con los que he convivido durante los últimos años. Gracias a Javier Valverde, por haberme recibido en el grupo de investigación y enseñarme todo lo que tenía que saber para poder desenvolverme rápidamente en el laboratorio, así como a realizar las cristalizaciones y a manejar el SQUID. Gracias a Lucía Piñeiro, por haber sido una gran compañera de laboratorio, aunque fueran solo un par de años los que coincidimos, me enseñaste mucho y fue una suerte haberte conocido. Gracias a Maksym Seredyuk, por esa conexión Valencia-Kyiv, la cual me permitió conocer Ucrania más en profundidad, tanto científicamente como personal. Espero que esa conexión perdure por muchos años más. Gracias a Rubén Turo, que has estado todo el periodo de mi Tesis Doctoral. Hemos tenido grandes discusiones científicas que me han servido de mucha ayuda, junto a tus consejos, los cuales, me han permitido poder resolver algunas dudas. Aunque somos bastante diferentes, siempre has estado ahí cuando me ha hecho falta. Gracias a Alejandro Orellana, a pesar de haber sido el último en llegar me has ayudado muchos con el trabajo y has demostrado tener unas grandes ganas de mejorar y aprender.

Gracias, también, a los técnicos del ICMol Gloría Agustí y José María Martínez, por su profesionalidad y gran ayuda ofrecida para la caracterización de los materiales que he sintetizados durante esta tesis doctoral. Muchas gracias también, por toda la ayuda que me habéis proporcionado para solucionar los problemas que de forma inesperada surgían con el SQUID.

Agradezco a Bruno Viana por haberme permitido realizar mi estancia de investigación en su grupo, donde aprendí a utilizar equipos muy diferentes a los que estoy acostumbrado. Gracias a toda la gente que me ayudó durante dicha estancia, sobre todo a Teresa Delgado, que me enseñó todo lo que me hizo falta para poder manejar todos los equipos necesarios para realizar todas las medidas que necesitamos.

Gracias a mis padres, Manolo y Mª de los Ángeles por todo el apoyo que me habéis dado en todo, desde que decidí venirme a Valencia a estudiar, lejos de toda la familia, y gracias a ese apoyo recibido he conseguido llegar hasta este punto. También me gustaría agradeceros todos los valores que me habéis inculcado desde pequeño, como la humildad, el respeto, la honestidad, apreciar lo que se tiene… lo que me ha ayudado a poder crecer como persona. Gracias por todas las regañinas que me he llevado cuando no hacia las cosas como debía. Gracias a mi hermana Esther, por ser como eres. A parte de hermana, siempre has sido como una gran amiga, con quien he podido hablar de cualquier cosa, y quien me ha ayudado en todo lo que ha podido, sobre todo con grandes consejos. Aunque no suela expresarlo muy a menudo, os quiero muchísimo.

Gracias a Carlos Lázaro, Miguel Ángel Barquero, Jorge Medina y Pablo Sanz, habéis sido unos grandes amigos, habéis sido un gran apoyo durante todo este periodo ayudándome en todo momento. Gracias por esas quedadas que me han ayudado a poder desconectar. También, gracias por todos los consejos que me habéis dado, tanto en el ámbito científico, como en el ámbito personal, los cuales han sido de gran ayuda. Gracias a vosotros he podido sentirme como en casa a pesar de estar tan lejos de toda mi familia.

Por último, agradecer al amor de mi vida, Yuliia. Nos conocimos gracias a la colaboración con la Universidad de Kyiv, y aunque al principio no podíamos vernos muy a menudo debido a la distancia, hemos hecho todo lo posible por hacer que la relación funcionase. A pesar de la distancia, te has convertido en una de las personas mas

importantes para mí. Muchas gracias por todo el apoyo que me has dado durante todo este tiempo y por no haber tirado la toalla en ningún momento. Una de las cosas que más fuerzas me ha dado en esta última etapa ha sido verte sonreír cada mañana al levantarme. Te quiero muchísimo.

Indice

Resumen 3

Summary 7

Capítulo 1.- Introducción

1.1.- Conceptos generales del fenómeno de transición de espín (SCO) 11

1.1.1.- Teoría del campo de ligandos y diagramas de energía potencial del fenómeno SCO 12

1.1.2.- Fotoconversión (efecto LIESST) en compuestos SCO 18

1.1.3.- Comportamiento conjunto del grupo de centros activos: cooperatividad 20

1.1.4.- Técnicas de detección del fenómeno SCO 24

1.2.- Objetivos de la tesis doctoral 24

1.3.- Metodología 25

1.4.- Bibliografía 26

Capítulo 2.- Thermo- and photo-modulation of exciplex fluorescence in a 3D spin crossover Hofmann-type coordination polymer

Artículo 31

Material suplementario 47

Capítulo 3.- Extrinsic vs intrinsic luminescence and their interplay with spin crossover in 3D Hofmann-type coordination polymers

Artículo 61

Material suplementario 86

Capítulo 4.- Enhanced Interplay between Host-Guest and Spin-Crossover Properties through the Introduction of an N Heteroatom in 2D Hofmann Clathrates

Artículo 107

Material suplementario 136

Capítulo 5.- Conclusiones finales

Conclusiones 153

Conclusions 157

Apéndice

Artículos 163

RESUMEN

Este trabajo de Tesis Doctoral se centra en la síntesis y caracterización de nuevos materiales moleculares conmutables basados en Fe^{II}, los cuales presentan el fenómeno de transición de espín (*spin crossover*, SCO). El objetivo principal de esta tesis doctoral ha sido el diseño y estudio de nuevos materiales multifuncionales de Fe^{II} que combinan el comportamiento SCO con otra propiedad físico-química de interés. La estrecha interrelación entre el fenómeno SCO y dicha propiedad ha sido seguida y estudiada por estudios magnéticos, cristalográficos y calorimétricos, entre otros.

El capítulo 1 de esta tesis describe los conceptos teóricos más importantes del fenómeno SCO, donde los centros SCO experimentan una conversión entre los estados HS↔LS (HS: estado de espín alto, LS: estado de espín bajo) en respuesta a una perturbación física externa o un estímulo químico como la variación de la temperatura, presión, irradiación con luz o inclusión de un analito. El cambio en el estado de espín en este tipo de materiales sensibles va acompañado de modificaciones en la estructura cristalina y de sus propiedades físicas importantes (p. ej. propiedades magnéticas, ópticas, dieléctricas).

Los objetivos que han inspirado el desarrollo de esta Tesis Doctoral junto con el procedimiento experimental general para la síntesis y caracterización físico-química de los diferentes compuestos presentados también están resumidos en este capítulo.

La búsqueda de materiales bifuncionales de base molecular que combinen sinergias SCO-luminiscencia ha atraído un interés sustancial, ya que son plataformas prometedoras para nuevas tecnologías optoelectrónicas de conmutación. En este contexto, el capítulo 2 describe la síntesis y caracterización del compuesto $\{Fe^{II}(bpben)[Au(CN)_2]\}$@pyr (bpben = 1,4-bis(4-piridil)benzeno) funcionalizado con pireno (pyr) como molécula huésped, el cuál representa el primer polímero de coordinación tridimensional de Fe^{II} de tipo Hofmann que exhibe propiedades SCO y luminiscencia. Este complejo experimenta un comportamiento SCO cooperativo en varias etapas, que ha sido investigado por difracción de rayos X en monocristal, espectroscopía de absorción UV-Vis en monocristal y medidas magnéticas y calorimétricas. La fluorescencia resultante que proviene de los huéspedes pireno -emisión de monómero- y de las interacciones anfitrión-huésped -emisión del excímero- está controlada por la dependencia de la irradiación térmica y luminosa (efecto LIESST) de la población de

los estados de espín alto/bajo del Fe^{II}. Por el contrario, el comportamiento SCO puede ser seguido monitoreando la emisión de fluorescencia. Esta interacción ON-OFF entre SCO y luminiscencia, combinada con la facilidad de los compuestos tipo Hofmann para ser procesados a nanoescala, ofrece perspectivas importantes para la generación de sensores basados en SCO y dispositivos espintrónicos.

El capítulo 3 profundiza en el estudio de cuatro nuevos compuestos que presentan acoplamiento SCO-fluorescencia. Estos polímeros tridimensionales de coordinación de Fe^{II} tipo Hofmann se investigan siguiendo dos estrategias principales: si el agente fluorescente está integrado como parte de la estructura principal de un polímero de coordinación SCO 3D $\{Fe^{II}(bpan)[M^{I}(CN)_2]_2\}$ (*bpan* = bis(4-piridil)antraceno, M^{I} = Ag (**FebpanAg**), Au (**FebpanAu**)) o es una molécula invitada insertada dentro de las cavidades de la red conmutable 3D $\{Fe^{II}(bpb)[M^{I}(CN)_2]_2\}\cdot$pireno (*bpb* = bis(4-piridil)butadiino, M^{I} = Ag (**FebpbAg·pyr**), Au (**FebpbAu·pyr**)). Esto es muy importante en el desarrollo de otros dispositivos de conmutación óptica y electrónica. Se realizaron medidas magnéticas, calorimétricas, estructurales, de absorción UV-Vis y fluorescencia confirmando la presencia de una interacción SCO-fluorescencia en los compuestos estudiados. Además, se discute la relevancia de la naturaleza intrínseca o extrínseca de la luminiscencia en la eficiencia de la interacción.

En el capítulo 4 se presenta la modulación controlada del comportamiento SCO a través de la adsorción-desorción de moléculas invitadas. Para este propósito, la comprensión de los mecanismos por los cuales las propiedades de conmutación de espín son alteradas por las moléculas invitadas es de suma importancia. Aquí, mostramos un enfoque experimental que revela cómo la interacción entre SCO y la química del huésped-invitado se activa notablemente al ajustar químicamente la estructura del anfitrión. Así, el ligando axial 4-fenilpiridina (**4-PhPy**) en los clatratos de Hofmann 2D $\{Fe(4\text{-}PhPy)_2[M(CN)_4]\}$ (**PhPyM**; M = Pt, Pd) se sustituye por 2,4-bipiridina (**2,4-Bipy**), dando lugar a los compuestos isomorfos $\{Fe(2,4\text{-}Bipy)_2[M(CN)_4]\}$ (**BipyM**; M = Pt, Pd), que básicamente difieren de los primeros en que tienen un heteroátomo N no coordinado en el sustituyente aromático auxiliar, es decir, 2-piridil en lugar de fenil. Nuestras caracterizaciones químicas, magnéticas, calorimétricas y estructurales demuestran que este sutil cambio en la composición química provoca modificaciones sobresalientes no solo en la capacidad de adsorber pequeñas moléculas invitadas como agua o metanol, sino también en la medida en que estas moléculas invitadas afectan las características SCO.

En el capítulo 5 se presentan las conclusiones finales de esta tesis doctoral.

Finalmente, se incluye un apéndice con todos los artículos científicos que han dado lugar a esta tesis doctoral.

SUMMARY

This thesis dissertation deals with the synthesis and characterization of new switchable Fe^{II} molecular based materials that display the spin crossover (SCO) phenomenon. The main goal of the present Doctoral Thesis has been the design of new multifunctional Fe^{II} materials that combine the SCO behavior with other interesting physico-chemical properties. The close interplay between SCO and the second property has been followed and studied by magnetic, crystallographic and calorimetric measurements, among others.

Chapter one describes the most relevant theoretical concepts of the SCO phenomena, where SCO centers experience HS↔LS spin conversion between the high-spin (HS) and the low-spin (LS) states in response to external physical or chemical stimuli like a variation of temperature, pressure, irradiation with light or inclusion of analytes. The spin-state switch in these responsive materials is accompanied by changes in relevant physical properties (e.g. magnetic, optical, dielectric) and structure.

The main motivations that have inspired the development of this Doctoral Thesis together with the general experimental procedure for the synthesis and physico-chemical characterization of the different, herein presented, compounds are also summarized in this chapter.

The search for robust bifunctional molecular based materials combining SCO-luminiscence synergies have attracted substantial interest since they are promising platforms for new switching optoelectronic technologies. In this context, chapter two describes the synthesis and characterization of the compound $\{Fe^{II}(bpben)[Au(CN)_2]\}$@pyr (bpben = 1,4-bis(4-pyridyl)benzene) functionalized with pyrene (pyr) as guest molecules, which represents the first three-dimensional Fe^{II} Hofmann-type coordination polymer exhibiting SCO properties and luminescence. This complex undergoes a cooperative multi-step SCO, which has been investigated by single crystal X-ray diffraction, single crystal UV-Vis absorption spectroscopy, and magnetic and calorimetric measurements. The resulting fluorescence arising from the pyrene guests -monomer emission- and from host-guest interactions -exciplex emission- is controlled by the thermal and light irradiation (LIESST effect) dependence of the high/low-spin state population of Fe^{II}. Conversely, the SCO can be tracked by monitoring the fluorescence emission. This ON-OFF interplay between SCO and luminescence combined with the

amenability of Hofmann-type materials to be processed at the nano-scale afford important perspectives for the generation of SCO-based sensors, actuators and spintronic devices.

Chapter three deepens into the coupling SCO-fluorescence investigating four new three-dimensional Fe^{II} Hofmann-type coordination polymers following two main strategies: whether the fluorescent agent is integrated as a part of the main structure of a 3D SCO coordination polymer $\{Fe^{II}(bpan)[M^{I}(CN)_2]_2\}$ (*bpan* = bis(4-pyridyl)anthracene, M^{I} = Ag (**FebpanAg**), Au (**FebpanAu**)) or is a guest molecule inserted within the cavities of the 3D switchable framework $\{Fe^{II}(bpb)[M^{I}(CN)_2]_2\}\cdot$pyrene (*bpb* = bis(4-pyridyl)butadiyne, M^{I} = Ag (**FebpbAg·pyr**), Au (**FebpbAu·pyr**)), as a research of new multifunctional materials, which undergoing SCO and luminescent properties. This is extremely important in the development of further optical and electronic switching devices. The magnetic, calorimetric, structural, UV-Vis absorption and fluorescent characterizations were performed confirming the occurrence of a SCO-fluorescence interplay in the studied compounds. Moreover, the relevance of the intrinsic or extrinsic nature of the luminescence on the efficiency of the interplay is discussed on the basis of the available information.

Chapter four introduces the controlled modulation of the SCO behavior through the sorption−desorption of invited molecules. For this purpose, understanding the mechanisms by which the spin-switching properties are altered by guest molecules is of paramount importance. Here, we show an experimental approach revealing a direct probe of how the interplay between SCO and host−guest chemistry is noticeably activated by chemically tuning the host structure. Thus, the axial ligand 4-phenylpyridine (**4-PhPy**) in the 2D Hofmann clathrates $\{Fe(4\text{-}PhPy)_2[M(CN)_4]\}$ (**PhPyM**; M = Pt, Pd) is replaced by 2,4-bipyridine (**2,4-Bipy**), resulting in the isomorphous compounds $\{Fe(2,4\text{-}Bipy)_2[M(CN)_4]\}$ (**BipyM**; M = Pt, Pd), which basically differ from the former in that they have a noncoordinated N heteroatom in the ancillary aromatic substituent, i.e., 2-pyridyl instead of phenyl. Our chemical, magnetic, calorimetric, and structural characterizations demonstrate that this subtle chemical composition change provokes outstanding modifications not only in the capability to adsorb small guests as water or methanol but also in the extent to which these guests affect the SCO characteristics.

Chapter five assembles the general conclusions of this doctoral thesis.

Finally, it is enlisted an appendix gathering all peer reviewed scientific articles that have led to this Doctoral Thesis.

CAPÍTULO 1

Introducción

CAPÍTULO 1
Introducción

1.1.- Conceptos generales del fenómeno de transición de espín (SCO)

El fenómeno de la transición de espín (SCO) se enmarca en el campo de la magnetoquímica, y ha estado enlazado históricamente y de manera fundamental al desarrollo de la química de coordinación.[1] Los centros SCO muestran configuraciones electrónicas lábiles intercambiables entre los estados de espín alto (HS) y espín bajo (LS), dando lugar a cambios característicos en el magnetismo, el color y la estructura de la materia, que pueden ser inducidos por variaciones de temperatura, presión, y por irradiación con luz. Cuando los cambios estructurales asociados a la transición de espín se transmiten de forma cooperativa a través del cristal se producen transiciones de espín cooperativas acompañadas de histéresis (efecto "memoria"), confiriendo carácter biestable al material.

La idea de que una molécula o conjunto de moléculas puede comportarse como un dispositivo electrónico ha estimulado la imaginación de los científicos desde hace mucho tiempo.[2-11] Una de las estrategias más simples se basa en el concepto de biestabilidad molecular que se fundamenta en el cambio entre dos estados moleculares tal y como sucede en un interruptor binario.[12]

La biestabilidad molecular ha sido definida como "la propiedad de un sistema molecular para cambiar entre dos estados estables de una manera reversible y detectable en respuesta a una perturbación apropiada".[13] En este contexto, el fenómeno de la transición de espín representa un ejemplo destacado de biestabilidad molecular. Este fenómeno tiene lugar tanto en disolución, en cristales líquidos y en estado sólido. En el primer caso, el proceso es esencialmente molecular debido al aislamiento de las moléculas. En estado sólido y en cristales líquidos la situación es muy diferente y, en general, el fenómeno viene acompañado por efectos cooperativos. La cooperatividad es una de las facetas más interesantes de las transiciones de espín, pues implica discontinuidad en las propiedades ópticas y magnéticas y, en ocasiones, viene acompañada de histéresis

térmica. Esto le confiere a dichos sistemas capacidad potencial para almacenar información a nivel molecular.

La dificultad en el estudio de la cooperatividad reside en su naturaleza intermolecular. El control de las interacciones no covalentes entre unidades individuales que constituyen un sólido es uno de los campos más activos de lo que hoy en día se conoce como química supramolecular[14-15] y, en particular, de la ingeniería cristalina. Sin embargo, a pesar de lo mucho que se ha avanzado en la última década, no es posible todavía predecir si una disposición molecular en una red puede ser más o menos efectiva que otra desde el punto de vista de la cooperatividad, o incluso si va a favorecer o impedir la conversión de espín. A este respecto, podemos decir que actualmente el químico carece de una guía conceptual que le permita la síntesis dirigida de sólidos con unas propiedades magnéticas determinadas.

A pesar de todos estos inconvenientes, el estudio de las transiciones de espín presenta una riqueza conceptual poco imaginable a primera vista. En este apartado se presentan los conceptos más importantes de las transiciones de espín.

1.1.1.- Teoría del campo de ligandos y diagramas de energía potencial del fenómeno SCO

En simetría octaédrica los complejos de metales de transición con configuraciones electrónicas $[Ar]3d^4$-$3d^7$ pueden presentar dos estados electrónicos fundamentales distintos, según el desdoblamiento de los orbitales d en los subconjuntos e_g y t_{2g}. Cuando la separación energética entre estos subconjuntos (fuerza del campo de ligandos), Δ, es mayor que la energía de repulsión interelectrónica, P, los electrones tienden a ocupar los orbitales de más baja energía, t_{2g}, y el complejo metálico adopta el estado de espín bajo (LS). Si Δ es menor que P los electrones d cumplen la regla de máxima multiplicidad de Hund y el complejo adopta el estado de espín alto. La mayoría de los complejos de Cr^{II}, Mn^{II}, Mn^{III}, Fe^{II}, Fe^{III}, Co^{II} y Co^{III} pueden presentar estas dos posibilidades electrónicas, si bien la familia de compuestos de Fe^{II} presentando transición de espín es la más importante y la más numerosa.

En los alrededores del punto de cruce, Δ_c, donde Δ y P tienen valores similares, la diferencia de energía entre los estados HS y LS es del orden de magnitud de la energía térmica (k_BT). En esta región singular nace una nueva familia de compuestos denominados de transición de espín (SCO). Éstos pueden adoptar ambos estados de espín e interconvertirse de manera controlada, detectable y reversible bajo el efecto de la temperatura, presión o irradiación de luz.

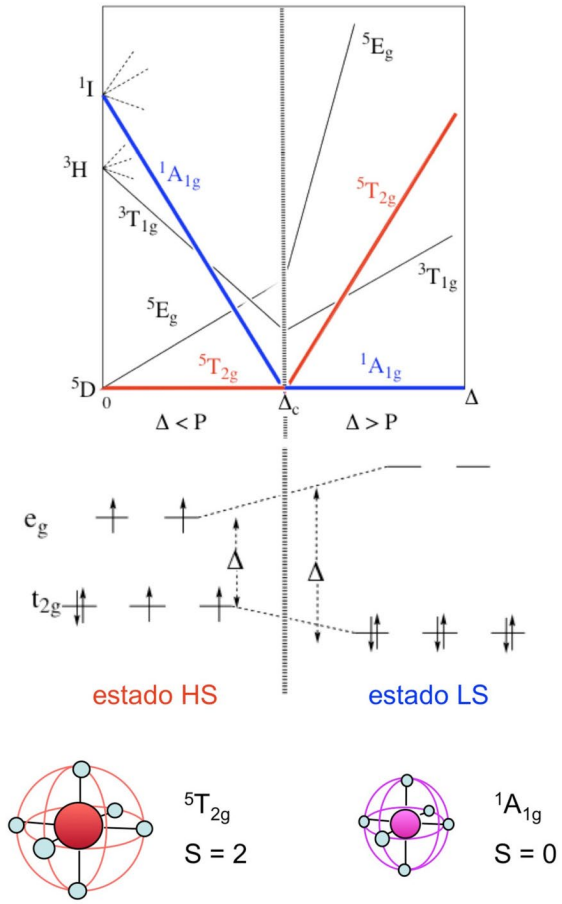

Figura 1. *Diagrama Tanabe-Sugano simplificado ilustrando la dependencia relativa de los estados HS y LS y las configuraciones electrónicas correspondientes.*

En el caso de compuestos de Fe^{II} los ligandos de campo débil, como el H_2O, favorecen la estabilización del estado HS (cuyo estado fundamental es el $^5T_{2g}$), mientras que al aumentar la fuerza del campo de ligandos el estado LS (cuyo estado fundamental es el $^1A_{1g}$), se estabiliza automáticamente, disminuyendo su energía.

El fenómeno de las transiciones de espín puede considerarse como una transferencia electrónica intra-iónica, donde los electrones se mueven entre los orbitales e_g y t_{2g}. Dado que el subconjunto e_g tiene carácter antienlazante, su población/despoblación tiene lugar junto a un aumento/disminución de las distancias de enlace metal-ligando. Un cambio opuesto se da en la población del subconjunto t_{2g} que afecta a la retro-donación entre el ion metálico y los orbitales π* vacantes de los ligandos. Ambos factores σ y π contribuyen al cambio de las distancias de enlace metal-ligando. El cambio en las distancias de enlace metal-ligando, ΔR, es de aproximadamente 0.2, 0.15 y 0.10 Å para el Fe^{II}, Fe^{III} y Co^{III}, respectivamente. Así pues, un cambio considerable de tamaño tiene lugar durante la transición de espín, no sólo en las distancias de enlace sino también en los ángulos. Consecuentemente, las moléculas experimentan un cambio drástico de Δ con el comportamiento SCO, que se estima de $\Delta_{LS}/\Delta_{HS} \approx (\Delta r_{HS}/\Delta r_{LS})^n$ con n = 5 - 6. Por ejemplo, $\Delta_{LS} \approx 1.75\Delta_{HS}$ para el Fe^{II}. Esta estimación abandona la dependencia angular de Δ y considera que Δr es el parámetro de cambio estructural más importante.[16]

La fuerza del campo de ligandos depende no sólo del ligando coordinado al centro metálico sino también de la distancia de enlace metal-ligando. Al pasar al estado de LS las distancias Fe-N disminuyen, lo que implica un cambio en el orden de enlace y por lo tanto un aumento de la energía de vibración (fácilmente observado por las espectroscopias IR y Raman), como consecuencia del aumento de la constante de fuerza del enlace, f.

Así pues, cada estado de espín puede asociarse en primera aproximación a una parábola caracterizada por una energía potencial:

$$Ep_i = \tfrac{1}{2}(f_i R_i^2) \qquad i = HS, LS \qquad (1)$$

R_i = distancia media Fe-N

Esta energía potencial representa esencialmente la energía electrónica de los estados HS y LS. Ambas parábolas están separadas en sus mínimos por las distancia R características para iones Fe^{II} $R_{LS} \approx 2.0$ Å y $R_{HS} \approx 2.2$ Å (siendo $\Delta R_{HL} \approx 0.2$ Å). Estas curvas contienen información acerca de la energía vibracional. Así pues, dichas parábolas representan también el modo de vibración totalmente simétrico de octaedro (A_{1g}). Una representación de las energías Ep_i de las parábolas asociadas a los estados HS y LS frente a R se presenta en la Figura 2. El desplazamiento horizontal de ambas parábolas corresponde a $\Delta R_{HL} \approx 0.2$ Å, mientras que el desplazamiento vertical indica que para una molécula aislada el estado LS está estabilizado con respecto al HS por una energía ΔE_{HL}.

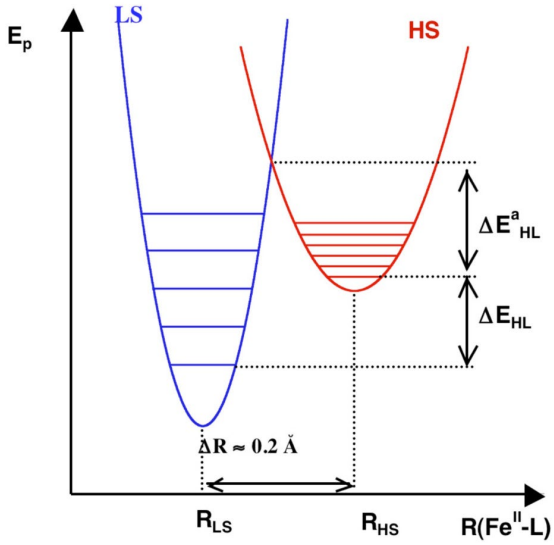

Figura 2. *Curvas de energía potencial de los estados HS y LS mostrando la diferencia entálpica ΔE_{HL}, la energía de activación ΔE^a_{HL} y los estados vibracionales correspondientes.*

La energía vibracional de los diferentes niveles será:

$$E^{vibr}_i (n) = (n + 1/2)\, h\nu_i \qquad \nu_i = 1/2\pi\, (f_i/m)^{1/2} \text{ (m es la masa reducida)} \qquad (2)$$

Los niveles vibracionales se representan como líneas horizontales igualmente espaciadas dentro de las correspondientes parábolas (Figura 2). Dado que $f_{LS} > f_{HS}$ el número de niveles vibracionales por unidad de energía es mayor para el estado HS que para el LS, es decir, la separación entre los niveles vibracionales es menor en el estado HS. Igualmente, la multiplicidad de espín del estado HS es mayor que la del estado LS.

A muy bajas temperaturas, la molécula se encuentra en el nivel vibracional fundamental (n = 0) del estado LS. A medida que aumenta la temperatura, la molécula va transformando la energía térmica aportada en energía vibracional ocupando niveles vibracionales excitados hasta alcanzar el punto de cruce de ambas parábolas donde se produce el cambio de estado de espín, en el que la geometría del estado precursor, el LS, y el sucesor, el HS, es la misma. De acuerdo con el principio de Franck-Condon es en este punto donde tiene lugar la transformación HS ↔ LS. Este punto de cruce, Δ_c, representa una región inestable donde las especies transitorias pueden cambiar su estado de espín.

El coste energético para salvar la diferencia entálpica, ΔE_{HL}, entre ambos estados está compensado por la diferencia de entropía de los mismos, que favorece la población del estado HS a altas temperaturas. Visto de otra forma, la molécula absorbe energía para compensar la diferencia entálpica ΔE_{HL} que desfavorece el estado HS. Dicha energía absorbida es de origen entrópico y tiene dos componentes diferentes. Por un lado, hay una componente electrónica relacionada con el cambio de multiplicidad de espín (2S + 1) [HS (S = 2) y LS (S = 0) para el ion Fe^{II}]:

$$AS_{el.} = R \ln [(2S + 1)_{HS}/[(2S + 1)_{LS}] = R \ln (5/1) = 13.45 \text{ J K}^{-1} \text{ mol}^{-1} \qquad (3)$$

Por otro lado, hay una componente vibracional que deriva del mayor número de niveles vibracionales por unidad de energía (g_i) asociado al estado HS, dada la menor magnitud de la constante de fuerza de enlace f_{HS}:

$$AS_{vibr.intr.} = R \ln (g_{HS}/g_{LS}) \qquad (4)$$

El acceso experimental a la relación g_{HS}/g_{LS} conlleva serias dificultades, pero es posible estimarla a partir de la entropía total obtenida de las medidas de calorimetría y del análisis de los espectros IR y/o Raman correspondientes a los estados HS y LS.[17] Por consiguiente el comportamiento SCO térmicamente inducido es un proceso controlado por la entropía.

La influencia de la presión en la transición de espín también puede entenderse a partir de los pozos de potencial. Sin tener en cuenta la fuente de la presión (química o mecánica) el efecto principal de la presión es la desestabilización del estado HS, ya que el volumen de éste es mayor que el del LS. Así pues, la presión disminuye ΔR_{HL} y aumenta ΔE_{HL}, por lo que la parábola se desplaza verticalmente.[18] Como consecuencia, la presión

produce la disminución de la energía de activación, E^a_{HL}, correspondiente a la diferencia en energía entre el nivel vibracional n = 0 del estado HS y el punto de cruce definido por los dos pozos de potencial.

Generalmente, a temperaturas mayores de 100 K la energía térmica, k_BT, es mayor que la energía de activación, E^a_{HL}, hecho que determina la cinética de la conversión HS ↔ LS, incluso a presión atmosférica. Por ello la cinética del proceso se caracteriza por una constante de velocidad, $k_{HL} \approx 10^6 – 10^8$ s^{-1}, que garantiza el equilibrio termodinámico de las magnitudes físicas observadas.

Cuando la energía térmica es del orden o menor que la energía de activación, $k_BT \leq E^a_{HL}$, esta afirmación ya no es válida y la constante k_{HL} disminuye hasta valores del orden de $10^{-1} – 10^{-7}$ s^{-1}, con lo que es posible "congelar" el estado HS a temperaturas donde no es estable, ya que la molécula no dispone de la energía suficiente para superar la barrera de paso E^a_{HL} desde el estado HS al LS.

A temperaturas del orden de 50 - 90 K es fácil estudiar las cinéticas de relajación, que en principio son de primer orden, pudiéndose correlacionar la variación térmica de k_{HL} en términos de la representación de Arrhenius.

Para temperaturas muy bajas, en los compuestos típicos SCO de Fe^{II}, se observa que el proceso de relajación ya no sigue una ley de Arrhenius pura, sino que se desvía, más cuanto menor es la temperatura, hasta observar una independencia térmica de $\ln(k_{HL})$, hecho que suele tener lugar por debajo de 40 K. De hecho por debajo de 30 K, k_{HL} es muy pequeña, $[k_{HL}(T \rightarrow 0)] \approx 10^{-7}$ s^{-1}, e independiente de la temperatura, y el proceso de relajación tiene lugar esencialmente vía efecto túnel. La velocidad de relajación en la región túnel puede relacionarse con los desplazamientos "vertical" y "horizontal" de las curvas de energía potencial de los estados HS y LS a través del marco conceptual de los procesos de relajación no adiabáticos multifonónicos.[19]

Sin embargo, este no es el caso para compuestos de Fe^{III} y Co^{II}, que normalmente presentan relajaciones muy rápidas incluso a temperaturas por debajo de 10 K. Para estos sistemas el cambio de energía configuracional es menor que para los compuestos de Fe^{II}, ya que el cambio en las distancias de enlace es mucho menor también. La relajación HS ↔ LS en compuestos SCO es un proceso modelo que participa del comportamiento clásico y

el mecano-cuántico, y ha sido estudiado en profundidad por Hauser y colaboradores entre otros.[20]

1.1.2.- Fotoconversión (efecto LIESST) en compuestos SCO

La luz es un camino muy eficaz para "comunicarse" con un sistema molecular sobre todo cuando se trata de encontrar posibles aplicaciones tecnológicas. La foto-inducción en compuestos SCO fue observada por primera vez por primera vez por McGarvey y Lawthers en disolución a temperaturas relativamente altas,[21] sin embargo, el tiempo de vida media de los estados inducidos era muy corto. Más adelante, en 1994, Decurtins y colaboradores observaron por primera vez el proceso de foto-inducción en materiales SCO en estado sólido a bajas temperaturas para el complejo $[Fe(1\text{-propiltetrazol})_6](BF_4)_2$.[22] Al irradiar la muestra en el estado LS con luz verde (λ = 514.5 nm) a temperaturas bor debajo de 50 K el color de la muestra pasa del púrpura del estado LS al blanco, propio del HS. El fenómeno fue denominado "light induced spin state trapping" (LIESST).

A temperaturas suficientemente bajas el estado LS está totalmente poblado y el espectro visible del sistema d^6 en simetría octaédrica se caracteriza por dos bandas relativamente intensas correspondientes a las transiciones v_1 ($^1A_{1g} \rightarrow {}^1T_{1g}$) (≈ 12000 – 20000 cm^{-1}) y v_2 ($^1A_{1g} \rightarrow {}^1T_{2g}$) (≈ 20000 – 25000 cm^{-1}) que a menudo están enmascaradas por las bandas de transferencia de carga metal ligando TCML ($d_M \rightarrow \pi^*_L$).

La irradiación con luz verde estimula la transición $^1A_{1g} \rightarrow {}^1T_{1g}$. El tiempo de vida media del estado excitado $^1T_{1g}$ es de tan sólo nanosegundos, por lo que el sistema se relaja rápidamente. Dicha relajación debería tener lugar normalmente al estado inicial $^1A_{1g}$. No obstante, existe una pequeña probabilidad de relajación a través de los estados de espín intermedio $^3T_{1g}$ y $^3T_{2g}$ por mecanismos de cruce entre sistemas ("intersystem crossing", ISC) permitidos por acoplamiento espín-órbita de segundo orden. La relajación desde los estados de espín intermedio puede ocurrir de nuevo por medio de dos procesos ISC, uno implica la relajación al estado fundamental $^1A_{1g}$ y otro al metastable $^5T_{2g}$ donde las moléculas permanecerán atrapadas, siempre que k_BT sea suficientemente menor que E^a_{HL}. A bajas temperaturas el estado metaestable $^5T_{2g}$ tiene un tiempo de vida media muy largo, dado que la relajación $^5T_{2g} \rightarrow {}^1A_{1g}$ está prohibida.

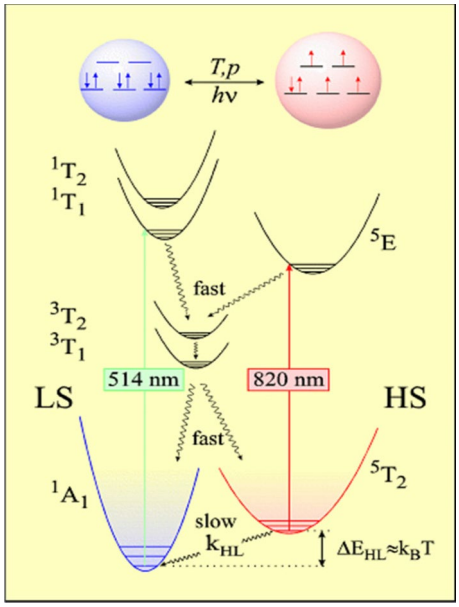

Figura 3. *Esquema representativo del fenómeno de foto-inducción de una transición de espín, efecto LIESST.*

La foto-excitación durante un período de tiempo suficiente, implica la población total del estado metaestable HS, $^5T_{2g}$, a costa del despoblamiento del LS, con lo que se invierte la población de los estados. El estado metaestable HS puede volver al estado LS de partida irradiando con luz roja (λ = 820 nm), el llamado efecto LIESST inverso ($^5T_{2g} \rightarrow {}^3T_{1g} \rightarrow {}^1A_{1g}$), o simplemente aumentado la temperatura.

El descubrimiento del efecto LIESST representó un avance importante el estudio de la dinámica del comportamiento SCO en estado sólido, dado que el rango de temperaturas en las cuales el equilibrio termodinámico podía ser foto-perturbado se extendió considerablemente. Desde entonces, el número de compuestos en los que se ha observado el efecto LIESST ha aumentado considerablemente.

1.1.3.- Comportamiento conjunto del grupo de centros activos: cooperatividad

Aunque el origen del fenómeno de transición de espín es puramente molecular la manifestación macroscópica del sólido es el resultado de la interacción cooperativa entre las moléculas que constituyen el material. La naturaleza cooperativa de la conversión de espín ha estimulado mucho interés dado que las transiciones de fase de primer orden que se producen acompañadas de histéresis térmica confieren a estos materiales un cierto grado de memoria, que podría ser potencialmente aprovechada en futuras aplicaciones. La cooperatividad radica esencialmente en la diferencia de tamaño que presenta la molécula en cada uno de los estados de espín. Así pues, tiene un origen elástico que da lugar a interacciones de largo alcance. Estas interacciones podrían ilustrarse como una presión interna, que crece con el aumento de las especies LS e interactúa con todas las moléculas del cristal con la misma intensidad, independientemente de las distancias.[23]

Es posible explicar el carácter continuo, discontinuo, histéresis o incluso la temperatura crítica $T_{1/2}$ (temperatura para la cual la fracción molar de especies HS y LS es 0.5) en términos de la termodinámica de transiciones de fase debida a Slichter y Drickamer.[24]

Si se considera un número N de moléculas que pueden dar lugar al fenómeno SCO, cada molécula podrá existir en el estado HS o en el estado LS, de manera que podemos definir la fracción molar de las moléculas HS como γ_{HS}, siéndola fracción molar de moléculas LS $(1 - \gamma_{HS})$. En ausencia de interacciones intermoleculares podemos introducir en la expresión de la energía libre de Gibbs, G, un término para la entropía de mezcla, S_{mix}. Este término representa las diferentes posibilidades de distribuión de las poblaciones HS (γ_{HS}) y LS $(1 - \gamma_{HS})$, para el total de moléculas N. La entropía de mezcla S_{mix} se expresa como:

$$S_{mix} = k\,[N \ln N - \gamma_{HS} N \ln \gamma_{HS} N - (1 - \gamma_{HS}) N \ln (1 - \gamma_{HS}) N] \qquad (5)$$

que puede rescribirse como:

$$S_{mix} = -R[\gamma_{HS} \ln \gamma_{HS} - (1 - \gamma_{HS})\ln(1 - \gamma_{HS})] \qquad (6)$$

donde R es la constante de gases. S_{mix} es máxima para $\gamma_{HS} = 0.5$ y desaparece para $\gamma_{HS} = 0$ o 1. Al tener en cuenta el término S_{mix}, la expresión de la energía libre de Gibbs queda:

$$G = \gamma_{HS}\, G_{HS} + (1 - \gamma_{HS})G_{LS} - T\, S_{mix} \qquad (7)$$

donde G_{HS} y G_{LS} corresponden a las energías libres de Gibss para los estados electrónicos HS y LS, respectivamente. La derivada parcial de G con respecto a γ_{HS} es

$$\left(\frac{\partial G}{\partial \gamma_{HS}}\right) = \Delta G + RT \ln\left(\frac{\gamma_{HS}}{1-\gamma_{HS}}\right) \qquad (8)$$

La condición de equilibrio térmodinámico para el fenómeno SCO a cualquier temperatura y presión es:

$$\left(\frac{\partial G}{\partial \gamma_{HS}}\right)_{T,\,P} = 0 \qquad (9)$$

por lo que

$$\ln\left(\frac{1-\gamma_{HS}}{\gamma_{HS}}\right) = \frac{\Delta G}{RT} = \frac{\Delta H}{RT} - \frac{\Delta S}{R} \qquad (10)$$

Teniendo en cuenta que $\Delta G = 0$ cuando $\gamma_{HS} = \gamma_{LS} = 0.5$ y que por tanto $T_{1/2} = \Delta H/\Delta S$, se obtiene

$$\gamma_{HS} = \frac{1}{1+\exp\left[\frac{\Delta H}{R}\left(\frac{1}{T} - \frac{1}{T_{1/2}}\right)\right]} \qquad (11)$$

Las interacciones moleculares vienen reflejadas en el modelo de Slichter y Drickamer por un parámetro de interacción, G_{int}.

$$G_{int} = \Gamma\, \gamma_{HS}\, (1 - \gamma_{HS}) \qquad (12)$$

donde Γ es el parámetro de la cooperatividad.

Tomando G_{LS} como el origen de energías, podemos escribir,

$$G = \gamma_{HS}\Delta H + \Gamma\gamma_{HS}(1 - \gamma_{HS}) + T[R\gamma_{HS}\ln\gamma_{HS} + R(1 - \gamma_{HS})\ln(1 - \gamma_{HS}) - \gamma_{HS}\Delta S] \qquad (13)$$

Esta ecuación permite representar curvas de energía libre, G, frente a la fracción molar de HS, γ_{HS}, para diferentes valores de ΔH, ΔS, Γ y T. Teniendo en cuenta de nuevo la condición de equilibrio se llega a

$$\ln\left(\frac{1-\gamma_{HS}}{\gamma_{HS}}\right) = \frac{\Delta H + \Gamma(1-2\gamma_{HS})}{RT} - \frac{\Delta S}{R} \qquad (14)$$

Si $\Delta G < 0$ el estado electrónico de las moléculas es HS y cuando $\Delta G > 0$ el estado de las moléculas es el LS. En condiciones de equilibrio termodinámico, $\Delta G = 0$ y $\gamma_{HS} = \gamma_{LS}$. Si además se tiene en cuenta la influencia de la presión en la TS, se introduce un nuevo término en la ecuación, quedando:

$$\ln\left(\frac{1-\gamma_{HS}}{\gamma_{HS}}\right) = \frac{\Delta H + P\Delta V + \Gamma(1-2\gamma_{HS})}{RT} - \frac{\Delta S}{R} \qquad (15)$$

Resumiendo, la ecuación de estado puede describirse de la forma siguiente:

$$\ln[(1-\gamma_{HS})/\gamma_{HS}] = [\Delta H + P\Delta V + \Gamma\,(1 - 2\,\gamma_{HS}) - T\,\Delta S] / RT \qquad (16)$$

siendo γ_{HS} la fracción molar de HS. ΔH y ΔS son las variaciones de entalpía y entropía por mol involucradas en el cambio de estado de espín y se pueden obtener directamente a partir de las medidas de calorimetría (C_p vs. T), y ΔV es el cambio de volumen molar asociado a SCO que se suele obtener directamente de las medidas de difracción de rayos X a bajas temperaturas (este término es despreciable a presión atmosférica). Es importante resaltar que la relación $\Delta H/\Delta S$ corresponde a la temperatura característica de la transición, T_c o $T_{1/2}$, a la cual $\gamma_{HS} = \gamma_{LS} = 0.5$, y se obtiene directamente de la curva SCO. Por otro lado, se considera que el término $P\Delta V$ es puramente entálpico y aumenta principalmente la diferencia de energía libre entre las fases HS y LS.

El parámetro de la cooperatividad, Γ, representa la tendencia que tiene una molécula o centro activo, en un estado de espín determinado, a rodearse de moléculas o centros activos con el mismo espín. Por tanto, Γ es un reflejo de la eficacia con que se transmiten a lo largo del cristal los cambios estructurales asociados a la transición de espín vía interacciones intermoleculares y es responsable de la manifestación cooperativa de las propiedades físicas del sistema.

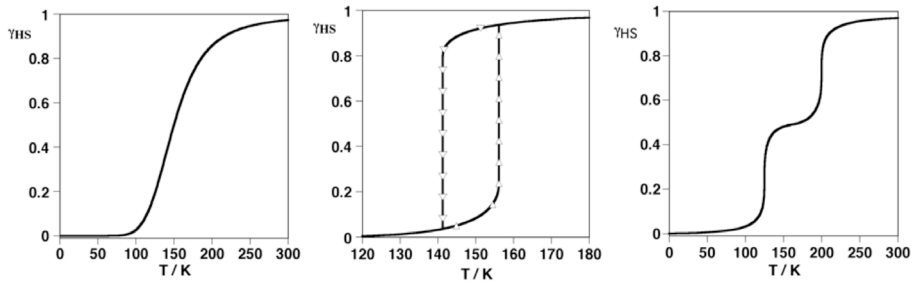

Figura 4.- *Tipos principales de curvas SCO representadas en la forma de γ_{HS} frente a T: gradual (izquierda), abrupta y con histéresis (centro) y en dos etapas (derecha).*

La ecuación de estado hace posible simular los comportamientos más representativos de las curvas SCO, que van desde la transición gradual ($\Gamma = 0$) a una transición de primer orden y con histéresis ($\Gamma > 2RT_c$) (Figura 4 izquierda y centro, respectivamente). Si se modifica esta ecuación de la manera conveniente pueden simularse también transiciones incompletas con fracciones residuales de HS y/o LS a temperaturas bajas y altas respectivamente, o incluso transiciones en dos etapas (4 derecha).

El parámetro γ_{HS} se obtiene normalmente a partir de medidas magnéticas, espectroscopía Mössbauer (en el caso de compuestos con hierro), espectroscopia electrónica (en el visible) y vibracional o incluso a partir de medidas de difracción de rayos X.

Este modelo, al igual que otros equivalentes explica los aspectos principales de la transición de fase. Por lo tanto, es insensible con respecto a pequeñas modificaciones estructurales y electrónicas, que afectan drásticamente a la cooperatividad y al campo de ligandos del centro metálico. Estas modificaciones vienen inducidas normalmente por grupos voluminosos, o ligandos capaces de dar lugar a apilamiento π o a interacción por puentes de H, pero también por la presencia de moléculas de disolvente y aniones en la red cristalina.

Otro punto importante es la aparición de polimorfismo, que puede surgir a raíz de pequeñas diferencias en el proceso de cristalización, tales como temperaturas distintas, métodos distintos, mezclas de disolventes, etc. Por desgracia, la racionalización de estos factores es relativamente difícil, dado que no son siempre coherentes de un sistema a otro y por lo general son impredecibles.

1.1.4.- Técnicas de detección del fenómeno SCO

Las técnicas experimentales que se emplean en la caracterización de los materiales con transición de espín pueden agruparse según el tipo de información que proporcionen.

Por un lado, se emplean técnicas para investigar las configuraciones electrónicas de los centros SCO, entre las que se encuentran la espectroscopia UV-Visible, la espectroscopia IR, la espectroscopia Mössbauer y las medidas de susceptibilidad magnética. Por otro lado, encontramos técnicas que permiten obtener los parámetros termodinámicos asociados al fenómeno SCO, entre las que se encuentran las medidas de calorimetría (DSC). Por último, los métodos de resolución estructural permiten estudiar los cambios estructurales que tienen lugar en la esfera de coordinación de los centros SCO, así como cambios en la red cristalina. Entre los distintos métodos encontramos la difracción de rayos X (para polvo y monocristal), estudios de radiación sincrotrón (XAS o "X-ray Absorption Spectroscopy", EXAFS o "Extended X-ray Absorption Fine Structure", XANES o "X-ray absorption near edge structure", NFS o "Nuclear Forward Scattering").[25]

Además de las técnicas arriba mencionadas, el desarrollo y el avance en el estudio de las transiciones de espín ha comenzado a hacer uso de técnicas no tan convencionales que permiten obtener información y realizar un seguimiento de la conversión, como por ejemplo la resonancia magnética nuclear (RMN), la resonancia paramagnética electrónica (EPR, sólo para compuestos de Fe^{III} y Co^{II}), la elipsometría, la espectroscopía de aniquilación de positrones (PAS) o la rotación del espín muónico (MuSR).[25]

1.2.- Objetivos de la tesis doctoral

Aprovechando la amplia experiencia de nuestro grupo de investigación en el estudio de materiales multifuncionales conmutables que presentan el fenómeno SCO, la presente tesis doctoral se ha centrado en el diseño racional de una nueva generación de complejos de Fe^{II} biestables que permitan estudiar nuevas sinergias entre el comportamiento SCO y otras propiedades físico-químicas de interés (luminiscencia, química huésped-anfitrión).

Durante este trabajo, se sintetizaron polímeros de coordinación porosos (PCP: Porous Coordination Polymers) de Fe^{II} con estructuras de tipo Hofmann que exhiben propiedades SCO. Estos compuestos fueron caracterizados mediante técnicas físico-químicas tales como medidas mágneticas, medidas DSC, medidas de drifracción de rayos X sobre monocristal y/o polvo, TGA y espectroscopía de absorción UV-Vis en monocristal. Además, se estudió la sinergia SCO-luminiscencia del primer polímero de coordinación 3D de tipo Hofmann $\{Fe^{II}(bpben)[Au(CN)_2]\}$@pyr, el cuál está funcionalizado con pireno (pyr) como molécula huésped. Por otra parte, también se estudió el acoplamiento SCO-luminiscencia siguiendo dos estragegias: incluyendo el agente fluorescente como parte de la estructura principal $\{Fe^{II}(\textit{bpan})[M^{I}(CN)_2]_2\}$ o siendo una molécula invitada insertada dentro de los poros de la red conmutable 3D $\{Fe^{II}(\textit{bpb})[M^{I}(CN)_2]_2\}\cdot$pyr.

Por último, se estudió la modulación controlada del comportamiento SCO a través de la adsorción-desorción de moléculas invitadas. Para llevar a cabo este estudio, intercambiamos el ligando 4-PhPy en los clatratos de Hofmann 2D $\{Fe(4\text{-}PhPy)_2[M(CN)_4]\}$ por 2,4-Bipy, dando lugar a los compuestos isomorfos $\{Fe(2,4\text{-}Bipy)_2[M(CN)_4]\}$, los cuales difieren básicamente de los primeros en que tienen un heteroátomo N no coordinado en el sustituyente aromático auxiliar.

1.3.- Metodología

Preparación de ligandos. Los ligandos no comerciales *bpben*, *bpb* y *bpan* se sintetizaron según procedimientos experimentales estandarizados y previamente publicados. Posteriormente, fueron caracterizados mediante estudios de resonancia magnética nuclear (RMN)

Síntesis de los compuestos SCO. La síntesis de los polímeros de coordinación SCO de tipo Hofmann se llevaron a cabo mediante técnicas de cristalización basadas en la difusión lenta de los reactivos. Principalmente, los recipientes utilizados para realizar las cristalizaciones fueron tubos en forma de H (o alguna de sus variantes, como son los tubos de 3 brazos) y tubos de ensayo. Los monocristales obtenidos se utilizaron para analizar su estructura mediante difracción de rayos X.

Caracterización físico-química. En una primera etapa, los compuestos SCO sintetizados se caracterizaron a través de análisis elemental, análisis EDX, análisis termogravimétrico (TGA) y espectroscopía infrarroja. Posteriormente, las propiedades magnéticas de cada material se evaluaron mediante el susceptómetro SQUID en el rango de temperaturas 2 – 400 K. A continuación, se realizaron medidas de calorimetría diferencial de barrido (DSC) en el intervalor de temperatura 120 – 410 K, lo cual permitió conocer los parámetros termodinámicos ΔH y ΔS asociados al fenómeno SCO. Finalmente, la estructura cristalina de los diferenes compuestos SCO se determinó a diferentes temperaturas mediante técnicas de difracción de rayos X sobre monocristal y/o polvo microcristalino, utilizando en alguno de los casos radiación sincrotrón. Además, en algún ejemplo en concreto, se monitorizó el comportamiento SCO en función de la temperatura mediante espectroscopia de absorción UV-vis.

1.4.- Bibliografia

[1] O. Kahn, *Molecular Magnetism*; VCH, New York, **1993**.

[2] R. Feynman, *Miniturization*, *Ed. A. Gilbert* (Reinhold, New York), **1961**, 282.

[3] W. A. Little, *Phys. Rev.*, **1964**, *A 134*, 1416.

[4] W. A. Little, *J. Polym. Sci.*, *Polym. Lett. Ed.*, **1970**, 29.

[5] K. E. Drexler, *Proc. Natl. Acad. Sci. USA*, **1981**, *78*, 5275.

[6] F. L. Cater, *Ed., Molecular Electronic Devices* (M. Dekker, New York), **1982**.

[7] F. L. Cater, *Ed., Molecular Electronic Devices II* (M. Dekker, New York), **1987**.

[8] J. S. Miller, *Adv. Mater.*, **1990**, *2*, 378.

[9] J. S. Miller, *Adv. Mater.*, **1990**, *2*, 495.

[10] J. S. Miller, *Adv. Mater.*, **1990**, *2*, 601.

[11] D. Goldhaber-Gordon, M. S. Montemerlo, J. C. Love, G. J. Opiteck, J. C. Ellenbogen, *Proceeding of the IEEE*, **1997**, *85*, 521.

[12] R. C. Haddon, A. A. Lamola, *Proc. Natl. Acad. Sci. USA*, **1985**, *82*, 1874.

[13] O. Kahn, J. P. Launay, *Chemtronics 3*, **1988**, 151.

[14] J. M. Lehn, *Supramolecular Chemistry. Concepts and persepctives*, VCH, Weinheim, **1995**.

[15] J. P. Sauvage, *Acc. Chem. Res*., **1990**, *23*, 151.

[16] A. Hauser, *J. Chem. Phys*., **1991**, *94*, 2741.

[17] a) A. Bousseksou, J. J. McGarvey, F. Varret, J. A. Real, J. P. Tuchagues, A. C. Dennis, M. L. Boillot, *Chem. Phys. Lett.*, **2000**, *318*, 419; b) N. Moliner, L. Salmon, L. Capes, M. C. Muñoz, J. F. Létard, A. Bousseksou, J. P. Tuchagues, J. J. McGarvey, A. C. Dennis, M. Castro, R. Burriel, J. A. Real, *J. Phys. Chem. B.,* **2002**, *106*, 4276; c) G. Molnár, V. Niel, A. B. Gaspar, J. A. Real, A. Zwick, A. Bousseksou, J. J. McGarvey, *J. Phys. Chem. B.*, **2002**, *106*, 9701; d) M. Sorai, S. Seki, *J. Phys. Chem. Solids,* **1974**, *35*, 555.

[18] a) T. Granier, B. Gallois, J. Gaultier, J. A. Real, J. Zarembowitch, *Inorg. Chem*., **1993**, *32,* 5305; b) P. Gütlich, V. Ksenofontov, A. B. Gaspar, *Coord. Chem. Rev*., **2005**, *249*, 1811-1829.

[19] a) E. Buhks, M. Bixon, J. Jortner, *J. Am. Chem. Soc*., **1980**, *102*, 2918; b) C. L. Xie, D. N. Hendrickson, *J. Am. Chem. Soc*., **1987**, *109*, 6981.

[20] A. Hauser, *Comments Inorg. Chem.*, **1995**, *17*, 17.

[21] J. J. McGarvey y I. Lawthers, *J. Chem. Soc., Chem. Commun.,* **1982**, 906.

[22] a) S. Decurtins, P. Gütlich, C. P. Köhler, H. Spiering, A. Hauser, *Chem. Phys. Lett.*, **1984**, *139*, 1; b) S. Decurtins, P. Gütlich, K. M. Hasselbach, H. Spiering, A. Hauser, *Inorg. Chem.,* **1985**, *24*, 2174.

[23] H. Spiering, T. Kohlhaas, H. Romstedt, A. Hauser, C. Bruns-Yilmaz, J. Kusz, P. Gütlich, *Coord. Chem. Rev*., **1999**, *190-192*, 471.

[24] a) C. P. Slichter, H G. Drickamer, *J. Chem. Phys*., **1972**, *56*, 2142; b) J. M. Honig, *J. Chem. Ed*., **1999**, *76*, 848.

[25] a) Eds. Gütlich, Goodwin, *Top. Curr. Chem.*, **2004**, vol. *233-235*; b) Ed. M. A. Halcrow, John Wiley & Sons, Ltd., **2013**.

CAPÍTULO 2

Thermo- and photo-modulation of exciplex fluorescence in a 3D spin crossover Hofmann-type coordination polymer

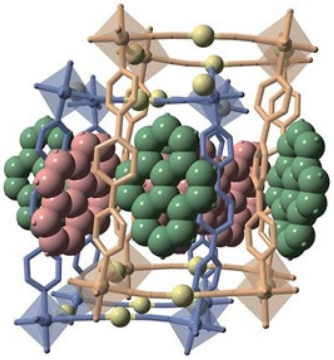

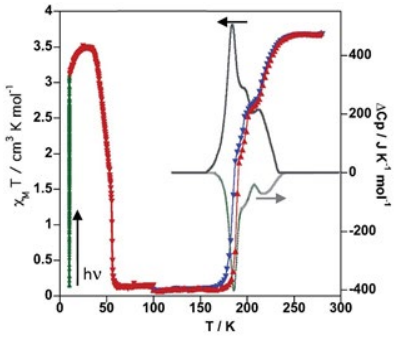

REVISTA: Chemical Science
ÍNDICE DE IMPACTO: 9.346

CAPÍTULO 2

Thermo- and photo-modulation of exciplex fluorescence in a 3D spin crossover Hofmann-type coordination polymer

2.1.- Abstract

The search for bifunctional materials showing synergies between spin crossover (SCO) and luminescence has attracted substantial interest since they could be promising platforms for new switching electronic and optical technologies. In this context, we present the first three-dimensional Fe^{II} Hofmann-type coordination polymer exhibiting SCO properties and luminescence. The complex $\{Fe^{II}(bpben)[Au(CN)_2]\}$@pyr (bpben = 1,4-bis(4-pyridyl)benzene) functionalized with pyrene (pyr) guests undergoes a cooperative multi-step SCO, which has been investigated by single crystal X-ray diffraction, single crystal UV-Vis absorption spectroscopy, and magnetic and calorimetric measurements. The resulting fluorescence from pyrene and exciplex emissions are controlled by the thermal and light irradiation (LIESST effect) dependence of the high/low-spin state population of Fe^{II}. Conversely, the SCO can be tracked by monitoring the fluorescence emission. This ON-OFF interplay between SCO and luminescence combined with the amenability of Hofmann-type materials to be processed at the nano-scale may be relevant for the generation of SCO-based sensors, actuators and spintronic devices.

2.2.- Introduction

Iron(II) spin crossover (SCO) complexes are responsive materials that switch between high-spin (HS) and low-spin (LS) states triggered by external stimuli (temperature, pressure, light, and analytes). This binary HS <-> LS behaviour entails strong electron-phonon coupling that involves drastic changes in the magnetic, electric, optical and mechanical properties of the SCO material when cooperative elastic interactions between the SCO centres are effective.[1] Cooperative SCO properties have attracted substantial interest specially when combined in a synergistic way with other relevant physical properties (i.e. electronic transport, chirality, luminescence, host-guest chemistry, tec) because the intrinsic ON-OFF nature of SCO may be transferred to the second property. This fact, together with the amenability of the

resulting functional material to be processed at micro- and nano-scale levels, has created important expectations for the discovery of new switching electronic and optical tchnologies.[2]

Luminescence is a relevant property that may used as an internal probe to report upon the spin state of SCO centres and conversely the control of the spin state may be used to modulate the luminescent signal. In this respect, it has been stated that the search for synergies between SCO and luminescence could be an important platform for thermometry and thermal imaging technologies.[3] Although, the interplay between SCO and luminescence was first reported 20 years ago,[4] it has been more recently that this binomial has gained much attention. Two main approaches have been designed to combine SCO and fluorescence in the same material. A first approach introduces fluorescence as an extrinsic property by physically doping the targeted SCO complex with a fluorescent dye during the fabrication of thin films or nanoparticles[5-10] In the second approach, luminescence is an intrinsic property if the SCO complex. Only a reduced number of examples of this second approach have been reported so far, which include discrete mononuclear[11-14] homodinuclear,[15] heterodinuclear Fe^{II}-Eu^{III},[4] heterotrinuclear Fe^{II}-Pt^{II},[16] and two 1-D coordination polymers.[17,18]

Hofmann-type Fe^{II} SCO coordination polymers (SCO-CP)[19,20] have afforded excellent examples of thermo-[21] and piezo-hysteretic behaviours,[22] multistep cooperative transitions,[23] relevant examples of porous systems where the SCO can be tuned by guest molecules favouring selective host-guest interactions,[24] post-synthetic chemical activity[25] and/or solid-state transformations.[26] In addition, they have demonstrated to be excellent platforms to investigate the SCO properties at the nano-scale (nanocrystals and thin films) as potential components for the generation of SCO-based sensors, actuators and spintronic devices.[27] In this context, and as a result of our systematic study of Hofmann-type Fe^{II} SCO-CP,[19] here we report on the thermo- and photo-induced multi-stable spin transition of a pyrene based 3-D Hofmann clathrate monitored by photoluminescence and on the corresponding thermo- and photo-modulation of the exciplex fluorescence emission. This study has been carried out based on single crystal UV-Vis absorption spectroscopy measurements, X-ray single crystal analysis at relevant temperatures and magnetic, photo-magnetic and calorimetric measurements on microcrystalline samples of the SCO-MOF {Fe^{II}(bpben)[Au(CN)2]}@pyr [**1Fe@pyr**] (bpben = 1,4-bis(4-pyridyl)benzene; py = pyrene). For comparative reasons, the homologous isostructural Zn^{II} derivate **1Zn@pyr** was also

synthesized and characterized and herein reported. As fas as we know this is the first SCO-CP implemented with luminescence properties.

2.3.- Results and discussion

2.3.1.- Synthesis and structure

Pale-yellow (**1Fe@pyr**) or white (**1Zn@pyr**) crystalline samples were obtained by slow diffusion methods from stoichiometric amounts of $M^{II}(BF_4)_2{\cdot}6H_2O$ (M^{II} = Fe, Zn), bpben and $K[Au(CN)_2]$ and an excess of pyrene dissolved in methanol (see the ESI).

Single crystal structure analysis of **1Fe@pyr** and **1Zn@pyr** at 120 and 280 K showed the non-centrosymmetric monoclinic space group *Cc*. Crystal data and structural parameters are given in Tables S1-S3 in the ESI.

There are two crystallographically distinct octahedral $[M^{II}N_6]$ sites constituted of 4 equatorial $[Au(CN)_2]^-$ groups and 2 axial bpben ligands (Fig. S1). The almost linear $[Au(CN)_2]^-$ groups bridge 4 equivalent $[M^{II}N_6]$ sites forming parallel stacks of $\{M_4^{II}[Au(CN)_2]_4\}_n$ 2D grids pillared by the bpben ligands, thus generating an open framework with **pcu** topology (Fig. 1). The wide $\{M_4^{II}[Au(CN)_2]_4\}$ window allow interpenetration of an identical framework made up of the other crystallographically independent $[M^{II}N_6]$ site (Fig. 1). This typo of structure is common for $\{Fe^{II}(L)[Au(CN)_2]\}$ SCO compounds where L is a bis-monodentate pyridine-type ligand.[19,20]

The two frameworks are held together by strong Au···Au interactions [average 3.0535(5) Å for **1Fe@pyr** and 3.10086(9) Å for **1Zn@pyr** at 120 K]. The average Fe-N bond length equal to 1.960 Å at 120 K and 2.154 Å at 280 K are typical of the Fe^{II} ion in LS and HS states, respectively. Thus, the average bond length variation associated with the spin-state change, 0.2 Å, is consistent with the occurrence of a complete LS ↔ HS conversion. This is in turn reflected in a change of the unit cell volume of 444.7 $Å^3$, which represents 6.7% of the HS unit cell volume or a volume change of 55.6 $Å^3$ per Fe^{II} upon SCO. This is a typical value observed for Hofmann clathrates.[19] It is worth nothing that, in the same interval of temperatures, a unit cell volume variation of 1% (68.4 $Å^3$) is observe for **1Zn@pyr**, which essentially corresponds to thermal contraction/expansion of the crystal in the temperature

interval 280-120 K where the average Zn^{II}-N bond length remains practically constant at *ca*. 2.145 Å.

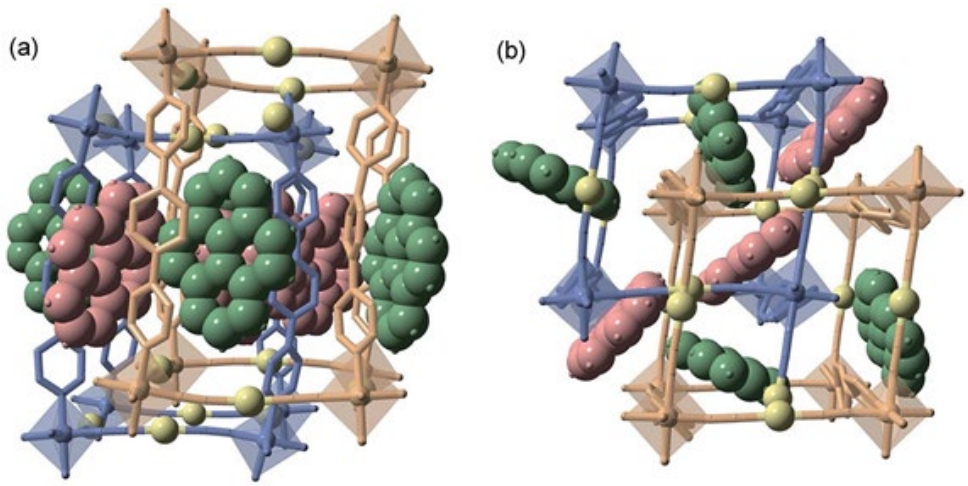

Fig. 1 *Two perpendicular perspective views ((a) side view and (b) topview) of the same fragment of the doubly interpenetrated frameworks* ***1M@pyr*** *(M^{II} = Fe, Zn) showing the bpben pillars, coordination centres and pyrene units. Two crystallographically distinct frameworks are represented in blue (network 1) and beige (network 2) colours, while the different pyrene molecules are depicted in red (pyr1) and green (pyr2) colours. Au centres are yellow spheres.*

The available space generated by the two interpenetrating frameworks is filled by two crystallographically independent pyr guest molecules that do not interact significantly with each other. In contrast, they define a large number of short π-π interactions with the bpben ligands (Fig. 2 and Table S4). The number and strength of these interactions are unequally distributed in each framework. The bpben1 pillars attached to the $[Fe_1N_6]$ nodes (blue colour, Fig. 1 and 2) define with the corresponding pyr1 guest (red colour) a face-to-face type interaction with 22 short C···C contacts smaller than the sum of the van der Waals radius (*ca*. 3.7 Å) ranging in the interval [3.44-3.68 Å] at 280 K (Table S4, Fig. S2). They markedly increase in number, up to 37 C···C contacts [3.30-3.66 Å], in the LS structure at 120 K (Fig. 2). It is worth nothing that this increase in short π-π interactions occurs synchronically with a small in-plane rotation of the pyr1 by *ca*. 6.1º (Fig. S2). In contrast, 22 [3.32-3.69 Å] and 12 [3.42-3.68 Å] short C···C contacts at 120 K and 280 K, respectively, are found between the bpben pillars attached to the $[Fe_2N_6]$ nodes (beige colour, Fig 1 and 2) and the corresponding pyr2 (green colour). This *ca*. 50% decrease of C···C interactions is due to parallel-displaced

π-π interactions in the latter. Although similar considerations can be made for **1Zn@pyr**, the larger ionic radius of Zn^{II} with respect to Fe^{II}-LS is reflected in a slight reduction in the number of π-π interactions (Table S4-bis, Fig. 2).

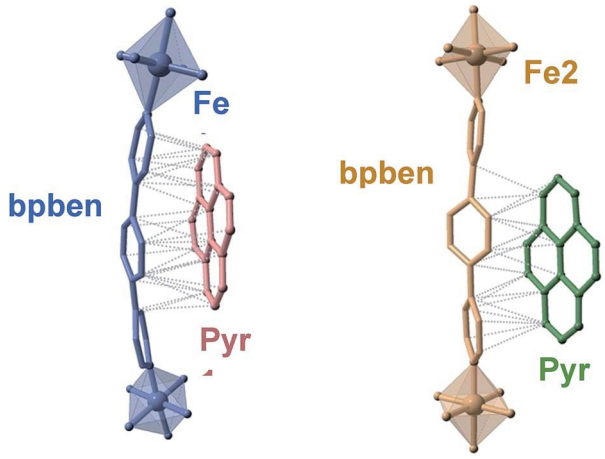

Fig. 2 *Crystallographically different bpben-pyrene pairs found in* ***1Fe@pyr*** *displaying the intermolecular π-π interactions (dotted lines) between bpben and pyrene (only short π-π contacts smaller than the sum of the C···C van der Waals radius ca. 3.7 are shown).*

A direct consequence of these strong π-π interactions is the bent geometry adopted by the bpben ligands. A similar situation was describe for the SCO Hofmann clhatrates $\{Fe(bpb)[M^{II}(CN)_4]\}\cdot 2G$, where the related rod-like bridging ligand bis(4-pyridyl)butadiyne (bpb) is markedly bent due to strong intermolecular interactions established with G = naphthalene or nitrobencene molecules.[28] For the titular compounds, we have estimated the magnitude of the bent in bpben measuring the distance of the pyridyl N atoms to the average plane defined by the central benzene ring (see Table S5a and Scheme I). It is important to note that the bent, and consequently the distance to the average plane, is larger for bpben1 than for bpben2 due to the larger number and more direct π-π interactions with pyr in the former. In addition to this, the pyridyl groups are alightly rotated with respect to the central benzene ring (Table S5b). Both, the bent distorsion and the angles defined by the intersection of the benzene and pyridyl rings do not change significantly upon the spin state change of Fe^{II}. Furthermore, these distances and angles are consistent with those found for **1Zn@pyr**. It is worth mentioning that the bent geometry found for the bpben pillars in the titular compounds strongly contrasts with the linear structure described previously for the solvate $[Fe(bpben)\{Au(CN)_2\}_2]\cdot S$ with S = $1.5DMF\cdot 0.3EtOH\cdot 0.2C_6H_{12}I$.[29]

2.3.2.- Spin crossover behaviour

Magnetic, photo-magnetic and calorimetric studies. The SCO was followed by magnetic measurements on bulk samples in the temperature interval 10-300 K (Fig. 3). At room temperature, the $\chi_M T$ product (χ_M = molar magnetic susceptibility and T = temperature) equal to 3.64 cm^3 K mol^{-1} is consistent with the Fe^{II} ion in the HS state. On cooling at a temperature scan rate of 1 K min^{-1}, $\chi_M T$ drops abruptly between 250 and 160 K, in three consecutive steps centred at 227, 195 and 180 K, to 0.14 cm^3 K mol^{-1} indicating a practically complete transformation to the LS state. In the heating mode, the magnetic curve does not match the cooling curve showing the presence of hysteresis in the second and third steps *ca*. 5 K wide. The overall equilibrium temperature, $T_{1/2}$, at which the HS and LS molar fractions are equal to 0.5 ($\gamma_{HS} = \gamma_{LS} = 0.5$; $\Delta G = 0$) is estimated to be centred at 190 K. This multi-step SCO behaviour is reminiscent of the one previously observed for the homologue solvate $[Fe(bpben)\{Au(CN)_2\}_2]\cdot S$ with S = 0.9 benzene, which undergoes a less steep three-step conversion centred at 214 K, 155 K and 141 K.[29] The occurrence of multi-step SCO is a relatively uncommon event in SCO that results from a competition between ferro- and antiferro-elastic interactions driven by the difference of volume associated with the LS and HS centres.[30] The steps involve stabilization of states characterized by different commensurate and/or incommensurate ordered fractional distributions of that dramatically depend on subtle structural changes of the solid, which are difficult to control.[31] Irradiation of the sample with red light (λ = 633 nm) at 10 K photo-generates the metastable HS* state (light induced excited spin state trapping (LIESST),[32] see the green line in Fig. 3).

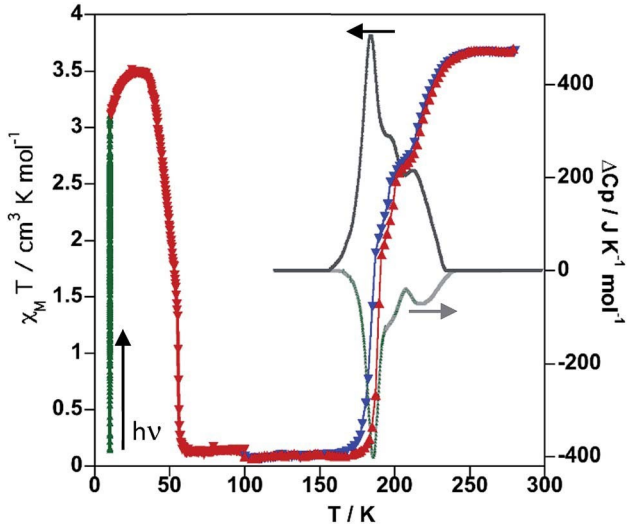

Fig. 3 *Magnetic, photomagnetic and calorimetric properties of 1Fe@pyr. Blue down triangles and red up triangles refer to cooling and heating modes, respectively. Green triangles show the increase of* χ_MT *upon irradiation at 10 K (LIESST effect), and red down triangles correspond to the heating from 10 K at 0.3 K min^{-1} to determine the* T_{LIESST} *temperature. Grey curves correspond to the anomalous variations of the molar specific heat* C_P *caused by the SCO for the cooling and heating modes.*

The subsequent heating at 0.3 K mol^{-1} in the dark shows an increase of $\chi_M T$, associated with the zero-field splitting of the S = 2 HS state of Fe^{II}, reaching a maximum value of 3.50 cm^3 K mol^{-1} in the temperature range 24-34 K, which suggests a quantitative population of the HS* state. Upon further heating the HS* relaxes back in two steps to the LS state with a characteristic $T_{LIESST} \approx 50$ K.[33]

The thermodynamic parameters obtained from differential scanning calorimetry were consistent with the $\chi_M T$ *vs.* T plot (grey lines in Fig. 3). The average enthalpy nand entropy variations ΔH = 10.9 kJ mol^{-1} and ΔS = 56 J K^{-1} mol^{-1} are typical of Fe^{II} SCO compounds.

Single crystal UV-Vis spectra. 1Fe@pyr displays a reversible thermo-chromic change between pale-yellow (HS) and red (LS). Consequently, the SCO behaviour was monitored on a single crystal through UV-Vis absorption spectra in the temperature range 300-10 K (cooling and heating modes) with temperature scan rates of 1 and 5 K min^{-1} while recording the spectra every 1 and 5 min (see Fig. 4a, S3 and S4, respectively). When cooling from 300 K to 10 K, the band centred at 800 nm associated with th HS state bleaches while a new band attributed to the LS state arises centred at 532 nm when cooling to 10 K.

Considering the thickness of the crystal, 50 ± 1 μm, and a concentration of Fe of around 1.6 M, a typical value of ferrous spin crossover systems, an extinction coefficient, *ε*, equal to 7 and 125 M^{-1} cm^{-1} was found, respectively, for the 800 and 532 nm bands. These values are consistent with the d-d transitions $^5T_2 \rightarrow {}^5E$ and $^1A_1 \rightarrow {}^1T_1$ characteristic of the HS and LS states of Fe^{II}, respectively.

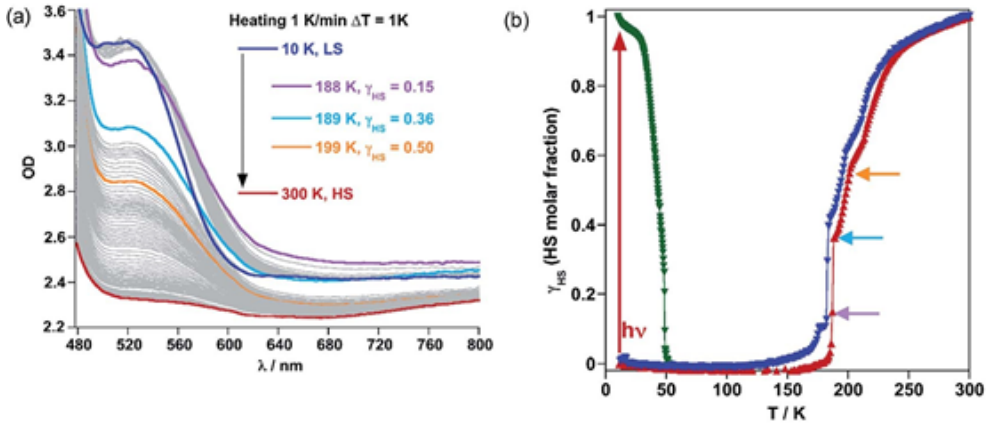

Fig. 4 *SCO properties of* ***1Fe@pyr*** *monitored by using single crystal UV-Vis spectra: (a) temperature variable UV-Vis absorption spectrum in the cooling mode and (b) HS molar fraction of the thermal and light induced SCO.*

Following the optical density difference between the maximum of the LS band at 532 nm and the tail of this band at 650 nm, the evolution of the HS molar fraction (γ_{HS}) with temperature was stablished by using Vergard's law (eqn (1)).

$$\gamma_{HS} = (OD_{LS} - OD_T)/(OD_{LS} - OD_{HS}), \quad (1)$$

where OD_{LS} is the optical density of the LS state, OD_{HS} is the optical density of the HS state at 300 K and OD_T is the optical density at a given temperature. The optical density (OD) is corrected from an eventual baseline jump or shift by taking the difference between the OD at 532 nm and the OD at 650 nm, where there is no noticeable absorption in the two states. The resulting SCO profile displays three main steps centred at 230, 195 and 184 K (Fig. 4b). Irradiation of the crystal with green light (λ = 532 nm) at 10 K quantitatively photo-generates the metastable HS*. The thermal stability of HS* was examined following the spectra when heating the crystal in the dark at 0.3 K min^{-1} from 10 to 60 K (Fig. 4b and S5). The thermal relaxation HS* → LS was characterized by a T_{LIESST} = 45 K. Both, thermal- and photo-induced SCO behaviours agree reasonably well with the complementary magnetic measurements.

2.3.3.- Synergy between fluorescence and spin crossover

The crystal structure of **1Fe@pyr** reveals that the pyr guest molecules and bpben bridging ligands lie in an environment thar is fully consistent to afford exciplex emission through π-π interactions.[34] Consistently with this, the excitation spectrum recorded at room temperature at 520 nm, shows a set of four different main bands, two of them highly resolved and centred at 254 and 332 nm. The other two bands are rather broad and centred at around 350 and 400 nm. Likewise, the emission spectrum of the sample has been recorded between 350 and 700 nm after excitation at 332 nm (Fig. S6). The two characteristici bands of the monomer and excimer of pyrene are centred at 400 and 500 nm, respectively. In order to study the influence of the thermal spin transition on the luminescence properties, the sample was cooled down to 10 K at 5 K min^{-1} and the luminescence spectra were recorded in the cooling and heating modes (Fig. 5a and S7). Upon cooling to 190 K from room temperature, the intensity of both peaks, excimer and monomer, slightly increase whereas with further cooling in the region of the spin transition at around 235-155 K the intensity of the monomer signal increase significantly concomitantly with the quenching of the excimer's signal (Fig.5a). The thermal dependence of fluorescence for the non-SCO isostructural compound **1Zn@pyr** after excitation at 332 nm shows two main maxima centred at 439 and 484 nm (Fig. 5b), whose intensity does not change significantly in the 235-155 K interval where **1Fe@pyr** displays the SCO behaviour (see Fig. 5c). Clearly the spin transition properties of **1Fe@pyr** have a strong influence on the photoluminescence properties. This observation is directly related to the absorption properties of the compound and the emission properties of the pyrene. The arising of the LS absorption band at 532 nm (Fig. 4a) upon cooling quenches the emission of the eximer signal of pyrene at 478 nm (Fig. 5a) due to the radiative energy transfer (emission-reabsorption) from the excited state of the pyrene to the MLCT-3d ($^1A_1 \rightarrow {}^1T_1$) band of the Fe^{II} complex in the LS state. The signal at 392 nm, that abruptly increase below the

spin transition, overlaps with the MLCT-3d ($^1A_1 \rightarrow {}^1T_1$) transition band of the compound at any

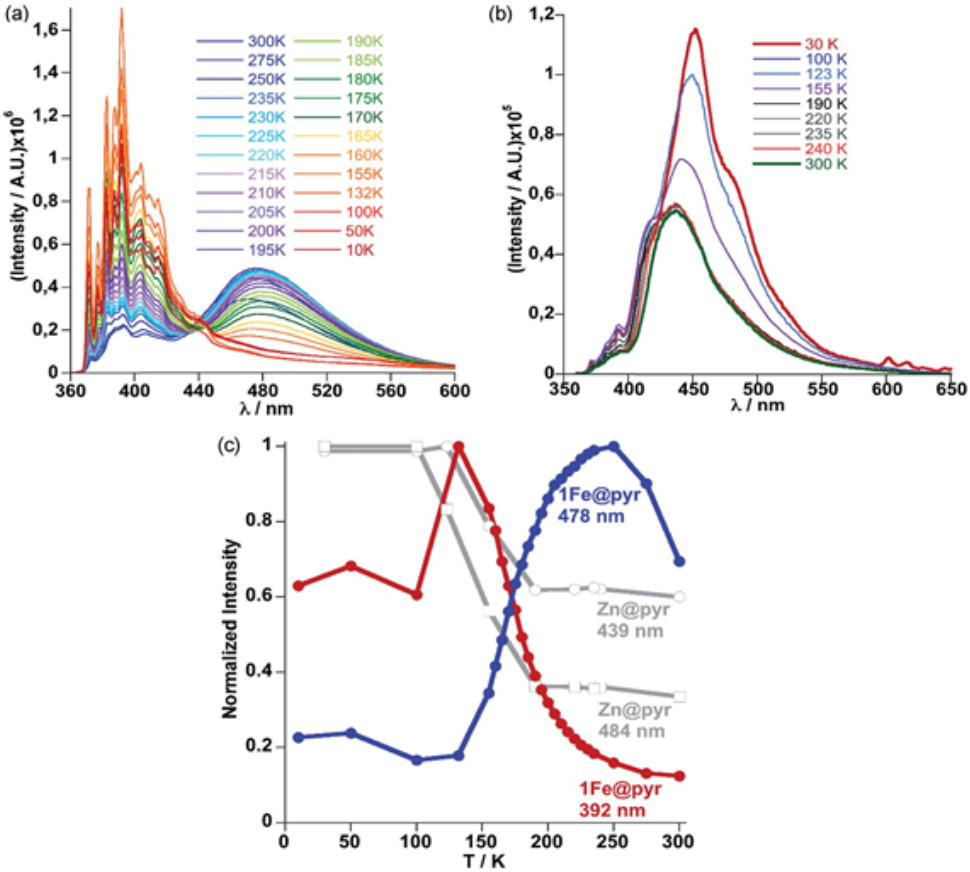

*Fig. 5 (a) Evolution of fluorescence spectra with temperature upon cooling from 300 K to 10 K at 5 K min^{-1} for **1Fe@pyr**. (b) Evolution of the luminescence spectra with temperature upon cooling from 300 K to 10 K at 5 K min^{-1} for **1Zn@pyr**. (c) Thermal dependence of normalized intensity of the monomer and excimer signals at 392 nm (red) and 478 nm (blue) for **1Fe@pyr** and 439 nm and 484 nm (grey) for **1Zn@pyr**.*

temperature. From the ratio between the intensity at 392 nm and 478 nm while heating and cooling at 5 K min^{-1} the thermal evolution of the normalized HS molar fraction $(\gamma_{HS})^{norm}$ has been obtained. The thermal spin transition stablished based on the luminescence properties of **1Fe@pyr** follows reasonably well the SCO profile obtained by absorption spectroscopy and magnetic measurements (Fig. 6). The differences observed, particularly at low temperatures, can be ascribed, on one hand, to the much more rapid temperature scan rate used for recording the SCO by luminescence and, on the other hand, to the difficulties to separate the

increasing signal of the monomer emission from that of the exciplex as temperature decreases. In spite of this, average equilibrium temperature at which $(\gamma_{HS})^{norm}$ = 0.5, $T_{1/2}$ = 189.5 K, centred in the middle of a hysteresis loop *ca*. 5 K wide, is virtually the same as that observed from magnetism and absorption spectroscopy. In a recent study, likely inspired by the complex $[Fe(abpt)_2(NCS)_2]$ with abpt = 4-amino-3,5-bis(pyridine-2-yl)-1,2,4-triazole,[35] pyrene was covalently coupled by condensation of 1-pyrenecarboxaldehyde with abpt to afford (pyrene-1-yl)-*N*-(3,5-di(pyridine-2-yl)-4*H*-1,2,4-triazol-4-yl)methanimine (L).[14] The resulting $[Fe(L)_2(NCS)_2]$ compound undergoes a SCO in the interval 200-350 K with $T_{1/2}$ = 267 K. The pyrene moieties interact with each other defining four face-to-face π-π interactions (3.66-3.85 Å). The lack of exciplex emission well separated from the intrinsic emission of pyrene moieties precluded from delineating a neat correlation between the thermal SCO and fluorescence profiles in this compound. However, the obvious differences observed in the temperature dependence of fluorescence between $[Fe(L)_2(NCS)_2]$ and the free ligand L, associated with a resonance energy tranfer process similar to that observed for **1Fe@pyr**, made possible to infer a clear influence of the SCO on the fluorescence. In particular, the partial population (*ca*. 21%) of the photo-generated HS* LIESST state of $[Fe(L)_2(NCS)_2]$ at 10 K also demonstrates the influence on the fluorescence.

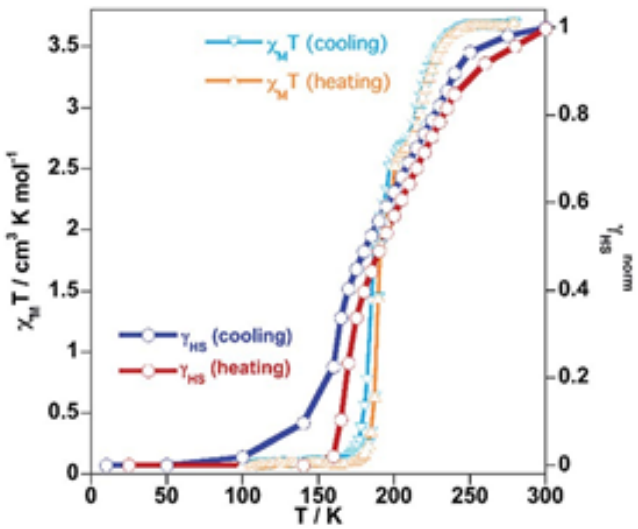

*Fig. 6 Comparison of the SCO profile obtained from magnetism and fluorescence for **1Fe@pyr**.*

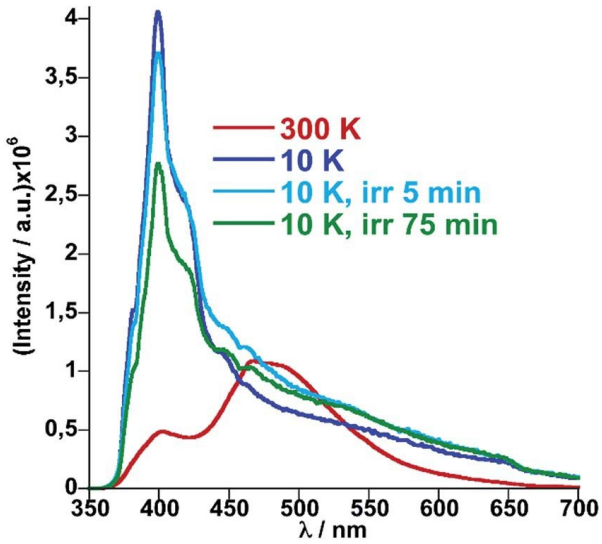

Fig. 7 Fluorescence spectra of 1Fe@pyr at 10 K before and after irradiation at 520 nm.

Similarly, photo-excitation of the titular compound **1Fe@pyr** from LS to HS* (LIESST effect) has been preliminary followed by luminescence. In Fig. 7 the fluorescence spectra at 10 K before and after irradiation of the sample at 520 nm at two different irradiation times are compared. Interestingly, the fluorescence of the monomer decreases concomitantly with an increase of excimer signal due to the excitation of the LS state into the metastable HS* state. Inthis sense, further analysis could be performed in order to study the cooperativity of the system though LIESST and HS to LS relaxations at low temperature by takin advantage of the photoluminescence properties of pyrene.

2.4.- Conclusions

In summary, we have successfully synthesized an unprecedented 3D Hofmann-type Fe^{II} SCO-CP functionalized with pyrene as a fluorescent guest. Strong π-π interactions between pyrene and the pillars of the **pcu** SCO framework result in exciplex emission. Both monomer and exciplex fluorescence are dependent on the spin state of the Fe^{II} nodes which in turn is controlled by temperature and light irradiation (LIESST effect), thereby resulting in ON-OFF switching of the luminescent signal. Implementing the prolific family of Hofmann-type SCO-MOFs with luminescence properties offers new opportunities for designing and probing devices at micro- and nano-scales for sensing and information processing. In this sense,

incorporation of a luminescent source in the pillars of the framework is a further desired step. Our preliminary results in this direction are very promising and will be reported elsewhere in due course.

2.5.- Notes and references

[1] See for example: (a) *Spin Crossover in Transition Metal Compounds I-III. Top. Curr. Chem.*, P. Gütlich, H.A. Goodwin, **2004**, vol. 233-235; (b) J. A. Real, A. B. Gaspar, M. C. Muñoz, *Dalton Trans.,* **2005,** 2062. (c) A. Bousseksou, G. Molnár, L. Salmon, W. Nicolazzi, *Chem. Soc. Rev.,* **2011**, *40*, 3313. (d) Spin-crossover materials: properties and applications, ed. M. A. Halcrow, John Wiley & Sons, **2013**.

[2] (a) M. Cavallini, I. Bergenti, S. Milita, J. C. Kengne, D. Gentili, G. Ruani, I. Salitros, V. Meded, M. Ruben, *Langmuir*, **2011**, *27*, 4076; (b) P. N. Martinho, C. Rajnak, M. Ruben, in *Spin-Crossover Materials: Properties and Applications*, ed. M. A. Halcrow, Wiley, **2013**, pp. 376–404; (c) G. Molnar, S. Rat, L. Salmon, W. Nicolazzi, A. Bousseksou, *Adv. Mater.*, **2018**, *30*, 17003862.

[3] H. J. Shepherd, C. M. Quintero, G. Molnar, L. Salmon, A. Bousseksou, in *Luminescent spin-crossover materials*, John Wiley & Sons Ltd., **2013**, p. 347.

[4] C. Piguet, E. Rivara-Minten, G. Bernardinelli, J.-C. Buenzli, G. Hopfgartner, *J. Chem. Soc., Dalton Trans.*, **1997**, 421.

[5] M. Matsuda, H. Isozaki, H. Tajima, *Thin Solid Films*, **2008**, 517, 1465.

[6] L. Salmon, G. Molnár, D. Zitouni, C. Quintero, C. Bergaud, J.-C. Micheau, A. Bousseksou, *J. Mater. Chem.*, **2010**, *20*, 5499.

[7] S. Titos-Padilla, J. M. Herrera, X.-W. Chen, J. J. Delgado. E. Colacio, *Angew. Chem., Int. Ed.*, **2011**, 50, 3290.

[8] C. M. Quintero, I. A. Gurals'kiy, L. Salmon, G. Molnar, C. Bergaud, A. Bousseksou, *J. Mater. Chem.*, **2012**, *22*, 3745.

[9] I. Suleimanov, O. Kraieva, J. Sánchez-Costa, I. O. Fritsky, G. Molnár, L. Salmon, A. Bousseksou, *J. Mater. Chem. C*, **2015**, *3*, 5026.

[10] I. Suleimanov, O. Kraieva, G. Molnár, L. Salmon, A. Bousseksou, *Chem. Commun*., **2015**, *51*, 15098.

[11] M. Hasegawa, F. Renz, T. Hara, Y. Kikuchi, Y. Fukuda, J. Okubo, T. Hoshi, W. Linert, *Chem. Phys*., **2002**, *277*, 21.

[12] H. Matzukizono, K. Kuroiwa, N. Kimikuza, *Chem. Lett*., **2008**, *37*, 446.

[13] A. Santoro, L. J. Kershaw Cook, R. Kulmaczewski, S. A. Barrett, O. Cespedes, M. A. Halcrow, *Inorg. Chem*., **2015**, *54*, 682.

[14] J.-L. Wang, Q. Liu, Y.-S. Meng, X. Liu, H. Zheng, Q. Shi, C.-Y. Duan, T. Liu, *Chem. Sci*., **2018**, *9*, 2892.

[15] Y. Garcia, F. Robert, A. D. Naik, G. Zhou, B. Tinant, K. Robeyns, S. Michotte, L. Piraux, *J. Am. Chem. Soc*., **2011**, *133*, 15850.

[16] B. Schafer, T. Bauer, I. Faus, J. A. Wolny, F. Dahms, O. Fuhr, S. Lebedkin, H.-C. Wille, K. Schlage, K. Chevalier, F. Rupp, R. Diller, V. Schünemann, M. M. Kappes, M. Ruben, *Dalton Trans*., **2017**, *46*, 2289.

[17] C.-F. Wang, R.-F. Li, X.-Y. Chen, R.-J. Wei, L.-S. Zheng, J. Tao, *Angew. Chem., Int. Ed*., **2015**, *54*, 1574.

[18] C. Lochenie, K. Schötz, F. Panzer, H. Kurz, B. Maier, F. Puchtler, S. Agarwal, A. Köhler, B. Weber, *J. Am. Chem. Soc*., **2018**, *140*, 700.

[19] M. C. Muñoz, J. A. Real, *Coord. Chem. Rev*., **2011**, *255*, 2068.

[20] Z.-P. Ni, J.-L. Liu, M. N. Hoque, W. Liu, J.-Y. Li, Y.-C. Chen, M. L. Tong*, Coord. Chem. Rev*., **2017**, *335*, 28.

[21] V. Niel, J. M. Martínez-Agudo, M. C. Muñoz, A. B. Gaspar, J. A. Real, *Inorg. Chem*., **2001**, *40*, 3838.

[22] A. Galet, A. B. Gaspar, M. C. Muñoz, G. V. Bukin, G. Levchenko, J. A. Real, *Adv. Mater*., **2005**, *17*, 2949.

[23] (a) N. F. Sciortino, K. R. Scherl-Gruenwald, G. Chastanet, G. J. Halder, K. W. Chapman, J. F. Létard, C. J. Kepert, *Angew. Chem., Int. Ed*., **2012**, *51*, 10154; (b) M. J. Murphy, K.

A. Zenere, F. Ragon, P. D. Southon, C. J. Kepert, S. M. Neville, *J. Am. Chem. Soc.*, **2017**, *139*, 1330.

[24] (a) M. Ohba, K. Yoneda, G. Agustí, M. C. Muñoz, A. B. Gaspar, J. A. Real, M. Yamasaki, H. Ando, Y. Nakao, S. Sakaki, S. Kitagawa, *Angew. Chem., Int. Ed.*, **2009**, *48*, 4767; (b) G. Agustí, R. Ohtani, K. Yoneda, A. B. Gaspar, M. Ohba, J. F. Sánchez-Royo, M. C. Muñoz, S. Kitagawa, J. A. Real, *Angew. Chem., Int. Ed.*, **2009**, *48*, 8944; (c) P. D. Southon, L. Liu, E. A. Fellows, D. J. Price, G. J. Halder, K. W. Chapman, B. Moubaraki, K. S. Murray, J. F. Létard, C. J. Kepert, *J. Am. Chem. Soc.*, **2009**, *131*, 10998; (d) R. Ohtani, K. Yoneda, S. Furukawa, N. Horike, S. Kitagawa, A. B. Gaspar, M. C. Muñoz, J. A. Real, M. Ohba, *J. Am. Chem. Soc.*, **2011**, *133*, 8600.

[25] J. E. Clements, J. R. Price, S. M. Neville, C. J. Kepert*, Angew. Chem., Int. Ed.*, **2014**, *53*, 10164.

[26] V. Niel, A. L. Thompson, M. C. Muñoz, A. Galet, A. E. Goeta, J. A. Real, *Angew. Chem., Int. Ed.*, **2003**, *42*, 3760.

[27] (a) V. Meded, A. Bagrets, K. Fink, R. Chandrasekar, M. Ruben, F. Evers, A. Bernand-Mantel, J. S. Seldenthuis, A. Beukman, H. S. J. van der Zant, *Phys. Rev. B: Condens. Matter Mater. Phys.*, **2011**, *83*, 245415; (b) F. Prins, M. Monrabal-Capilla, E. A. Osorio, E. Coronado, S. J. van der Zant, *Adv. Mater.*, **2011**, *23*, 1545; (c) M. Cavallini, I. Bergenti, S. Milita, J. C. Kengne, D. Gentili, G. Ruani, I. Salitros, V. Meded, M. Ruben, *Langmuir*, **2011**, *27*, 4076; (d) T. Miyamachi, M. Gruber, V. Davesne, M. Bowen, S. Boukari, L. Joly, F. Scheurer, G. Rogez, T. K. Yamada, P. Ohresser, E. Beaurepaire, W. Wulfhekel, *Nat. Commun.*, **2012**, *3*, 938; (e) P. N. Martinho, C. Rajnak, M. Ruben, in *Spin-Crossover Materials: Properties and Applications, ed. M. A. Halcrow, Wiley*, **2013**, p. 376 and references therein; (f) H. J. Shepherd, G. Molnár, W. Nicolazzi, L. Salmon, A. Bousseksou, *Eur. J. Inorg. Chem.*, **2013**, 653; (g) A. Rotaru, J. Dugay, R. P. Tan, I. A. Guralskiy, L. Salmon, P. Demont, J. Carrey, G. Molnár, M. Respaud, A. Bousseksou, *Adv. Mater.*, **2013**, *25*, 1745; (h) I. A. Gural'skiy, C. M. Quintero, J. Sánchez-Costa, P. Demont, G. Molnár, L. Salmon, H. J. Shepherd, A. Bousseksou, *J. Mater. Chem. C*, **2014**, *2*, 2949; (i) A. C. Aragonés, D. Aravena, J. I. Cerdá, Z. Acís-Castillo, H. Li, J. A. Real, F. Sanz, J. Hihath, E. Ruiz, I. Díez-Pérez, *Nano Lett.*, **2016**, *16*, 218.

[28] (a) L. Piñeiro-López, M. Seredyuk, M. C. Muñoz, J. A. Real, *Chem. Commun*., **2014**, *50*, 1833; (b) L. Piñeiro-López, F. J. Valverde-Munoz, M. Seredyuk, M. C. Muñoz, M. Haukka, J. A. Real, *Inorg. Chem*., **2017**, *56*, 7038.

[29] J.-Y. Li, C.-T. He, Y.-C. Chen, Z.-M. Zhang, W. Liu, Z.-P. Ni, M. L. Tong, *J. Mater. Chem. C*, **2015**, *3*, 7830.

[30] (a) E. Trzop, D. Zhang, L. Piñeiro-Lopez, F. J. Valverde-Muñoz, M. C. Muñoz, L. Palatinus, L. Guerin, H. Cailleau, J. A. Real, E. Collet, *Angew. Chem., Int. Ed*., **2016**, *55*, 1; (b) J. E. Clements, J. R. Price, S. M. Neville, C. J. Kepert, *Angew. Chem., Int. Ed*., **2016**, *55*, 15105; (c) D. Zhang, E. Trzop, F. J. Valverde-Muñoz, L. Piñeiro-López, M. C. Muñoz, E. Collet, J. A. Real, *Cryst. Growth Des*., **2017**, *17*, 2736; (d) N. F. Sciortino, K. A. Zenere, M. E. Corrigan, G. J. Halder, G. Chastanet, J. F. Létard, C. J. Kepert, S. M. Neville, *Chem. Sci*., **2017**, *8*, 70; (e) M. J. Murphy, K. A. Zenere, F. Ragon, P. D. Southon, C. J. Kepert, S. M. Neville, *J. Am. Chem. Soc*., **2017**, *139*, 1330.

[31] N. Ortega-Villar, M. C. Muñoz, J. A. Real, *Magnetochemistry*, **2016**, *2*, 6.

[32] S. Decurtins, P. Gütlich, P. C. Köhler, H. Spiering, A. Hauser, *Chem. Phys. Lett*., **1984**, *105*, 1.

[33] J. F. Létard, P. Guionneau, L. Rabardel, J. A. K. Howard, A. Goeta, D. Chasseau, O. Kahn, *Inorg. Chem*., **1998**, *87*, 4432.

[34] B. D. Wagner, G. J. McManus, B. Moulton, M. Zaworotko, *Chem. Commun*., **2002**, 2176.

[35](a) N. Moliner, A. B. Gaspar, M. C. Muñoz, S. Létard, J. F. Létard, X. Solans, R. Burriel, M. Castro, O. Kahn, J. A. Real, *Inorg. Chim. Acta*, **1999**, *291*, 279; (b) A. B. Gaspar, M. C. Muñoz, N. Moliner, V. Ksenofontov, G. Levchenko, P. Gütlich, J. A. Real, *Monatsh. Chem*., **2003**, *134*, 285.

2.6.- Supplementary Information

2.6.1. Experimental Section

2.6.1.1. Materials

$K[Au(CN)_2]$, $Fe(BF_4)_2{\cdot}6H_2O$ and $Zn(BF_4)_2{\cdot}6H_2O$ were purchased from commercial sources and used as received whereas the synthesis of the bpben ligand was performed as described elsewhere.[1]

2.6.1.2. Crystal growth

Single crystals of **1Fe@pyr** were grown by slow liquid-liquid diffusion technique using a modified H-vessel with a third tube added due to the limited solubility of the bpben in methanol where the $Fe(BF_4)_2{\cdot}6H_2O$ and $K[Au(CN)_2]$ salts were dissolved. The peripheral tubes (total volume ca. 10 mL) contained $Fe(BF_4)_2{\cdot}6H_2O$ (0.049 mmol, 16.47 mg) and $K[Au(CN)_2]$ (0.098 mmol, 33.38 mg) salts, respectively. The central tube (total volume ca. 10 mL) contained bpben ligand (0.058 mmol, 13.58 mg). Each individual tube was filled with methanol and finally with a saturated solution of pyrene in methanol. Afterwards, the tube were closed and two weeks later, light-yellow single crystals were formed in the tube which originally contained $Fe(BF_4)_2{\cdot}6H_2O$ salt with relative high yield (ca. 50%). The synthesis of the homologue **1Zn@pyr** was carried out following the same procedure.

EDX analysis (Energy dispersive X-Ray analysis) confirmed the stoichiometric relationship between metallic coordination centres [Fe:Au] and [Zn:Au] = [1:2]. *Elemental Analysis* for **1Fe@pyr**: Calculated for $C_{36}H_{22}Au_2FeN_6$ (988.4) (%): C 43.73; H 2.24; N 8.50. Found (%): C 44.40; H 2.31; N 8.35. *Elemental Analysis* for **1Zn@pyr**: Calculated for $C_{36}H_{22}Au_2ZnN_6$ (997.9) (%): C 43.33; H 2.22; N 8.42. Found (%): C 43.75; H 2.29; N 8.28.

2.6.1.3. Physical characterization

Single crystal absorption spectroscopy.

Single crystal of **1Fe@pyr** and **1Zn@pyr** were mounted on a copper plate with a previously drilled hole. One crystal was deposited in the middle of the hole and fixed with silver

paste to ensure a good thermal conductivity. The sample was then introduced into a closed cycle cryostat (Janis-Sumimoto SHI-4.5), which operates between 4 and 300 K and is equipped with a programmable temperature controller (Lakeshore Model 331). The cryostat was introduced into a double beam spectrometer (Varian Cary 5000).

Photoluminescence spectroscopy

The excitation and luminescence spectra were recorded on a Fluorolog 3-22 (Horiba Jobin Yvon), equipped with a water-cooled photo multiplier tube (PMT). A calibration function was applied to account for the wavelength-dependent sensitivity of the photomultiplier tube, the wavelength dependent sensitivity of the photomultiplier tube, the throughput of the analyzing monochromator and the power fluctuation of the xenon lamp. For the ambient temperature measurements, a quartz capillary was filled with 5 mg of **1Fe@pyr** or **1Zn@pyr** crystals. For the temperature dependence measurements, an ensemble of **1Fe@pyr** or **1Zn@pyr** crystals are deposited in a cooper plate and fixed with silver paste nanoparticles to ensure a good thermal conductivity. The sample was then introduced into a closed cycle cryostat (Janis-Sumimoto SHI-4.5), which operates between 4 and 300 K and is equipped with a programmable temperature controller (Lakeshore Model 331). The cryostat was introduced in the Fluorolog.

Magnetic and Photomagnetic measurements

The variable temperature magnetic susceptibility measurements were carried out by using microcrystalline samples (15-20 mg) of the **1Fe@pyr**, using a Quantum Design MPMS2 SQUID susceptometer equipped with a 5.5 T magnet, operation at 1 T and at temperatures from 300-1.8 K. Experimental susceptibilities were corrected for diamagnetism of the constituent atoms by the use of Pascal's constants.

Differential Scanning Calorimetry (DSC)

Calorimetric measurements were performed using a differential scanning calorimeter Mettler Toledo DSC 821e. Low temperatures were obtained with an aluminium block attached to the sample holder, refrigerated with a flow of liquid nitrogen and stabilized at a temperature of 110 K. The sample holder was a kept in a dry box under a flow of dry nitrogen gas to avoid water condensation. The measurements were carried out using around 20 mg of powdered sample sealed in aluminium pans with a mechanical crimp. Temperature and heat flow calibrations were made with standard samples of indium by using its melting transition (429.6

K, 28.45 J g^{-1}). An overall accuracy of ±0.2 K in temperature and ±2% in the heat capacity is estimated. The uncertainty increases for the determination of the anomalous enthalpy and entropy due to the subtraction of an unknown baseline.

Single-Crystal X-ray Diffraction

Single-crystal X-ray data were collected with an Oxford Diffraction Supernova diffractometer. In all cases, Mo-Kα radiation (λ = 0.71073) was used. Data scaling and empirical or multiscan absorption corrections were performed. The structures were solved by direct methods with SIR2004[2] and refined by full-matrix least squares techniques on F^2 with SHELXL.[3] Non-hydrogen atoms were refined anisotropically, and hydrogen atoms were placed in calculated positions and refined in idealized geometries (riding model) with fixed isotropic displacement parameters. Relevant crystallographic data, bond lengths and angles for **1Fe@pyr** and **1Zn@pyr** are gathered in Tables S1 - S3. CCDC 1847351-1847353 and 1862017 contain the supplementary crystallographic data for this paper. These data can be obtained free of charge from The Cambridge Crystallographic Data Centre.

Table S1. *Crystal data of compounds* ***1Fe@pyr*** *and* ***1Zn@pyr****.*

T (K)	**Fe 120 K**	**Fe 280 K**	**Zn 120 K**	**Zn 280 K**
Empirical formula	$C_{72}H_{44}N_{12}Au_4Fe_2$		$C_{72}H_{44}N_{12}Au_4Zn_2$	
Mr	1976.76		1995.80	
Crystal system		monoclinic		
Space group	*Cc*	*Cc*	*Cc*	*Cc*
a (Å)	33.2202(13)	33.557(6)	33.219(3)	33.4492(11)
b (Å)	13.2404(5)	13.117(2)	12.9439(10)	13.0989(5)
c (Å)	15.2020(5)	16.174(2)	16.3125(13)	16.2467(6)
β	113.3920(10)	112.407(5)	111.934(3)	112.538(3)
V ($Å^3$)	6137.0(4)	6581.7(19)	6506.4(9)	6574.8(4)
Z	4			
F(000)	3712		3744	
D_c (mg cm^{-3})	2.139	1.995	2.037	2.016
μ (Mo-K_α)(mm^{-1})	10.042	9.364	9.763	9.662
No. of total reflections [I>2σ(I)]	23132	10829	27866	7442
R [I>2σ(I)]	0.0438	0.0404	0.0738	0.0679
wR [I>2σ(I)]	0.0809	0.0716	0.1969	0.0766
S	1.090	1.012	1.054	0.970

References

[1] J. T. Culp, C. Madden, K. Kauffman, F. Shi, C. Matranga, *Inorg. Chem*. **2013**, *52*, 4205-4216.

[2] M. C. Burla, R. Caliandro, M. Camalli, B. Carrozzini, G. L. Cascarano, L. De Caro, C. Giacovazzo, G. Polidori, R. J. Spagna, *Appl. Cryst*. **2005**, *38*, 381-388. (SIR2004)

[3] G. M. Sheldrick, *Acta. Crystallogr. C Struct. Chem*. **2015** Jan. 1; *71*(Pt 1): 3-8. (SHELXL 2015)

Table S2. *Fe-N and Zn-N bond lengths (Å) for* ***1Fe@pyr*** *and* ***1Zn@pyr*** *respectively.*

	M = Fe		**M = Zn**	
	120 K	**280 K**	**120 K**	**280 K**
M1-N1	2.015(8)	2.220(10)	2.187(11)	2.19(2)
M1-N2	2.011(7)	2.208(11)	2.159(12)	2.16(2)
M1-N3	1.940(8)	2.163(11)	2.180(15)	2.18(2)
M1-N4	1.937(8)	2.137(11)	2.110(14)	2.10(3)
M1-N5	1.958(8)	2.179(11)	2.172(13)	2.20(3)
M1-N6	1.930(8)	2.140(11)	2.136(14)	2.14(2)
M2-N7	2.009(7)	2.169(10)	2.126(12)	2.14(2)
M2-N8	1.999(7)	2.136(10)	2.156(12)	2.14(2)
M2-N9	1.920(7)	2.109(12)	2.128(15)	2.17(3)
M2-N10	1.934(7)	2.125(11)	2.147(14)	2.18(2)
M2-N11	1.936(7)	2.147(11)	2.133(14)	2.14(2)
M2-N12	1.926(7)	2.104(12)	2.115(14)	2.16(3)
dM-N	1.965/1.954	2.175/2.132	2.157/2.134	2.16/2.16

Table S3. *N-Fe-N and N-Zn-N bond angles (º) for* ***1Fe@pyr*** *and* ***1Zn@pyr*** *respectively.*

	M = Fe		**M = Zn**	
	120 K	**280 K**	**120 K**	**280 K**
N1-M1-N2	179.4(4)	178.5(5)	178.9(5)	178.5(12)
N1-M1-N3	92.3(3)	93.6(4)	92.9(5)	91.9(9)
N1-M1-N4	88.3(3)	89.1(4)	88.9(5)	89.8(10)
N1-M1-N5	90.5(3)	89.9(4)	89.6(5)	90.0(9)
N1-M1-N6	88.8(3)	88.5(4)	88.5(5)	88.3(9)
N2-M1-N3	88.0(3)	87.6(4)	88.1(5)	87.3(9)
N2-M1-N4	91.3(3)	89.7(4)	90.1(6)	91.0(10)
N2-M1-N5	90.0(3)	90.9(4)	90.8(5)	91.3(10)
N2-M1-N6	90.7(3)	90.6(4)	91.0(5)	90.3(10)
N3-M1-N4	179.4(4)	177.2(6)	178.2(7)	178.2(12)
N3-M1-N5	91.3(3)	91.4(4)	91.8(5)	91.3(9)
N3-M1-N6	89.0(3)	88.8(5)	87.1(6)	87.1(10)
N4-M1-N5	88.7(3)	88.0(5)	88.5(5)	89.4(12)
N4-M1-N6	90.9(3)	91.9(5)	92.7(6)	92.3(11)
N5-M1-N6	179.3(4)	178.4(5)	177.8(6)	177.6(11)
N7-M2-N8	178.9(3)	179.3(5)	178.6(5)	178.3(10)
N7-M2-N9	89.9(3)	89.5(4)	90.3(5)	89.3(9)
N7-M2-N10	91.7(3)	89.9(4)	89.1(5)	89.7(9)
N7-M2-N11	89.1(3)	92.3(4)	91.9(5)	93.1(9)
N7-M2-N12	89.5(3)	90.0(4)	90.4(6)	88.5(9)
N8-M2-N9	90.5(3)	89.9(4)	90.5(6)	89.3(9)
N8-M2-N10	89.4(3)	90.0(4)	89.7(5)	91.3(9)
N8-M2-N11	90.4(3)	88.3(4)	87.3(6)	88.3(9)
N8-M2-N12	89.4(3)	90.1(4)	90.8(6)	90.4(9)
N9-M2-N10	88.3(3)	87.0(5)	88.6(7)	88.6(11)
N9-M2-N11	178.8(4)	178.1(5)	177.6(6)	177.6(11)
N9-M2-N12	91.1(3)	91.3(4)	90.2(7)	90.5(10)
N10-M2-N11	92.4(3)	92.4(4)	90.4(6)	91.6(8)
N10-M2-N12	178.7(3)	178.3(5)	178.7(8)	178.0(12)
N11-M2-N12	88.2(3)	89.3(5)	90.9(7)	89.4(10)

Figure S1. *Coordination centres F1 and F2.*

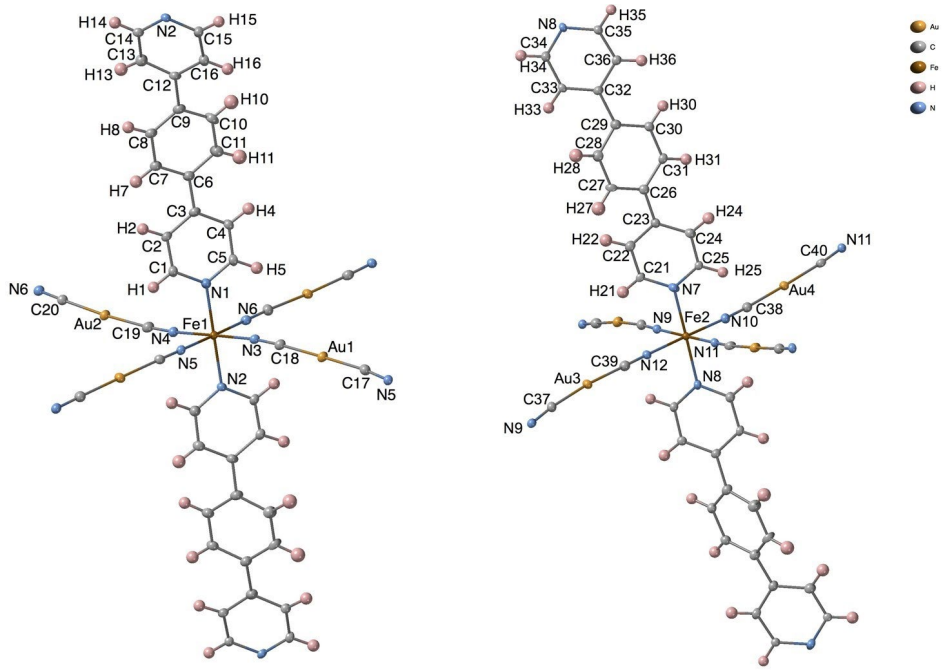

Intermolecular short π-π contacts between pyrene and bpben for **1Fe@pyr**.

Table S4-cont. *Intermolecular short π-π contacts between pyrene and bpben for 1Zn@pyr.*

Framework Zn1				Framework Zn2			
Pyrene1	Bpben1	d/Å 120K	d/Å 280K	Pyrene2	Bpben2	d/Å 120K	d/Å 280K
C62	C12	3.59	3.63	C53	C33	3.37	3.53
C71	C5	3.44	3.51	C45	C32	3.62	3.61
C59	C7	3.45	3.52	C53	C32	3.54	3.57
C60	C7	3.41	3.42	C53	C29	3.54	3.55
C60	C6	3.57	3.62	C52	C29	3.60	3.61
C62	C9	3.50	3.55	C44	C30	3.68	3.71
C71	C4	3.53	3.57	C52	C30	3.63	3.68
C62	C8	3.35	3.35	C50	C30	3.53	3.54
C65	C2	3.54	3.55	C51	C30	3.54	3.53
C66	C6	3.55	3.57	C51	C31	3.40	3.46
C62	C9	3.50	3.55	C56	C31	3.52	3.57
C58	C8	-	3.63	C56	C26	3.58	3.64
C63	C2	3.69	-	C56	C23	3.64	3.66
C65	C4	3.66	-	C50	C31	3.64	3.68
C65	C3	3.48	3.50	C54	C23	-	3.679
C60	C8	3.67	3.63	C56	C23	3.57	-
C66	C3	3.57	3.61				
C64	C2	3.38	3.43				
C61	C8	3.44	3.50				
C57	C8	3.49	3.43				
C70	C4	3.50	3.52				
C70	C5	3.31	3.31				
C69	C10	3.57	3.58				
C61	C9	3.48	3.54				
C69	C9	3.64	3.58				
C64	C1	3.53	3.63				
C66	C3	3.56886	3.610				
C70	C2	3.57762	-				
C60	C6	3.60622	-				
C70	C3	3.66019	-				
C68	C11	3.66169	-				
C70	C4	3.66507	3.558				
C61	C10	3.67164	-				
C66	C7	3.67272	-				
C57	C12	3.68590	-				
C63	C7	3.69025	-				
C70	C2	3.57762	-				
C60	C6	3.60622	3.626				
C70	C3	3.66019	-				
C68	C11	3.66169	-				
C70	C4	3.66507	-				
C61	C9		3.536				
C69	C9		3.680				
C64	C1	-	3.568				

Figure S2. *Overlay of a representative fragment of the frameworks and pyrene molecule at 280 K (red) and 120 K (green) for (a) Fe(1), (b) Fe(2), (c) Zn(1) and (d) Zn(2) sites.*

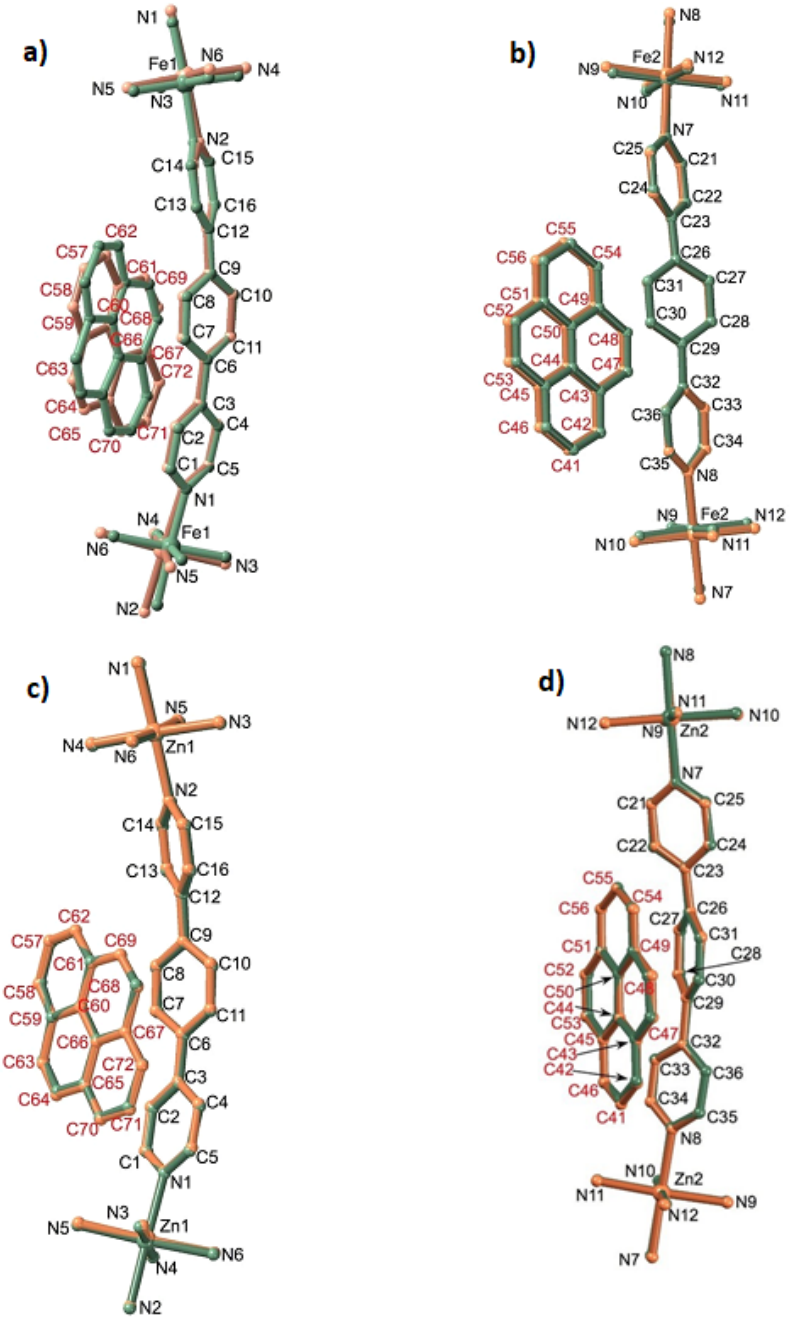

Table S5. *Geometrical distorsion of the bpben ligands: (a) Out of benzene plane distances, D (Å), of the pyridine N atoms coordinated to Fe^{II} (see Scheme I below); (b) Dihedral angles defined between the benzene and pyridine rings. The pyridine rings are denoted by the corresponding N atoms.*

(a)	Distance D from benzene plane (Å)			
Compound	**1Fe@pyr**		**1Fe@pyr**	
T/K	**120**	**280**	**120**	**280**
N-pyridine atom				
N1	0.545	0.583	0.663	0.713
N2	0.816	0.699	0.619	0.645
N7	0.650	0.424	0.416	0.457
N8	0.556	0.494	0.557	0.685

(b)	Dihedral angle pyridine-benzene plane (º)			
Compound	**1Fe@pyr**		**1Fe@pyr**	
T/K	**120**	**280**	**120**	**280**
Pyridine ring				
N1	11.0	10.9	11.9	13.0
N2	27.7	27.7	28.9	28.3
N7	34.1	34.3	35.5	27.4
N8	30.0	26.1	29.7	32.8

Scheme I. *View illustrating the separation of the pyridine N atoms from the average benzene plane as a measure of the bent nature of the bpben ligands.*

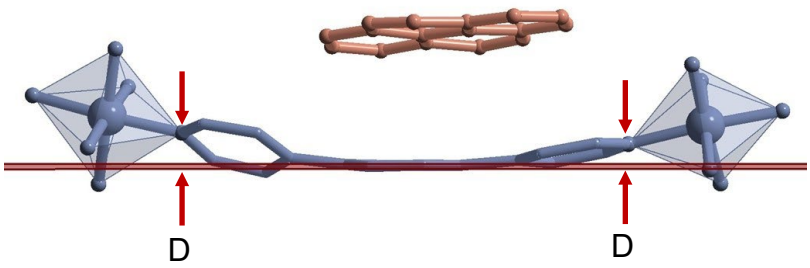

Figure S3. *Absorption spectra of a single crystal of* ***1Fe@pyr*** *at room temperature and 10 K in the HS (red) and LS (blue) state respectively (left) and temperature variable absorption spectra of* ***1Fe@pyr*** *in the cooling mode (right).*

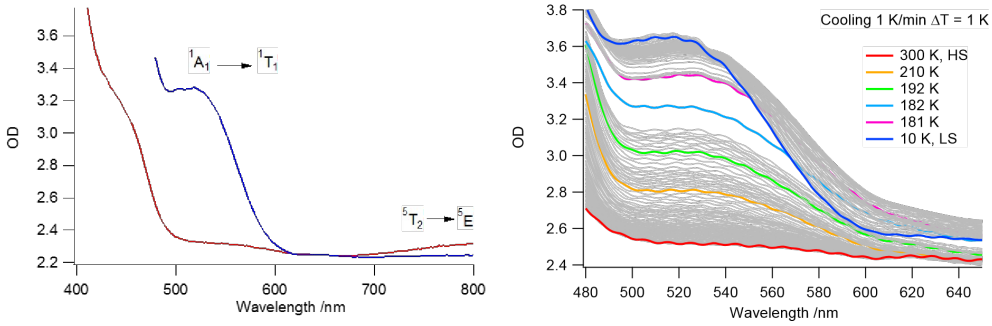

Figure S4. *Evolution of the absorption spectra at variable temperature during cooling (top left) and heating (top right) at 5 K/min, and corresponding HS fraction as a function of the temperature established from the optical density difference between 575 and 650 nm (bottom).*

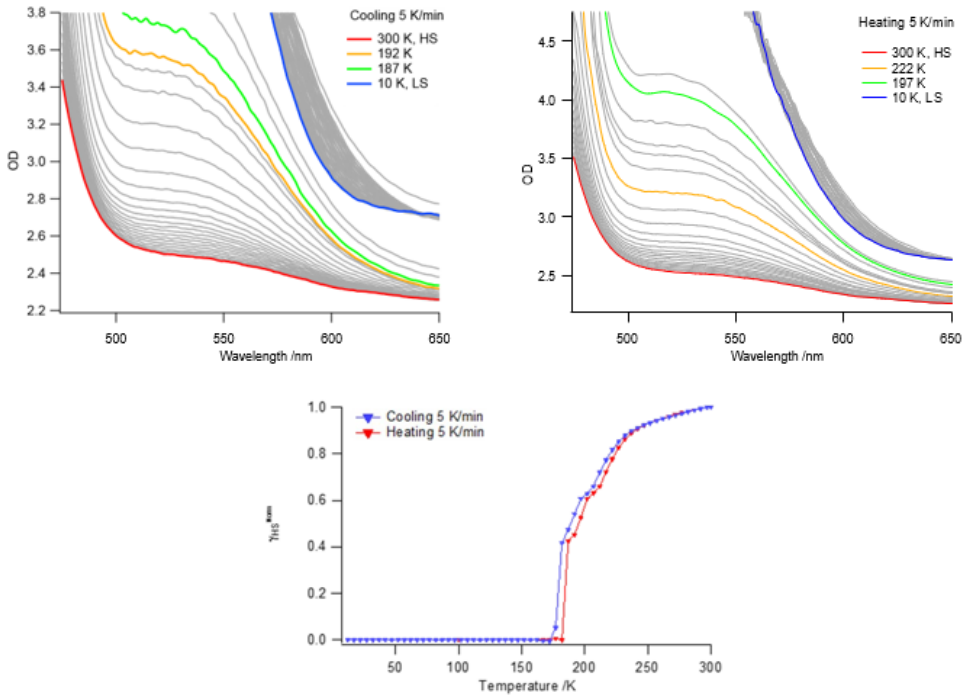

Figure S5. *Evolution of the absorption spectra during the HS to LS relaxation after LIESST during heating from 10 to 60 K at 0.3 K/min.*

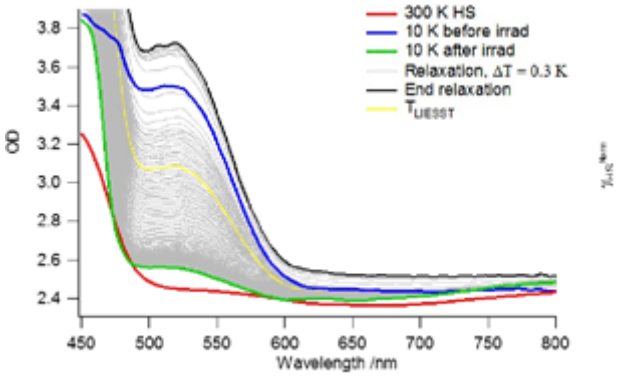

Figure S6. *Excitation spectrum of the sample between 250 and 490 nm recorded at 520 nm and corresponding emission spectrum after excitation at 332 nm.*

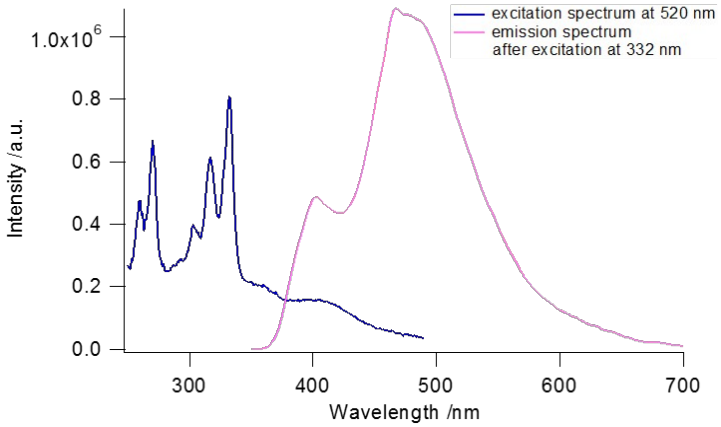

Figure S7.*Evolution of the photoluminescence spectra with the temperature during heating at 5 K/min from 10 K to 300 K.*

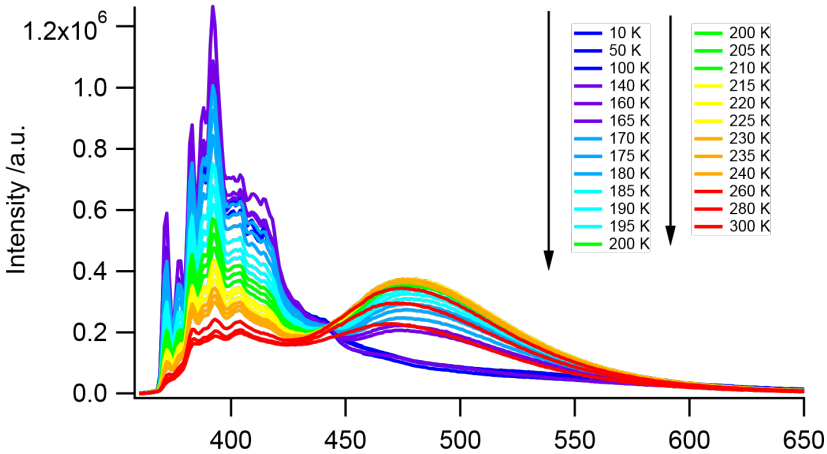

CAPÍTULO 3

Extrinsic vs intrinsic luminescence and their interplay with spin crossover in 3D Hofmann-type coordination polymers

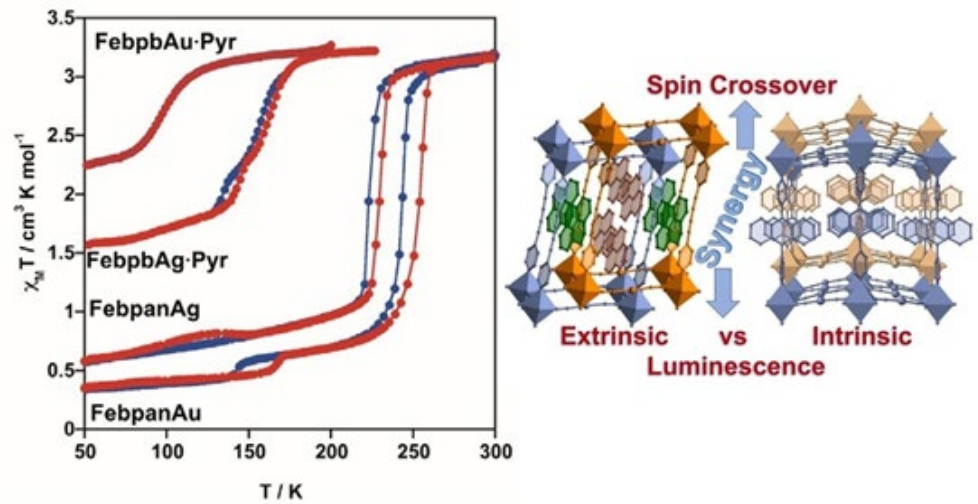

REVISTA: Journal of Materials Chemistry C

ÍNDICE DE IMPACTO: 7.059

CAPÍTULO 3

Extrinsic vs intrinsic luminescence and their interplay with spin crossover in 3D Hofmann-type coordination polymers

3.1.- Abstract

The research of new multifunctional materials, as those undergoing spin crossover (SCO) and luminescent properties, is extremely important in the development of further optical and electronic switching devices. As a new step towards this ambitious aim, the coupling of SCO and fluorescence is presented here following two main strategies: whether the fluorescent agent is integrated as a part of the main structure of a 3D SCO coordination polymer $\{Fe^{II}(bpan)[M^{I}(CN)_2]_2\}$ (*bpan* = bis(4-pyridyl)anthracene, M^{I} = Ag (**FebpanAg**), Au (**FebpanAu**)) or is a guest molecule inserted within the cavities of the 3D switchable framework $\{Fe^{II}(bpb)[M^{I}(CN)_2]_2\}\cdot$pyrene (*bpb* = bis(4-pyridyl)butadiyne, M^{I} = Ag (**FebpbAg·pyr**), Au (**FebpbAu·pyr**)). The magnetic, calorimetric, structural, UV-Vis absorption and fluorescent characterizations were performed confirming the occurrence of a SCO-fluorescence interplay in the studied compounds. Moreover, the relevance of the intrinsic or extrinsic nature of the luminescence on the efficiency of the interplay is discussed on the basis of the available information.

3.2.- Introduction

The spin crossover (SCO) phenomena, exhaustively studied for Fe^{II} pseudo-octahedral complexes, deals with the reversible, detectable and controllable switching between the paramagnetic high-spin (HS) and the diamagnetic low-spin (LS) electronic configurations.[1-3] The HS ↔ LS transition can be achieved via an external perturbation (i.e. temperature or pressure change, light, an electric field or the adsorption/desorption of analytes) and is accompanied by substantial changes in optical, magnetic and structural properties. Therefore, the SCO event can be monitored by a wide range of different techniques such as magnetic susceptibility measurements, Mössbauer spectroscopy, UV-Vis-NIR absorption spectroscopy, X-ray diffraction, X-ray absorption or heat capacity measurements, among others. Due to their potential applications in electronics and/or opto-

electronic devices,[4,5] these switchable compounds have attracted much attention in the realms of materials physics and chemistry.

Modulation of luminescence by controlling the HS/LS population and/or, conversely, tracking the HS/LS population during the SCO behavior by measuring the relative intensity of the luminescence signal are appealing features that may facilitate the integration of a SCO system into a real device. Although the approach of combining SCO and luminescence in the same material dates from two decades ago, it has been only recently that this idea has entailed a significant number of studies. They are classified according to the way by which the fluorophore is integrated in the SCO material as: i) doping agent (mechanophysical mixture);[6-9] ii) decorative element of coreshell nanoparticles;[10-14] iii) intrinsic part of the SCO structure;[15-25] and iv) counterion.[26] With the exception of ref. 25 which deals with 2D compound, the aforementioned luminescent SCO materials are based on Fe^{II} discrete mononuclear or binuclear complexes and 1D polymeric compounds derived from triazole ligand. In general, all these synthetic strategies successfully resulted in a more or less marked modulation of the luminescence triggered by the spin state change. Regarding the synergy mechanism, the spectral overlap between the luminophore (the sensitizer) and the SCO center (the acceptor) results in an emission-re-absorption process in which the latter acts as a quencher of the luminescence.[27] In this case, the mechanism can be easily explained by the superposition of the metal-to-ligand charge transfer (MLCT) band or spin-allowed metal-centered *d-d* transitions ($^1A_1 \rightarrow {}^1T_1$, $^1A_1 \rightarrow {}^1T_2$) band observed in the LS state and the corresponding region of the emission fluorescent spectrum. However, if the distance between the sensitizer and the acceptor is shorter than 10 nm, as long as there is spectral overlap, non-radiative energy transfer can also be taken place.

The porous funstionality offered by most of the 3D SCO Hofmann-type coordination polymers[28-31] represents an interesting platform, yet almost unexplored, to investigate the interplay between SCO and luminescence. As a first example utilizing this approach, we recently reported on the clathration of the pyrene (pyr) fluorophore in the SCO framework $\{Fe^{II}(bpben)[Au^{I}(CN)_2]_2\}$ (*bpben* = 1,4-bis(4-pyridyl)benzene). This compound displays synergic thermo- and photo-modulation of the pyrene guest monomer and host-guest (*bpben*-pyrene) excimer fluorescence signals that reflects the parallel thermo- and photo-induced HS ↔ LS spin state change in the host framework.[32]

These interesting results encouraged us to explore new bifunctional porous $\{Fe^{II}(L)[M^{I}(CN)_2]_2\}$ (MI = Ag, Au) 3D frameworks capable to combine SCO and luminescence in a synergistic way. As a new step in this direction, here we report on the synthesis and characterization of two unprecedented series of doubly interpenetrated Hofmann-type coordination polymers formulated as $\{Fe^{II}(bpb)[M^{I}(CN)_2]_2\}\cdot$pyrene (bpb = bis(4-pyridyl)butadiyne, M^{I} = Ag (**FebpbAg·Pyr**), Au (**FebpbAu·Pyr**)) and $\{Fe^{II}(bpan)[M^{I}(CN)_2]_2\}$ (bpan = bis(4-pyridyl)anthracene, M^{I} = Ag (**FebpanAg**), Au (**FebpanAu**)) (Scheme 1). In the series based on the bpb bridging pillar ligand, luminescence is, similarly as in the aforementioned bpben system, an extrinsic property that stems from the pyrene guest molecule. In contrast, the series based on the anthracene-bearing bpan bridging ligand, represents the first example of a 3D Hofmann-type SCO coordination polymer with intrinsic luminescence.

3.3.- Results and discussion

3.3.1.- Synthesis

Single crystals of compounds $\{Fe^{II}(bpan)[M^{I}(CN)_2]_2\}$ (M^{I} = Ag (**FebpanAg**) or Au (**FebpanAu**)) were obtained using liquid-to-liquid diffusions from $Fe^{II}(BF_4)_2\cdot 6H_2O$, $KM^{I}(CN)_2$ (M^{I} = Ag or Au) and bpan ligand in methanol-dichloromethane solutions. Same conditions were used for the synthesis of the zinc analogue complex **ZnbpanAu** albeit using $Zn^{II}(BF_4)_2\cdot 6H_2O$ instead of the Fe^{II} salt. Similarly, crystals of $\{Fe^{II}(bpb)[M^{I}(CN)_2]_2\}\cdot$Pyrene ($M^{I}$ = Ag (**FebpbAg·Pyr**) or Au (**FebpbAu·Pyr**)) were synthesized following similar liquid phase diffusion methodology but using saturated methanol solutions of the pyrene fluorophore (see Experimental section). Despite considerable efforts to obtain single crystals of the bpb Zn^{II} complex, the desired product was not formed.

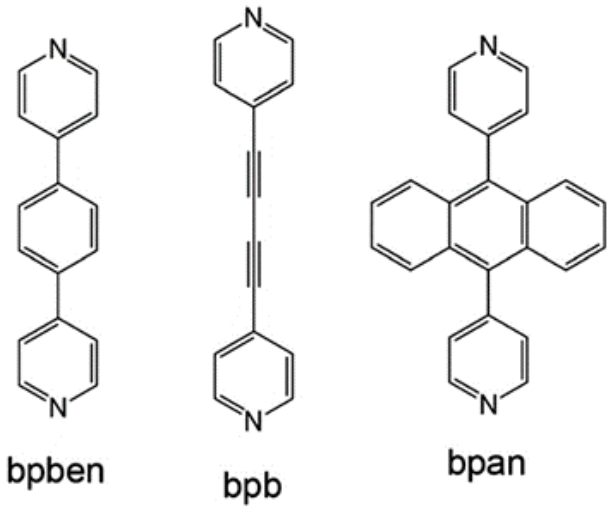

Scheme 1. *Structure of the pillar ligands used in the study of synergies between SCO and luminescence in Hofmann-type coordination polymers.*

Elemental analysis and powder X-ray diffraction (PXRD) measurements confirmed the high purity of the obtained polycrystalline samples (see Experimental section and Figure S1, respectively, ESI†). Comparison of the PXRD spectra also reveals that the Au and Ag counterparts are isostructural in both series of complexes as the more intense peaks are well reproduced from one derivative to the other. Thermogravimetric analysis were performed for **FebpbAg·Pyr**/**FebpbAu·Pyr** and **FebpanAg**/**FebpanAu** clathrates confirming the presence of about 1 molecule of pyrene per Fe^{II} ion for the former and the absence of trapped solvent for the latter (Figure S2, ESI†) in good agreement with the elemental analysis and structural data shown hereafter.

3.3.2.- SCO properties

Magnetic and calorimetric studies. The temperature dependence of the $\chi_M T$ product (where χ_M is the molar susceptibility and T is the temperature) for compounds **FebpanAg/FebpanAu** and **FebpbAg·Pyr/FebpbAu·Pyr** is depicted in Figure 1. In all cases, at room temperature, the value of $\chi_M T$ is about 3.2 cm^3 K mol^{-1} indicating that practically all the Fe^{II} centers are in the HS state (S = 2). Upon cooling, the $\chi_M T$ value of **FebpanAu/FebpanAg** remains almost constant until dropping abruptly at $T_{1/2}\downarrow^1$ = 242/222 K

($T_{1/2}$ = temperature at which the population of the HS and LS Fe^{II} ions is equal to 50%) reaching a value *ca.* 0.70/1.09 cm^3 K mol^{-1} at 205 K. For **FebpanAu**, this $\chi_M T$ value remains almost constant upon cooling defining a plateau 65 K wide before undergoing a second small drop at $T_{1/2}\downarrow^2$ = 143 K reaching a value of 0.34 cm^3 K mol^{-1} at 50 K. Considering these variations of $\chi_M T$, *ca.* 80% and 10% of the Fe^{II} ions are involved in the spin state change in the first and the second step, respectively, whereas about 10% of the Fe^{II} centers remain as residual HS species at low temperature. In the heating mode, the $\chi_M T$ *vs.* T curve for **FebpanAu** does not match ($T_{1/2}\uparrow^2$ = 163 K and $T_{1/2}\uparrow^1$ = 252 K) with the cooling mode, thereby defining a hysteresis 10 K (first step) and 20 K (second step) wide.

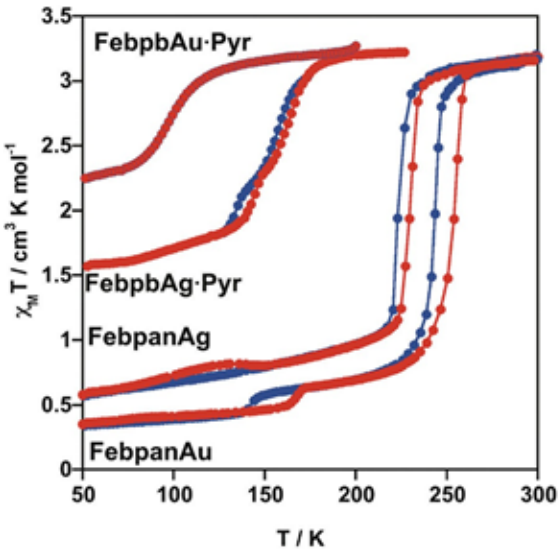

Figure 1. *$\chi_M T$ vs. T plots of compounds* ***FebpbAuPyr, FebpbAgPyr, FebpanAu*** *and* ***FebpanAg*** *(blue and red filled circles correspond to the cooling and heating modes, respectively).*

Below 215 K, the magnetic behavior of **FebpanAg** slightly differs from that of the homologous Au derivative. After the first abrupt transition in the cooling mode, the $\chi_M T$ decreases gradually reaching a value of 0.6 cm^3 K mol^{-1} at 50 K. Whereas in the heating mode, a slight increase in the $\chi_M T$ increase is observed above 85 K and stabilized at 130 K ($\Delta\chi_M T$ = 0.2 cm^3 K mol^{-1}) defining an asymmetric hysteresis loop. At higher temperatures, an abrupt increase in $\chi_M T$ ($T_{1/2}\uparrow^1$ = 228 K) is observed resulting in a hysteresis loop 6 K wide.

Compound **FebpbAu·Pyr** presents a gradual and incomplete spin transition without hysteresis centered at $T_{1/2}$ ≈ 100 K with a remaining HS fraction of 72% at 50 K. Unlikely,

the analogous compound **FebpbAg·Pyr** displays a gradual decrease of the $\chi_M T$ value with two steps associated with HS-to-LS transitions involving *ca.* 31% (from 180 to 150 K) and 15% (from 150 to 125 K) of the Fe^{II} ions, respectively. At 50 K, the value of $\chi_M T$ is 1.56 cm^3 K mol^{-1} showing that about 52% of the Fe^{II} ions remain in the HS state. The heating and cooling mode curves do not match thereby defining two hysteresis loops 4 K ($T_{1/2}\downarrow^1$ = 156 K, $T_{1/2}\uparrow^1$ = 160 K) and 7 K ($T_{1/2}\downarrow^2$ = 136 K, $T_{1/2}\uparrow^2$ = 143 K) wide. Repeating cycles on this sample shows very reproducible results (Figure S3, ESI†).

The thermodynamic parameters associated with the SCO have been obtained from the differential scanning calorimetry (DSC) measurements for all samples except for **FebpbAu·Pyr** since its characteristic $T_{1/2}$ is out the temperature window of our calorimeter. The thermal dependence of the anomalous heat capacity variation (ΔC_p) for **FebpanAu, FebpanAg** and **FebpbAg·Pyr** is displayed in Figure S4 (ESI†). The average enthalpy (ΔH) and entropy ($\Delta S = \Delta H/T_i$) variations as well as the average temperatures (T_i) of the maxima/minima of the ΔC_p *vs. T* plots are gathered in Table 1. The average T_i temperatures of the observed anomalies are consistent with those obtained from the magnetic measurements for the SCO. For **FebpanAu** and **FebpanAg**, the overall ΔH and ΔS values associated with the SCO are consistent with those reported for related 3D SCO Hofmann-type coordination polymers with cooperative SCO. For **FebpbAg·Pyr**, extrapolation of the HS ↔ LS transformation to 100% affords ΔH and ΔS values (*ca.* 8 kJ mol^{-1} and 54 J K^{-1} mol^{-1}) consistent with the gradual character of the thermal spin transition.

Table 1. *Thermodynamic parameters obtained from DSC measurements.*

		$T_{1/2}^{av}$ (K)	ΔH_{av} (kJ mol^{-1})	ΔS_{av} (J K^{-1} mol^{-1})
FebpanAu	1st step	250.0	19.22	76.9
	2nd step	152.1	0.19	1.3
	Overall		19.41	78.2
FebpanAg	1st step	236.5	28.3	80.7
	2nd step	150.0[a]	0.6	4.2
	Overall		18.9	84.9
FebpbAg·P	1st step	160.0	2.3[b]	16.3[b]
	2nd step	140.0	1.8[b]	10.5[b]
	Overall		4.1	26.8

[a] Only heating mode. [b] Evaluated for the 50% incomplete SCO.

Single crystal optical absorption spectroscopy. Figure 2a and b display the thermal evolution of the optical absorption spectra for a single crystal of **FebpbAg·Pyr** and of **FebpanAu**, respectively, in the heating mode recorded at 5 K min^{-1} (see Figure S5 for the cooling mode, ESI†). The thickness of both crystals was approximately 100 µm. In both cases, the tail of the very intense metal–ligand-charge-transfer (MLCT) band is observed between 450 and 800 nm at room temperature. Below 450 nm, the MLCT band saturates due to its high extinction coefficient. When both crystals are cooled down below the spin transition temperature, the $^1A_1 \rightarrow {}^1T_1$ d–d transition band ($\varepsilon_{530-550nm} \approx 50$ M^{-1} cm^{-1}) characteristic for the LS state of Fe^{II}, reaches a maximum at 10 K. The difference in optical density at 533/800 nm as well as 550/716 nm has been used for the silver and gold derivatives, respectively, to establish the thermal dependence of the HS molar fraction (γ_{HS}) through Vegard's law as stated elsewhere.[33] The γ_{HS} *vs.* T curves obtained for **FebpbAg·Pyr** or **FebpanAu** (Figure 2c) match very well the SCO behaviors found *via* magnetic studies albeit higher spin transition temperatures have been observed ($T_{1/2}\downarrow^1$ = 158 K, $T_{1/2}\downarrow^2$ = 136 K and $T_{1/2}\uparrow^1$ = 161 K, $T_{1/2}\uparrow^2$ = 140 K for **FebpbAg·Pyr;** $T_{1/2}\downarrow$ = 242 K and $T_{1/2}\uparrow$ = 275 K for **FebpanAu**). The subtle difference in the SCO temperature may be attributed to the faster temperature scan rate employed for the single crystal optical absorption measurements (5 K min^{-1} *vs.* 1 K min^{-1}), that is, the real temperature of the sample may be lower than the nominal one during heating. In the case of **FebpbAg·Pyr**, the values of the HS fraction have been corrected by using the residual HS fraction obtained at low temperatures extracted from the χT *vs.* T curve. The size of the **FebpbAu·Pyr** and **FebpanAg** crystals was too small to record their absorption spectra individually. Therefore, dilution of the grinded crystals in KBr pellets and dispersion in mineral oil have been tried out but, as shown in Figure S6 (ESI†), the quality of the optical absorption spectra is poor due to sample inhomogeneity.

3.3.3.- Crystal structures

Structural data of **FebpanAu** were successfully recorded at 280, 200, and 120 K allowing to identify the structures at the different steps defined by the SCO curve. However, despite numerous attempts, we were not able to get good single crystals of the isostructural **FebpanAg** and **ZnbpanAu** thus preventing a complete analysis of their structures. The structures of complexes **FebpbAu·Pyr** and **FebpbAg·Pyr** were determined at 120 and

250/100 K, respectively. Tables S1 and S2 (ESI†) show the main crystallographic parameters obtained from the single crystal X-ray data of all studied compounds.

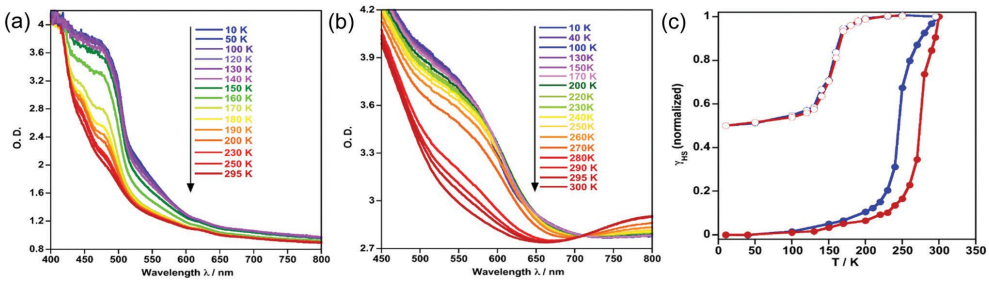

Figure 2. *Thermal dependence of single crystal absorption spectra during the thermal transition for* ***FebpbAg·Pyr*** *(a) and* ***FebpanAu*** *(b), and the corresponding HS fraction (γ_{HS}) vs. T curves obtained from the optical density difference at 533 and 800 nm for* ***FebpbAg·Pyr*** *(empty circles) and between 550 and 716 nm for* ***FebpanAu*** *(filled circles) (c).*

Structure of FebpanAu. At 280 K, the structure of **FebpanAu** shows the monoclinic *P2/c* space group. It is constituted of two crystallographically non-equivalent pseudooctahedral [$Fe^{II}N_6$] environments. The equatorial positions of the octahedrons are coordinated by four $[Au(CN)_2]^-$ groups which connect non-equivalent adjacent Fe^{II} centers (Fe1–Fe2–Fe1–...) building up 2D infinite $\{Fe_4[Au(CN)_2]_4\}_\infty$ sheets. The apical positions are occupied by two crystallographically distinct ditopic bpan ligands acting as pillars between adjacent sheets, thereby defining a 3D framework with primitive cubic unit (**pcu**) topology (Figure 3). Each type of axial bpan ligand bridges one type of inequivalent Fe centers (Fe1 or Fe2) (Figure 3). Although the NC–Au–CN moieties are essentially linear, the coordination bonds between the NC–Au–CN groups and the FeII ions form an angle strongly deviated from 180º (Fe1–N3–C15 = 165.78º; Fe1–N8–C34 = 158.97º; Fe2–N6–C32 = 163.69º; Fe2–N7–C33 = 164.78º), thereby conferring to the $\{Fe_4[Au(CN)_2]_4\}_\infty$ layers a corrugated shape. Indeed, if we consider the four NC–Au–CN groups radiating from Fe2, the four connected Fe1 sites are 1.029 Å below the equatorial plane Fe2N6N7N6N7. Consequently, the {Fe4[Au(CN)2]4} rhomboidal windows, whose Fe···Fe diagonals make 11.584 and 17.007 Å long, are slightly folded with respect to the short diagonal deviating 14.38º from planarity. The angles of the rhomboid are 68.099º and 110.579º. At 280 K, the Fe–N average distances, Fe1–N = 2.148 Å and Fe2–N = 2.157 Å, are typical of the Fe^{II} ions in the HS state in agreement with the magnetic data. The sum of the deviation from 90º of the twelve *cis* N–Fe–N bond angles (∑) are 20.17º and 22.49º for Fe1 and Fe2 respectively.

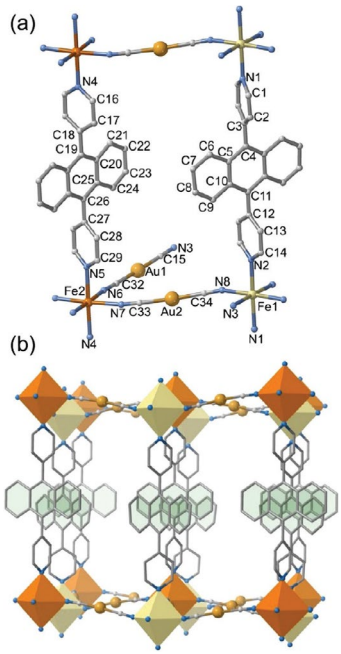

Figure 3. *(a) Representative fragment of the framework with the atom numbering of the asymmetric unit for* ***FebpanAu*** *at 280 K and (b) view of a single 3D network. Yellow and orange octahedrons correspond to Fe1 and Fe2, respectively.*

The open nature of the framework favors the interpenetration of a second equivalent 3D structure, in such a way that each bpan ligand of one network passes exactly through the center of the $Fe_4[Au(CN)_2]_4$ rhomboids of the other.

The interpenetration is stabilized by aurophilic interactions (Au1···Au2 = 3.428 Å) (Figure 4a and b). The anthracene moieties of the two independent bpan ligands display different orientations with respect to the plane defined by the atoms N1N2N3N3'(bpan1) around Fe1 and N4N5N6N6'(bpan2) around Fe2, being respectively 26.37º and 19.41º. The planes containing the pyridine rings asymmetrically bisect the equatorial angles N3Fe1N8 [pyridine containing N1 (51.41º) and N2 (67.66º)] and N6Fe2N7 [pyridine containing N4 (62.42º) and N5 (73.79º)]. Furthermore, the pyridine moieties are nearly orthogonal with respect to the anthracene fragment [bpan1: pyridine(N1) = 77.76º, pyridine(N2) = 94.03º; bpan2: pyridine(N4) = 93.20º and pyridine(N5) = 81.84º] (see Figure 3). This arrangement is adopted to minimize the inter- and intra-network repulsion between the hydrogen atoms of the anthracene groups. In addition, anthracene moieties from different networks display very

weak π···π interactions with C···C contacts well above 4.1 Å (centroid–centroid distances of ca. 5.4 Å).

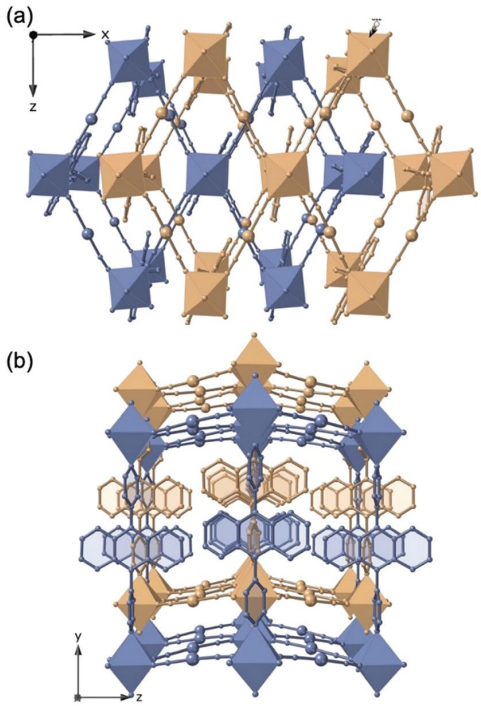

Figure 4. *Perspective views of the interpenetrated frameworks down to (a) [010] and (b) [100] directions for* ***FebpanAu*** *at 280 K.*

When cooling down to 200 K, the crystal color changes from pale-yellow to red indicating the occurrence of the spin transition, consistently with the magnetic and optical absorption measurements. Furthermore, the SCO is accompanied by a change of the space group from monoclinic P2/c to orthorhombic *Cmma*.

As a consequence of the symmetry breaking, the asymmetric unit now contains a unique octahedral Fe^{II} center, which is coordinated equatorially to four identical $[Au(CN)_2]^-$ groups and axially to only one crystallographically distinct bpan ligand. The average Fe–N bond length, equal to 1.954 Å, is 0.204 Å shorter than at 280 K, confirming that the HS ↔ LS transition is almost complete. Consistently, the angular distortion of the octahedron, ∑, decreases significantly to a value of 9.87º while the Fe–N–C(Au) angle increases up to 171.12º making the framework less distorted than in the monoclinic HS phase.

Consequently, the two pyridine moieties are now practically coplanar and their planes bisect the N3–Fe–N3' angles into two identical portions of 46.01º. In contrast, the anthracene group is disordered in two crystallographically equivalent orientations forming an angle of 31.42º to each other (Figure S7a, ESI†). However, the average orientation is strictly orthogonal with respect to the pyridine groups. Furthermore, the constraining of the grid during the SCO process occurs in an anisotropic manner since the long Fe···Fe diagonal of the $\{Fe_4[Au(CN)_2]_4\}$ rhomboid decreases by 1.133 Å until 15.874(1) Å, while the short one increases by 0.736 Å up to 12.320(1) Å.[34] The Au–Au interactions between the two equivalent interpenetrated nets show a distance of 3.273 Å, 0.155 Å shorter with respect to the distance at 280 K.

When further cooling to 120 K, the structure undergoes a second crystallographic phase transition displaying the monoclinic *P2/n* space group. The structure is very similar to that at 200 K but it shows some important differences: (i) the average orientation of the anthracene groups, which are still disordered at 50% in two non-equivalent orientations (now rotated with respect to each other by 22.57º, Figure S7b, ESI†), is no longer orthogonal to the pyridine rings defining angles of 73.28º (pyridineN1) and 77.17º (pyridineN2); (ii) the plane containing the two pyridine rings bisects the N3–Fe–N4 angles forming an angle of 54.56º with respect to the N1N3N2N3' plane; (iii) the Fe–N average distance of 1.944 Å is slightly shorter (*ca.* 0.010 Å) than that at 200 K and reflects on the additional low- temperature step observed in the magnetic measurements; (iv) the aurophilic interactions are also stronger after this second phase transition showing a Au–Au distance value of 3.260 Å; and (v) the long/short Fe···Fe diagonal of the $\{Fe_4[Au(CN)_2]_4\}$ rhomboid slightly increases/decreases upon additional conversion to reach values of 15.914 and 12.298 Å, respectively.

Structure of FebpbM·Pyr (M = Ag, Au). FebpbM·Pyr (M = Ag, Au) are isostructural. Therefore, we will delineate in detail the structure of the Ag derivative at 250 and 100 K. The structure of the Au derivative was measured at 120 K where it remains in the HS state and is comparable with that of the Ag analogue at 250 K (see Table S2, ESI†).

FebpbAg·Pyr displays the triclinic $P\bar{1}$ space group at 250 and 100 K. Topologically, the structure of **FebpbAg·Pyr** is essentially the same as for **FebpanAu** discussed above. The most significant difference is that the corresponding $\{Fe_4[Ag(CN)_2]_4\}_\infty$ layers are pillared by the longer and much less bulky bpb bridging ligand forming a much open **pcu** framework

(Figure 5). The average Fe–N bond length and octahedral angular distortion ∑ of the crystallographically unique Fe^{II} center are respectively, 2.180 Å and 18.37º at 250 K and 2.073 Å and 17.67º at 100 K. The equatorial Fe–N–C(Ag) bond angles, found in the range of 7.09–13.5º (250 K) and 6.66–10.61º (100 K), slightly deviate from the linearity. The moderate variation, 0.107 Å, of the average Fe–N bond length corresponds to the occurrence of a HS-to-LS conversion of 53.5%, which is in perfect agreement with the magnetic and optical data. The crystals change from yellow (HS)-to-dark orange (LS) when cooling from 250 K to 100 K.

As a consequence of its high void volume, this network is interpenetrated with a second equivalent structure as observed in Figure 6a. Unlike the bpan pillar ligand in **FebpanAu,** the bpb ligands of one network passes slightly shifted from the center of the $\{Fe_4(Ag(CN)_2)_4\}$ rhomboids of the other network (Figure 6b) thereby leaving wide channels for the intercalation of two crystallographically independent pyrene guest molecules within the generated pores. The two trapped pyrene guests are positioned face-to-face with respect to the pyridine coordinating groups of the bpb ligands, establishing a large number of π···π interactions (Figure S8, ESI†). In one of the pyrene molecules, the π···π interactions are modified as a consequence of the spin state change (Table S3, ESI†).

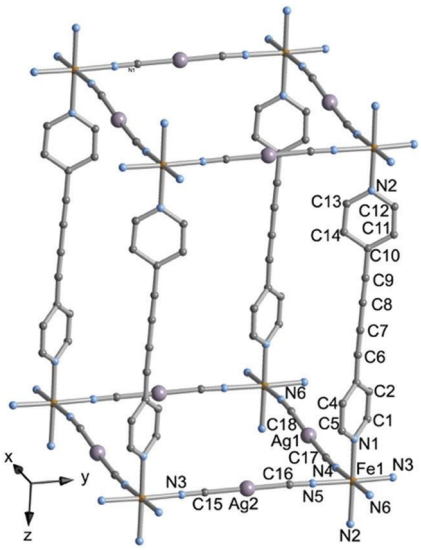

Figure 5. *Fragment of the* ***FebpbM·Pyr*** *(M = Ag, Au) framework emphasizing the atom numbering of the asymmetric unit.*

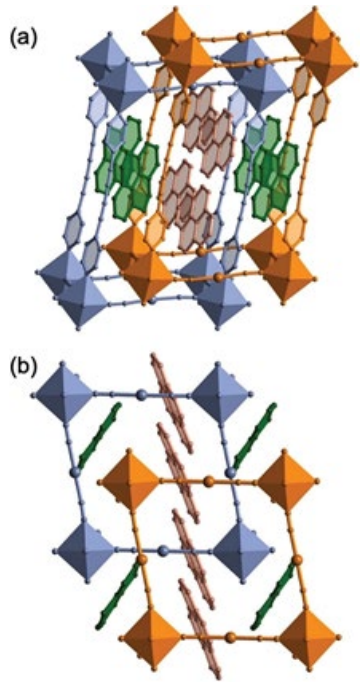

Figure 6. *(a) Side and (b) top views of a fragment of the* ***FebpbM·Pyr*** *(M = Ag, Au) structure showing the interpenetration of the two frameworks (blue/orange) and intercalation of the two crystallographically distinct pyrene molecules marked in color green (pyr1) and salmon (pyr2).*

3.3.4.- Coupling between luminescence and SCO

The interplay between the two concurrent properties, *i.e.* luminescence and SCO, has been investigated for the dicyanoargentate derivatives **FebpbAg·Pyr** and **FebpanAg.** This choice was based on the fact that the dicyanoargentate counterpart of the bpb derivative displays a more complete SCO which takes place at higher temperature. Therefore, among **FebpanAg** and **FebpanAu,** the former was studied for comparison with **FebpbAg·Pyr.** The thermal evolution of the luminescence spectra has been followed for an ensemble of single crystals of the selected compounds. In the case of **FebpbAg·Pyr,** a very similar behavior to that described for the analogous compound $\{Fe^{II}(bpben)[(Au(CN)_2)_2]\}$@pyrene[32] has been found even though in the present case the transition is much more incomplete. As observed in Figure 7a, two main contributions are present in the luminescence spectra at room temperature upon irradiation at 345 nm (see corresponding excitation spectra in Figure S9a, ESI†). In the interval 350–450 nm, a

multicomponent band, split into two main peaks, associated with the monomer form of pyrene is observed. From 450 to 700 nm a much broader and less defined band appears. This contribution is associated with the emission arising from the heterodimeric excimer formed by the pyrene molecules and the bpb bridging ligand due to strong π···π interactions established between them.[35] Upon cooling from room temperature, the intensity of the monomer and excimer signal increases due to reduction of thermal quenching, that is, in the configurational coordinate model, the probability of finding a crossing point between the potential energy surfaces of the ground state and the higher energy excited states, populated at high temperatures, increases leading to non-radiative transitions.[27] However, at ca. 200 K, the intensity of the excimer signal is stabilized and, upon further cooling, it decreases abruptly whereas the intensity of the monomer band keeps on increasing. At 10 K, where $\gamma_{HS} \approx \gamma_{LS} \approx 0.5$, the monomer signal intensity reaches to a maximum in intensity and displays a highly defined doublet due to the reduction of vibrational degrees of freedom at such low temperatures, whereas the excimer signal is significantly quenched. This observation can be attributed to the overlap of the optical absorption spectra in the LS state and the excimer emission.

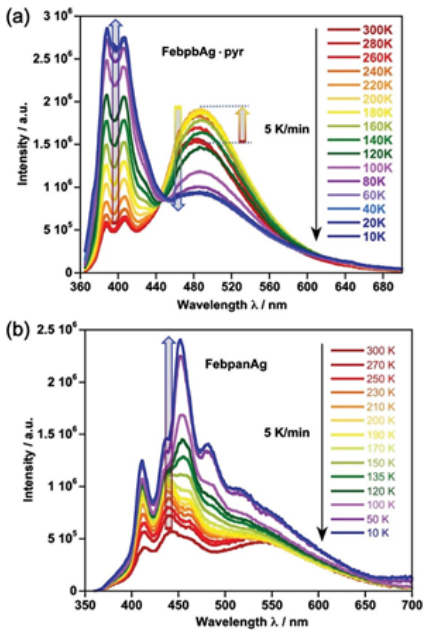

Figure 7. *Thermal evolution of the fluorescence of an ensemble of crystals of (s)* ***FebpbAg·Pyr*** *and (b)* ***FebpanAg*** *during cooling at 5 K min^{-1}.*

Figure 7b shows the fluorescence emission of **FebpanAg** as a function of temperature (see corresponding excitation spectra in Figure S9b, ESI†). At room temperature, irradiation at 345 nm induces the observation of two main contributions: a more resolved signal in the wave-length range 350–490 nm from the monomer and a broader and less defined band in the interval 490–700 nm from the excimer.[36–38] The fluorescence behavior of the anthracene excimer is usually characterized by a very short lifetime and makes difficult to detect it at room temperature albeit high pressure conditions in the crystalline state lead to its observation.[36] In the present case, the crystallinity of the sample and the rigidity of the lattice may contribute to the observation of the excimer signal from anthracene. Nonetheless, these interactions are less significant than in **FebpbAg·Pyr,** what would explain the lower intensity of the excimer signal in FebpanAg with respect to **FebpbAg·Pyr.** Upon cooling, both monomer and excimer signals increase in intensity. However, below 230 K, in correlation with the thermal spin transition of the complex, the excimer band undergoes some modifications in shape and seems to disappear upon further cooling whereas the intensity of the monomer signal increases giving rise to well-structured bands. As in the previous case, this behavior may be ascribed to the high optical absorption of the LS species within the range of the excimer emission.

In order to analyze in more detail the thermal dependence of the fluorescence for compound **FebpbAg·Pyr,** the intensities of the excimer and monomer signal were extracted from the corresponding spectra during cooling (Figure 7a) and heating (Figure S10a, ESI†) and plotted as a function of temperature (Figure 8a and Figure S10b, ESI†). The HS fraction, γ_{HS}, was calculated as the ratio between both signals and its thermal evolution is depicted in Figure 8b. The resulting profile is consistent with the SCO observed from single crystal optical absorption spectroscopy although the thermal hysteresis is wider and the spin transition temperature is shifted towards lower temperatures. These discrepancies are likely related to differences in the temperature scanning rate used for each measurement method. Hence, as previously observed in $\{Fe^{II}(bpben)[(Au(CN)_2)_2]\}$@pyrene,[32] the modification of the luminescence behavior of pyrene has been demonstrated to be a sensitive technique to monitoring the SCO for compound **FebpbAg·Pyr.** In both cases, for the bpben- and bpb-containing compounds, the SCO observed through the thermal variation of the magnetic susceptibility can be accurately reproduced by the luminescence measurements (Figure S11, ESI†).

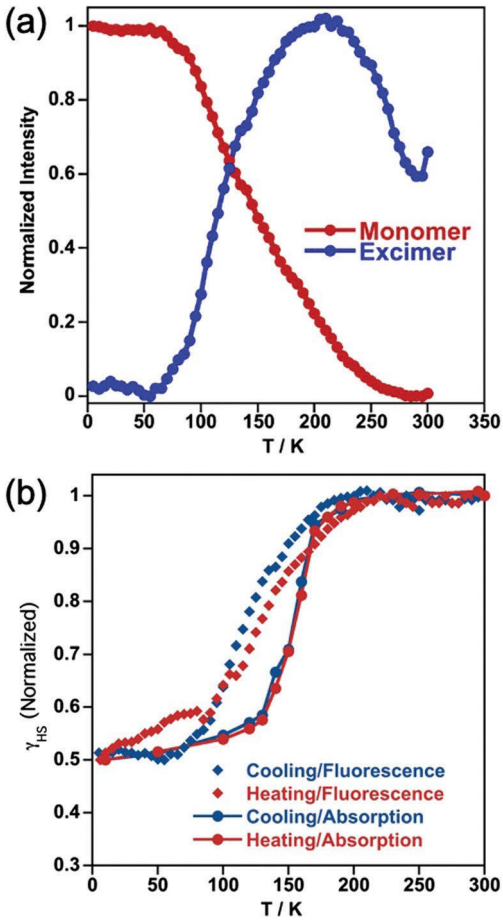

Figure 8. *(a) Thermal dependence of the monomer and excimer emission intensity of* ***FebpbAg·Pyr*** *in the cooling mode. (b) Comparison of the HS fraction, γ_{HS}, obtained from the ratio of the monomer emission over the excimer emission (filled diamonds) and from single crystal absorption spectroscopy (filled circles) in the heating and cooling mode at 5 K min^{-1}.*

Similarly, the thermal SCO of the intrinsically luminescent compound **FebpanAg** was also obtained by calculating γ_{HS} as the ratio of the excimer and the monomer signal. However, in this case the monomer signal was calculated as the average of the maximum intensity of the different observed peaks (see peaks from [1] to [5] in Figure 9a (and Figure S10c, ESI†) and the intensity *vs. T* plots for the cooling and heating modes in (Figure S10b and d, respectively, ESI†). Although the resulting thermal dependence of the luminescence partially agrees with that obtained by magnetic susceptibility measurements (even the multi-step feature), the former displays a more gradual shape (Figure 9c). These small differences

can be ascribed to the faster temperature scan rates used for recording the thermal dependence of luminescence and the fact of exciting an ensemble of crystals. On the other hand, it is worth mentioning that the emission spectra of **FebpanAg** was obtained from exciting in the different structured-excitation bands with the origin of the different vibrational contributions between the ground and excited electronic states S_0 and S_1 (see excitation spectrum in Figure S12a, ESI†)[39,40].

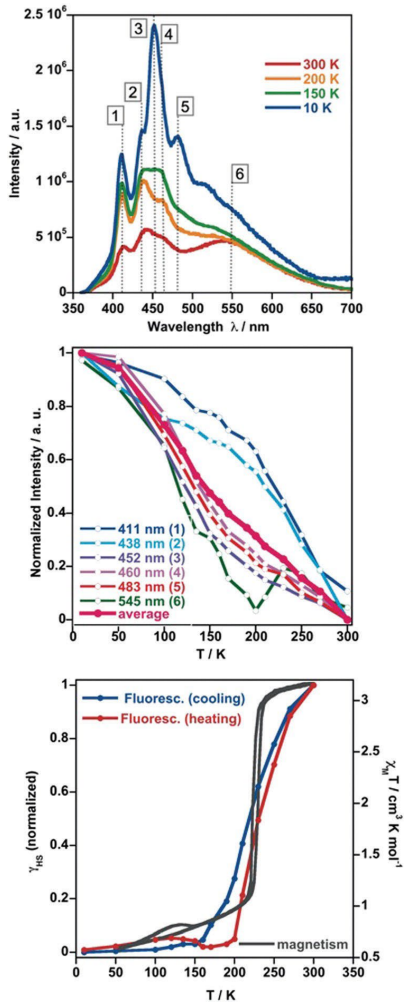

Figure 9. *Compound* ***FebpanAg.*** *Thermal evolution of: the monomer and excimer emission spectra (a); the different intensity maxima 1–6 (b); and the HS fraction (γ_{HS}) obtained from the ratio of the monomer emission over the excimer emission during the heating and cooling modes at 5 K min^{-1} (the results are compared with the thermal transition obtained by magnetism).*

However, if one excites into the π– π* band of anthracene at approximately 260 nm, the emission is slightly different and in fact, when following the thermal evolution of the emission spectra the intensities of all peaks equally increase upon cooling, but the relative intensity of all the vibrational bands stays constant and the excimer signal is not present (see Figure S12b and c for comparison, ESI†). Interestingly, other studies point to the same relative intensities and shape of the emission spectrum of anthracene regardless of whether the excitation is carried out at 280 or 360 nm.[41]

In order to verify whether the fluorescence-SCO synergy observed for **FebpbAg·Pyr** and **FebpanAg** also takes place in the corresponding **FebpbAu·Pyr** and **FebpanAu** analogues, their fluorescence spectra have been recorded at 300 K and at 80 K (see Figure S13 containing a full characterization of the absorption, excitation and fluorescence spectra, ESI†). Whereas at 300 K the 100% of the Fe^{II} ions exhibit the HS state, at 80 K **FebpbAu·Pyr** and **FebpanAu** display 70%/30% and 0%/100% HS/LS state, respectively. Indeed, in the LS state, the intensities of the monomer signal increase significantly with respect to the excimer one, which exhibits once again a quench due to the strong optical absorption of the samples in the excimer region. Consistently, the excimer quenching is complete for the bpan derivative whereas it is partial for **FebpbAu·Pyr** confirming the incomplete character of its spin transition. Finally, the thermal dependence of the fluorescence spectra of the isostructural analogue **ZnbpanAu** has been recorded in the heating mode and, as expected, both monomer and excimer intensities increase at low temperatures since the Zn counterpart is not SCO-active (Figure S14, ESI†).

3.3.5.- Light induced spin state trapping (LIESST) experiments

First, LIESST effect studies were carried out for compounds **FebpbAg·Pyr** and **FebpanAu** *via* single crystal optical absorption since, as mentioned above, these are the samples from which big enough single crystals are obtained for absorption spectroscopy studies. The irradiation with a 532 nm laser for 10 minutes at 10 K revealed a LS-to-HS photoconversion of 100% for **FebpbAg·Pyr** and 80% for **FebpanAu** (Figure S15a and d, respectively, ESI†). The temperature at which 50% of the photogenerated HS centers have relaxed to the LS state at a heating rate of 0.3 K min^{-1} is $T_{LIESST} \approx 43$ and 40 K for pyrene- and anthracene-containing SCO compounds, respectively (Figure S15b and e, ESI†). These results have been confirmed by magnetic measurements (Figure S16, ESI†). The

photoswitching experiments were also followed by fluorescence spectroscopy for **FebpbAg·Pyr** and **FebpanAu.** In the case of **FebpbAg·Pyr**, as long as the temperature is not modified, the monomer signal remains stable upon irradiation whereas the excimer signal increases significantly evidencing the LS to HS conversion due to light stimulus (Figure S15c, ESI†). In the case of **FebpanAu** no significant change occurs upon excitation at 532 nm and the excimer signal is not formed probably because the efficiency of LIESST effect is slightly lower than we previously observed by absorption spectroscopy (Figure S15f, ESI†). Besides, as evidenced during the thermal transition, the excimer signal is observed only when γ_{HS} approaches 1.

3.4.- Concluding remarks

This work has been undertaken as a new step in the study of the interplay between SCO and luminescence in 3D Hofmann-type coordination polymers. We have proposed two different approaches, one of them takes advantage of the porous nature of the framework to include a fluorescent guest, as recently reported for $\{Fe^{II}(bpben)[Au^{I}(CN)_2]_2\}\cdot Pyr$, in which luminescence is an extrinsic property of the framework. The other approach, for the first time, includes luminescence as an intrinsic function of the SCO framework using a fluorescent bridging pillar ligand. In the first case we have chosen the bridging ligand bpb previously used in the synthesis of the coordination polymers $\{Fe^{II}(bpb)[M^{II}(CN)_4]\}\cdot G$ (M^{II} = Ni, Pd, Pt) and $\{Fe^{II}(bpb)[Ag^{I}(CN)_2]_2\}$.[42,43] The tetracyanometallate derivatives exhibit cooperative one- or two-step SCO behavior when two molecules of naphthalene or nitrobenzene (G) are docked inside the pores. However, the much longer dicyanoargentate ligand, facilitates a singular four-fold interpenetration of identical open frameworks, with **pcu** topology, even in presence of high concentrations of naphthalene or nitrobenzene guests. The inter-framework packing is so tight that does not leave room for guest molecules, thereby favoring strong elastic frustration[44] and, consequently, the occurrence of an incomplete SCO centered at *ca.* 130 K. In contrast, self-assembling of Fe^{II}, bpb and $[M^{I}(CN)_2]^-$ (M^{I} = Ag, Au) in presence of the much larger pyrene guest molecule favors the formation of a supramolecular isomer consisting of two-fold interpenetrated frameworks while the pyrene molecules are docked in the available spaces in a similar fashion as described for the bpben derivative. Despite the probable decongestion of the crystal packing in **FebpbM·Pyr** (M = Ag, Au), elastic frustration seems to remain since the SCO in both

compounds is very incomplete and occurs at very low temperatures. Apparently, the interpenetration of the frameworks and the large number of host–guest π···π short-range interactions strongly influence the SCO behavior of this system. The lower SCO temperature observed for **FebpbAu·Pyr** compared to **FebpbAg·Pyr** is usually expected in Hofmann-type coordination polymers and is attributed to the slightly weaker ligand field induced by $[Au(CN)_2]^-$.[29]

Concerning the system **FebpanM** (M = Ag, Au), a reverse situation is observed with respect to the average critical temperatures above mentioned for the bpb derivatives. Both bpan derivatives undergo rather complete hysteretic SCO behaviors but, unexpectedly, the critical average temperature of the main transition is *ca.* 15 K lower for the Ag derivative. This suggests that, despite their isostructural nature, subtle effects of the crystal packing contribute to the effective ligand field experienced by the Fe^{II} center with a slightly larger destabilization of the LS state in case of the Ag derivative. Interestingly, both SCO behaviors can be classified as two-step transitions with very asymmetric steps. For example, compound **FebpanAu** presents a first step at high temperatures involving *ca.* 80% of the Fe^{II} centers and, separated by a large plateau *ca.* 70 K wide, and a second step occurs at lower temperatures involving *ca.* 10% of Fe^{II} centers. This behavior is associated with two consecutive symmetry breaking transformations. In addition to the expected structural changes associated with the coordination environment of Fe^{II}, the rotational freedom of the bulky anthracene group situated between the two coordinating pyridines of the bpan ligand seems to be in the origin of this singular behavior. Indeed, there is a clear correlation between the change in orientation of the anthracene groups, the change in crystallographic phase and the stabilization of the distinct HS/LS Fe^{II} fractions. In the HS state (280 K) the anthracene groups of the two crystallographically distinct bpan ligands are ordered. However, at 200 K after the first phase transition where *ca.* 80% of the Fe^{II} are LS, the structure features a unique bpan ligand but the anthracene displays positional disorder with two anthracene moieties distributed at 50% separated by 31.42º. One of the orientations practically matches that of the HS structure but the other is rotated 32.14º for the framework containing the Fe1 and 47.78º for the framework containing the Fe2 (see Figure S7a, ESI†). At 120 K, the positional disorder remains but the angle between the two orientations is 22.57º. When comparing the position of the average planes of the two orientations defined by each anthracene at 120 and 200 K a subsequent rotation of 17.59º and 26.44º occurs (see Figure S7b, ESI†). The latter reorientation is responsible for the additional symmetry

breaking and small hysteretic spin state change at low temperature. Thus, throughout the HS ↔ LS transition, while the network shrinks, the anthracene moieties rotate most likely to minimize the interatomic repulsions. The SCO behavior of the isostructural silver derivative is perfectly comparable with that of the Au counterpart, although, the low temperature hysteretic spin transition is less pronounced in the Ag derivative, particularly in the cooling branch. This different behavior may be related to the higher flexibility of the $[Ag(CN)_2]^-$ bridge, and hence, to the larger adaptability to the steric constraints progressively generated by the anthracene groups while lowering the temperature.

As far as the SCO-fluorescence synergy is concerned, the excimer signal of **FebpbAg·Pyr** is strongly quenched upon cooling due to the strong absorption of the Fe^{II} in the LS state whereas it is maximum at room temperature when the HS state is fully populated. Besides, the relatively short-distances between pyrene molecule and Fe centers may favor non-radiative energy transfer between both species. Similar behavior has been recently reported for **FebpbenAu·Pyr.**[32] In the case of **FebpanAg,** radiative energy transfer occurs due to spectral overlap between the Fe^{II} and the anthracene molecules being minimum at room temperature when the excimer signal is observed due to the lower oscillator strength of the optical absorption transition of the Fe^{II} in the HS state. However, due to the longer distance between anthracene moiety and Fe^{II} atom in **FebpanAg** with respect to the distance between pyrene guest and Fe^{II} atom in **FebpbAg·Pyr,** non-radiative energy transfer is rather attributable to the latter compound resulting in a more obvious synergy. Besides, the π···π interactions operating between anthracene moieties in **FebpanAg** are much weaker than the frontal π···π interactions between pyrene and bpb bridging ligand in **FebpbAg·Pyr** giving rise to a weaker fluorescence signal of the excimer. This might be the reason why the synergy between the spin state and the luminescence is much more significant for **FebpbAg·Pyr** than for **FebpanAg.** Moreover, a third aspect to take into account is that the excimer signal in both **FebpbAg·Pyr** and **FebpanAg** could be partially affected by self-concentration quenching. However, the large Stokes shift between the monomer absorption and excimer emission signals make it rather unlikely.

Likewise, in the case of **FebpbAg·Pyr** the relative intensity of the excimer signal increases very significantly, with respect to that of the monomer, upon photoexcitation at low temperature (LIESST effect, λ^{irr} = 532 nm) due to the LS to HS photoconversion. This was previously observed for **FebpbenAu·Pyr.**[32] Hence, further experiments will be carried out in the future in this respect to study the thermal dependence of the HS to LS relaxation after

LIESST probed by fluorescence measurements. Comparison with analogous results obtained by absorption spectroscopy would provide a different approach to study the SCO-luminescence synergy.

The differences in the SCO-fluorescence coupling when considering either an intrinsic or an extrinsic luminescent 3D Hofmann-type compound is difficult to rationalize because even if the quantum yield of the luminophores are similar (0.36 and 0.32 for anthracene and pyrene respectively in cyclohexane)[45] and the oscillator strength of the acceptors are comparable, the synergy strongly depends on the geometry of the whole arrangement. In this sense, the extrinsic luminescence obtained through the insertion of different guest fluorescent molecules such as pyrene seems very promising due to the capacity of controlling the geometry and, in consequence, the guest–guest, guest–ligand and guest–Fe^{II} distances. Nonetheless, the nature of the energy transfer processes occurring based on the location of the luminophore and SCO centres within the structure plays a key role in the deep understanding of the parameters governing the SCO-luminescence synergy. In this sense, the change of the luminescence lifetimes and quantum yields of the luminophore depend upon incorporation into the Fe^{II} SCO 3D network. In addition, the comparison of results with the equivalent non-switchable material based on Zn^{II} would give an idea of the extent of non-radiative energy transfer involved in the synergy and of the importance of the lattice rigidity in the quantum yield values. In principle, stiffness is expected to prevent non-radiative decays hence leading to higher quantum yield.[27,46] Thus, further studies will be directed towards analysing the luminescence lifetime and the quantum yield of the studied compounds as a function of the spin fraction.

3.5.- References

[1] P. Gütlich, A. Hauser and H. Spiering, *Angew. Chem., Int. Ed. Engl.*, **1994**, *33*, 2024–2054.

[2] J. A. Real, A. B. Gaspar, V. Niel, M. C. Muñoz, *Coord. Chem. Rev.*, **2003**, *236*, 121–141.

[3] (a) P. Gütlich, G. Goodwin, *Top. Curr. Chem.*, **2004**, *233*, 234–235; (b) J. A. Real, A. B. Gaspar, M. C. Muñoz, *Dalton Trans.*, **2005**, 2062–2079; (c) *Spin-Crossover Materials: Properties and Applications,* ed. M. A. Halcrow, John Wiley & Sons Ltd, Chichester,

2013; (*d*) see special issue in Comptes Rendues "Spin crossover phenomenon" A. Bousseksou, *C. R. Chim.*, **2018**, *21*, 1152–1169; (e) P. Gülitch, Y. Garcia, H. A. Goodwin, *Chem. Soc. Rev.*, **2000**, *29*, 419–427.

[4] J.-F. Létard, P. Guionneau, L. Goux-Capes, *Spin Crossover Transit. Met. Compd III*, **2004**, *1*, 221–249.

[5] A. Bousseksou, G. Molnár, L. Salmon, W. Nicolazzi, *Chem. Soc. Rev.*, **2011**, *40*, 3313.

[6] M. Matsuda, H. Isozaki, H. Tajima, *Thin Solid Films*, **2008**, *517*, 1465–1467.

[7] L. Salmon, G. Molnár, D. Zitouni, C. Quintero, C. Bergaud, J.-C. Micheau, A. Bousseksou, *J. Mater. Chem.*, **2010**, *20*, 5499.

[8] S. Bertazzo, K. Rezwan, *Langmuir*, **2010**, *26*, 3364–3371.

[9] C. M. Quintero, I. A. Gural'skiy, L. Salmon, G. Molnár, C. Bergaud, A. Bousseksou, *J. Mater. Chem.*, **2012**, *22*, 3745.

[10] I. Suleimanov, O. Kraieva, G. Molnar, L. Salmon, A. Bousseksou, *Chem. Commun.*, **2015**, *51*, 15098–15101.

[11] J. M. Herrera, S. Titos-Padilla, S. J. A. Pope, I. Berlanga, F. Zamora, J. J. Delgado, K. V. Kamenev, X. Wang, A. Prescimone, E. K. Brechin, E. Colacio, *J. Mater. Chem. C*, **2015**, *3*, 7819–7829.

[12] I. Suleimanov, O. Kraieva, G. Molnár, L. Salmon, A. Bousseksou, *Chem. Commun.*, **2015**, *51*, 15098–15101.

[13] I. Suleimanov, O. Kraieva, J. Sánchez Costa, I. O. Fritsky, G. Molnár, L. Salmon, A. Bousseksou, *J. Mater. Chem. C*, **2015**, *3*, 5026–5032.

[14] S. Titos-Padilla, J. M. Herrera, X.-W. Chen, J. J. Delgado, E. Colacio, *Angew. Chem., Int. Ed.*, **2011**, *50*, 3290–3293.

[15] B. Benaicha, K. Van Do, A. Yangui, N. Pittala, A. Lusson, M. Sy, G. Bouchez, H. Fourati, C. J. Gómez-García, S. Triki, K. Boukheddaden, *Chem. Sci.*, **2019**, *10*, 6791–6798.

[16] J. Yuan, S.-Q. Wu, M.-J. Liu, O. Sato, H.-Z. Kou, *J. Am. Chem. Soc.*, **2018**, *140*,

9426–9433.

[17] J.-L. Wang, Q. Liu, Y.-S. Meng, X. Liu, H. Zheng, Q. Shi, C.-Y. Duan, T. Liu, *Chem. Sci.*, **2018**, *9*, 2892–2897.

[18] C. Lochenie, K. Schö Tz, F. Panzer, H. Kurz, B. Maier, F. Puchtler, S. Agarwal, A. Kö, B. Weber, *J. Am. Chem. Soc.*, **2018**, *140*, 700–709.

[19] B. Schäfer, T. Bauer, I. Faus, J. A. Wolny, F. Dahms, O. Fuhr, S. Lebedkin, H.-C. Wille, K. Schlage, K. Chevalier, F. Rupp, R. Diller, V. Schünemann, M. M. Kappes, M. Ruben, *Dalton Trans.*, **2017**, *46*, 2289–2302.

[20] C.-F. Wang, R.-F. Li, X.-Y. Chen, R.-J. Wei, L.-S. Zheng, J. Tao, *Angew. Chem., Int. Ed.*, **2015**, *54*, 1574–1577.

[21] Y. Garcia, F.-O. Robert, A. D. Naik, G. Zhou, B. Tinant, K. Robeyns, S. Ebastien Michotte, L. Piraux, *J. Am. Chem. Soc.*, **2011**, *133*(40), 15850–15853.

[22] M. Hasegawa, F. Renz, T. Hara, Y. Kikuchi, Y. Fukuda, J. Okubo, T. Hoshi, W. Linert, *Chem. Phys.*, **2002**, *277*, 21–30.

[23] C. Piguet, E. Rivara-Minten, G. Bernardinelli, J.-C. G. Bünzli, G. Hopfgartner, *J. Am. Chem. Soc.*, **1997**, 421–433.

[24] C. Piguet, E. Rivara-Minten, G. Hopfgartner, J.-C. G. Bünzli, *Helv. Chim. Acta*, **1995**, *78*, 1651–1672.

[25] J.-Y. Ge, Z. Chen, L. Zhang, X. Liang, J. Su, M. Kurmoo, J.-L. Zuo, *Angew. Chem., Int. Ed.*, **2019**, *58*, 8789–8793.

[26] H. Matsukizono, K. Kuroiwa, N. Kimizuka, *Chem. Lett.*, **2008**, *37*, 446–447.

[27] H. J. Shepherd, C. M. Quintero, G. Molnár, L. Salmon, Bousseksou, *Spin-Crossover Materials,* John Wiley & Sons Ltd, Oxford, UK, **2013**, pp. 347–373.

[28] Y. Garcia, V. Niel, M. C. Muñoz, J. A. Real, *Top. Curr. Chem.*, **2004**, *233*, 229–257.

[29] M. C. Muñoz, J. A. Real, *Coord. Chem. Rev.*, **2011**, *255*(17–18), 2068–2093.

[30] R. Ohtani, S. Hayami, *Chem. – Eur. J*, **2017**, *23*(10), 2236–2248.

[31] Z.-P. Ni, J.-L. Liu, M. M. Hoque, W. Liu, J.-Y. Li, Y.-C. Chen, M.-L. Tong, *Coord. Chem. Rev.*, **2017**, *335*, 28–43.

[32] T. Delgado, M. Meneses-Sánchez, L. Piñeiro-López, C. Bartual-Murgui, M. C. Muñoz, J. A. Real, *Chem. Sci.*, **2018**, *9*, 8446–8452.

[33] L. Vegard, Z. Kristallogr. – *Cryst. Mater.*, **1928**, *67*, 239–259.

[34] B. R. Mullaney, L. Goux-Capes, D. J. Price, G. Chastanet, J. F. Létard, C. J. Kepert, *Nat. Commun.*, **2017**, *8*, 1053.

[35] M. A. Slifkin, *Nature*, **1963**, *200*, 766–767.

[36] M. Sugino, Y. Araki, K. Hatanaka, I. Hisaki, M. Miyata, N. Tohnai, *Cryst. Growth Des.*, **2013**, *13*, 4986–4992.

[37] R. Akatsuka, A. Momotake, Y. Shinohara, Y. Kanna, T. Sato, M. Moriyama, K. Takahashi, Y. Nishimura, T. Arai, *J. Photochem. Photobiol., A*, **2011**, *223*, 1–5.

[38] C. Tang, X. Zhu, Y. Song, W. Liu, Q. Yang, Z. Lv, Y. Yang, *J. Photochem. Photobiol., A*, **2019**, *376*, 263–268.

[39] H. G. O. Becker, *J. Prakt. Chem./Chem.-Ztg.*, **1980**, *322*, 704.

[40] J. C. Lindon, G. E. Tranter, D. W. Koppenaal, *Encyclopedia of spectroscopy and spectrometry*, Academic Press, Oxford, 3rd edn, **2017**, pp. 636–653.

[41] T. Z. Janosi, J. Korppi-Tommola, Z. Csok, L. Kollar, P. Myllyperkio, J. Erostyak, *J. Spectrosc.*, **2014**, *2014*, 1–8.

[42] L. Piñeiro-López, M. Seredyuk, M. C. Muñoz, J. A. Real, *Chem. Commun.*, **2014**, *50*, 1833–1835.

[43] L. Piñeiro-López, F. J. Valverde-Muñoz, M. Seredyuk, M. C. Muñoz, M. Haukka, J. A. Real, *Inorg. Chem.*, **2017**, *56*, 7038–7047.

[44] M. Paez-Espejo, M. Sy, K. Boukheddaden, *J. Am. Chem. Soc.*, **2016**, *138*, 3202–3210.

[45] Oregon Medical Laser Center.org, https://omlc.org/.

[46] A. S. Marfunin, *Spectroscopy, Luminescence and Radiation Centers in Minerals*, Springer-Verlag, Berlin, Germany, **1979**, p. 352.

3.6.- Supporting Information

3.6.1. Experimental Section

3.6.1.1. Synthesis procedures

Bpb ligand was prepared according to the synthesis described in the literature.[1]

*Synthesis of **1,4-bis(4-pyridyl)anthracene (bpan).*** To a mixture of 4-pyridylboronic acid (2.2 g, 18 mmol), 9,10-dibromoanthracene (1.7 g, 5 mmol) and palladium tetrakis(triphenylphosphine) (381.6 mg, 0.33 mmol) in dioxane (40 mL) purged with Ar was added dropwise a solution of K_2CO_3 (2.6 g, 18.8 mmol) in H_2O (20 mL). After being stirred at 100 ºC for 18 h, the mixture was cooled to room temperature and removed the aqueous phase. The dioxane layer was filtered and removed under reduced pressure. The product was dissolved in dichloromethane (100 mL), filtrated and washed twice with 5 g of Na_2CO_3 in 25 mL of water. The dichloromethane solution was dried over Na_2SO_4 and concentrated under reduced pressure getting 1.2 g (72%) of yellow product.

*Synthesis of **FebpanAu, FebpanAg** and **ZnbpanAu.*** Single crystals of **FebpanAu/FebpanAg** were grown by slow liquid-to-liquid diffusion methods using a layering tube. The bottom was filled with a mixture of $Fe(BF_4)_2{\cdot}6H_2O$ (27.8 mg, 0.1 mmol) in 1 mL of methanol and bpan (33.2 mg, 0.1 mmol) in 2 mL of dichloromethane. The middle was filled with an interphase of 5 mL of methanol-dichloromethane (1:1). The top was filled with a solution of potassium dicyanoaurate/dicyanoargentate (57.6/39.8 mg, 0.2 mmol). Similar diffusion conditions were used for obtaining the **ZnbpanAu** derivative but using $Zn(BF_4)_2{\cdot}6H_2O$ (34.6 mg, 0.1 mmol) instead of the Fe^{II} salt. Afterwards, the tube was closed and light-yellow rhomboid crystals (almost colorless for the Zn counterpart) were formed within two days with relative high yield (c.a. 45%). *Elemental Analysis*: Calculated for **FebpanAu** [$C_{28}H_{16}Au_2FeN_6$ (886.3) (%)]: C 37.95; H 1.82; N 9.48. Found (%): C 38.09; H 1.71; N 9.13. Calculated for **FebpanAg** [$C_{28}H_{16}Ag_2FeN_6$ (707.9) (%)]: C 47.50; H 2.28; N 11.87. Found (%): C 47.89; H 2.16; N 11.46. Calculated for **ZnbpanAu** [$C_{28}H_{16}Au_2ZnN_6$ (895.8) (%)]: C 37.54; H 1.80; N 9.38. Found (%): C 37.92; H 1.92; N 9.63.

*Synthesis of **FebpbAu·pyr** and **FebpbAg·pyr.*** Single crystals of **FebpbAu·pyr/FebpbAg·pyr** were obtained through liquid-to-liquid diffusion methods using a modified H-shape tube with 3 arms. The peripheral arms were filled 2 mL methanol solutions containing 0.1 mmol (33.7 mg) of $Fe(BF_4)_2{\cdot}6H_2O$ and 0.2 mmol of $K[Au^I(CN)_2]/K[Ag^I(CN)_2]$ (57.6/39.8 mg) respectively, and the center arm was filled with a 2 mL methanol solution of 0.1 mmol (20 mg) of the bpb ligand. Afterwards, the rest of the tube was carefully filled with a methanolic solution saturated with pyrene and sealed with parafilm. After two weeks, orange **FebpbAu·pyr/FebpbAg·pyr** blocks suitable for single crystal X-ray analysis appeared within the H tube. *Elemental Analysis*: Calculated for **FebpbAu·pyr** [$C_{34}H_{18}Au_2FeN_6$ (960.3) (%)]: C 42.52; H 1.89; N 8.75. Found (%): C 42.23; H 1.86; N 8.91. Calculated for **FebpbAg·pyr** [$C_{34}H_{18}Ag_2FeN_6$ (782.2) (%): C 52.21; H 2.32; N 10.75. Found (%): C 52.81; H 2.48; N 10.44.

3.6.1.2. Physical characterization

Elemental analyses (C, H, and N) were performed with a CE Instruments EA 1110 CHNS Elemental analyzer. Magnetic measurements were performed with a Quantum Design MPMS-XL-5 SQUID magnetometer in the 2 to 400 K temperature range with an applied magnetic field of 0.1 T. Experimental susceptibilities were corrected for diamagnetism of the constituent atoms by the use of Pascal's constants. Photomagnetic measurements were performed irradiating with a Diode Pumped Solid State Laser DPSS-532-20 from Chylas and a coupled via an optical fiber to the cavity of the SQUID magnetometer. The optical power at the sample surface was adjusted to ~3 $mW{\cdot}cm^{-2}$, and it was verified that it resulted in no significant change in magnetic response due to heating of the sample. The photomagnetic samples consisted of a thin layer of compound whose weight was corrected by comparison of a thermal spin crossover curve with that of a more accurately weighted sample of the same compound. Calorimetric measurements were performed using a differential scanning calorimeter Mettler Toledo DSC 821e. Low temperatures were obtained with an aluminium block attached to the sample holder, refrigerated with a flow of liquid nitrogen and stabilized at a temperature of 110 K. The sample holder was kept in a dry box under a flow of dry nitrogen gas to avoid water condensation. The measurements were carried out using around 15 mg of polycrystalline samples sealed in aluminium pans with a mechanical crimp. Temperature and heat flow

calibrations were made with standard samples of indium by using its melting transition (429.6 K, 28.45 J g^{-1}). An overall accuracy of ±0.2 K in temperature and ±2% in the heat capacity is estimated. The uncertainty increases for the determination of the anomalous enthalpy and entropy due to the subtraction of an unknown baseline. Powder X-ray measurements where performed on a PANalytical Empyrean X-ray powder diffractometer (monochromatic CuKα radiation).

Single crystal absorption spectroscopy. Single crystals of **FebpbAg·py**r and **FebpanAu** were mounted on a copper plate with a previously drilled hole. One crystal was deposited in the middle of the hole and fixed with silver paste nanoparticles (Agar Scientific Ltd.) to ensure a good thermal conductivity. The sample was then introduced into a closed cycle cryostat (Janis-Sumimoto SHI-4.5), which operates between 4 and 300 K and it is equipped with a programmable temperature controller (Lakeshore Model 331). The cryostat was introduced into a double beam spectrometer (Varian Cary 5000). The irradiation for the photoinduced experiments (LIESST) was performed with a HeNe laser at 532 nm with a power of 2 mW/ mm^2.

Photoluminescence spectroscopy. The excitation and luminescence spectra of **FebpbAg·pyr, FebpbAu·pyr, FebpanAg** and **FebpanAu** were recorded on a Fluorolog 3-22 (Horiba Jobin Yvon), equipped with a water-cooled photo multiplier tube (PMT). A calibration function was applied to account for the wavelength-dependent sensitivity of the photomultiplier tube, the throughput of the analyzing monochromator and the power fluctuation of the xenon lamp. For the ambient temperature and 80 K measurements a quartz capillary was filled with 20 mg of the crystals and was introduced in a liquid nitrogen dewar made of quartz which was filled with liquid nitrogen for the 80 K measurements until the high-spin to low-spin conversion was observed by the color change from yellow to red respectively. For the temperature dependence measurements an ensemble of **FebpbAg·pyr** or **FebpanAg** crystal are deposited in a cooper plate and fixed with silver paste nanoparticles to ensure a good thermal conductivity. The sample was then introduced into the above described cryostat, that was in turn aligned in the Fluorolog.

Single crystal X-ray measurements. Single crystals were mounted on a glass fiber using a viscous hydrocarbon oil to coat the crystal and then transferred directly to the cold nitrogen stream for data collection. X-ray data were collected on a Supernova diffractometer equipped with a graphite-monochromated Enhance (Mo) X-ray Source (λ = 0.71073 Å). The

program CrysAlisPro, Oxford Diffraction Ltd., was used for unit cell determinations and data reduction. Empirical absorption correction was performed using spherical harmonics, implemented in the SCALE3 ABSPACK scaling algorithm. The structures of were solved with the ShelXT structure solution program[2] and refined with the SHELXL-2013 program,[3] using Olex2.[4] Non-hydrogen atoms were refined anisotropically, and hydrogen atoms were placed in calculated positions refined using idealized geometries (riding model) and assigned fixed isotropic displacement parameters.

Figure S1. *Experimental (black lines) and simulated (grey lines) powder X-ray diffraction patterns of the studied compounds.*

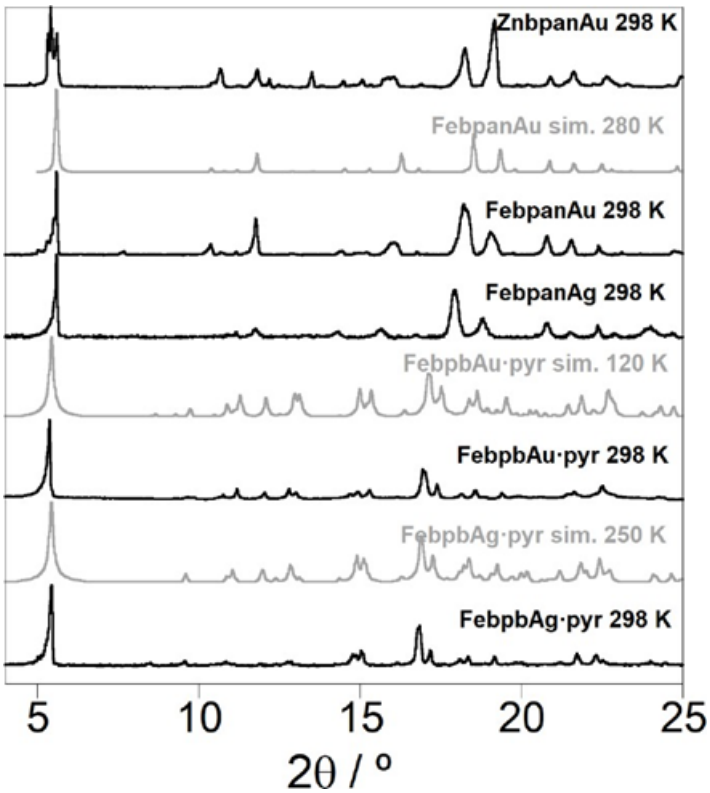

Figure S2. *Thermogravimetric analysis of a)* ***FebpbAg·pyr****, b)* ***FebpbAu·pyr****, c)* ***FebpanAg*** *and* ***FebpanAu***

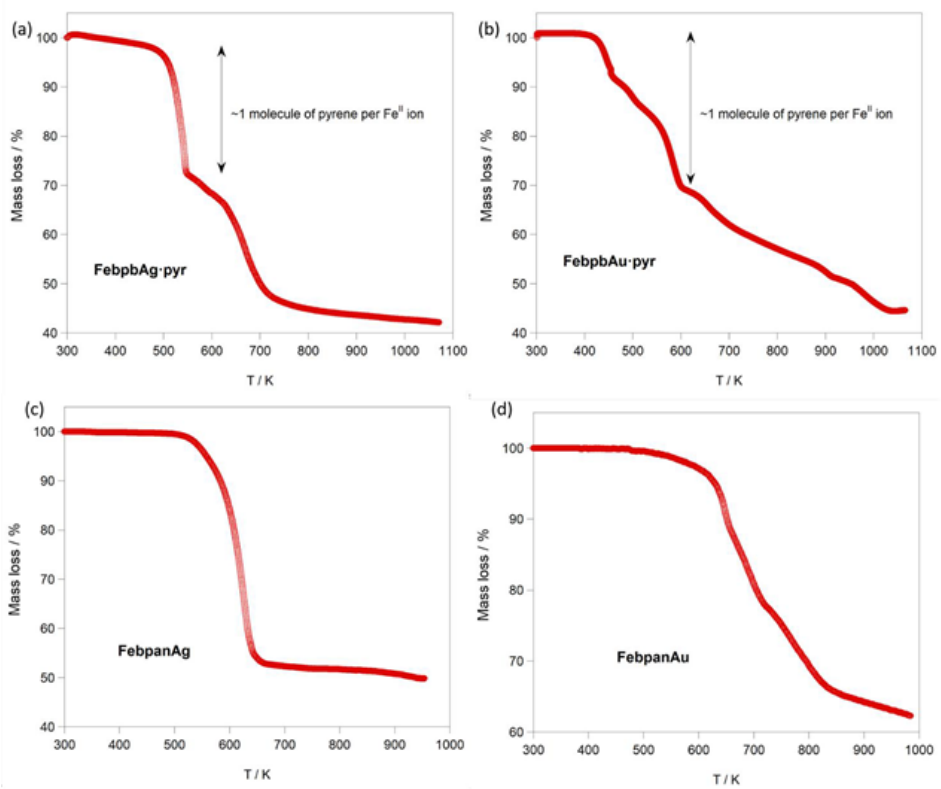

Figure S3. *$\chi_M T$ vs T curves obtained for compound* ***FebpbAg·pyr*** *registered within two successive cooling and heating cycles.*

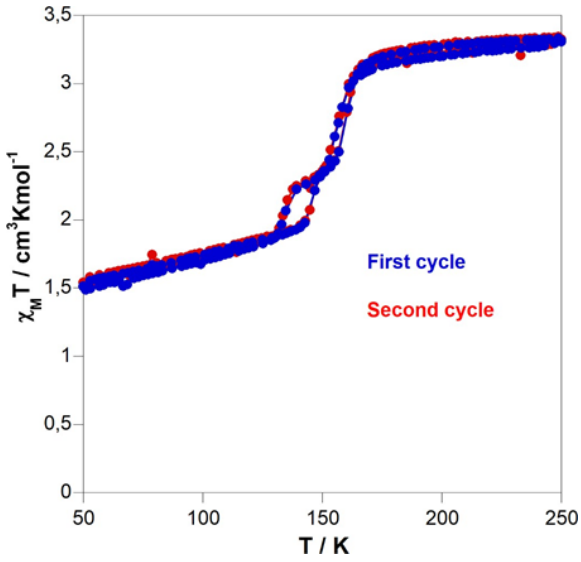

Figure S4. *DSC curves for compounds a)* ***FebpanAg,*** *b)* ***FebpanAu*** *and c)* ***FebpbAg·pyr.*** *The blue and red lines represent the cooling and heating modes, respectively. Magnetic curves are also represented for comparison. Inset: DSC regions of interest enlarged.*

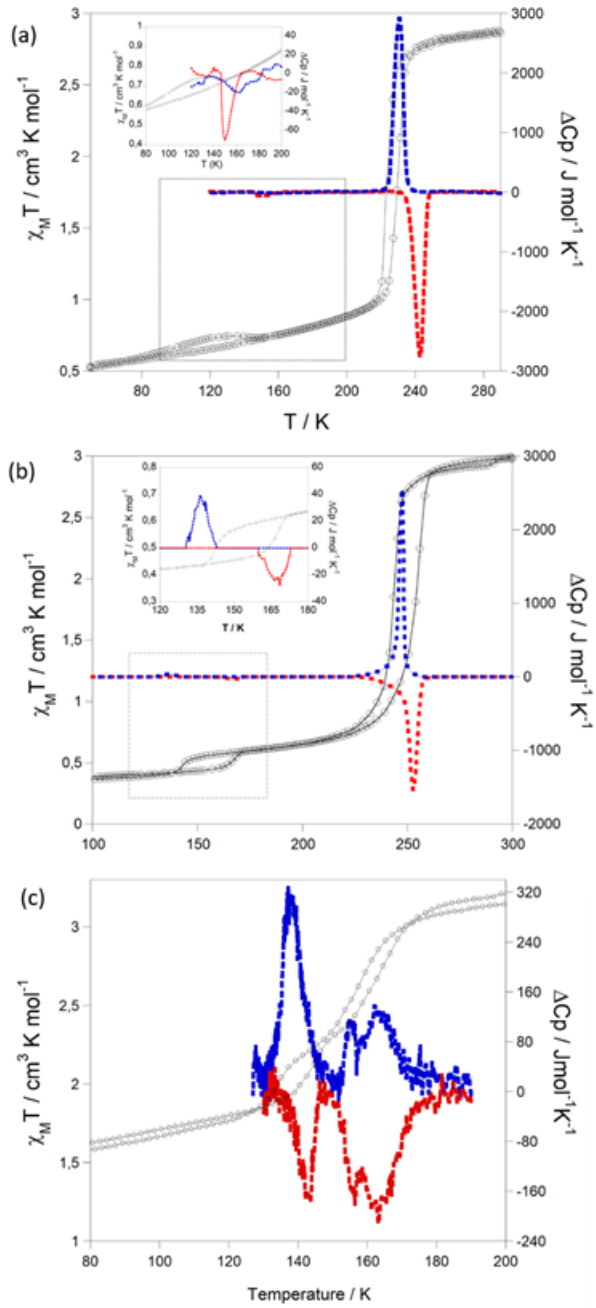

Figure S5. *Thermal dependence of the single crystal absorption spectra during the thermal transition in the cooling mode for a)* ***FebpbAg·pyr*** *and b)* ***FebpanAu.***

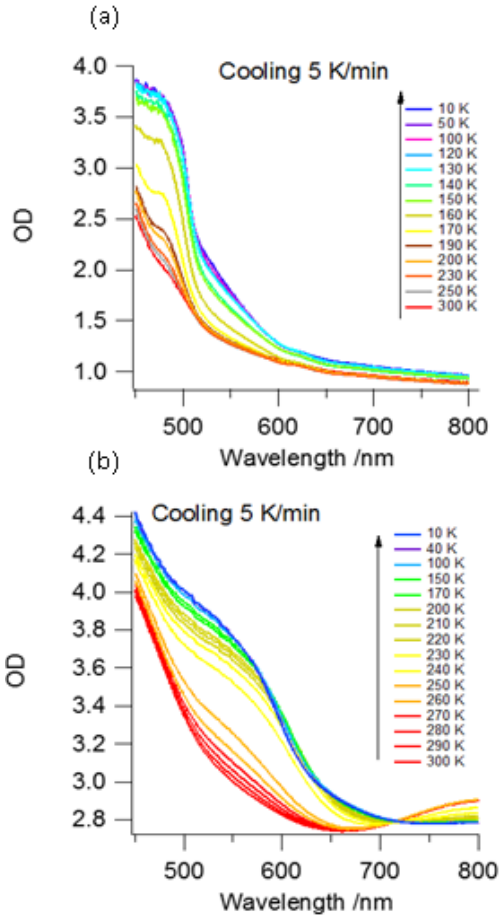

Figure S6. *Absorption spectra at 300 and 10 K of grinded crystals of* ***FebpanAg*** *a) diluted and pressed in a KBr pellet and b) dispersed in a mineral oil. In both cases the sample is strongly affected by the preparition and the MLCT and d-d bands of* Fe^{II} *observed for* ***FebpanAu*** *and* ***FebpbAg·pyr*** *are not observed. Instead, the relatively week band observed at around 220 nm could be tentatively assigned to the absorption band of anthracene.*

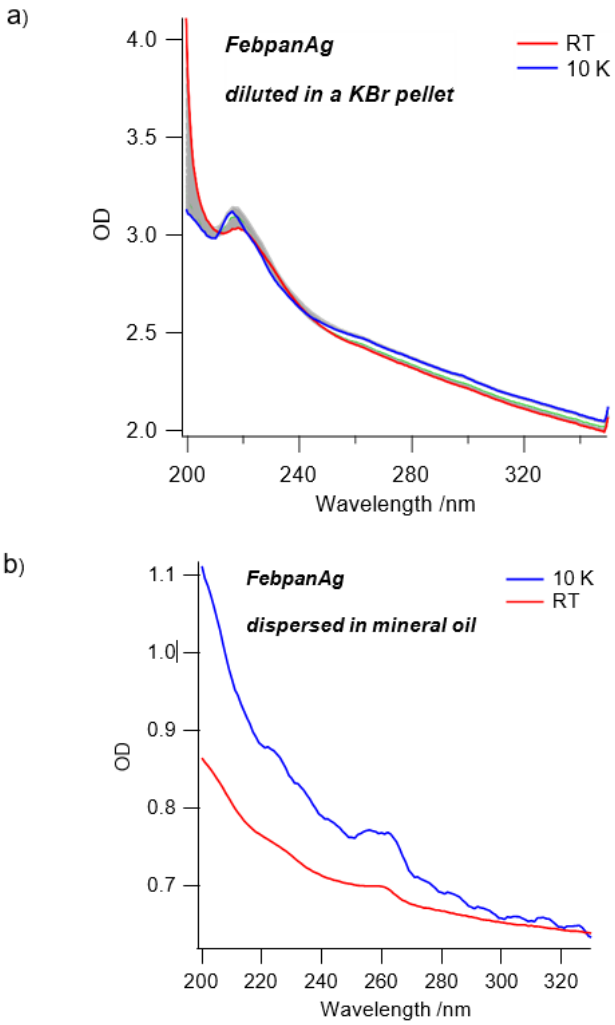

Figure S7. *Side and top perspectives for a representative fragment of the* ***FebpanAu*** *framework upon successive crystallographic transformations (a) 280 K → 200 K and b) 200 K → 120 K) involving the rotation of the anthracene moiety.*

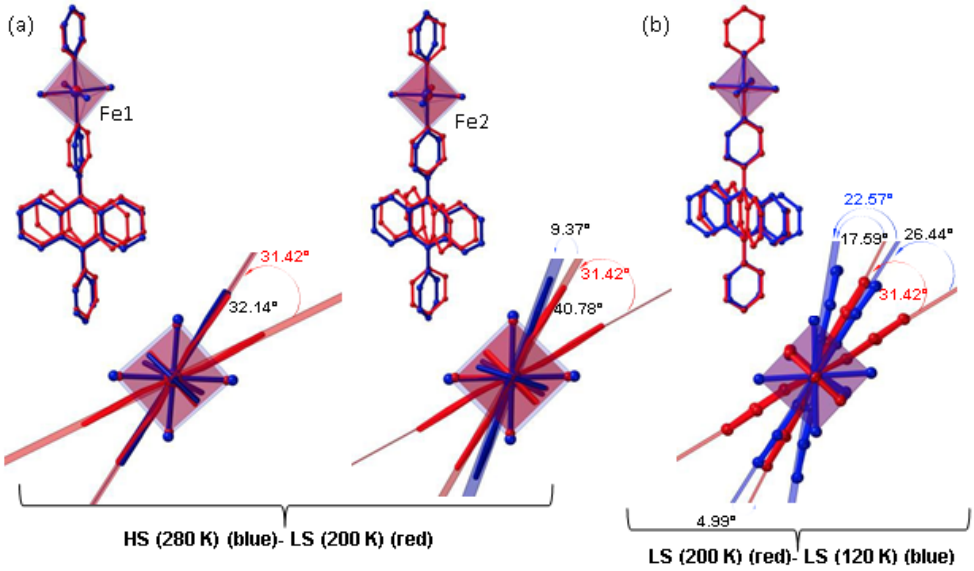

Figure S8. *Intermolecular short C···C π-contacts smaller than the sum of the Van der Waals radii (c.a. 3.7 Å) for the two types of pyrene molecules.*

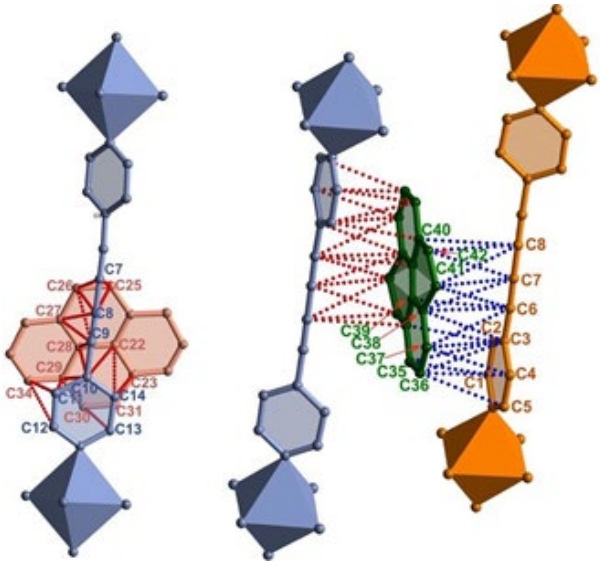

Figure S9. *Excitation spectrum of an ensemble of crystals of a)* ***FebpbAg·pyr*** *and b)* ***FebpanAg*** *measured at 525 nm in a quartz capillary.*

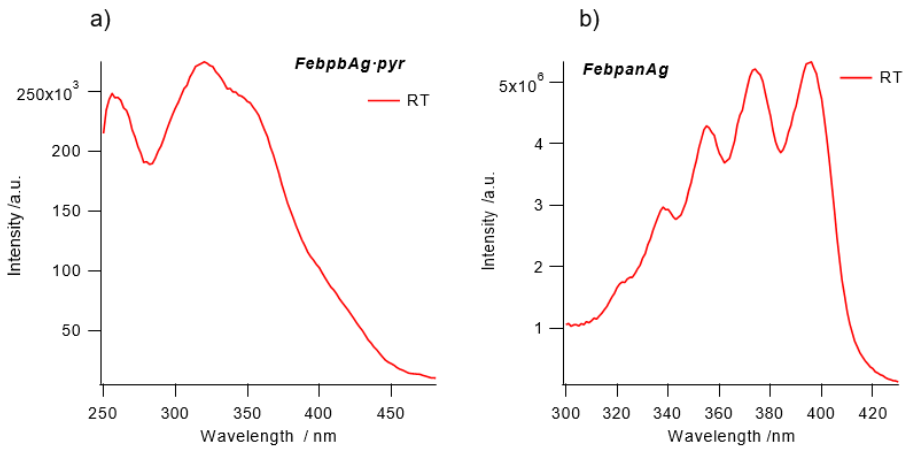

Figure S10. *Thermal evolution of the fluorescence of an ensemble of crystals of* ***FebpbAg·pyr*** *(a) and* ***FebpanAg*** *(c) during heating at 5 K/min and extracted normalized evolution of the excimer and monomer intensity for* ***FebpbAg·pyr*** *(b) and* ***FebpanAg*** *(d).*

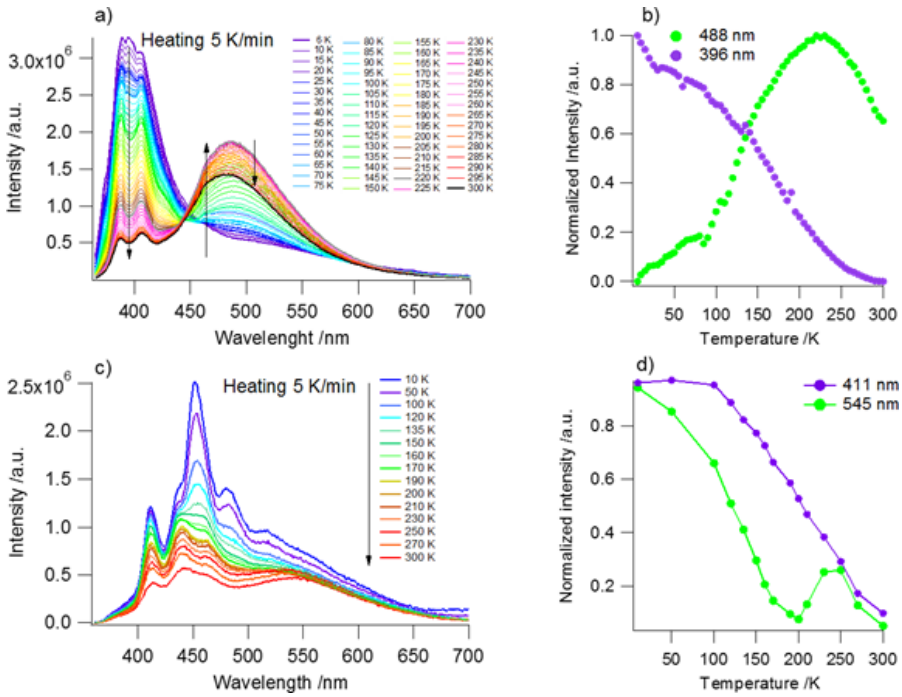

Figure S11. *Thermal evolution of the excimer signal for a) {Fe^{II}(bpb)[(Ag(CN)$_2$)$_2$]}@pyrene and b) {Fe^{II}(bpben)(Au(CN)$_2$)$_2$} during heating at 5 K/min. Two similar ligands give rise to two clearly different thermal spin transitions, which can be followed by fluorescence.*

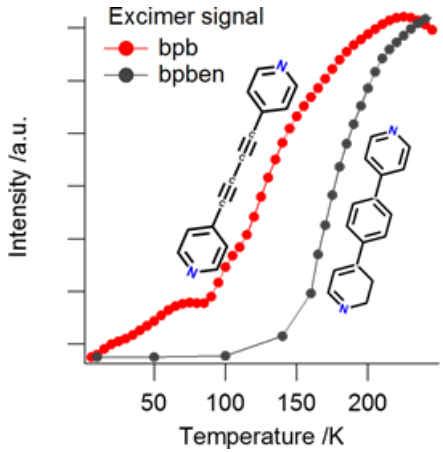

Figure S12. *a) Emission wavelength dependence of the excitation spectra of* ***FebpanAg*** *and corresponding thermal dependence of fluorescence spectra upon excitation at b) 345 nm and c) 262 nm.*

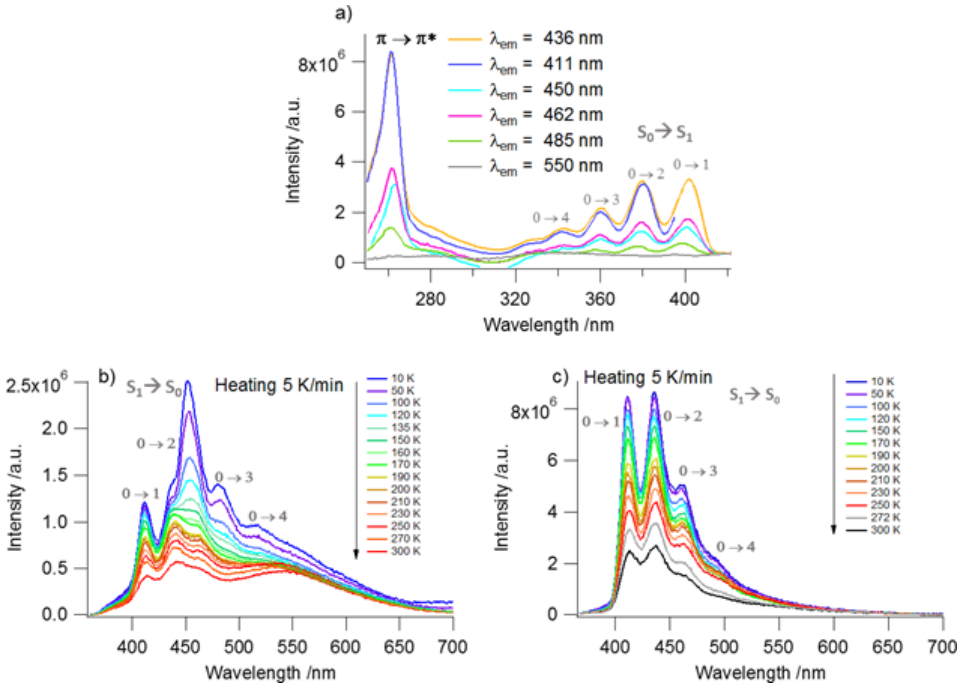

Figure S13. *Single crystal absorption spectra of a)* ***FebpbAu·pyr*** *and b)* ***FebpanAu*** *at 300 and 10 K in the HS and LS state respectively; room temperature excitation spectra of an ensemble of crystals of c)* ***FebpbAu·pyr*** *and d)* ***FebpanAu*** *measured at 525 nm, and corresponding fluorescence spectra of an ensemble of crystals of e)* ***FebpbAu·pyr*** *and f)* ***FebpanAu*** *after excitation at 245 nm at 300 and 80 K in HS and LS state, respectively.*

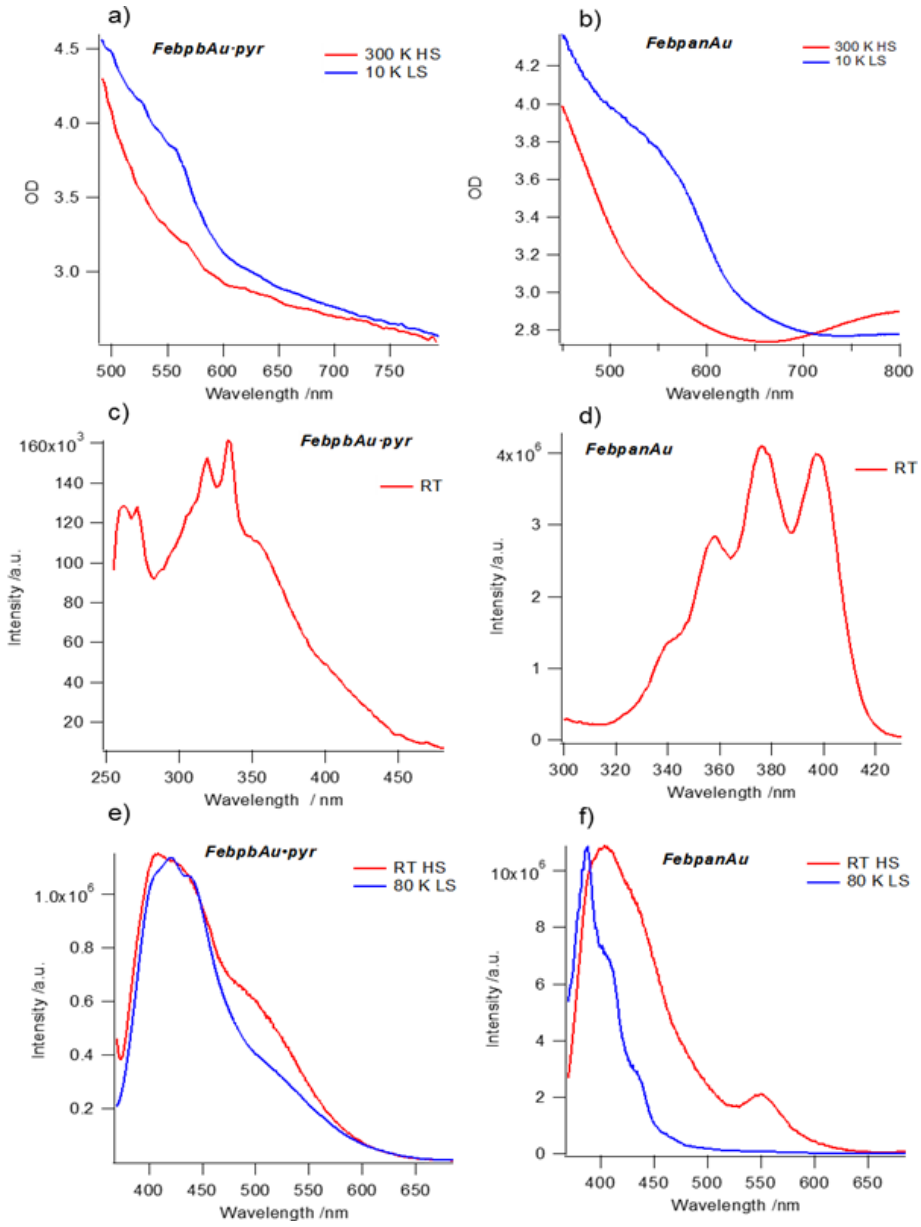

Figure S14. *Fluorescence spectra of an ensemble of crystals of* ***ZnbpanAu*** *after excitation at 345 nm during heating from 10 K to 300 K at 5 K/min.*

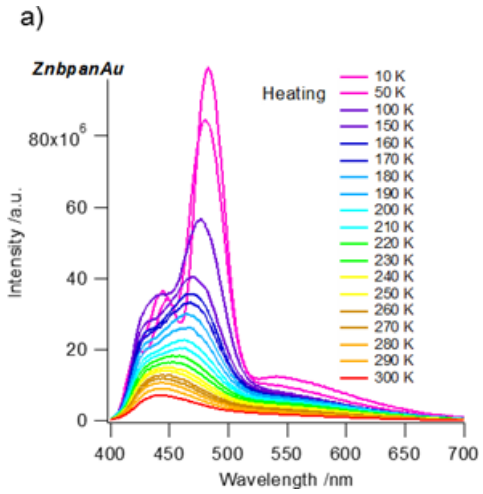

Figure S15. *Photo-induced LS to HS transition at 10 K and subsequent HS to LS relaxation while heating at 0.3 K/min up to 60 K for a)* ***FebpbAg·pyr*** *and d)* ***FebpanAu.*** *Evolution of the HS fraction during the thermal HS to LS relaxation with the corresponding* T_{LIESST} *indicated in the figure for b)* ***FebpbAg·pyr*** *and e)* ***FebpanAu.*** *Fluorescence spectra of the sample at room temperature and at 10 K before LIESST and 10 K after LIESST for c)* ***FebpbAg·pyr*** *and f)* ***FebpanAu.***

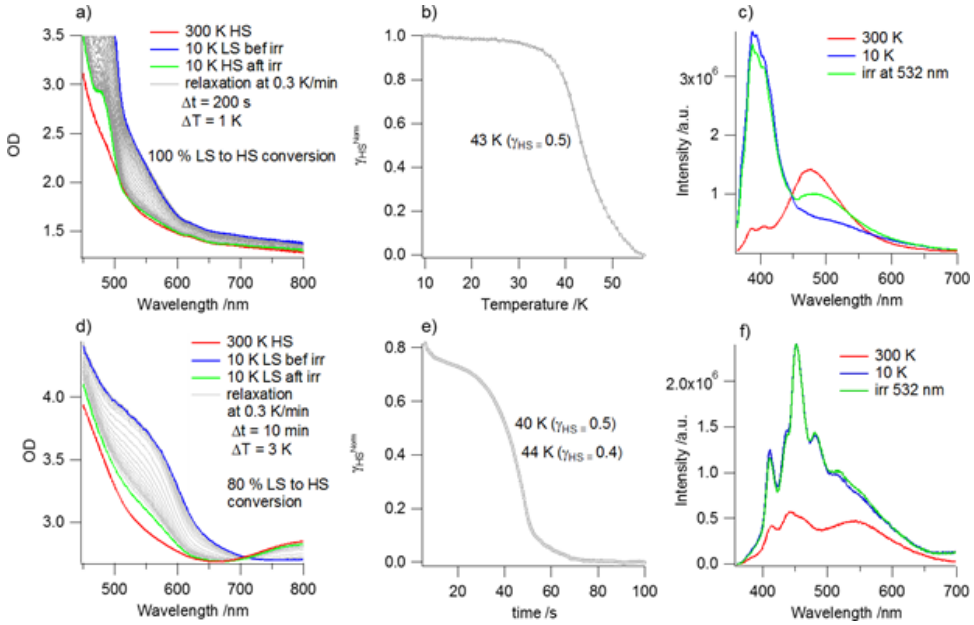

Figure S16. *Cooling mode thermal transition at 1 K/min (blue diamonds), photo-induced LS to HS transition at 10 K upon irradiation at 632 nm (green triangles), HS to LS relaxation while heating at 0.3 K/min (orange triangles) and subsequent heating mode thermal transition (red diamonds) obtained by magnetic susceptibility measurement on a multicrystalline sample of a)* ***FebpanAu*** *and b)* ***FebpbAg·pyr.*** *The percentage of LS fraction photoconverted through LIESST and the* T_{LIESST} *are in agreement with the data obtained by single crystal absorption spectroscopy upon irradiation at 532 nm.*

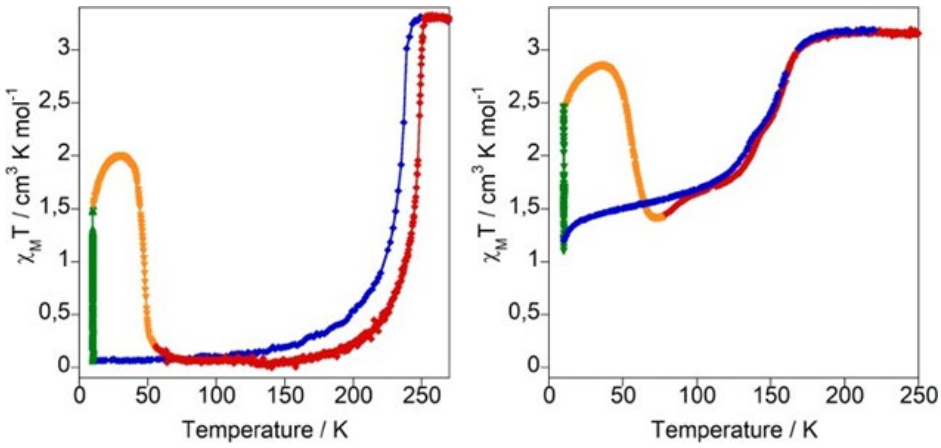

Table S1. *Selected crystallographic parameters for* ***FebpanAu*** *at 280, 200 and 120 K.*

Sample		**FebpanAu**	
***T* (K)**	**280**	**200**	**120**
Empirical formula	$C_{56}H_{32}Au_4Fe_2N_{12}$	$C_{22}H_{12}Au_2FeN_6$	$C_{28}H_{16}Au_2FeN_6$
Mr	1772.50	810.16	886.25
Crystal system	Monoclinic	Orthorhombic	Monoclinic
Space group	*P2/c*	*cmma*	*P2/n*
a (Å)	11.6053(5)	12.3200(8)	10.0487(11)
b (Å)	15.8026(5)	15.8744(10)	15.414(2)
c (Å)	16.9870(5)	15.3989(12)	10.0635(13)
α	90	90	90
β	90.113(3)	90	104.609(3)
γ	90	90	90
V ($Å^3$)	3115.3 (2)	3011.6(4)	1508.3(3)
Z	2	4	2
F(000)	1640	1480	820
D_c (mg cm^{-3})	1.890	1.787	1.951
μ (Mo-K_α)(mm^{-1})	9.879	10.210	10.202
No. of total reflections [$I>2\sigma(I)$]	16766	18353	17833
R [$I>2\ \sigma\ (I)$]	0.0612	0.0688	0.0685
wR [$I>2\ \sigma\ (I)$]	0.0793	0.1867	0.1700
Goodness-of-fit on F2	1.032	1.050	1.000

Table S2. *Selected crystallographic parameters for* ***FebpbAg·pyr*** *and* ***FebpbAu·pyr.***

Sample	**FebpbAg·pyr**		**FebpbAu·pyr**
***T* (K)**	**250**	**100**	**120**
Empirical formula	$C_{42}H_{23}Ag_2FeN_6$	$C_{42}H_{23}Ag_2FeN_6$	$C_{42}H_{23}Au_2FeN_6$
Mr	883.25	883.25	1061.45
Crystal system		Orthorhombic	
Space group		*P*-1	
a (Å)	10.6198(6)	10.4725(5)	10.4750(9)
b (Å)	10.6201(6)	10.4766(5)	10.4803(10)
c (Å)	16.6476(9)	16.4736(8)	16.5967(16)
α	101.223(5)	93.637(4)	93.218(8)
β	93.765(5)	100.867(4)	100.823(8)
γ	96.999(5)	97.191(4)	97.269(8)
V ($Å^3$)	1820.22(18)	1754.01(15)	1769.2(3)
Z	2	2	2
F(000)	874.0	874.0	1002.0
D_c (mg cm^{-3})	1.612	1.672	1.992
μ (Mo-K_α)(mm^{-1})	1.497	1.554	8.716
No. of total reflections [$I>2\sigma(I)$]	13228	19947	17844
R [$I>2\ \sigma\ (I)$]	0.0666	0.0703	0.0857
wR [$I>2\ \sigma\ (I)$]	0.1660	0.1805	0.1690
Goodness-of-fit on F2	1.039	1.038	1.061

Table S3. *Intermolecular π-π distances smaller than the sum of the C···C Vander Waals distance (c.a. 3.7 Å) between pyrene and the pyridine moieties of the brigding ligand bpb for* ***FebpbAg·pyr.***

Pyrene1[a]	T = 100 K	T = 250 K	Pyrene2[b]	T = 100 K	T = 250 K
C8···C26	3.28(2)	3.29(1)	C4···C36	3.34(2)	3.58(1)
C8···C25	3.37(2)	3.39(1)	C7···C41	3.35(2)	3.69(1)
C7···C26	3.38(2)	3.41(1)	C2···C35	3.38(2)	3.37(1)
C7···C25	3.38(2)	3.42(1)	C6···C38	3.40(2)	3.46(1)
C10···C28	3.41(2)	3.45(1)	C2···C40	3.40(2)	3.46(1)
C9···C27	3.44(2)	3.49(1)	C1···C35	3.43(2)	3.38(1)
C13···C31	3.44(2)	3.54(1)	C8···C42	3.48(2)	3.57(1)
C13···C30	3.47(2)	3.63(1)	C3···C36	3.50(2)	3.61(1)
C14···C23	3.51(2)	3.61(1)	C5···C36	3.53(2)	3.60(1)
C11···C34	3.52(2)	3.55(1)	C4···C37	3.54(2)	3.55(1)
C11···C29	3.53(2)	3.55(1)	C3···C37	3.55(2)	3.55(1)
C9···C28	3.54(2)	3.59(1)	C8···C41	3.57(2)	
C9···C26	3.56(2)	3.56(1)	C3···C35	3.58(2)	
C14···C22	3.56(2)	3.64(1)	C7···C38	3.60(2)	
C10···C29	3.58(2)	3.68(1)	C6···C39	3.61(2)	3.66(1)
C14···C31	3.58(2)	----	C6···C41	3.62(2)	
C8···C27	3.63(2)	3.67(1)	C6···C37	3.67(2)	
C10···C22	3.67(2)	3.69(1)	C7···C42	3.68(2)	3.56(1)
C12···C34	3.68(2)	---	C3···C38	3.68(2)	3.64(1)
			C8···C40	3.68(2)	3.67(1)
			C2···C36		3.69(1)

[a]Color code: salmon; [b]Color code Green in the Figure S7

References

[1] L. D Ciana, A. Haim, *J. Heterocycl. Chem.,* **1984**, *21* (2), 607–608.

[2] G. M. Sheldrick, *Acta Cryst.,* **2015**, *A71*, 3.

[3] G. M. Sheldrick, *Acta Cryst.,* **2015**, *C71*, 3.

[4] O. V. Dolomanov, L. J. Bourhis, R. J. Gildea, J. A. K. Howard, H. Puschmann, *J. Appl. Cryst.,* **2009**, *42*, 339.

CAPÍTULO 4

Enhanced Interplay between Host-Guest and Spin-Crossover Properties through the Introduction of an N Heteroatom in 2D Hofmann Clathrates

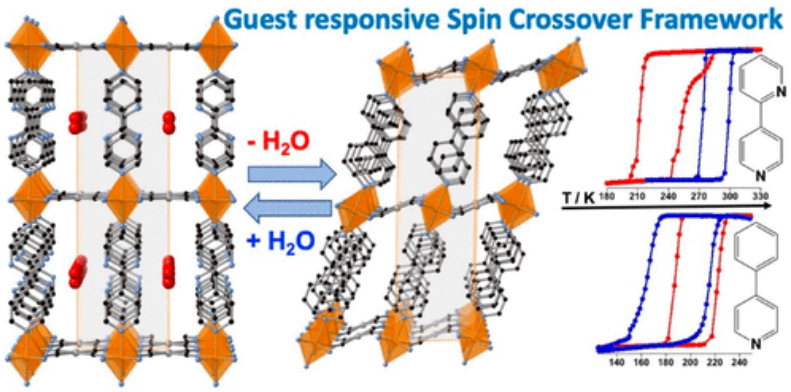

REVISTA: Inorganic Chemistry
ÍNDICE DE IMPACTO: 5.165

CAPÍTULO 4

Enhanced Interplay between Host-Guest and Spin-Crossover Properties through the Introduction of an N Heteroatom in 2D Hofmann Clathrates

4.1.- Abstract

Controlled modulation of the spin-crossover (SCO) behavior through the sorption−desorption of invited molecules is an extensively exploited topic because of its potential applications in molecular sensing. For this purpose, understanding the mechanisms by which the spin-switching properties are altered by guest molecules is of paramount importance. Here, we show an experimental approach revealing a direct probe of how the interplay between SCO and host−guest chemistry is noticeably activated by chemically tuning the host structure. Thus, the axial ligand 4-phenylpyridine (**4-PhPy**) in the 2D Hofmann clathrates $\{Fe(4\text{-}PhPy)_2[M(CN)_4]\}$ (**PhPyM**; M = Pt, Pd) is replaced by 2,4-bipyridine (**2,4-Bipy**), resulting in the isomorphous compounds $\{Fe(2,4\text{-}Bipy)_2[M(CN)_4]\}$ (**BipyM**; M = Pt, Pd), which basically differ from the former in that they have a noncoordinated N heteroatom in the ancillary aromatic substituent, i.e., 2-pyridyl instead of phenyl. Our chemical, magnetic, calorimetric, and structural characterizations demonstrate that this subtle chemical composition change provokes outstanding modifications not only in the capability to adsorb small guests as water or methanol but also in the extent to which these guests affect the SCO characteristics.

4.2.- Introduction

The spin-crossover (SCO) behavior is essentially a molecular phenomenon exhibited by some octahedral transition-metal complexes with electronic configurations $3d^4$−$3d^7$ that involves the reversible, controllable, and detectable switching between the low-spin (LS) and high-spin (HS) states.[1,2] This switchable behavior has predominantly been studied for hexacoordinated $\{Fe^{II}N_6\}$ $3d^6$ complexes because a large number of common N-donor ligands accomplish the necessary condition; i.e., the energy balance between the ligand-field strength and the interelectronic repulsion is of the order of magnitude of $k_B T$.[3-5] The HS ↔ LS switching can be triggered by a series of external stimuli (temperature, pressure, light,

guest analytes, etc.), implicating remarkable variations of the optical, structural, magnetic, and electric properties. Interestingly, this external perturbation−physical signal change coupling, together with the possibility of obtaining nanometric architectures,[6] is the basis for potential applications of SCO materials in areas of chemical sensing, switching devices, display, or information storage.[7-10] However, from an application-perspective point of view, the SCO requires, in general, a high degree of cooperativity within the crystalline network. Cooperativity stems from long-range elastic interactions between the SCO centers in such a way that the spin-state change is efficiently transmitted within the material.[3] Hence, cooperative thermally driven SCO materials may exhibit abrupt or even hysteretic γHS versus *T* curves (γ_{HS} = HS-state molar fraction), giving way to bistable properties. In the last 2 decades, chemists have made many efforts in order to achieve strong bistable SCO compounds. To do so, the synthesis of extended 1−3D coordination polymers (CPs), in which the SCO centers are connected by coordination/covalent bonds, has been one of the main synthetic strategies.[11,12]

Fe^{II} Hofmann-type CPs (Fe^{II}-HCPs) have been one the most investigated classes of CPs within the SCO community. From the vast family of reported Fe^{II}-HCPs, those frameworks presenting the general formula $\{Fe^{II}(L)_x[M^{II}(CN)_4]\}$ (x =2 or 1 for 2D or 3D systems, respectively) are constituted of bimetallic layers where the Fe^{II} ions are connected through $[M^{II}(CN)_4]^{2-}$ anions (M = Pt, Pd, Ni).[13,14] The cyanometallate-based layers are stacked in such a way that the organic axial ligands (L; typically substituted pyridines or triazole-based ligands) either are monodentate and interdigitated in the case of 2D networks or act as bis-monodentate bridges between adjacent layers for 3D derivatives. One of the reasons explaining the strong interest raised by Fe^{II}-HCPs in the last years lies in the intrinsic porosity (or guest-induced porosity) offered by their networks and the possibility of decorating their pores through chemical functionalization. This feature, which has been studied mainly for 3D systems because of their permanent porosity, permits the uptake of a high variety of guest molecules, which, in turn, are capable of modulating the SCO properties of the HCP.[15,16] The mechanism by which the SCO is modulated through a guest molecule depends on the nature of the interactions established between the host framework and adsorbed molecule. For example, trapped bulky guests in the 3D Fe^{II}-HCP $\{Fe(Pz)[Pt(CN)_4]\}$ (Pz = pyrazine) generate steric hindrance, tending to stabilize the HS state.[17] Conversely, other specific host−guest interactions operating in the same framework

lead to stabilization of the LS state, likely due to indirect modification of the ligand-field strength of the Fe^{II} center.

Because of their interdigitated nature and therefore the lack of porosity, guest effect studies on 2D Fe^{II}-HCP SCO systems are scarce and rather limited to the inclusion of small guest molecules such as water (H_2O) or ethanol (EtOH). Often, the presence of these guests provokes elastic frustration, namely, the hindering of the metal−organic framework's natural expansion−contraction during the HS ↔ LS transition, which usually is reflected on a decrease of the SCO temperature and/or multistepped SCO behavior.[18-27] An increase of the SCO temperature upon H_2O adsorption was only observed in compound $\{Fe(thtrz)_2[Pd(CN)_4]\}$ and attributed to modification of the ligand-field strength of Fe^{II} via host−guest interactions.[18] Recently, SCO modulation of the flexible 2D Fe^{II}-HCP $\{Fe(5\text{-}NH_2Pym)_2[M^{II}(CN)_4]\}$ (5-NH_2Pym = 5-aminopyrimidine; M^{II} = Pt, Pd) mediated by the adsorption of H_2O, methanol (MeOH), or EtOH was reported and justified by both electronic and steric effects operating between the protic guest molecules and 5-NH_2Pym axial ligands.[28] A similar guest effect was found in the related family of 2D porous compounds $\{Fe^{II}(NCS)_2(L)_2\}\cdot$guest [L = 1,2-bis(4'-pyridyl)ethene (tvp),[29] 4,4'-azopyridine (azpy),[30] 2,3-bis(4'-pyridyl)-2,3-butanediol (bpbd),[31,32] 1,2-bis(4'-pyridyl)-1,2-ethanediol (bped),[33] 1,2-bis(4'-pyridyl)ethane (bpe);[34] guest = acetonitrile, acetone, MeOH, EtOH, and 1-propanol], whose modifications of the SCO temperature and hysteresis width were related to specific host−guest interactions involving the L bridging ligand. All of these results indicate that functionalization of the host framework is crucial not only to promoting the binding of the guest molecule to the host framework but also to modifying through this interaction the SCO characteristics in a controlled manner.

Aiming at providing new insights regarding the influence of host−guest interactions over the SCO behavior, here we report on a comparative study of two closely related series of 2D Fe^{II}-HCPs generically formulated as $\{Fe^{II}(L)_2[M^{II}(CN)_4]\cdot nG$, with L = 4-phenylpyridine (4-PhPy) or 2,4-bipyridine (2,4-Bipy) (Scheme 1), M^{II} = Pd or Pt, and G = H_2O and/or MeOH. Both series differ from each other by the presence or absence of a peripheral noncoordinated N heteroatom in the ancillary aromatic ring (phenyl or 2-pyridine). Although the SCO properties of the unsolvated 4-PhPy derivatives were investigated in a precedent work,[35] their structures and foreseeable structural changes stemming from the presence/ absence of guests as well as their correlation with the SCO properties have remained unknown so far. Consequently, here we analyze the structural, magnetic, and guest

adsorption properties of the unsolvated and solvated forms of both series of compounds. Our results show the following: (i) from ab initio X-ray structural determinations, the unsolvated $\{Fe^{II}(4\text{-}PhPy)_2[M^{II}(CN)_4]$ (**PhPyM;** M = Pd, Pt) and $\{Fe^{II}(2,4\text{-}Bipy)_2[M^{II}(CN)_4]$ (**BipyM;** M = Pd, Pt) forms are isostructural; (ii) the presence of the N heteroatom in **BipyM** enhances considerably its sensing properties with respect to those of **PhPyM** because of the generation of stronger intermolecular interactions with the adsorbed guest molecules; (iii) single-crystal analyses of the corresponding solvated forms for both series of compounds show the occurrence of noticeable structural modifications, which, in turn, have a remarkable impact over the SCO behavior.

Scheme 1. *Ligands Employed in This Work: 4-Phpy and 2,4-Bipy.*

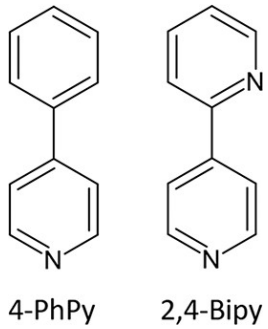

4.3.- Experimental Section

4.3.1.- Synthesis

The 4-PhPy and 2,4-Bipy ligands are commercially available and were purchased from Acros Organics and Apollo Scientific, respectively.

Single crystals of **PhPyM·*x*MeOH·*y*H_2O** (M = Pd, Pt) were obtained by slow diffusion techniques. A solution of $Fe(BF_4)_2{\cdot}6H_2O$ (33.8 mg, 0.1 mmol) and the 4-PhPy ligand (31.0 mg, 0.2 mmol) in 2 mL of H_2O/MeOH (2:1) was placed in one side of an H-shaped vessel, whereas a solution of $K_2[M(CN)_4]$ [M = Pd (28.9 mg, 0.1 mmol), Pt (43.1 mg, 0.1 mmol)] in 2 mL of H_2O was placed in the other side. Finally, the vessel was filled with a mixture of H_2O/MeOH (1:1) and sealed with parafilm. Yellow square-plate single crystals were obtained in 1 week with a yield of ca. 50%. Anal. Calcd for **PhPyPt** [$C_{26}H_{18}FeN_6Pt$ (665.4)]: C, 46.93;

H, 2.73; N, 12.63. Found: C, 46.24; H, 2.81; N, 12.42. Anal. Calcd for **PhPyPd** [$C_{26}H_{18}FeN_6Pd$ (576.7)]: C, 54.15; H, 3.15; N, 14.57. Found: C, 53.23; H, 3.26; N, 14.31.

Single crystals of **BipyM·H_2O** (M = Pd, Pt) were obtained by slow diffusion techniques. A solution of $Fe(BF_4)_2·6H_2O$ (33.8 mg, 0.1 mmol) and the 2,4-Bipy ligand (31.2 mg, 0.2 mmol) in 2 mL of H_2O/MeOH (3:1) was placed in one side of a H-shaped vessel, whereas a solution of $K_2M(CN)_4$ [M = Pd (28.9 mg, 0.1 mmol), Pt (43.1 mg, 0.1 mmol)] in 2 mL of H_2O was placed in the other side. Finally, the vessel was filled with a mixture of H_2O/MeOH (1:1) and sealed with parafilm. Yellow square-plate single crystals were obtained in 1 week with a yield ca. 50%. Anal. Calcd for **BipyPt·H_2O** [$C_{24}H_{18}FeN_8OPt$ (685.4)]: C, 42.06; H, 2.65; N, 16.35. Found: C, 41.88; H, 2.51; N, 16.48. Anal. Calcd for **BipyPd·H_2O** [$C_{24}H_{18}FeN_8OPd$ (596.7)]: C, 48.31; H, 3.04; N, 18.78. Found: C, 48.49; H, 2.92; N, 19.02.

4.3.2.- Physical Measurements

Magnetic Measurements. Variable-temperature magnetic susceptibility data were recorded with a Quantum Design MPMS2 SQUID magnetometer equipped with a 7 T magnet, operating at 1 T and at temperatures 50−400 K using a scan rate of 2 K min^{-1}. Experimental susceptibilities were corrected for diamagnetism of the constituent atoms using Pascal's constants.

Calorimetric measurements were performed using a Mettler Toledo DSC 821e differential scanning calorimeter. Low temperatures were obtained with an aluminum block attached to the sample holder, refrigerated with a flow of liquid nitrogen, and stabilized at a temperature of 110 K. The sample holder was kept in a drybox under a flow of dry nitrogen gas to avoid H_2O condensation. The measurements were carried out using around 15 mg of a microcrystalline sample sealed in aluminum pans with a mechanical crimp. Temperature and heat-flow calibrations were made with standard samples of indium by using its melting transition (429.6 K; 28.45 J g^{-1}). An overall accuracy of ±0.2 K in the temperature and ±2% in the heat capacity is estimated. The uncertainty increases for determination of the anomalous enthalpy and entropy due to the subtraction of an unknown baseline.

Single-Crystal X-ray Diffraction. Single-crystal X-ray diffraction data were collected on an Oxford Diffraction Supernova diffractometer using graphite-monochromated Mo K*α* radiation (λ = 0.71073 Å). A multiscan absorption correction was performed. The structures

were solved by direct methods using *SHELXS-2014* and refined by full-matrix least squares on F^2 using *SHELXL-2014*.[36] Non-H atoms were refined anisotropically, and H atoms were placed in calculated positions refined using idealized geometries (riding model) and assigned to fixed isotropic displacement parameters. All details can be found in CCDC 2090594 (**BipyPt·H_2O**_120 K), 2090595 (**BipyPd·H_2O**), 2090596 (**PhPyPd·MeOH·0.5H_2O**), 2090599 (**BipyPt·H_2O·MeOH**), 2090600 (**PhPyPd·MeOH·0.5H_2O**), and 2090601 (**BipyPt·H_2O**_283 K), which contain the supplementary crystallographic data for this paper.

Powder X-ray Diffraction (PXRD). Measurements were performed on a PANalytical Empyrean powder X-ray diffractometer (monochromatic Cu K*α* radiation) in capillary measurement mode. Because of the spontaneous rehydration of **BipyPt** and **BipyPd,** these samples were prepared by heating the hydrated forms into open capillaries inside an oven at 120 °C for 1 h and rapidly sealing them to keep air from entering. Crystal structures of compounds **PhPyM** and **BipyM** were solved ab initio using the *Topas Academic v6* program (http://www.topas-academic.net/). Very similar monoclinic unit cell parameters were found for both cases, and the atomic positions of the Pt and Fe atoms were located using the charge-flipping method.[37] Subsequent difference Fourier maps showed the missing electron densities for the cyanide and organic ligand, which were located at the expected positions (using the corresponding solvated crystal structures as description models). The final Rietveld[38] refinements, which showed excellent agreement between the calculated and experimental patterns, included restraints on the Pt/Fe−cyanide and Fe−organic ligand distances; the organic ligand was described by applying a semirigid body description. All details can be found in CCDC 2090597 (**PhPyPt**) and 2090598 (**BipyPt**).

Elemental Analyses. C, H, and N analyses were performed with a CE Instruments EA 1110 CHNS elemental analyzer.

Thermogravimetric analysis (TGA) experiments were carried out with a TA Instruments TGA550 device equipped with a Pt/Rh oven (T_{max} = 1000 °C). The time-dependent TGA experiments were performed by connecting the TGA apparatus to a flow mass controller. Thus, humid air was passed at room pressure and a temperature of 30 °C and driven into the TGA chamber, where a previously desolvated sample of **BipyPt** or **BipyPd** was mounted in a Pt pan.

4.4.- Results

4.4.1.- Synthesis and Chemical Characterization

Single crystals of **PhPyM·*x*MeOH·*y*H_2O** and **BipyM·H_2O** (M = Pt, Pd) were grown by liquid−liquid slow diffusion using H-shaped tubes containing, on the one side, a H_2O/MeOH solution of a Fe^{II}-4-PhPy or -2,4-Bipy mixture and, on the other side, an aqueous solution of the corresponding $[M(CN)_4]^{2-}$ potassium salt (see the Experimental Section for more details).

PXRD (Figure S1) and magnetic measurements (vide infra) of pristine crystals of **PhPyM·*x*MeOH·*y*H_2O** soaked in the mother liquor indicate that the synthesis method affords an imprecise mixture of solvates with *x* and *y* in the intervals 0−1 and 0−0.5, respectively. Only the crystal structure of the majority component of these solvates was successfully identified and presents the formula **PhPyM·MeOH·0.5H_2O.** Once removed from the mother liquor, crystals of **PhPyM·*x*MeOH·*y*H_2O** spontaneously desorb most of the guest molecules, provoking a total loss of crystallinity. This was confirmed by elemental analysis, PXRD, TGA (see the Experimental Section and Figures S1 and S2), and magnetic measurements (vide infra). Indeed, according to TGA, only an equivalent weight of 0.2−0.4 molecules of H_2O remains in the dried samples at ambient conditions. Besides, solvent-free **PhPyM** derivatives are easily obtained from a thermal treatment at 400 K for 10 min. In view of the changes detected in the PXRD patterns upon solvent desorption (Figure S1), the loss of guest molecules is accompanied by relevant structural changes.

It is worth noting that **PhPyM** does not readsorb H_2O from air moisture. This was deduced from TGA measurements performed on desorbed **PhPyM** samples exposed to air for several days, which showed no mass loss up to 530 K when the structures start to decompose (Figure S2).

Chemical characterization of **BipyM·H_2O** (M = Pt, Pd) shows that the guest H_2O molecule is retained within the structure once the samples are removed from the mother liquor and exposed at ambient conditions (see elemental analysis, PXRD patterns, and TGA measurements in the Experimental Section and Figures S3 and S4, respectively). Nonetheless, according to the TGA measurements (Figure S4), the H_2O molecule can be easily desorbed with gentle heating above 300 K, giving rise to the dehydrated **BipyM** counterparts. Similar to that observed in **PhPyM,** H_2O desorption provokes relevant

structural modifications in view of the differences detected from the PXRD patterns of the solvated and desolvated compounds (Figure S3).

TGA studies show, in contrast to that observed for **PhPyM,** that both **BipyPt** and **BipyPd** are capable of gradually readsorbing one molecule of H_2O per Fe^{II} ion from air moisture. Indeed, the H_2O readsorption monitored in situ by TGA reveals that **BipyM** recovers the original monohydrated phase in less than 1 h (see Scheme 2 and Figure S5). Importantly, the close similarity between the PXRD patterns of compounds **PhPyM** and **BipyM** (Figure S6) points out that the corresponding desorbed phases are isostructural.

Scheme 2. *Adsorption and Desorption Processes Observed for Compounds* ***PhPyM·xMeOH·yH₂O*** *and* ***BipyM·H₂O*** *upon Different Treatments.*

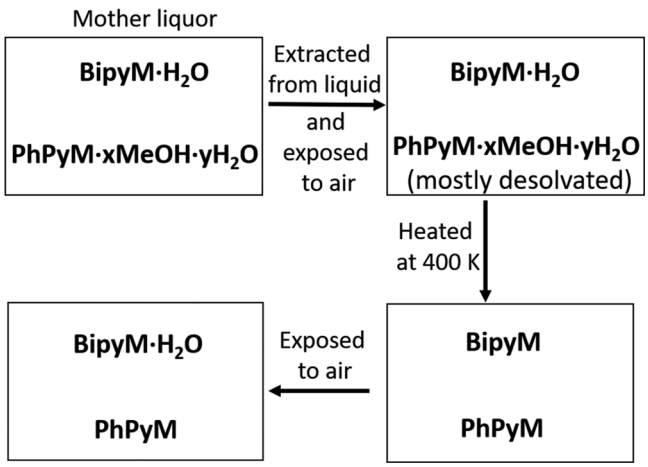

4.4.2.- Magnetic Characterization

SCO Properties of **PhPyM·*x*MeOH·*y*H₂O** and **BipyM·H₂O** (M = Pt, Pd). Figure 1 displays the thermal dependence of $\chi_M T$ (where χ_M is the molar magnetic susceptibility and T is the temperature) for **PhPyM·*x*MeOH·*y*H₂O** and **BipyM·H₂O** and for their respective complete desolvated forms ($\chi_M T$ vs T plots of the partially desolvated **PhPyM·*x*MeOH·*y*H₂O** forms are shown in Figure S7). In order to monitor the SCO behavior of the pristine solvated forms and considering their propensity to lose the included solvent molecules, the magnetic properties were measured soaked in their mother liquor (open circles in Figure 1a,b). At 240 K, $\chi_M T$ is ca. 3.5 cm^3 K mol^{-1} for compound **PhPyPt·*x*MeOH·*y*H₂O,** which is assignable to a

fully HS (S = 2) Fe^{II} ion (Figure 1a). This value remains practically constant within the temperature range 240−50 K, proving that this compound does not exhibit SCO properties. Similarly, compound **PhPyPd·*x*MeOH·*y*H₂O** shows a $\chi_M T$ value of 3.5 cm^3 K mol^{-1} between 300 and 170 K (Figure 1b). However, below this temperature, $\chi_M T$ decreases abruptly by 0.5 cm^3 K mol^{-1} ($T_{1/2}^{\downarrow}$ = 164 K), denoting the occurrence of a HS-to-LS transition involving ca. 14% of the Fe^{II} centers. In the heating mode, the $\chi_M T$ versus T plot does not match the cooling mode, with the latter being more gradual and shifted to higher temperatures ($T_{1/2}^{\uparrow}$ = 185 K), thereby defining an asymmetric hysteresis loop with $T_{1/2}$ = 174.5 K and ΔT = 21 K [$T_{1/2}^{\downarrow}/T_{1/2}^{\uparrow}$ are the equilibrium temperatures at which 50% of the SCO-active Fe^{II} ions have changed from spin state during the cooling/heating modes, $T_{1/2} = (T_{1/2}^{\uparrow} + T_{1/2}^{\downarrow})/2$, and ΔT is the hysteresis width $T_{1/2}^{\uparrow} - T_{1/2}^{\downarrow}$].

As was already mentioned, removing crystals of **PhPyM·*x*MeOH·*y*H₂O** (M = Pt, Pd) from their mother liquor provokes instantaneous loss of most of the guest molecules (Figure S2), causing important modifications in the magnetic properties of both the Pt and Pd derivatives. Indeed, the SCO of both air-dried samples defines an almost complete and asymmetric hysteresis loop characterized by a double step in the cooling mode ($T_{1/2}^{\downarrow 1}$ = 202 K and $T_{1/2}^{\downarrow 2}$ = 180 K for Pt; $T_{1/2}^{\downarrow 1}$ = 182 K and $T_{1/2}^{\downarrow 2}$ = 163 K for Pd) and a single step in the heating mode ($T_{1/2}^{\uparrow}$ = 218 K, ΔT^1 = 16 K, and ΔT^2 = 38 K for Pt; $T_{1/2}^{\uparrow}$ = 200 K, ΔT^1 = 18 K, and ΔT^2 = 37 K for Pd) (Figure S7). The subsequent treatment at 400 K for 1 h leads to the completely desorbed forms **PhPyPt** and **PhPyPd,** which exhibit abrupt, complete, and hysteretic one-step spin transitions with $T_{1/2}/\Delta T$ of 204/36 K and 185/29 K, respectively (filled circles in Figure 1a,b). These curves were perfectly reproduced for the same samples several days after exposure to ambient conditions (Figure S8), confirming, in good agreement with the TGA studies (Figure S2), that these compounds are not prone to readsorb H_2O from air moisture.

Freshly prepared soaked crystals of **BipyM·H₂O** (M = Pt, Pd) exhibit abrupt, complete, and hysteretic spin transitions centered at room temperature with $T_{1/2}/\Delta T$ of 286.5/25 K and 282.5/35 K, respectively (open circles in Figure 1c,d). According to the TGA data (Figure S4), the H_2O molecule included in **BipyPt·H₂O** and **BipyPd·H₂O** is retained at $T \leq 300$ K in contact with air. Consequently, to ensure the retention of H_2O and considering the dry atmosphere and vacuum conditions of the SQUID chamber, the magnetic properties

of the air-dried samples were checked first in the temperature sequence 290−220 K in order to compare them with those of the soaked samples. As expected, the SCO curves recorded upon cooling [$T_{1/2}^{\downarrow}$ = 272 K (Pt) and 273 K (Pd); Figure S9] are close to those obtained for the crystals soaked in the mother liquor [275 K (Pt) and 266 K (Pd)], confirming that the H_2O molecule persists within the structure at ambient conditions. In order to analyze the heating branch, $\chi_M T$ was measured in the temperature range 220−320 K, obtaining $T_{1/2}^{\uparrow}$ values of 303 K (Pt) and 293 K (Pd). The resulting SCO curves are very similar to those of the soaked samples (Figure S9), suggesting that, although the solvates can be subjected to dehydration during the process of heating above 300 K, either the effective desolvation must be very small or it does not affect the $T_{1/2}^{\uparrow}$ value. When compounds **BipyPt·H_2O/BipyPd·H_2O** are heated at 400 K for 1 h inside the SQUID magnetometer, the H_2O molecule is totally evacuated, affording the desorbed counterparts **BipyPt/BipyPd.** The dehydrated derivatives also display strongly cooperative SCO behaviors (filled circles in Figure 1c,d) but dramatically downshifted in temperature by 54 K (Pt) and 61.5 K (Pd) with respect to their corresponding hydrated counterparts. Nevertheless, the hysteresis widths are overall maintained (ΔT = 41/28 K for **BipyPt/BipyPd**). In good agreement with the TGA measurements, the room temperature centered SCO curves of the original monohydrated derivatives are completely recovered when the desorbed samples are exposed to air for ca. 1 h (Figure S10).

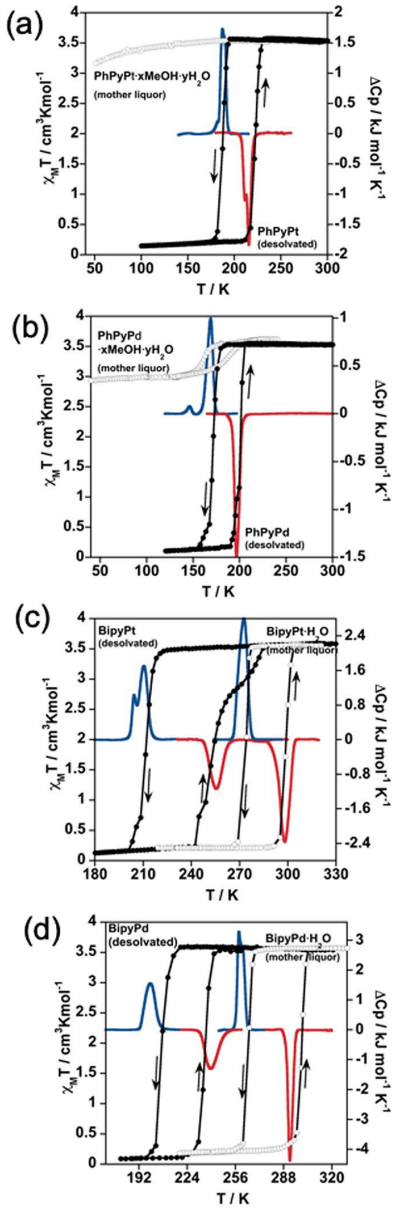

Figure 1. *Thermal dependence of $\chi_M T$ for: (i)* ***PhPyM·xMeOH·yH₂O*** *[M = Pt (a), Pd (b)] measured in the mother liquor (open circles) and after treatment at 400 K for 1 h (filled circles) and (ii)* ***BipyM·H₂O*** *[M = Pt (c), Pd (d)] measured in the mother liquor (open circles) and after treatment at 400 K for 1 h (filled circles). Calorimetric measurements in the cooling (blue curves) and heating (red curves) modes of the desolvated counterparts of* ***PhPyPt*** *(a),* ***PhPyPd*** *(b),* ***BipyPt*** *(c), and* ***BipyPd*** *(d) and the hydrated air-dried products of* ***BipyPt·H₂O*** *(c) and* ***BipyPd·H₂O*** *(d).*

In order to investigate the capability of the unsolvated samples to reinclude MeOH or H_2O molecules in the structure and to assess the degree of reversibility of the magnetic behavior described above, the desolvated **PhPyM** and **BipyM** derivatives were dispersed in MeOH or H_2O for several hours. In order to evaluate the eventual structural changes associated with the adsorption processes, PXRD patterns were performed for the solids immersed in the corresponding solvents (Figures S11 and S12). The results show the occurrence of important modifications in the patterns of both **PhPyM** and **BipyM** when they are soaked in MeOH. In particular, the shift of the 002 peak centered around 7.6º toward lower 2θ values reflects an increase in separation between two consecutive bimetallic layers as a consequence of inclusion of the MeOH molecule. Besides, whereas noticeable modifications of the patterns of **BipyM** soaked in H_2O confirm the adsorption of H_2O in this network, patterns of **PhPyM** are virtually unchanged in H_2O, indicating a negligible amount of adsorbed H_2O. The $\chi_M T$ versus T curves of the soaked crystals (Figures 2 and S13 for Pt and Pd derivates, respectively) clearly reveal thet the adsorption of MeOH stabilizes the HS state at all temperatures for the four compounds (black curves in Figures 2 and S13). In contrast, the adsorption of H_2O in **PhPyM** and **BipyM** provokes opposite effects on their respective spin transitions. For **PhPyM,** the average $T_{1/2}$ values slightly decrease from 204 to 190 K (M = Pt) and from 185 to 180 K (M = Pd), and the hysteresis width ΔT increase from 35 to 51 K (M = Pt) and from 29 to 36 K (M = Pd). For **BipyM,** their $T_{1/2}$ values increase considerably from 238 to 281.5 K (M = Pt) and from 221 to 282 K (M = Pd), while ΔT decrease from 32 to 23 K (M = Pt) and remains unchanged for M = Pd. Importantly, magnetic (Figure S14) and TGA (Figure S15) characterizations performed for compounds **PhPyM·*x*solv** (solv = H_2O, MeOH) and **BipyM·*x*MeOH** a few minutes after removing them from the corresponding solvent clearly suggest the occurrence of rapid desorption of the guest molecules, a fact that avoids a proper estimation of *x*. In contrast, as aforementioned, the air-dried samples of **BipyM·H_2O** (M = Pt^{II}, Pd^{II}) maintain the H_2O molecule per Fe^{II} ion of the initial as-synthesized hydrated framework.

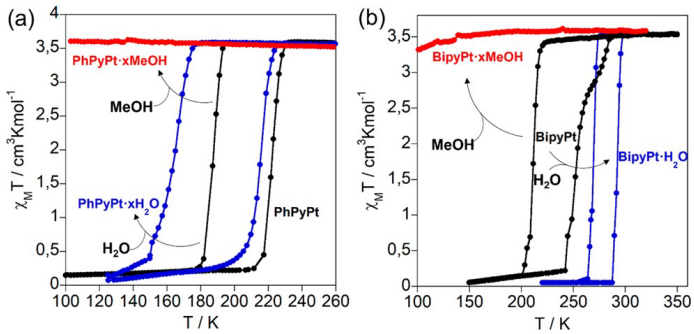

Figure 2. SCO properties of (a) ***PhPyPt*** *and (b)* ***BipyPt*** *before (black curves) and after adsorption of H_2O (blue curves) and MeOH (red curves).*

4.4.3.- Included H2O-Dependent SCO in BipyPt·*x*H2O (*x* = 0-1)

The marked difference observed between the SCO temperatures of the dehydrated (x = 0) and hydrated (x = 1) counterparts in the **BipyM·*x*H2O** systems (Figure 2b) encouraged us to investigate the SCO profiles of some intermediate degrees of hydration. Even if we were unable to estimate the exact amount of H_2O for these intermediate hydrates, we managed to get hydration degrees from x = 1 to 0 by the sequential controlled heating of a pristine hydrated sample of **BipyPt·H2O** inside the SQUID magnetometer. First, a fresh **BipyPt·H2O** sample was measured in the 290−180−305 K temperature sequence, obtaining the expected SCO behavior of the completely hydrated framework (Figure 3a). Then, the solid was heated up to 305 K for 10 min and the thermal variation of $\chi_M T$ subsequently registered in the 305− 180−320 K temperature range. The resulting curve shows the split of the SCO in two defined steps with $T_{1/2}^{\downarrow 1}/T_{1/2}^{\downarrow 2}$ = 278/298 K and $T_{1/2}^{\downarrow 2}/T_{1/2}^{\uparrow 2}$ = 220/264 K, which are reminiscent of the SCO behaviors of the completely hydrated and dehydrated compounds, respectively (Figure 3b). After that, the sample was heated at 320 K for 10 min followed by monitoring of the $\chi_M T$ values with the 320−180−320 K temperature range. Surprisingly, the SCO curve registered after this thermal treatment exhibits an outstanding hysteresis loop with a ΔT value of 84 K and values of $T_{1/2}^{\downarrow}$ and $T_{1/2}^{\uparrow}$ of 208 and 292 K, respectively (Figure 3c). Hence, whereas $T_{1/2}^{\downarrow}$ is comparable to that of the dehydrated compound, $T_{1/2}^{\downarrow}$ is very similar to that of the hydrated counterpart. Afterward, the sample was heated again at 320 K and measured within the same temperature range,

observing an exclusive modification of the heating branch, which reflects the apparition of two steps ($T_{1/2}^{\uparrow 2}$ = 256 K and $T_{1/2}^{\uparrow 1}$ = 286 K), therefore delineating an asymmetric hysteresis loop (Figure 3d). Finally, subsequent treatment at 400 K led to the above-mentioned SCO behavior of the dehydrated compound (Figure 3e).

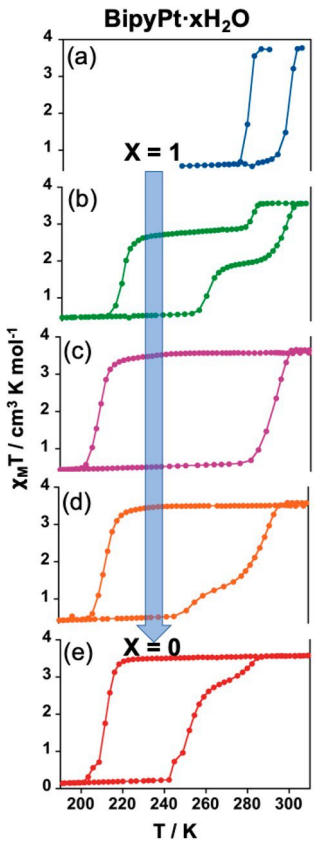

Figure 3. *Evolution of the SCO properties of* ***BipyPt·xH$_2$O*** *from the (a) fully hydrated (x = 1) to the (e) completely dehydrated (x = 0) derivatives. $\chi_M T$ versus T curves displayed in parts b-d were obtained by the in situ sequential heating of the original hydrated sample (see the text).*

4.4.4.- Calorimetric Measurements

Differential scanning calorimetry analysis was performed in order to confirm the SCO behaviors obtained by the SQUID measurements. The calorimetry data of desolvated **PhPyPt**, **PhPyPd**, **BipyPt**, and **BipyPd** and hydrated **BipyPt·H$_2$O** and **BipyPd·H$_2$O**

compounds were conducted with a scan rate of 10 K min^{-1} in the cooling and heating modes, obtaining the corresponding ΔC_p versus T curves displayed in Figure 1. The $T_{1/2}$ and ΔT values extracted from these curves (Table 1) are in very good accord with the magnetic data. The slight discrepancies obtained (notably in the $T_{1/2}^{\downarrow}$ values) are related to the different scan rates used for the different techniques. Furthermore, the double peaks observed for some of the samples reflect subtle changes of the slope of the γ_{HS} vs T curve during the HS−LS transformation and usually are associated with structural rearrangements concomitant with the spin transition. The estimated average ΔH and ΔS variations involved in the spin-state changes (Table 1) are comparable with those observed for cooperative SCO of related 2D Hofmann-type clathrates.[11−13] The $\Delta C_p(T)$ curve of an intermediate hydrated state was also registered after gentle heating of compound **BipyPt·H$_2$O** inside the calorimeter device. As a result, the cooling and heating ΔC_p versus T curves reflect a double-step SCO consistent with that observed in the magnetic study (Figure S16). The average ΔH (kJ mol^{-1})/ΔS (J mol^{-1} K^{-1}) values associated with the first and second steps are 6.565/28.484 and 7.058/24.626, respectively.

Table 1. Thermodynamic Parameters Extracted from the Magnetic and Calorimetric Measurements.

	Magnetism		Calorimetric			
Compound	$T_{1/2}$ (K)	ΔT (K)	$T_{1/2}$	ΔT	ΔH (kJ	ΔS (J
BipyPt	238	32	233	44	13.23	63.31
BipyPt·H$_2$O	286.5	25	285	24	17.99	63.22
BipyPd	221	28	219.5	39	12.90	59.15
BipyPd·H$_2$O	282.5	35	273.5	37	16.57	61.75
PhPyPt	No SCO					
PhPyPt·*x*MeOH·*y*H$_2$O	204	36	201.5	29	10.29	47.98
PhPyPd	174.5	21				
PhPyPd·*x*MeOH·*y*H$_2$O	185	29	181	28.5	11.41	57.09

4.4.5.- Crystal Structures

Crystal structures of **PhPyM·MeOH·0.5H$_2$O** (M = Pt, Pd) were successfully obtained at 120 K (HS), while that of **BipyPt·H$_2$O** was measured at 283 K (HS) and 120 K (LS). However, the structure of **BipyPd·H$_2$O** was analyzed only at 120 K (LS) because these crystals rapidly lose their crystallinity when measured above 280 K. Furthermore, the structure of compound **BipyPt·H$_2$O·MeOH,** obtained by soaking crystals of **BipyPt·H$_2$O** in pure MeOH for several days, was determined at 120 K (HS). The crystal structures of the unsolvated **PhPyPt** and **BipyPt** counterparts were solved at 298 K (HS) from ab initio

methods using the *Topas Academic v6* program through the treatment and Rietveld refinement of the corresponding PXRD patterns (see the Experimental Section for more details). Relevant crystallographic data for all compounds are gathered in Tables S1−S3, while the corresponding significant metal-to-ligand bond lengths, angles, and intermolecular interactions are given in Tables S4−S6, respectively. Rietveld plots are given in Figure S17 for the final refinements.

Structure of PhPy·MeOH·0.5H_2O (M = Pt, Pd). At 120 K, the crystal structures of **PhPyM·MeOH·0.5H_2O** (M = Pt, Pd) were determined in the orthorhombic *Imma* space group. They consist of a crystallographic unique type of octahedral {FeN_6} site coordinated equatorially by four N atoms belonging to four equivalent square-planar $[M(CN)_4]^{2-}$ units, which bridge four other equivalent Fe^{II} centers, forming bimetallic $\{Fe^{II}[M^{II}(CN)_4]\}_n$ layers. The axial positions are occupied by two equivalent terminal 4-phenylpyridine ligands (Figure 4a), thereby completing the 2D framework. At 120 K, the average Fe−N bond length is 2.179 and 2.181 Å for Pt and Pd derivatives, respectively, reflecting that, even at low temperature, the Fe^{II} ions are in the HS state, in good agreement with the magnetic data and the yellow color of the crystals. The $\{Fe^{II}(4\text{-PhPy})_2[M^{II}(CN)_4]\}_n$ layers are pillared in such a way that the axial 4-PhPy ligands of adjacent layers are interdigitated, establishing π−π stacking interactions where the centroid-to-centroid distances of the face-to-face aromatic rings are 3.720 Å (M^{II} = Pt) and 3.740 Å (M^{II} = Pd) (Figure S18a). Moreover, one molecule of MeOH and a half molecule of H_2O per unit cell are hosted within the interlayer hydrophobic space, inducing a tilt of the [FeN_6] octahedra and a slight corrugation of the bimetallic $\{Fe^{II}[M^{II}(CN)_4]\}_n$ planes (Figure 4b). Indeed, the $[Fe(N_{eq})_4]$ equatorial plane of the [FeN_6] octahedron defines average angles of 8.6º (M^{II} = Pt) and 9.1º (M^{II} = Pd) with the square-planar units $[M^{II}(CN)_4]^{2-}$, thereby generating by symmetry two inequivalent channels between the interdigitated layers. Whereas one of these channels does not contain any guest due to the small void left by the neighboring 4-PhPy ligands, the other is wide enough to host the solvent molecules. These guest molecules are distributed along the channel in such a way that they define a plane that is stabilized through hydrogen bonds and situated at 2.6 Å with respect to the aromatic H atoms of the 4-PhPy ligand.

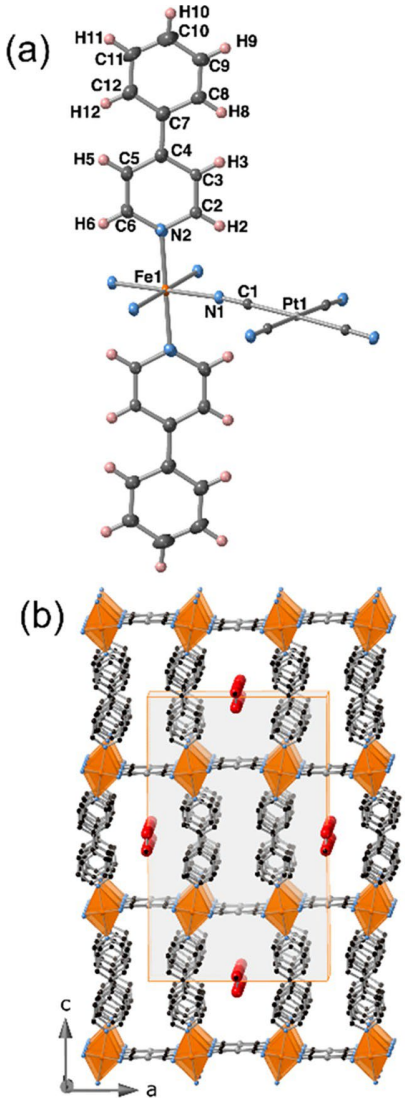

*Figure 4. (a) ORTEP representation of the Fe^{II} environment displayed by **PhPyM·MeOH·0.5H_2O** (M = Pt, Pd). (Atoms are represented at 50% probability). (b) Fragment of the 2D networks formed by four stacked layers showing the channels where the solvent molecules are located in **PhPyM·MeOH·0.5H_2O.***

Structure of BipyM·H2O (M = Pt, Pd). At 120 K, the crystal structures of **BipyM·H_2O** present the orthorhombic *Cmmm* space group. The structure consists of a unique octahedral $\{FeN_6\}$ site coordinated by four equivalent square-planar $[M(CN)_4]^{2-}$ bridging ligands in the equatorial positions and by the 4-substituted pyridine N atom of two

equivalent terminal 2,4-bipy ligands in the axial positions (Figure 5a). It is worth noting that atoms N3 and C6 are disordered by symmetry and have been modeled with an occupancy of 0.5 in each position. Conversely to the 4-Phpy-based compounds, the average Fe−N distances are 1.953 and 1.958 Å for **BipyPt·H_2O** and **BipyPd·H_2O,** respectively, indicating that the Fe^{II} ion is in the LS state, in good agreement with the magnetic data and the red color of the crystals. Furthermore, the $\{Fe^{II}[M^{II}(CN)_4]\}_n$ layers are strictly planar (Figure 6a), in contrast to that observed for **PhPyM·MeOH·0.5H_2O.** As a result of their higher structural homogeneity, only one type of channel is generated between the interdigitated bimetallic layers where one molecule of H_2O is hosted, occupying discrete positions and interacting via moderate hydrogen bonds with the N3 heterocyclic atom of the 2,4-bipy ligand (O1⋯N3 intermolecular distance of 2.953 Å for Pt and 3.000 Å for Pd). Moreover, the pillared layers are stabilized by π−π interactions established between the pyridine moieties of the interdigitated 2,4-bipy ligands with centroid-to-centroid distances of 3.665 and 3.671 Å for **BipyPt·H_2O** and **BipyPd·H_2O,** respectively (Figure S18b). In good agreement with the magnetic data, crystals of **BipyPt·H_2O** become yellow upon heating, evidencing the occurrence of a LS-to-HS transition. This was confirmed by analysis of the structure at 283 K, which is basically the same as that at 120 K but exhibiting, as the main difference, an increase of 0.206 Å in the Fe−N average distance.

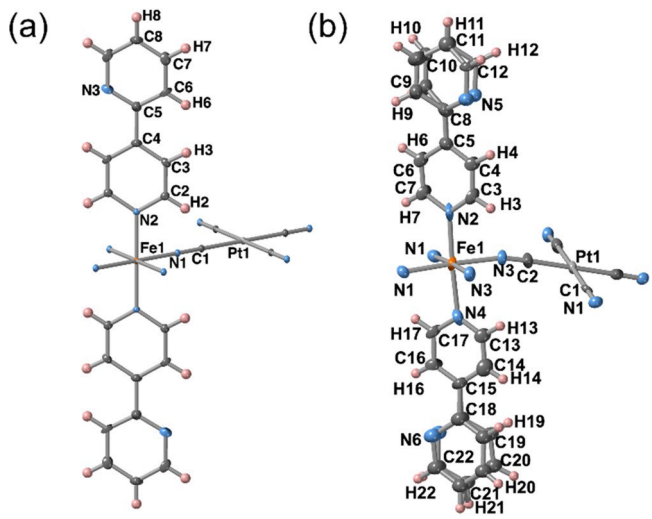

Figure 5. ORTEP representations of the Fe^{II} environment displayed by (a) ***BipyPt·H_2O*** *and (b)* ***BipyPt·H_2O·MeOH.*** *Atoms are represented at 50% probability.*

Structure of BipyPt·H_2O·MeOH. When crystals of **BipyPt·H_2O** are immersed in pure MeOH for several days, they adsorb one molecule of MeOH, leading to compound **BipyPt·H_2O·MeOH.** The MeOH uptake is accompanied by a single-crystal-to-single-crystal transformation from the orthorhombic *Cmmm* space group to the orthorhombic *Pnma* space group. This loss of symmetry is reflected in the apparition of two nonequivalent 2,4-Bipy ligands as well as two distinct types of equatorial coordinating N atoms (N1 and N3). Furthermore, the entry of MeOH induces the occurrence of a positional disorder on the noncoordinated pyridine of the 2,4-bipy ligand (Figure 5b). At 120 K, crystals of **BipyPt·H_2O·MeOH** are yellow and consist, analogously to **BipyPt·H_2O,** of a layered structure. However, in contrast with the monohydrated phase, the bimetallic layers are considerably corrugated likely provoked by inclusion of the molecule of MeOH, which distorts the 2D network (Figure 6b). This corrugation is reflected on the angles of 6.54º and 23.01º defined between the $[Fe(N_{eq})_4]$ equatorial plane of the $[FeN_6]$ octahedron and the adjacent square-planar units $[Pt^{II}(CN)_4]^{2-}$. The guest MeOH molecules are accommodated along the channels generated between the protruding interdigitated 2,4-bipy axial ligands of consecutive layers, where one molecule of H_2O has also been detected. Both guests establish hydrogen-bonding interactions (N−O distances in the 2.8−3.3 Å range) with the noncoordinated N heteroatom of the axial 2,4-bipy ligand. The Fe−N average distance is 2.160 Å, which indicates that the structure is blocked at the HS state even at 120 K.

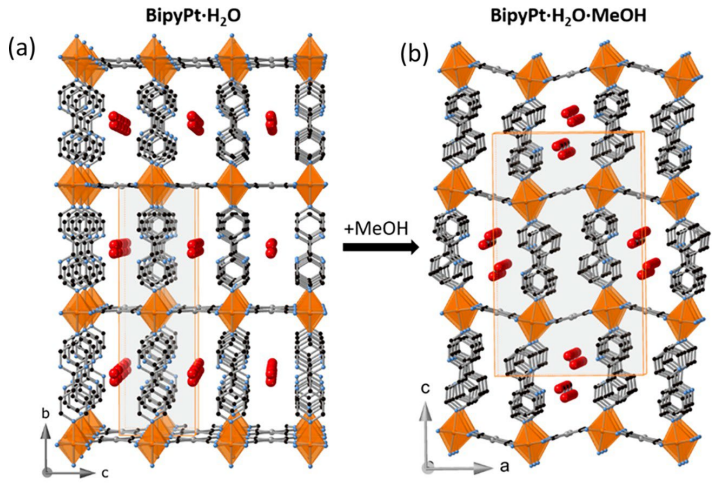

Figure 6. *Structural modifications observed on the (a)* ***BipyPt·H_2O*** *(isostructutal to* ***BipyPd·H_2O****) network upon MeOH adsorption and the corresponding transformation in (b)* ***BipyPt·H_2O·MeOH.*** *The two disordered positions of the noncoordinated pyridine are shown for compound* ***BipyPt·H_2O·MeOH.***

Structures of BipyPt and PhPyPt. The solvent-free **BipyPt** and **PhPyPt** compounds are isostructural and adopt the monoclinic *I2/m* space group at 298 K. The Fe^{II} ion lies in an inversion center with average Fe−N bond lengths of 2.167 and 2.168 Å for **BipyPt** and **PhPyPt,** respectively, which are consistent with the HS state of the Fe^{II} site. Analogously to the corresponding solvated forms, the structure is composed of an infinite stack of bimetallic $\{Fe(L)_2[Pt(CN)_4]\}$ layers. However, at variance with the previously described structures, the layers of unsolvated forms are strongly corrugated (Figure 7). Indeed, the angle defined by the average equatorial planes $[Fe(N_{eq})_4]$ and $[Pt(CN)_4]^{2-}$ is around 38º for both derivatives. This corrugation induces a marked tilt of the axial ligands with respect to the mean plane defined by the Fe^{II}-M^{II} bimetallic layer favoring a considerably more dense and efficient packing between layers in such a manner that no solvent-accessible channels are present within the structures.

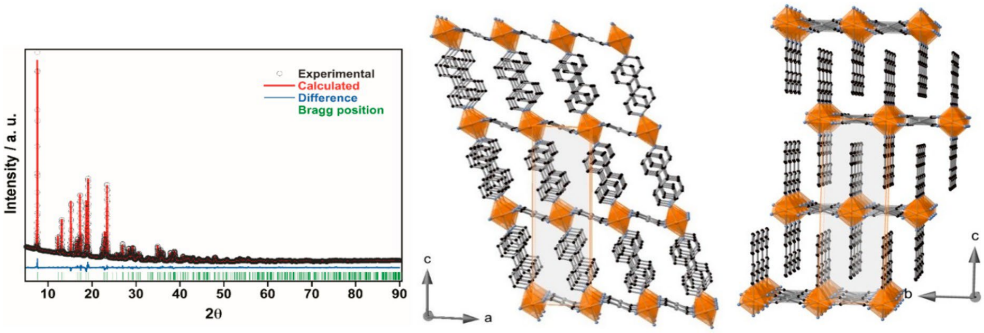

*Figure 7. Rietveld fitting of the experimental XRPD pattern for **PhPyPt** (left) (for **BipyPt,** see Figure S17). Views along the b (middle) and a (right) axes of a fragment of the desolvated **PhPyPt** framework.*

4.5.- Discussion

The main objective of this work was to evaluate the affinity toward adsorption of hydrophilic guests in two equivalent series of 2D Hofmann-type $\{Fe^{II}(L)_2[M^{II}(CN)_4]\}$ (M^{II} = Pt^{II}, Pd^{II}) CPs based on the axial ligands L = 4-PhPy (**PhPyM**) and 2,4-Bipy (**BipyM**) and to assess the structural effects induced by adsorption/desorption of the guest and its consequences on the SCO properties. Both series of 2D frameworks essentially differ in the presence/absence of an extra N heteroatom and consequently in the distinct hydrophobicity of the interlayer spaces generated between the interdigitated 2,4-Bipy and 4-PhPy ligands.

4.5.1.- Solvent Affinity and Structural Rearrangements

The different capabilities of compounds **PhPyM** and **BipyM** for retaining MeOH or H_2O can be rationalized by analyzing the structures of the corresponding solvates. For example, in the **PhPyM·MeOH·0.5H_2O** and **BipyM·H_2O·MeOH** clathrates, the interactions of the MeOH molecules with the host framework are rather repulsive because of the steric require- ments created by the methyl group of the MeOH molecule. As a result, the interdigitated 4-PhPy or 2,4-bipy ligands are tilted, maximizing the host−guest distances and forcing the aperture of channels in the interlayer space to facilitate the inclusion of MeOH. However, on the basis of the magnetic behavior (Figures 2 and S13) and PXRD (Figure S11), these distorted structures are adopted when the crystals are soaked in MeOH, but they are not stable once exposed to air, thereby losing the guest molecules and reverting to the desorbed **PhPyM** and **BipyM** phases. In contrast, the H_2O molecules located between adjacent layers in **BipyM·H_2O** occupy discrete positions in such a way that they establish hydrogen bonds with the N heteroatom of the noncoordinating pyridine of the 2,4-bipy ligand. As a result of this hydrogen bonding, the H_2O molecule remains attached to the host framework unless a heating treatment is applied. The H_2O molecules are situated at the center of the square windows defined by four neighboring interdigitated 2,4-bipy ligands and the equatorial CN^- groups. Hence, their presence does not suppose any steric repulsion over the host network, promoting a very regular, ordered, and stable structure reminiscent of those of the analogues 2D-Hofmann compounds {Fe(pyrimidine)$_2$[M(CN)$_4$]}·$x$$H_2O$ (**PymM**)[39] and {Fe(pyridazine)$_2$[M(CN)$_4$]·$x$$H_2O$} (**PdzM**).[24]

Whereas desorbed compounds **PhPyM** are not capable of recovering H_2O from humid air, compounds **BipyM** exhibit a strong affinity to H_2O, readsorbing it spontaneously within a few minutes. It is important to stress that this marked difference cannot be ascribed to structural factors because both unsolvated forms are isostructural and isomorphous; con- sequently, the interstitial space generated within the interdigitated axial ligands of two consecutive layers is similar in both series of compounds. Indeed, the presence of the N heteroatom in **BipyM** is the driving force responsible for its high affinity toward H2O, which is sequestered by the host framework, triggering a crystal transformation. Thus, crystals convert from the desorbed phase **BipyM** (monoclinic *C*) to the monohydrated phase **BipyM·H_2O** (orthorhombic *C*), inducing a large “wine-rack”-like transformation to accommodate the H_2O molecules. These marked structural changes are unprecedented within the family of 2D Hofmann-type frameworks, which show the ability to recover H_2O

from humidity.[18,19,21,28,39] The H_2O affinity of the unsolvated **BipyM** system strongly contrasts with that exhibited by the related compounds {Fe(pyrimidine)$_2$[M(CN)$_4$]} (M = Pt, Pd), which also display an available uncoordinated N atom in the axial pyrimidine ligands. In their monohydrated forms, the H_2O molecule seems more labile, exhibiting full (M = Pt) and partial (M = Pd) spontaneous desorption. However, only the Pt derivative can recover half of the H_2O molecule, while the Pd derivative does not show H_2O adsorption in contact with air. This smaller affinity for H_2O may be related to the much smaller interlayer distance and likely larger rigidity exhibited by the pyrimidine derivatives, which prevent the framework from hosting the H_2O molecules.

The lack of structural modifications observed from the PXRD patterns upon soaking **PhPyM** in H_2O (Figure S11) suggests a minimal adsorption of this guest. This observation is likely due to the hydrophobic nature of the intralayer cavities in these derivatives. In contrast, the PXRD patterns for these derivatives immersed in MeOH (Figure S11) denote remarkable changes in their structure, suggesting a greater tolerance toward MeOH adsorption, a fact that is likely due to the stronger affinity of MeOH to hydrophobic voids.[40]

4.5.2.- Nature of the Axial Ligand and Its Influence on the SCO

Although here we contribute to a detailed structural study and guest-dependent SCO experiments for compounds **PhPyPt** and **PhPyPd,** their magnetic behavior in the unsolvated form was already reported[35] and successfully reproduced in this work. The formal replacement of 4-PhPy with 2,4-Bipy as the axial ligand in the 2D Hofmann-type {Fe(L)$_2$[M(CN)$_4$]} series provokes remarkable changes in the SCO behavior. As far as the isostructural unsolvated forms are concerned, the average $T_{1/2}$ temperatures of the 2,4-Bipy derivatives are 38 K (M = Pt) and 44 K (M = Pd) larger than those of the 4-Phpy counterparts. Without excluding the possible influence of subtle structural effects, this marked difference should be mainly ascribed to the electronic effects induced by the peripheral 4-pyridyl or 4-phenyl groups on the coplanar coordinating pyridine ring. In this respect, although similar coordinating capabilities are expected for both ligands, the slightly larger electronegativity of 2,4-Bipy associated with the presence of the noncoordinating pyridine group, on the one hand, makes the N lone pair of the coordinating pyridine group less diffuse, thereby decreasing its σ-donor character but, on the other hand, simultaneously increases the π-acceptor character of 2,4-bipy, with the resulting effect being an increase of the ligand-field strength and, hence, the $T_{1/2}$ values for the **BipyM** derivatives.

4.5.3.- Guest-Dependent SCO Behavior

Concerning the solvated forms, the changes observed in the SCO reflect the ability of the framework to include the guest molecules and the resulting host−guest interplay. For example, the **PhPyM** derivatives soaked in H_2O exhibit SCO behaviors centered at temperatures only slightly smaller (5 K for M = Pd and 14 K for M = Pt) than the ones observed for the unsolvated counterparts (note that only $T_{1/2}^{\downarrow}$ is reduced, whereas $T_{1/2}^{\uparrow}$ is not modified). This suggests that the amount of adsorbed H_2O is very small, prompting a slight stabilization of the HS via elastic frustration. In contrast, the **BipyM** derivatives soaked in H_2O essentially recover the original SCO of the as-synthesized samples. It is worth mentioning that the $T_{1/2}$ values of the **BipyM·H₂O** solvates are in the range of 50−60 K higher than those of their unsolvated counterparts. This important stabilization of the LS state shifting $T_{1/2}$ near room temperature must be facilitated by the highly regular orthorhombic *Cmmm* structure adopted by **BipyM·H₂O**, which favors the lack of elastic frustration. The increase of $T_{1/2}$ with the adsorption of H_2O is relatively common in 3D Hofmann-type compounds and has been associated with structural changes produced upon the hydration process and/or the host−guest interactions (i.e., hydrogen bonding) between H2O and the ligands surrounding the FeII ion.[15] However, a $T_{1/2}$ increase mediated by H_2O adsorption is rare in 2D Hofmann structures. This is the case of compound $\{Fe(thtrz)_2[Pd(CN)_4]\}$, for which a difference of 40 K between the empty and monohydrated derivatives was also explained by host−guest interactions influencing the Fe^{II} environment.[19] Conversely, the majority of the reported 2D-layered Hofmann structures present an increase of $T_{1/2}$ upon dehydration, which has been mainly justified by a reduction of the elastic frustration. In the present case, inclusion of the H_2O molecule not only is not a source of steric hindrance but also is responsible for the $T_{1/2}$ upshift until attaining the room temperature range. Importantly, whatever the degree of solvation, examples of 2D Hofmann frameworks presenting hysteretic SCO properties centered around room temperature are still scarce[18,24] and are needed for future applications.

The progressive and controlled desorption of H_2O in **BipyM·H₂O** to afford **BipyM** is accompanied by a reduction in $T_{1/2}$ and the occurrence of a crystallographic transformation from the orthorhombic *Cmmm* to the monoclinic *I2/m* space group. The latter defines a less regular network, which is reflected in an important increase of corrugation in the bimetallic layers. Interestingly, this decrease in T_c does not seem to be homogeneous with the sample showing intermediate dehydrated phases, whose SCO behaviors suggest the presence of

mixtures of pure hydrated and dehydrated species. However, interestingly, the evolution of this dehydration process gives rise to an intermediate phase that displays a huge square-shaped hysteresis loop 84 K, which clearly suggests the presence of a homogeneous genuine phase instead the overlap of two distinct phases. The presence of such an intermediate state was detected through sophisticated single-crystal X-ray diffraction analysis in the mononuclear system $[Fe(bpp)(H_2L)](ClO_4)_2 \cdot 1.5C_3H_6O$ [bpp = 2,6-bis-(pyrazol-3-yl)pyridine; H_2L = 2,6-bis[5-(2-methoxyphenyl)-pyrazol-3-yl]pyridine; C_3H_6O = acetone].[41]

The introduction of MeOH in both the **PhPyM** and **BipyM** frameworks induces deactivation of the SCO. Indeed, the magnetic measurements of these compounds soaked in liquid MeOH yield paramagnetic curves. This result is consistent with the structures of **PhPyM·MeOH·0.5H$_2$O** and **BipyPt·MeOH·H$_2$O,** where the Fe^{II} ions are HS at all temperatures. As mentioned above, the adsorption of MeOH implicates important structural changes in the host framework, i.e., the adjacent axial ligand 2,4-Bipy (or 4-PhPy) of a layer tilt in opposite directions, opening channels along which the MeOH is accommodated. These structural changes generate short intermolecular contacts featuring steric repulsions, i.e., those established between the methylene H atoms of MeOH and the aromatic H atoms of the coordinating pyridine. Likely, this steric factor is responsible for the elastic frustration that involves stabilization of the HS state. Along this line, the small fraction of SCO-active Fe^{II} ions observed for crystals of **FePhPy·*x*MeOH·*y*H$_2$O** (Figure 1b) soaked in the mother liquor is likely due to the existence of MeOH-free phases containing H_2O or exhibiting complete absence of solvent. Indeed, the presence of this SCO-active phase was detected by PXRD (Figure S1).

4.6.- Conclusions

In summary, guest-dependent structural and SCO properties of the isomorphous 2D Hofmann CPs $\{Fe(4\text{-}PhPy)_2[M(CN)_4]\}$ (**PhPyM**) and $\{Fe(2,4\text{-}Bipy)_2[M(CN)_4]\}$ (**BipyM**) (M = Pd, Pt) were characterized and compared. Our results indicate that, although the sole difference between both families of compounds stems from the presence/absence of a non-coordinated N heteroatom within the interlayer space, this subtle difference in the chemical composition deeply impacts not only the adsorption capability of the clathrate but also the degree to which the SCO is modulated upon guest uptake. Thus, whereas the adsorption of

H_2O in **BipyM** is rapid and spontaneous at ambient conditions, it occurs to a very low extent for **PhPyM,** even when soaked in H_2O. The driving force of the higher H_2O affinity of the former is necessarily ascribed to the hydrogen bonds established between H_2O and the noncoordinated N heteroatom. These interactions induce the opening of interlayer channels along which the H_2O molecules are accommodated, leading to regular and homogeneous layered structures. The uptake of H_2O in **BipyM** provokes a remarkable increase of the SCO temperatures (by 50−60 K), shifting the wide hysteresis loops at around room temperature. This SCO shift has been correlated with a combination of structural and electronic factors. In contrast, the small amount of H_2O adsorbed by **PhPyM** marginally influences the SCO temperature, likely due to subtle elastic frustration effects. Besides, although MeOH molecules are efficiently absorbed in solution by both series of compounds leading to distorted layered networks, steric repulsions between the MeOH molecules and host network are behind its rapid desorption under an ambient atmosphere. This steric factor also provides elastic frustration to the system because the SCO properties of both families of compounds are deactivated when soaked in MeOH. This comparative study sheds light on how fine-tuning the host framework greatly modifies the coupling of host−guest and SCO properties and contributes to paving the way toward the application of these materials as chemical sensors.

4.7.- References

[1] König, E. Nature and dynamics of the spin-state interconversion in metal complexes. *Struct. Bonding (Berlin, Ger.)* **1991**, *76*, 51.

[2] Gütlich, P., Goodwin, G., Eds. Spin crossover in transition metal compound I−III. *Topics in Current Chemistry*; Springer, **2004**; pp 233−235.

[3] Gütlich, P.; Hauser, A.; Spiering, H. Thermal and Optical Switching of Iron(II) Complexes. Angew. Chem., *Int. Ed. Engl*. **1994**, *33*, 2024−2054.

[4] Gütlich, P.; Garcia, Y.; Goodwin, H. A. Spin crossover phenomena in Fe(ii) complexes. *Chem. Soc. Rev*. **2000**, *29*, 419−427.

[5] See the special issue “Spin Crossover Phenomenon”: Wolny, J. A.; Schunemann, V.; Nemeth, Z.; Vanko, G. Spectroscopic techniques to characterize the spin state:

Vibrational, optical, Mössbauer, NMR, and X-ray spectroscopy. *C. R. Chim*. **2018**, *21*, 1152−1169.

[6] Kahn, O.; Martinez, J. Spin-Transition Polymers: From Molecular Materials Toward Memory Devices. *Science* **1998**, *279*, 44.

[7] Halcrow, M. A. *Spin-Crossover Materials: Properties and Applications*; Wiley: West Sussex, U.K., **2013**.

[8] Létard, J.-F.; Guionneau, P.; Goux-Capes, L. Towards spin crossover applications. *Top. Curr. Chem*. **2004**, *235*, 221−249.

[9] Bousseksou, A.; Molnár, G.; Salmon, L.; Nicolazzi, W. Molecular spin crossover phenomenon: recent achievements and prospects. *Chem. Soc. Rev*. **2011**, *40*, 3313.

[10] Molnár, G.; Rat, S.; Salmon, L.; Nicolazzi, W.; Bousseksou, A. Spin Crossover Nanomaterials: From Fundamental Concepts to Devices. *Adv. Mater*. **2018**, *30*, 1703862−23.

[11] Real, J. A.; Gaspar, A. B.; Niel, V.; Muñoz, M. C. Communication between Iron(II) Building Blocks in Cooperative Spin Transition Phenomena. *Coord. Chem. Rev*. **2003**, *236*, 121−141.

[12] Garcia, Y.; Niel, V.; Muñoz, M. C.; Real, J. A. Spin Crossover in 1D, 2D and 3D Polymeric Fe(II) Networks. *Top. Curr. Chem*. **2004**, *233*, 229−257.

[13] Muñoz, M. C.; Real, J. A. Thermo-, Piezo-, Photo- and Chemo-Switchable Spin Crossover Iron(II)-Metallocyanate Based Coordina- tion Polymers. *Coord. Chem. Rev*. **2011**, *255*, 2068−2093.

[14] Kucheriv, O. I.; Fritsky, I. O.; Gural'skiy, I. A. Spin crossover in FeII cyanometallic frameworks. *Inorg. Chim. Acta* **2021**, *521*, 120303.

[15] Ohtani, R.; Hayami, S. Guest-Dependent Spin-Transition Behavior of Porous Coordination Polymers. *Chem. - Eur. J*. **2017**, *23*, 2236−2248.

[16] Ni, Z. P.; Liu, J. L.; Hoque, M. N.; Liu, W.; Li, J. Y.; Chen, Y. C.; Tong, M. L. Recent Advances in Guest Effects on Spin-Crossover Behavior in Hofmann-Type Metal-Organic Frameworks. *Coord. Chem. Rev*. **2017**, *335*, 28−43.

[17] Ohba, M.; Yoneda, K.; Agustí, G.; Munoz, M. C.; Gaspar, A. B.; Real, J. A.; Yamasaki, M.; Ando, H.; Nakao, Y.; Sakaki, S.; Kitagawa, S. Bidirectional chemo-switching of spin state in a microporous framework. *Angew. Chem., Int. Ed*. **2009**, *48*, 4767.

[18] Zenere, K. A.; Duyker, S. G.; Trzop, E.; Collet, E.; Chan, B.; Doheny, P. W.; Kepert, C. J.; Neville, S. M. Increasing spin crossover cooperativity in 2D Hofmann-type materials with guest molecule removal. *Chem. Sci*. **2018**, *9*, 5623−5629.

[19] Sciortino, N. F.; Ragon, F.; Klein, Y. M.; Housecroft, C. E.; Davies, C. G.; Jameson, G. N. L.; Chastanet, G.; Neville, S. M. Guest- Responsive Elastic Frustration "On−Off" Switching in Flexible, Two- Dimensional Spin Crossover Frameworks. *Inorg. Chem*. **2018**, *57*, 11068−11076.

[20] Milin, E.; Patinec, V.; Triki, S.; Bendeif, E.-E.; Pillet, S.; Marchivie, M.; Chastanet, G.; Boukheddaden, K. Elastic Frustration Triggering Photoinduced Hidden Hysteresis and Multistability in a Two-Dimensional Photoswitchable Hofmann-Like Spin-Crossover Metal−Organic Framework. *Inorg. Chem*. **2016**, *55*, 11652−11661.

[21] Sciortino, N. F.; Ragon, F.; Zenere, K. A.; Southon, P. D.; Halder, G. J.; Chapman, K. W.; Piñeiro-Lopez, L.; Real, J. A.; Kepert, C. J.; Neville, S. M. Exploiting Pressure To Induce a "Guest-Blocked" Spin Transition in a Framework Material. *Inorg. Chem*. **2016**, *55*, 10490−10498.

[22] Brennan, A. T.; Zenere, K. A.; Kepert, C. J.; Clegg, J. K.; Neville, S. M. Three Distinct Spin-Crossover Pathways in Halogen- Appended 2D Hofmann Frameworks. *Inorg. Chem*. **2021**, *60* (6), 3871−3878.

[23] Brennan, A. T.; Zenere, K. A.; Brand, H. E. A.; Price, J. R.; Bhadbhade, M. M.; Turner, G. F.; Moggach, S. A.; Valverde-Muñoz, F. J.; Real, J. A.; Clegg, J. K.; Kepert, C. J.; Neville, S. M. Guest Removal and External Pressure Variation Induce Spin Crossover in Halogen-Functionalized 2-D Hofmann Frameworks. *Inorg. Chem*. **2020**, *59* (19), 14296−14305.

[24] Gural'skiy, I. A.; Shylin, S. I.; Ksenofontov, V.; Tremel, W. Pyridazine-Supported Polymeric Cyanometallates with Spin Tran- sitions. *Eur. J. Inorg. Chem.* **2019**, *2019*, 4532−4537.

[25] Sciortino, N. F.; Zenere, K. A.; Corrigan, M. E.; Halder, G. J.; Chastanet, G.; Létard, J.-F.; Kepert, C. J.; Neville, S. M. Four-step iron(ii) spin state cascade driven by antagonistic solid state interactions. *Chem. Sci*. **2017**, *8*, 701.

[26] Murphy, M. J.; Zenere, K. A.; Ragon, F.; Southon, P. D.; Kepert, C. J.; Neville, S. M. Guest Programmable Multistep Spin Crossover in a Porous 2-D Hofmann-Type Material. *J. Am. Chem. Soc*. **2017**, *139*, 1330−1335.

[27] Klein, Y. M.; Sciortino, N. F.; Ragon, F.; Housecroft, C. E.; Kepert, C. J.; Neville, S. M. Spin crossover intermediate plateau stabilization in a flexible 2-D Hofmann-type coordination polymer. *Chem. Commun*. **2014**, *50*, 3838−3840.

[28] Turo-Cortés, R.; Bartual-Murgui, C.; Castells-Gil, J.; Muñoz, M. C.; Martí-Gastaldo, C.; Real, J. A. Reversible guest-induced gate- opening with multiplex spin crossover responses in two-dimensional Hofmann clathrates. *Chem. Sci*. **2020**, *11*, 11224−11234.

[29] Real, J. A.; Andres, E.; Muñoz, M. C.; Julve, M.; Granier, T.; Bousseksou, A.; Varret, F. Spin Crossover in a Catenane Supra- molecular System. *Science* **1995**, *268*, 265.

[30] Halder, G. J. Guest-Dependent Spin Crossover in a Nanoporous Molecular Framework Material. *Science* **2002**, *298*, 1762.

[31] Neville, S. M.; Moubaraki, B.; Murray, K. S.; Kepert, C. J. A Thermal Spin Transition in a Nanoporous Iron(II) Coordination Framework Material. *Angew. Chem., Int. Ed*. **2007**, *46*, 2059.

[32] Neville, S. M.; Halder, G. J.; Chapman, K. W.; Duriska, M. B.; Moubaraki, B.; Murray, K. S.; Kepert, C. J. Guest Tunable Structure and Spin Crossover Properties in a Nanoporous Coordination Framework Material. *J. Am. Chem. Soc*. **2009**, *131*, 12106−12108.

[33] Halder, G. J.; Chapman, K. W.; Neville, S. M.; Moubaraki, B.; Murray, K. S.; Létard, J.-F.; Kepert, C. J. Elucidating the Mechanism of a Two-Step Spin Transition in a Nanoporous Metal−Organic Framework. *J. Am. Chem. Soc*. **2008**, *130*, 17552.

[34] Neville, S. M.; Halder, G. J.; Chapman, K. W.; Duriska, M. B.; Southon, D.; Cashion, J. D.; Létard, J.-F.; Moubaraki, B.; Murray, K. S.; Kepert, C. J. Single-Crystal to Single-

Crystal Structural Trans- formation and Photomagnetic Properties of a Porous Iron(II) Spin- Crossover Framework. *J. Am. Chem. Soc*. **2008**, *130*, 2869.

[35] Seredyuk, M.; Gaspar, A. B.; Ksenofontov, V.; Verdaguer, M.; Villain, F.; Gütlich, P. Thermal- and Light-Induced Spin Crossover in Novel 2D Fe(II) Metalorganic Frameworks $\{Fe(4\text{-}PhPy)_2[M^{II}(CN)_x]_y\}\cdot sH_2O$: Spectroscopic, Structural, and Magnetic Studies. *Inorg. Chem*. **2009**, *48*, 6130−6141.

[36] (a) Sheldrick, G. M. *Acta Crystallogr., Sect. A: Found. Crystallogr*. **2008**, *64*, 112. (b) Sheldrick, G. M. *SHELXL-2014*; University of Göttingen, **2014**.

[37] Oszlányi, G.; Sütő, A. Ab initio structure solution by charge flipping. *Acta Crystallogr., Sect. A: Found. Crystallogr*. **2004**, *60*, 134−141.

[38] Rietveld, H. M. A profile refinement method for nuclear and magnetic structures. *J. Appl. Crystallogr*. **1969**, *2*, 65−71.

[39] Bartual-Murgui, C.; Rubio-Giménez, V.; Meneses-Sánchez, M.; Valverde-Muñoz, F. J.; Tatay, S.; Martí-Gastaldo, C.; Muñoz, M. C.; Real, J. A. Epitaxial Thin-Film vs Single Crystal Growth of 2D Hofmann-Type Iron(II) Materials: A Comparative Assessment of their Bi-Stable Spin Crossover Properties. *ACS Appl. Mater. Interfaces* **2020**, *12* (26), 29461−29472.

[40] Gounder, R.; Davis, M. E. Beyond shape selective catalysis with zeolites: Hydrophobic void spaces in zeolites enable catalysis in liquid water. *AIChE J*. **2013**, *59*, 3349−3358.

[41] Aromí, G.; Beavers, M.; Sánchez Costa, J.; Craig, G. A.; Mínguez Espallargas, G.; Orera, A.; Roubeau, O. Snapshots of a solid- state transformation: coexistence of three phases trapped in one crystal. *Chem. Sci*. **2016**, *7*, 2907−2915.

4.8.- Supporting Information

Figure S1. *Powder X-ray diffraction spectra at room temperature of a)* ***PhPyPt·xMeOH·yH$_2$O*** *and b)* ***PhPyPd·xMeOH·yH$_2$O*** *measured in their mother liquor (black) and after exposed to air and air-dried for several minutes (red) and (c and d) their corresponding enlarged 6.5-8º windows. Simulated spectra of the solvates* ***PhPyM·MeOH·0.5H$_2$O*** *are also shown as reference.*

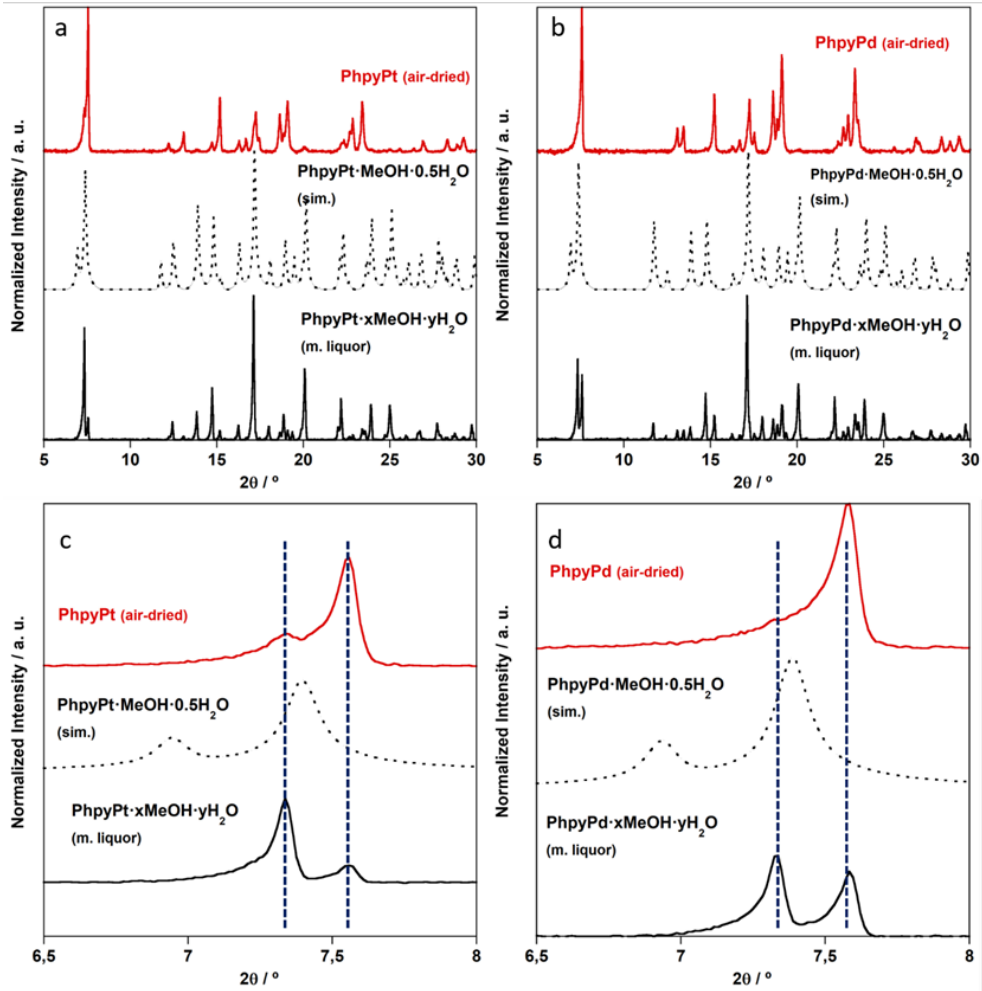

Figure S2. *Thermogravimetric analyses of* ***PhPyM·xMeOH·yH$_2$O*** *(a) M = Pt and b) M = Pd) recorded upon removing the crystals from mother liquor and air dried at room temperature (blue) and several days after heating the samples at 400 K for 1 h and re-exposed to air (red).*

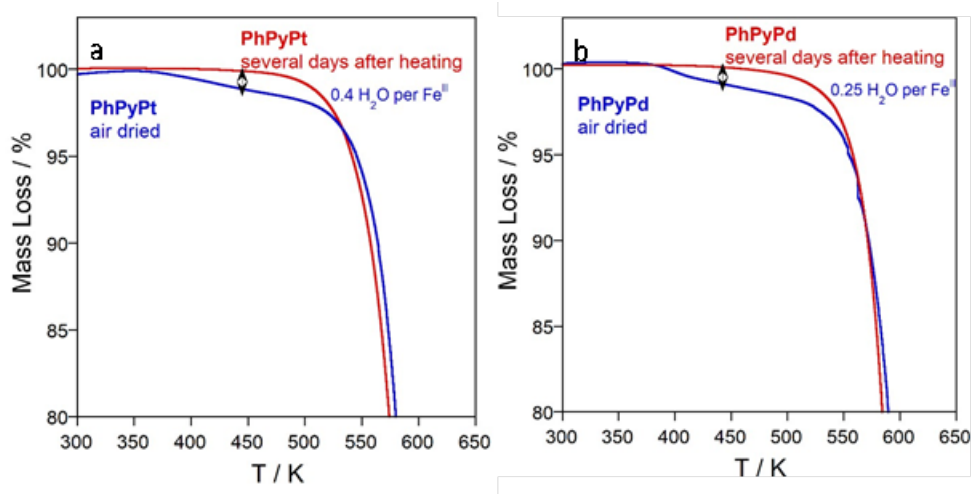

Figure S3. *Powder X-ray diffraction spectra at room temperature of a)* ***BipyPt·H$_2$O*** *and b)* ***BipyPd·H$_2$O*** *measured in their mother liquor (black), after exposed to air and air-dried at room temperature for several minutes (blue) and once heated at 400 K for one hour (red). Simulated spectra of compounds* ***BipyM·H$_2$O*** *are also shown as reference.*

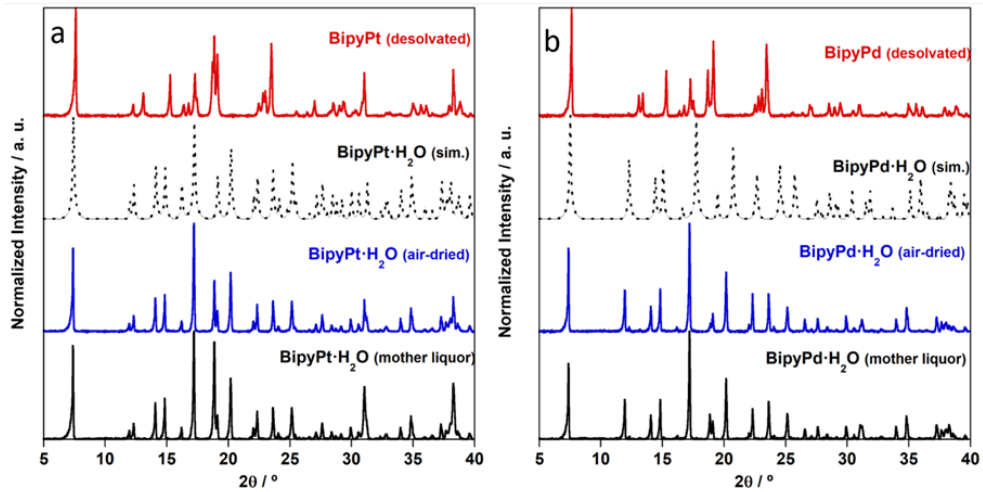

Figure S4. *Thermogravimetric analyses of* ***BipyM·H₂O*** *(M = Pt (red) and Pd (blue)) recorded upon removing the crystals from mother liquor and air dried at room temperature.*

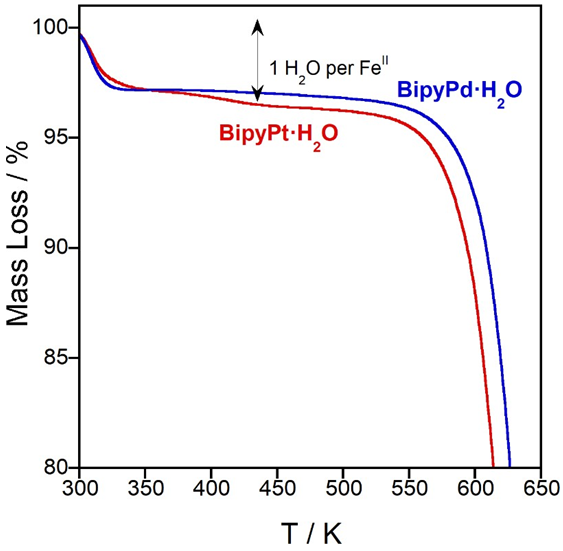

Figure S5. *Time dependent TGA measurements registered upon desorption and reabsorption of water for a)* ***BipyPt*** *and b)* ***BipyPd****.*

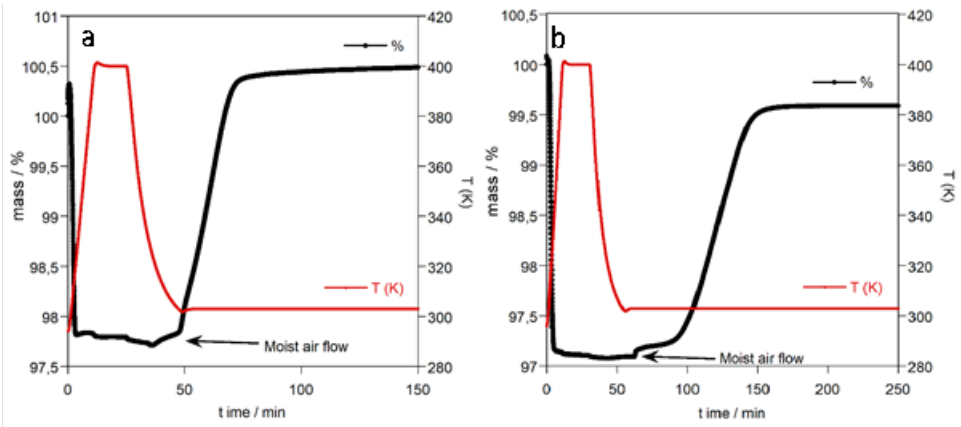

Figure S6. *Powder X-ray diffraction spectra at room temperature of the desolvated networks based on the 2,4-Bipy (black) or 4-PhPy (blue) ligands.*

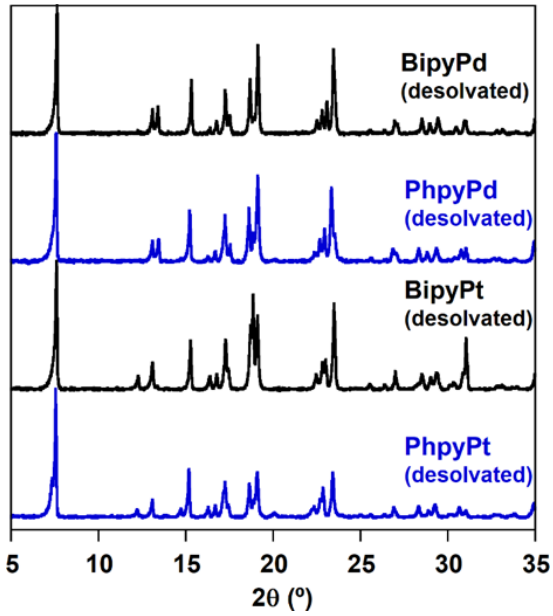

Figure S7. *Thermal dependence of the $\chi_M T$ value for compounds* ***PhPyM·xMeOH·yH₂O*** *(M = Pt (a) or Pd (b)) measured in the mother liquor (black), once extracted from the mother liquor and air dried (blue) and after a treatment at 400 K for 1 hour (red).*

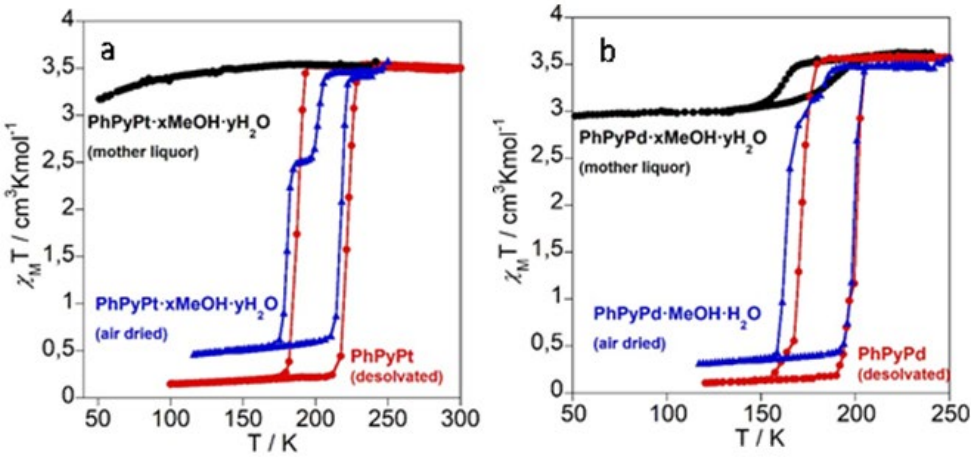

Figure S8. *Thermal dependence of the $\chi_M T$ value for compounds a)* ***PhPyPt*** *and b)* ***PhPyPd*** *just after dehydrating at 400 K for 1 h (red) and after exposing the sample to air for several days (blue).*

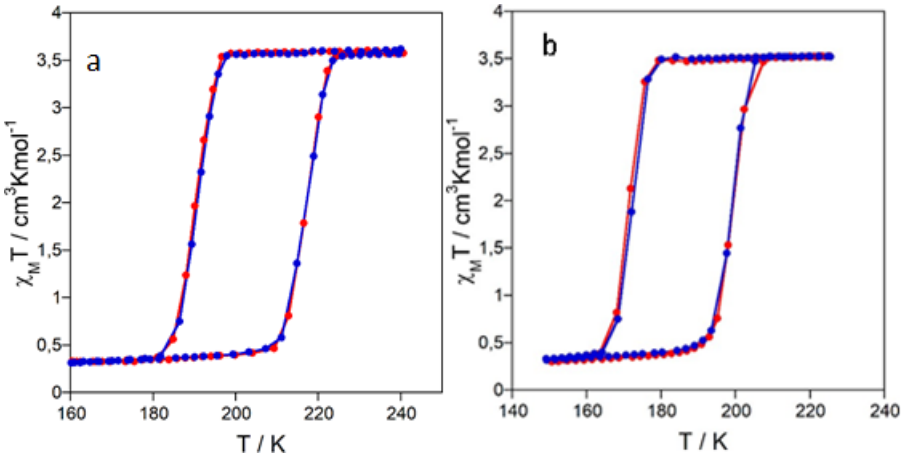

Figure S9. *Thermal dependence of the $\chi_M T$ value for compounds a)* ***BipyPt·H₂O*** *and b)* ***BipyPd·H₂O*** *after removing the crystals from the mother liquor and air drying at ambient conditions.*

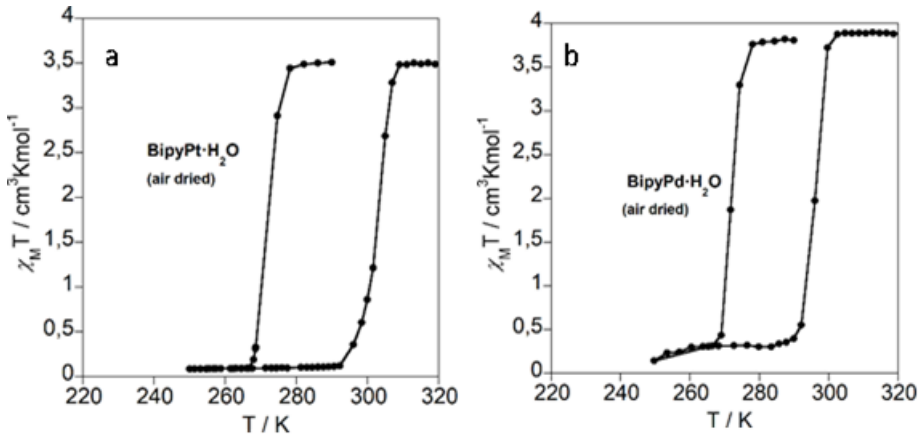

Figure S10. *Thermal dependence of the $\chi_M T$ value for dehydrated compounds a)* ***BipyPt*** *and b)* ***BipyPd*** *after ca. one hour exposed to air. The resulting SCO curves are similar to those of* ***BipyPt·H₂O*** *and* ***BipyPd·H₂O*** *indicating that the dehydrated phase recovers water in these conditions.*

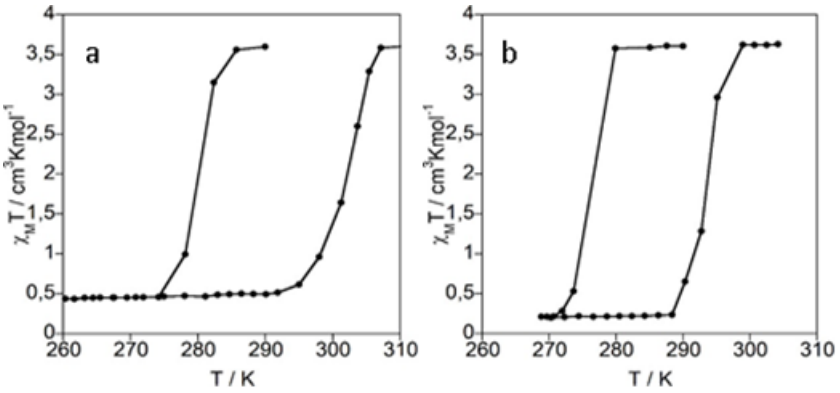

Figure S11. *Powder X-ray diffraction patterns at room temperature of compounds a)* ***PhPyPt*** *and b)* ***PhPyPd*** *after dehydrating at 400 k for 1h (red), immersed in water (blue) or methanol (black). The simulated spectra of solvates* ***PhPyPt·MeOH·0.5H₂O*** *and* ***PhPyPd·MeOH·0.5H₂O*** *are also displayed for comparison.*

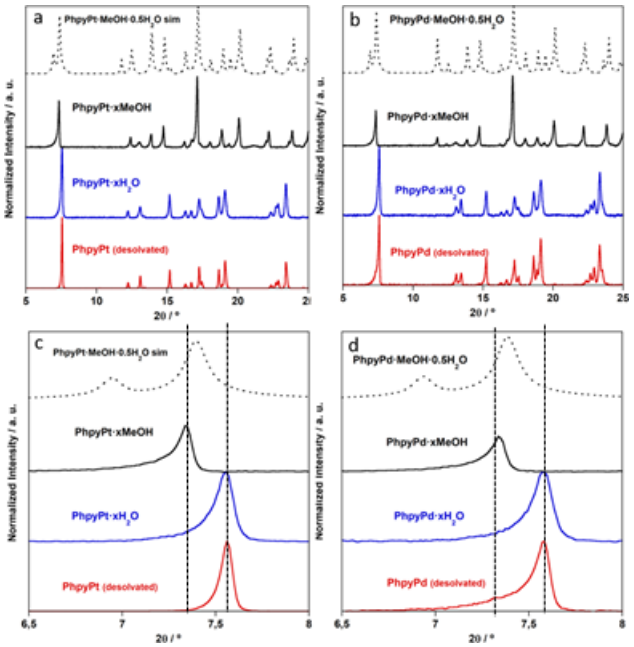

Figure S12. *Powder X-ray diffraction patterns at room temperature of compounds a)* ***BipyPt*** *and b)* ***BipyPd*** *after dehydrating at 400 k for 1h (red), immersed in water (blue) or methanol (black). The simulated spectra of the solvate* ***BipyPt·H2O·MeOH*** *is also displayed for comparison.*

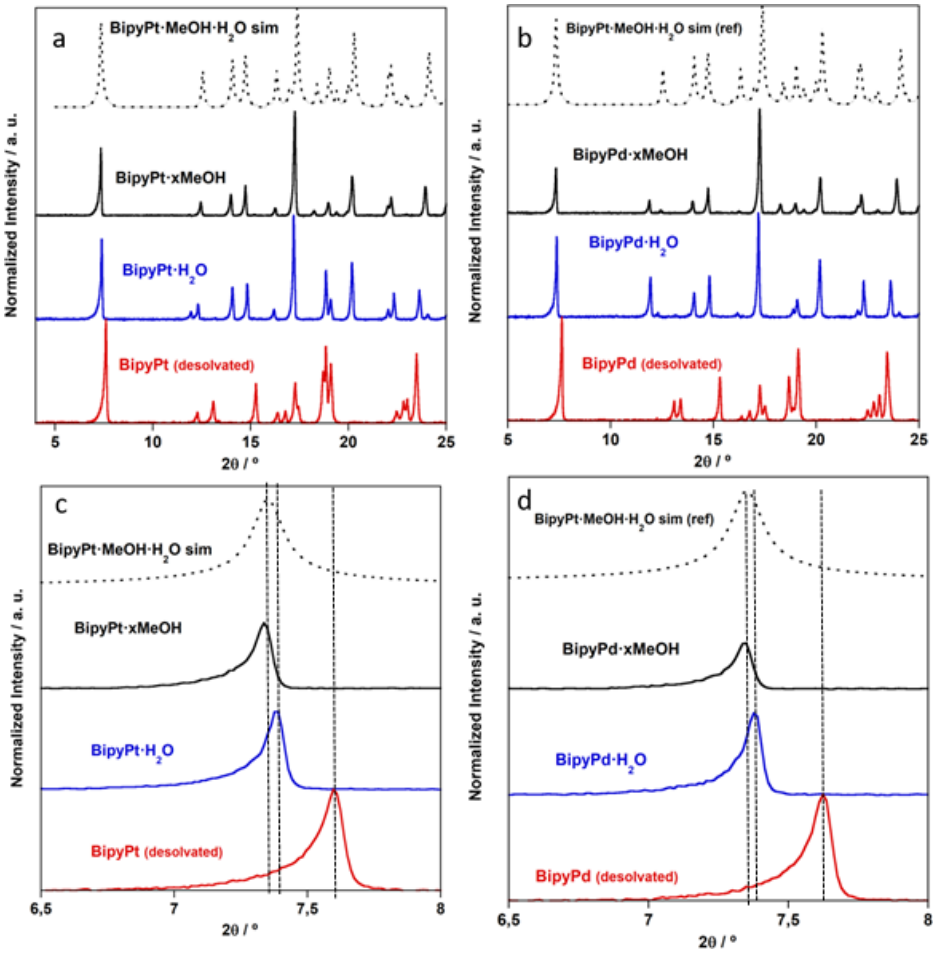

Figure S13. *SCO properties of a)* ***PhPyPd*** *and b)* ***BipyPd*** *before (black curves) and after absorbing water (blue curves) and methanol (red curves). SCO red and blue curves were registered with the samples soaked in the corresponding solvent.*

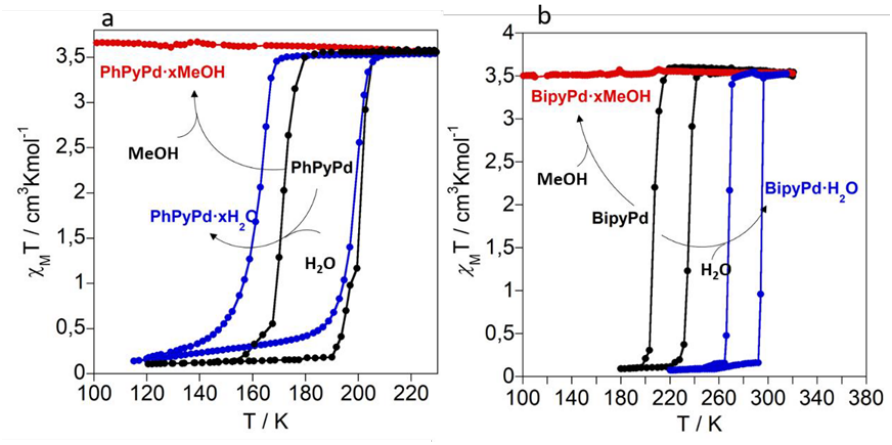

Figure S14. *SCO properties of* ***PhPyPt*** *(a and b) and* ***PhPyPd*** *(d and e) inmersed in H_2O and MeOH (black curves), respectively, and after removing the crystals from the corresponding solvent and exposed to air (blue curves). SCO of c)* ***BipyPt*** *and f)* ***BipyPd*** *inmersed in MeOH (black curves) and after removing from methanol and exposed to air (blue curves).*

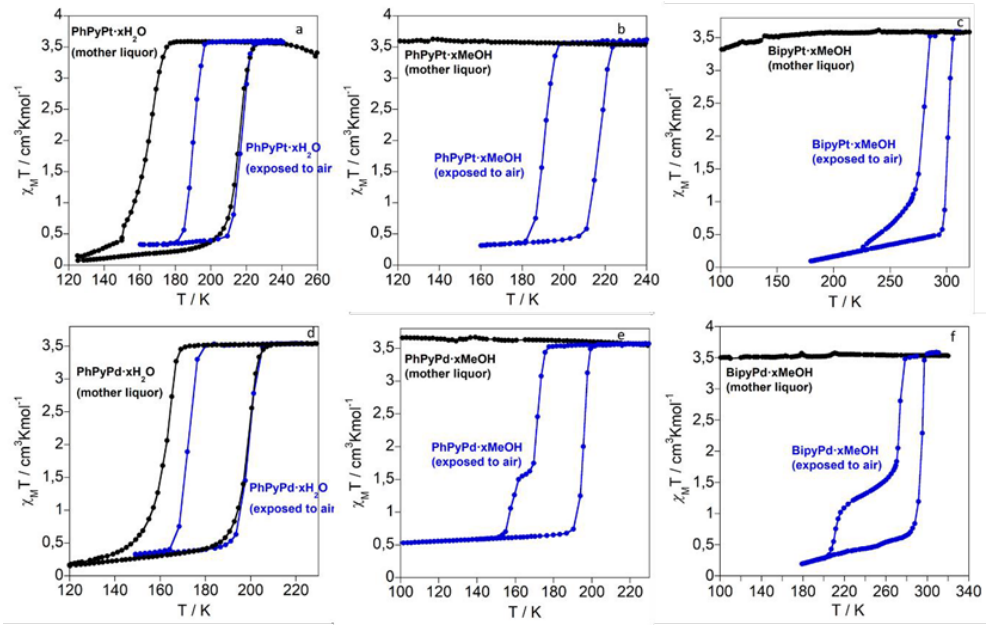

Figure S15. *Thermogravimetric analyses of* ***PhPyPt*** *(a and b),* ***BipyPt*** *(c and d)* ***PhPyPd*** *(e and f), and* ***BipyPd*** *(g and h) upon removing from H_2O and MeOH, respectively, and exposed to air. Note that, in view of the magnetic properties, the mass loss registered in curves d and h is mostly associated to water molecules that has been interchanged by those of methanol at ambient conditions.*

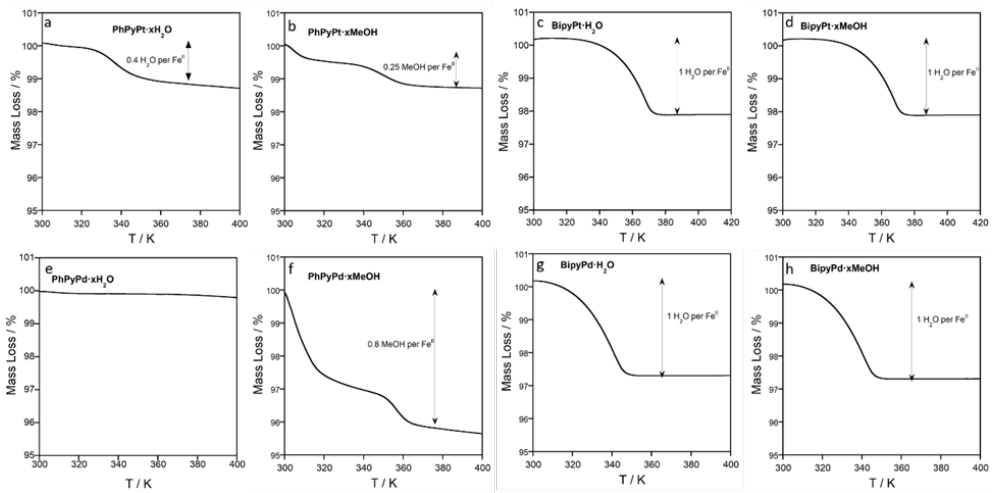

Figure S16. *DSC measurements for compound* ***BipyPt·H₂O*** *registered after heating inside the calorimeter device at 305 K for a few minutes. Blue and red curves represent the cooling and heating modes, respectively. Magnetic measurements of a* ***BipyPt·H₂O*** *sample subjecte to a similar heating treatment are displayed for comparison.*

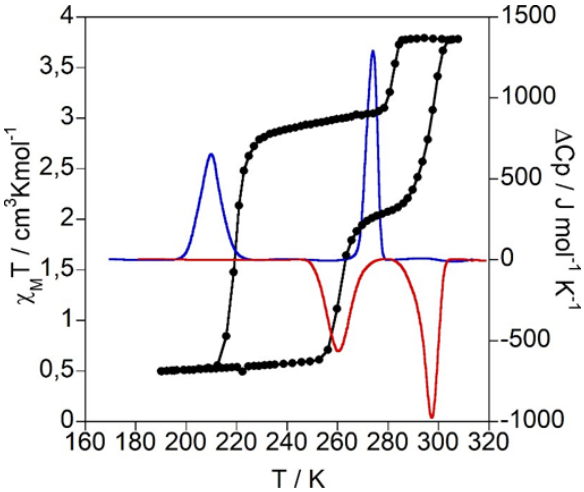

Table S1. *Crystal data for* ***PhPyM·MeOH·0.5H$_2$O*** *at 120 K (M = Pt, Pd).*

	PhPyPt·MeOH·0.5H$_2$O	**PhPyPd·MeOH·0.5H$_2$O**
Empirical formula	$C_{27}H_{18}N_6O_{1.5}PtFe$	$C_{27}H_{18}N_6O_{1.5}PdFe$
Mr	701.41	612.72
Crystal system	orthorhombic	orthorhombic
Space group	*Imma*	*Imma*
a (Å)	15.0241(4)	15.0473(3)
b (Å)	7.4189(2)	7.4095(2)
c (Å)	23.8844(6)	23.9166(5)
V (Å^3)	2662.21(12)	2666.53(11)
Z	4	4
D_c (mg cm^{-3})	1.750	1.526
F(000)	1352	1224
μ (Mo-K$_\alpha$) (mm^{-1})	5.826	1.251
Crystal size (mm)	0.01x0.08x0.08	0.01x0.12x0.12
No. of total reflections	1815	1699
No. of reflections [I>2σ(I)]	1808	1620
R [I>2 σ(I)]	0.0175	0.0353
wR [I>2 σ(I)]	0.0483	0.0977
S	1.171	1.126

Table S2. *Crystal data for* ***BipyPt·H$_2$O*** *at 120 K and 283 K,* ***BipyPt·H$_2$O·MeOH*** *at 120 K and* ***BipyPd·H$_2$O*** *at 120 K.*

	BipyPt·H$_2$O 120K	**BipyPt·H$_2$O 283K**	**BipyPt·H$_2$O·MeOH 120K**	**BipyPd·H$_2$O 120K**
Empirical formula	$C_{24}H_{18}N_8OPtFe$	$C_{24}H_{16}N_8OPtFe$	$C_{25}H_{20}N_8O_2PtFe$	$C_{24}H_{18}N_8OPdFe$
Mr	685.40	683.39	715.43	596.71
Crystal system	orthorhombic	orthorhombic	orthorhombic	orthorhombic
Space group	*Cmmm*	*Cmmm*	*Pnma*	*Cmmm*
a (Å)	7.2122(3)	7.5176(8)	14.754(4)	7.2266(2)
b (Å)	23.3642(9)	23.803(2)	7.370(2)	23.4174(5)
c (Å)	7.1140(3)	7.3695(7)	24.028(8)	7.1253(2)
V (Å^3)	1198.76(8)	1318.7(2)	2612.8(13)	1205.80(5)
Z	2	2	4	2
D_c (mg cm^{-3})	1.899	1.721	1.819	1.643
F(000)	660	656	1384	596
μ (Mo-K$_\alpha$) (mm^{-1})	6.468	5.879	5.942	1.381
Crystal size (mm)	0.02x0.12x0.12	0.02x0.12x0.12	0.02x0.10x0.10	0.04x0.12x0.12
No. of total reflections	716	789	2999	820
No. of reflections [I>2σ(I)]	710	675	2466	740
R [I>2 σ(I)]	0.0337	0.0675	0.0797	0.0253
wR [I>2 σ(I)]	0.0600	0.1343	0.2041	0.0526
S	1.091	1.103	1.235	1.080

Table S3. *Crystallographic data and Rietveld refinement summary for compounds* ***PhPyPt*** *and* ***BipyPt.***

Compound	**BipyPd**	**BipyPt**
Empirical formula	$(C_{11}H_9N)_2$ $(CN)_4$ Fe Pt	$(C_{10}H_8N_2)_2$ $(CN)_4$ Fe Pt
Formula weight (g/mol)	665.39	667.38
Temperature (K)	298	298
Crystal system	Monoclinic	Monoclinic
Space group	*I* 2/*m*	*I* 2/*m*
a (Å)	6.96068(12)	6.96916(12)
b (Å)	7.58951(10)	7.56020(11)
c (Å)	23.3210(4)	23.1696(4)
b (°)	92.4728(13)	92.2282(14)
Volume (Å^3)	1230.86(3)	1219.84(4)
Z	2	2
Radiation	Cu K$\alpha_{1,2}$	Cu K$\alpha_{1,2}$
2θ range (°)	5 – 90	5 – 90
R_p (%)	2.26	2.45
R_{wp} (%)	3.18	3.33
R_{exp} (%)	2.26	2.45
GoF	1.40	1.36
Fe-N(1)	2.224(7)	2.222(7)
Fe-N(4)	2.141(10)	2.140(12)
Pt-C(12)	1.983(14)	1.983(18)
N(1)-Fe-N(4)	90.9(4)	91.0(5)
Cl(12)-Pt-Cl(12)	180.00	180.00

Table S4. *Selected bond lengths [Å] and angles [°] for* ***PhPyM·MeOH·0.5H$_2$O*** *(M = Pt, Pd) at 120K.*

	PhPyPt	**PhPyPd**
Fe-N(1)	2.157(2)	2.159(3)
Fe-N(2)	2.223(2)	2.225(3)
M-C(1)	1.989(3)	1.993(3)
N(1)-Fe-N(2)	90.10(12)	90.21(14)
C(1)-M-C(1)	178.90(12)	178.7(2)

Table S5. *Selected bond lengths [Å] and angles [°]* ***BipyPt·H$_2$O*** *at 120 K and 283 K,* ***BipyPt·H$_2$O·MeOH*** *at 120 K and* ***BipyPd·H$_2$O*** *at 120 K.*

	bipyPt·H$_2$O 120K	**bipyPt·H$_2$O 283K**	**bipyPt·H$_2$O·MeOH 120K**	**bipyPd·H$_2$O 120K**
Fe-N(1)	1.932(5)	2.133(13)	2.122(14)	1.937(2)
Fe-N(2)	1.993(7)	2.225(19)	2.16 (2)	2.000(3)
Fe-N(3)			2.163(14)	
Fe-N(4)			2.24(2)	
M-C(1)	1.989(6)	1.993(15)	1.99(2)	1.991(3)
M-C(2)			2.00(2)	
N(1)-Fe-N(2)	90.0	90.0	92.6(5)	90.0
N(1)-Fe-N(3)			176.9(6)	
N(1)-Fe-N(4)			90.0(5)	
N(2)-Fe-N(3)			90.4(5)	
N(2)-Fe-N(4)			176.4(7)	
N(3)-Fe-N(4			87.1(6)	
C(1)-M-C(1)	180.0	180.0		180.0
C(1)-M-C(2)			178.8(6)	

Table S6. *π-π interaction and H-bonding distances [Å] found for the different compounds.*

	π-π		**H-bonding**	
	LS	**HS**	**HO-H···N(pyridine)**	**MeO-H···N(pyridine)**
PhPyPt·MeOH·0.5H$_2$O	-	3.720	-	-
PhPyPd·MeOH·0.5H$_2$O	-	3.740	-	-
BipyPt·H$_2$O	3.665	3.786	2.953(LS)-3.202(HS)	-
BipyPd·H$_2$O	3.671	-	3.000(LS)	-
BipyPt·H$_2$O·MeOH	-	3.722	3.331	2.835
BipyPt	-	3.988	-	-
PhPyPt	-	4.003	-	-

Figure S17. *Final Rietveld refinement plots for compounds (a)* ***PhPyM*** *and (b)* ***BipyM,*** *showing the experimental (red circles), calculated (black line) and difference profiles (grey line); blue marks indicate reflection positions.*

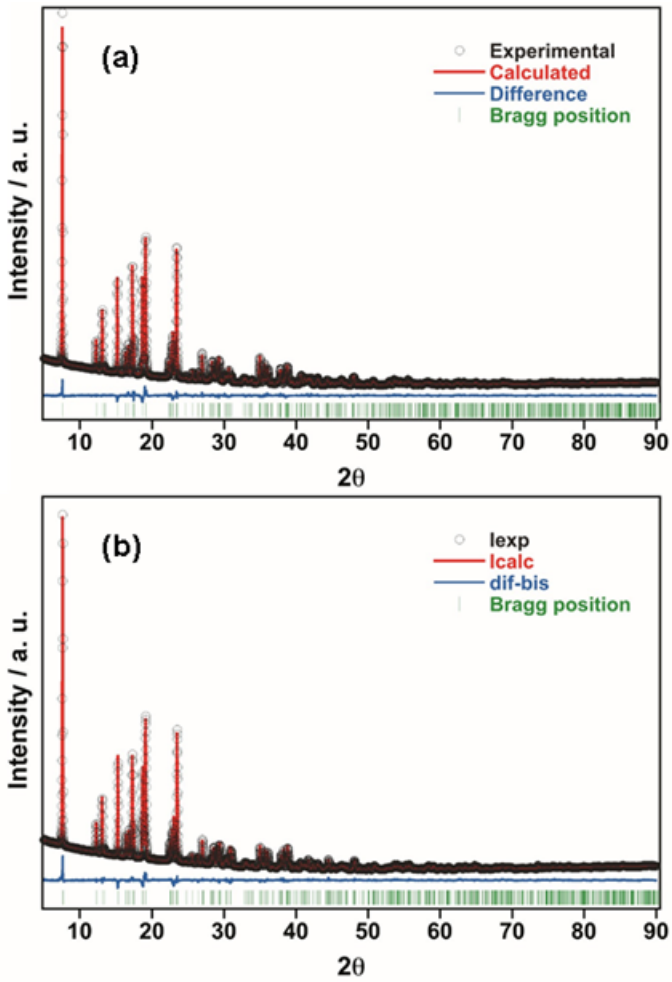

Figure S18. *Views of the structures of a)* ***PhPyM·MeOH·0.5H$_2$O*** *and* ***BipyM·H$_2$O*** *along the (100) and (001) directions, respectively, showing the interdigitation of four consecutive bimetallic layers.*

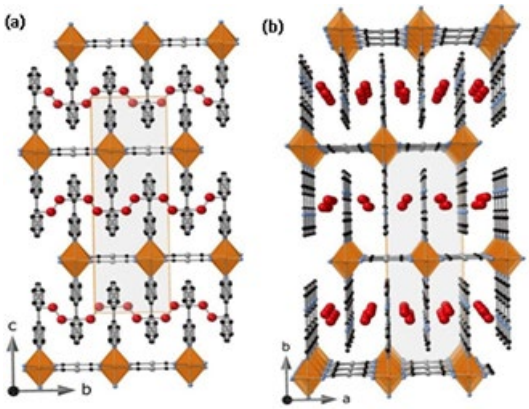

CAPÍTULO 5

Conclusiones finales

CAPÍTULO 5

CONCLUSIONES FINALES

Thermo- and photo-modulation of exciplex fluorescence in a 3D spin crossover Hofmann-type coordination polymer

En el capítulo 2 hemos sintetizado con éxito el primer polímero de coordinación 3D tipo Hofmann de Fe^{II} SCO-CP {Fe(bpben)[Au(CN)$_2$]}@pyr funcionalizado con pireno como invitado fluorescente. Las interacciones fuertes de tipo π-π entre el pireno y los pilares bpben de la red **pcu** SCO dan como resultado una emisión exciplex, además de la emision intrinseca del pireno (emisión del monómero). La fluorescencia tanto del monómero como del excímero dependen del estado de espín de los nodos Fe^{II}, que a su vez está controlado por la temperatura y la irradiación por luz (efecto LIESST), dando lugar a la conmutación ON-OFF de la señal luminiscente. Estos compuestos SCO-MOFs de tipo Hofmann con propiedades luminiscentes ofrecen nuevas posibilidades para diseñar e investigar dispositivos a micro y nanoescalas para la detección y el procesamiento de información. En este sentido, la incorporación de una fuente luminiscente en el ligando puente orgánico de la red es otra estrategia importante a explorar.

Extrinsic vs intrinsic luminescence and their interplay with spin crossover in 3D Hofmann-type coordination polymers

El capítulo 3 se ha llevado a cabo como un nuevo paso en el estudio de la interacción entre SCO y luminiscencia en polímeros de coordinación 3D tipo Hofmann. Hemos propuesto dos nuevos sistemas doblemente interpenetrados:

i) El polimero de coordinación poroso $\{Fe^{II}(bpb)[M^{I}(CN)_2]_2\}\cdot Pyr$ (**FebpbM·Pyr**) (M = Ag, Au) que exhibe fluorescencia intrínseca gracias a la molécula de pireno incluida en los poros, de forma similar a la descrita en el capítulo 2.

ii) El polimero de coordinación $\{Fe^{II}(bpan)[M^{I}(CN)_2]_2\}$ (**FebpanM**) (M = Ag, Au), en el cual la luminiscencia es incluida por primera vez como una función intrínseca del sistema SCO a través del ligando puente fluoróforo antraceno bpan.

El sistema **FebpbM·Pyr** muestra un SCO inducido térmicamente muy incompleto incluso a baja temperatura reflejando la aparicion de una frustración elástica entre las estructuras doblemente interpenetradas debido a las moléculas de pireno situadas en los espacios disponibles. Aparentemente, la interpenetración de las estructuras y el gran número las interacciones de corto alcance anfitrión⋯huésped y π⋯π influyen fuertemente en el SCO de este sistema.

Sin embargo, el sistema **FebpanM** (M = Ag, Au), muestra un comportamiento SCO prácticamente completo teniendo lugar en dos etapas muy distintas. La asimetría en las etapas se ha asociado con dos transformaciones consecutivas que rompen la simetría, causadas por el cambio de orientación (rotación) de los grupos antraceno del ligando bpan, un hecho necesario para la acomodación y estabilización de las distintas fracciones HS/LS del Fe^{II}.

La sinergia entre el SCO y la fluorescencia se ha investigado para los sistemas **FebpbM·Pyr** y **FebpanM** siendo comparable para cada familia de derivados de Ag y Au. Existe una correlación razonablemente buena entre el decrecimiento de la luminiscencia y el aumento/decrecimiento térmicamente controlado de la población de los centros LS/HS a través de la transferencia de energía radiativa, es decir, la emisión fluorescente del pyr es absorbida eficientemente por el Fe^{II} en el estado LS. Sin embargo, esta sinergia es mucho

más significante para **FebpbM·Pyr** debido a: i) la mayor proximidad de las moléculas de pireno a los centros de Fe^{II}, lo que también favorece una transferencia de energía no radiativa; y ii) interacciones de tipo π···π más eficientes y fuertes entre el pireno y el ligando bpb que incrementa la intensidad de la banda del excímero.

Las diferencias en el acoplamiento SCO-fluorescencia cuando se considera un compuesto luminiscente intrínseco o extrínseco de tipo Hofmann son difíciles de racionalizar porque incluso si el rendimiento cuántico de los luminóforos es similar (0.36 y 0.32 para antraceno y pireno respectivamente en ciclohexano) y la resistencia del oscilador de los aceptores es comparable, la sinergia depende en gran medida de la geometría de toda la estructura. En este sentido, la luminiscencia extrínseca obtenida a través de la inserción de diferentes moléculas fluorescentes invitadas como el pireno parece muy prometedora debido a la capacidad de controlar la geometría y, en consecuencia, las distancias invitado-invitado, invitado-ligando e invitado-Fe^{II}.

Enhanced Interplay between Host-Guest and Spin-Crossover Properties through the Introduction of an N Heteroatom in 2D Hofmann Clathrates

En el capítulo 4 se describen las propiedades invitado-dependencia estructural y SCO de los clatratos isomorfos 2D tipo Hofmann $\{Fe(4\text{-}PhPy)_2[M(CN)_4]\}$ (**PhPyM**) y $\{Fe(2,4\text{-}Bipy)_2[M(CN)_4]\}$ (**BipyM**) (M = Pd, Pt). Nuestros resultados indican que, aunque la única diferencia entre ambas familias de compuestos se deriva de la presencia/ausencia de un heteroátomo N no coordinado en los ligandos axiales (4-Phpy)/(2,4-Bipy), esta sutil diferencia en la composición química impacta profundamente no solo en la capacidad de adsorción del polímero de coordinación resultante, sino también en el grado en que el SCO se modula tras la captación de invitados. Así, mientras que la adsorción de H_2O en **BipyM** es rápida y espontánea en condiciones ambientales, se produce en muy baja medida para **PhPyM,** incluso cuando se empapa en H_2O. La fuerza motriz de la mayor afinidad por el H_2O del primero se atribuye necesariamente a los enlaces de hidrógeno establecidos entre la molécula de H_2O y el heteroátomo N no coordinado del 2,4-Bipy en **BipyM.** Estas interacciones inducen la apertura de canales entre capas a lo largo de los cuales se

acomodan las moléculas de H_2O, lo que lleva a estructuras en capas regulares y homogéneas. La adsorción de H_2O en **BipyM** provoca un aumento notable de las temperaturas de SCO (en 50-60 K), desplazando la anchura de los bucles de histéresis alrededor de temperatura ambiente. Este desplazamiento del SCO se ha correlacionado con una combinación de factores estructurales y electrónicos. Por el contrario, la pequeña cantidad de H_2O adsorbida por **PhPyM** marginalmente influye en la temperatura de SCO, probablemente debido a un efecto sutil de frustración elástica. Además, aunque las moléculas de MeOH son absorbidas eficientemente en solución por ambas series de compuestos que conducen a redes en capas distorsionadas, las repulsiones estéricas entre las moléculas de MeOH y la red huésped están detrás de su rápida desorción bajo una atmósfera ambiental. Este factor estérico también proporciona frustración elástica al sistema porque las propiedades SCO de ambas familias de compuestos se desactivan cuando se empapan en MeOH. Este estudio comparativo arroja luz sobre cómo el ajuste de la red huésped modifica en gran medida el acoplamiento entre las propiedades anfitrión-invitado y SCO, y contribuye a allanar el camino hacia la aplicación de estos materiales como sensores químicos.

CAPÍTULO 5

CONCLUSIONS

Thermo- and photo-modulation of exciplex fluorescence in a 3D spin crossover Hofmann-type coordination polymer

In chapter two we have successfully synthesized the unprecedented 3D Hofmann-type Fe^{II} SCO-CP {Fe(bpben)[Au(CN)$_2$]}@pyr functionalized with pyrene as a fluorescent guest. Strong π-π interactions between pyrene and the bpben pillars of the **pcu** SCO framework result in an exciplex emission, in addition to the intrinsic emission of pyrene (monomer emission). Both monomer and exciplex fluorescence are dependent on the spin state of the Fe^{II} nodes which in turn is controlled by temperature and light irradiation (LIESST effect), thereby resulting in ON-OFF switching of the luminescent signal. Implementing the prolific family of Hofmann-type SCO-MOFs with luminescence properties offers new opportunities for designing and probing devices at micro- and nano-scales for sensing and information processing. In this sense, incorporation of a luminescent source in the pillars of the framework is a further desired step.

Extrinsic vs intrinsic luminescence and their interplay with spin crossover in 3D Hofmann-type coordination polymers

Chapter three has been undertaken as a further step in the study of the interplay between SCO and luminescence in 3D Hofmann-type coordination polymers. We have proposed two new double-interpenetrated systems:

i) The porous coordination polymers $\{Fe^{II}(bpb)[M^{I}(CN)_2]_2\}\cdot Pyr$ (**FebpbM·Pyr**) (M = Ag, Au) that exhibit extrinsic fluorescence thanks to the pyrene molecule included in the pores, in a similar way as it has been described in chapter 2.

ii) The coordination polymers $\{Fe^{II}(bpan)[M^{I}(CN)_2]_2\}$ (**FebpanM**) (M = Ag, Au), in which for the first-time luminescence is included as an intrinsic function of the SCO framework through the anthracene fluorophore moiety of the bridging ligand bpan.

The system **FebpbM·Pyr** displays a very incomplete thermal induced SCO event at low temperature reflecting the occurrence of elastic frustration between the two-fold interpenetrated frameworks mediated by the pyrene molecules docked in the available spaces. Apparently, the interpenetration of the frameworks and the large number of host···guest π···π short-range interactions strongly influence the SCO of this system.

However, the system **FebpanM** (M = Ag, Au), displays a practically complete SCO behavior taking place in two strongly asymmetric stepped transitions. The asymmetry in the steps has been associated with two consecutive symmetry-breaking transformations caused by the change in orientation (rotation) of the anthracene groups of the bpan ligand, a fact required to accommodate and stabilize the distinct HS/LS Fe^{II} fractions.

The synergy between the SCO and fluorescence has been investigated for the sytems **FebpbM·Pyr** and **FebpanM** being comparable within each family for the Ag and Au derivatives. There is a reasonably good correlation between the decrease of luminescence and the thermally controlled increase/decrease of population of the LS/HS centers via radiative energy transfer, namely the fluorescent emission of pyr is effectively absorbed by the Fe^{II} inLS state. However, this synergy is much more significant for **FebpbM·Pyr** due to: i) the close proximity of the pyrene molecule to the Fe^{II} centers, which also favors a non-radiative transfer of energy; and ii) the more efficient and stronger π···π interactions between pyrene and the bpb ligand that increases the intensity of the excimer band.

The differences in the SCO-fluorescence coupling when considering either an intrinsic or an extrinsic luminescent 3D Hofmann-type compound are difficult to rationalize because even if the quantum yield of the luminophores is similar (0.36 and 0.32 for anthracene and pyrene respectively in cyclohexane) and the oscillator strength of the acceptors are comparable, the synergy strongly depends on the geometry of the whole arrangement. In this sense, the extrinsic luminescence obtained through the insertion of different guest fluorescent

molecules such as pyrene seems very promising due to the capacity of controlling the geometry and, in consequence, the guest–guest, guest–ligand and guest–Fe^{II} distances.

Enhanced Interplay between Host-Guest and Spin-Crossover Properties through the Introduction of an N Heteroatom in 2D Hofmann Clathrates

Chapter four describe the guest-dependent structural and SCO properties of the isomorphous 2D Hofmann CPs $\{Fe(4\text{-}PhPy)_2[M(CN)_4]\}$ (**PhPyM**) and $\{Fe(2,4\text{-}Bipy)_2[M(CN)_4]\}$ (**BipyM**) (M = Pd, Pt). Our results indicate that, although the sole difference between both families of compounds stems from the presence/absence of a non-coordinated N heteroatom in the axial ligands (4-Phpy)/(2,4-Bipy), this subtle difference in chemical composition deeply impacts not only the adsorption capability of the resulting coordination polymer but also the degree to which the SCO is modulated upon guest uptake. Thus, whereas the adsorption of H_2O in **BipyM** is rapid and spontaneous at ambient conditions, it occurs to a very low extent for **PhPyM**, even when soaked in H_2O. The driving force of the higher H_2O affinity of the former is necessarily ascribed to the hydrogen bonds established between the H_2O molecule and the noncoordinated N heteroatom of the 2,4-Bipy in **BipyM.** These interactions induce the opening of interlayer channels along which the H_2O molecules are accommodated, leading to regular and homogeneous layered structures. The uptake of H_2O in **BipyM** provokes a remarkable increase of the SCO temperatures (by 50−60 K), shifting the wide hysteresis loops at around room temperature. This SCO shift has been correlated with a combination of structural and electronic factors. In contrast, the small amount of H_2O adsorbed by **PhPyM** marginally influences the SCO temperature, likely due to subtle elastic frustration effects. Besides, although MeOH molecules are efficiently absorbed in solution by both series of compounds leading to distorted layered networks, steric repulsions between the MeOH molecules and host network are behind its rapid desorption under an ambient atmosphere. This steric factor also provides elastic frustration to the system because the SCO properties of both families of compounds are deactivated when soaked in MeOH. This comparative study sheds light on how fine-tuning the host framework greatly modifies the coupling between

host−guest and SCO properties and contributes to paving the way toward the application of these materials as chemical sensors.

Apéndice

Chemical Science

EDGE ARTICLE

View Article Online
View Journal | View Issue

Open Access Article. Published on 11 September 2018. Downloaded on 12/20/2019 3:04:47 PM.
This article is licensed under a Creative Commons Attribution-NonCommercial 3.0 Unported Licence.

Check for updates

Cite this: *Chem. Sci.*, 2018, **9**, 8446

All publication charges for this article have been paid for by the Royal Society of Chemistry

Thermo- and photo-modulation of exciplex fluorescence in a 3D spin crossover Hofmann-type coordination polymer†

Teresa Delgado,‡[a] Manuel Meneses-Sánchez,‡[b] Lucía Piñeiro-López,[b] Carlos Bartual-Murgui,[b] M. Carmen Muñoz[c] and José Antonio Real *[b]

The search for bifunctional materials showing synergies between spin crossover (SCO) and luminescence has attracted substantial interest since they could be promising platforms for new switching electronic and optical technologies. In this context, we present the first three-dimensional Fe^{II} Hofmann-type coordination polymer exhibiting SCO properties and luminescence. The complex $\{Fe^{II}(bpben)[Au(CN)_2]\}$@pyr (bpben = 1,4-bis(4-pyridyl)benzene) functionalized with pyrene (pyr) guests undergoes a cooperative multi-step SCO, which has been investigated by single crystal X-ray diffraction, single crystal UV-Vis absorption spectroscopy, and magnetic and calorimetric measurements. The resulting fluorescence from pyrene and exciplex emissions are controlled by the thermal and light irradiation (LIESST effect) dependence of the high/low-spin state population of Fe^{II}. Conversely, the SCO can be tracked by monitoring the fluorescence emission. This ON–OFF interplay between SCO and luminescence combined with the amenability of Hofmann-type materials to be processed at the nano-scale may be relevant for the generation of SCO-based sensors, actuators and spintronic devices.

Received 18th June 2018
Accepted 7th September 2018

DOI: 10.1039/c8sc02677g

rsc.li/chemical-science

Introduction

Iron(II) spin crossover (SCO) complexes are responsive materials that switch between high-spin (HS) and low-spin (LS) states triggered by external stimuli (temperature, pressure, light, and analytes). This binary HS ↔ LS behaviour entails strong electron–phonon coupling that involves drastic changes in the magnetic, electric, optical and mechanical properties of the SCO material when cooperative elastic interactions between the SCO centres are effective.[1] Cooperative SCO properties have attracted substantial interest specially when combined in a synergistic way with other relevant physical properties (*i.e.* electronic transport, chirality, luminescence, host–guest chemistry, *etc*) because the intrinsic ON–OFF nature of SCO may be transferred to the second property. This fact, together with the amenability of the resulting functional material to be processed at micro- and nano-scale levels, has created important expectations for the discovery of new switching electronic and optical technologies.[2]

Luminescence is a relevant property that may be used as an internal probe to report upon the spin state of SCO centres and conversely the control of the spin state may be used to modulate the luminescent signal. In this respect, it has been stated that the search for synergies between SCO and luminescence could be an important platform for thermometry and thermal imaging technologies.[3] Although, the interplay between SCO and luminescence was first reported 20 years ago,[4] it has been more recently that this binomial has gained much attention. Two main approaches have been designed to combine SCO and fluorescence in the same material. A first approach introduces fluorescence as an extrinsic property by physically doping the targeted SCO complex with a fluorescent dye during the fabrication of thin films or nanoparticles.[5–10] In the second approach, luminescence is an intrinsic property of the SCO complex. Only a reduced number of examples of this second approach have been reported so far, which include discrete mononuclear[11–14] homodinuclear,[15] heterodinuclear Fe^{II}–Eu^{III},[4] heterotrinuclear Fe^{II}–Pt^{II},[16] and two 1-D coordination polymers.[17,18]

Hofmann-type Fe^{II} SCO coordination polymers (SCO-CP)[19,20] have afforded excellent examples of thermo-[21] and piezo-hysteretic behaviours,[22] multistep cooperative transitions,[23] relevant examples of porous systems where the SCO can be tuned by guest molecules favouring selective host–guest interactions,[24] post-synthetic chemical activity[25] and/or solid-state

[a]Départment de Chimie Physique, Université de Genève, Rue Ernest Ansermet, 30, 1211 Genève, Switzerland

[b]Departament de Química Inorgánica, Institut de Ciència Molecular (ICMol), Universitat de València, Catedrático José Beltrán Martínez, 2, 46980 Paterna, Spain

[c]Departamento de Física Aplicada, Universitat Politècnica de València, Camino de Vera s/n, 46022 Valencia, Spain

† Electronic supplementary information (ESI) available: Experimental information, and synthesis and characterisation of materials (PDF). CCDC 1847351–1847353 & 1862017. For ESI and crystallographic data in CIF or other electronic format see DOI: 10.1039/c8sc02677g

‡ These authors contributed equally.

This journal is © The Royal Society of Chemistry 2018

Open Access Article. Published on 11 September 2018. Downloaded on 12/20/2019 3:04:47 PM.
This article is licensed under a Creative Commons Attribution-NonCommercial 3.0 Unported Licence.

transformations.[26] In addition, they have demonstrated to be excellent platforms to investigate the SCO properties at the nano-scale (nanocrystals and thin films) as potential components for the generation of SCO-based sensors, actuators and spintronic devices.[27] In this context, and as a result of our systematic study on Hofmann-type Fe^{II} SCO-CP,[19] here we report on the thermo- and photo-induced multi-stable spin transition of a pyrene based 3-D Hofmann clathrate monitored by photoluminescence and on the corresponding thermo- and photo-modulation of the exciplex fluorescence emission. This study has been carried out based on single crystal UV-Vis absorption spectroscopy measurements, X-ray single crystal analysis at relevant temperatures and magnetic, photo-magnetic and calorimetric measurements on microcrystalline samples of the SCO-MOF $\{Fe^{II}(bpben)[Au(CN)_2]\}$@pyr [**1Fe@pyr**] (bpben = 1,4-bis(4-pyridyl)benzene; pyr = pyrene). For comparative reasons the homologous isostructural Zn^{II} derivative **1Zn@pyr** was also synthesised and characterised and herein reported. As far as we know this is the first SCO-CP implemented with luminescence properties.

Results and discussion

Synthesis and structure

Pale-yellow (**1Fe@pyr**) or white (**1Zn@pyr**) crystalline samples were obtained by slow diffusion methods from stoichiometric amounts of $M^{II}(BF_4)_2\cdot 6H_2O$ (M^{II} = Fe, Zn), bpben and $K[Au(CN)_2]$ and an excess of pyrene dissolved in methanol (see the ESI†).

Single crystal structure analysis of **1Fe@pyr** and **1Zn@pyr** at 120 and 280 K showed the non-centrosymmetric monoclinic space group *Cc*. Crystal data and structural parameters are given in Tables S1–S3 in the ESI.†

There are two crystallographically distinct octahedral $[M^{II}N_6]$ sites constituted of 4 equatorial $[Au(CN)_2]^-$ groups and 2 axial bpben ligands (Fig. S1†). The almost linear $[Au(CN)_2]^-$ groups bridge 4 equivalent $[M^{II}N_6]$ sites forming parallel stacks of $\{M_4^{II}[Au(CN)_2]_4\}_n$ 2D grids pillared by the bpben ligands, thus generating an open framework with **pcu** topology (Fig. 1). The wide $\{M_4^{II}[Au(CN)_2]_4\}$ windows allow interpenetration of an identical framework made up of the other crystallographically independent $[M^{II}N_6]$ site (Fig. 1). This type of structure is common for $\{Fe^{II}(L)[Au(CN)_2]\}$ SCO compounds where L is a bis-monodentate pyridine-type ligand.[19,20]

The two frameworks are held together by strong Au···Au interactions [average 3.0535(5) Å for **1Fe@pyr** and 3.1086(9) Å for **1Zn@pyr** at 120 K]. The average Fe–N bond length equal to 1.960 Å at 120 K and 2.154 Å at 280 K are typical of the Fe^{II} ion in the LS and HS states, respectively. Thus, the average bond length variation associated with the spin-state change, 0.2 Å, is consistent with the occurrence of a complete LS ↔ HS conversion. This is in turn reflected in a change of the unit cell volume of 444.7 $Å^3$, which represents 6.7% of the HS unit cell volume or a volume change of 55.6 $Å^3$ per Fe^{II} upon SCO. This is a typical value observed for Hofmann clathrates.[19] It is worth noting that, in the same interval of temperatures, a unit cell volume variation of 1% (68.4 $Å^3$) is observed for **1Zn@pyr**, which

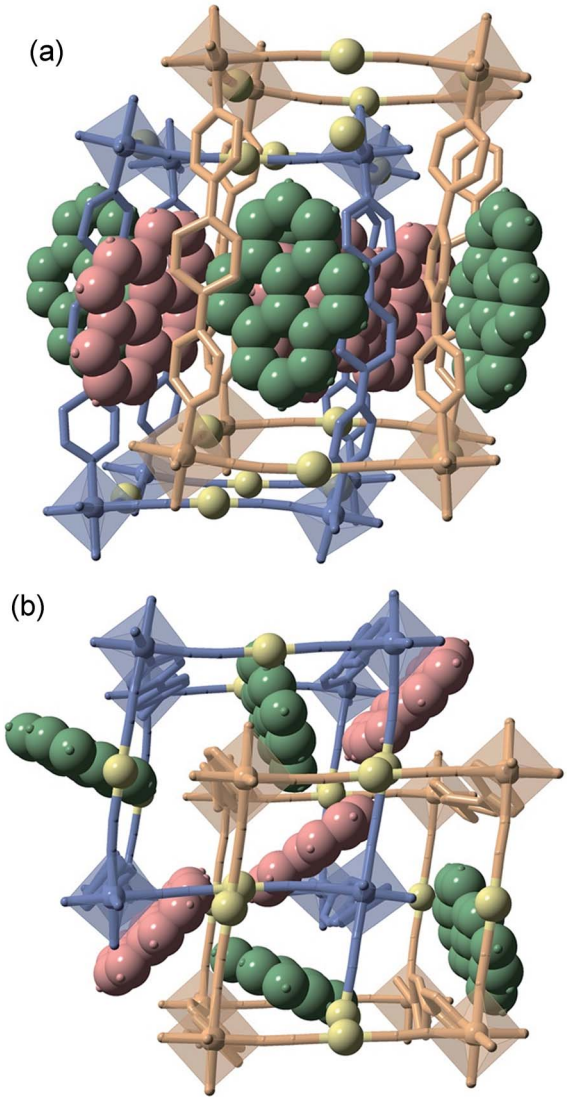

Fig. 1 Two perpendicular perspective views ((a) side view and (b) top view) of the same fragment of the doubly interpenetrated frameworks **1M@pyr** (M^{II} = Fe, Zn) showing the bpben pillars, coordination centres and pyrene units. The two crystallographically distinct frameworks are represented in blue (network 1) and beige (network 2) colours, while the different pyrene molecules are depicted in red (pyr1) and green (pyr2) colours. Au centres are yellow spheres.

essentially corresponds to thermal contraction/expansion of the crystal in the temperature interval 280–120 K where the average Zn^{II}–N bond length remains practically constant at *ca.* 2.145 Å.

The available space generated by the two interpenetrating frameworks is filled by two crystallographically independent pyr guest molecules that do not interact significantly with each other. In contrast, they define a large number of short π–π interactions with the bpben ligands (Fig. 2 and Table S4†). The number and strength of these interactions are unequally distributed in each framework. The bpben1 pillars attached to the $[Fe_1N_6]$ nodes (blue colour, Fig. 1 and 2) define with the corresponding pyr1 guests (red colour) a face-to-face type interaction with 22 short C···C contacts smaller than the sum of the van der Waals radius (*ca.* 3.7 Å) ranging in the interval

Open Access Article. Published on 11 September 2018. Downloaded on 12/20/2019 3:04:47 PM.
This article is licensed under a Creative Commons Attribution-NonCommercial 3.0 Unported Licence.

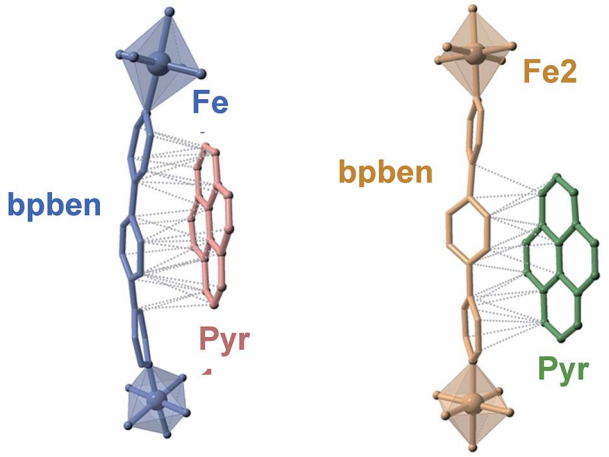

Fig. 2 Crystallographically different bpben-pyrene pairs found in **1Fe@pyr** displaying the intermolecular π–π interactions (dotted lines) between bpben and pyrene (only short π–π contacts smaller than the sum of the C···C van der Waals radius *ca.* 3.7 Å are shown).

[3.44–3.68 Å] at 280 K (Table S4, Fig. S2†). They markedly increase in number, up to 37 C···C contacts [3.30–3.66 Å], in the LS structure at 120 K (Fig. 2). It is worth noting that this increase in short π–π interactions occurs synchronically with a small in-plane rotation of the pyr1 by *ca.* 6.1° (Fig. S2†). In contrast, 22 [3.32–3.69 Å] and 12 [3.42–3.68 Å] short C···C contacts at 120 K and 280 K, respectively, are found between the bpben2 pillars attached to the $[Fe_2N_6]$ nodes (beige colour, Fig. 1 and 2) and the corresponding pyr2 (green colour). This *ca.* 50% decrease of C···C interactions is due to parallel-displaced π–π interactions in the latter. Although similar considerations can be made for **1Zn@pyr**, the larger ionic radius of Zn^{II} with respect to Fe^{II}-LS is reflected in a slight reduction in the number of π–π interactions (Table S4-bis, Fig. S2†).

A direct consequence of these strong π–π interactions is the bent geometry adopted by the bpben ligands. A similar situation was described for the SCO Hofmann clathrates $\{Fe(bpb)[M^{II}(CN)_4]\}\cdot 2G$, where the related rod-like bridging ligand bis(4-pyridyl)butadiyne (bpb) is markedly bent due to strong intermolecular interactions established with G = naphthalene or nitrobenzene molecules.[28] For the titular compounds, we have estimated the magnitude of the bent in bpben measuring the distance of the pyridyl N atoms to the average plane defined by the central benzene ring (see Table S5a and Scheme I†). It is important to note that the bent, and consequently the distance to the average plane, is larger for bpben1 than for bpben2 due to the larger number and more direct π–π interactions with pyr in the former. In addition to this, the pyridyl groups are slightly rotated with respect to the central benzene ring (Table S5b†). Both, the bent distortion and the angles defined by the intersection of the benzene and pyridyl rings do not change significantly upon the spin state change of Fe^{II}. Furthermore, these distances and angles are consistent with those found for **1Zn@pyr**. It is worth mentioning that the bent geometry found for the bpben pillars in the titular compounds strongly contrasts with the linear structure described previously for the solvate $[Fe(bpben)\{Au(CN)_2\}_2]\cdot S$ with $S = 1.5DMF\cdot 0.3EtOH\cdot 0.2C_6H_{12}l$.[29]

Spin crossover behaviour

Magnetic, photo-magnetic and calorimetric studies. The SCO was followed by magnetic measurements on bulk samples in the temperature interval 10–300 K (Fig. 3). At room temperature, the $\chi_M T$ product (χ_M = molar magnetic susceptibility and T = temperature) equal to 3.64 cm^3 K mol^{-1} is consistent with the Fe^{II} ion in the HS state. On cooling at a temperature scan rate of 1 K min^{-1}, $\chi_M T$ drops abruptly between 250 and 160 K, in three consecutive steps centred at 227, 195 and 180 K, to 0.14 cm^3 K mol^{-1} indicating a practically complete transformation to the LS state. In the heating mode, the magnetic curve does not match the cooling curve showing the presence of hysteresis in the second and third steps *ca.* 5 K wide. The overall equilibrium temperature, $T_{1/2}$, at which the HS and LS molar fractions are equal to 0.5 ($\gamma_{HS} = \gamma_{LS} = 0.5$; $\Delta G = 0$) is estimated to be centred at 190 K. This multi-step SCO behaviour is reminiscent of the one previously observed for the homologue solvate $[Fe(bpben)\{Au(CN)_2\}_2]\cdot S$ with S = 0.9 benzene, which undergoes a less steep three-step conversion centred at 214 K, 155 K and 141 K.[29] The occurrence of multi-step SCO is a relatively uncommon event in SCO that results from a competition between ferro- and antiferro-elastic interactions driven by the difference of volume associated with the LS and HS centres.[30] The steps involve stabilization of states characterized by different commensurate and/or incommensurate ordered fractional distributions of the HS/LS sites that often require symmetry breaking and that dramatically depend on subtle structural changes of the solid, which are difficult to control.[31]

Irradiation of the sample with red light (λ = 633 nm) at 10 K photo-generates the metastable HS* state (light induced excited spin state trapping (LIESST),[32] see the green line in Fig. 3).

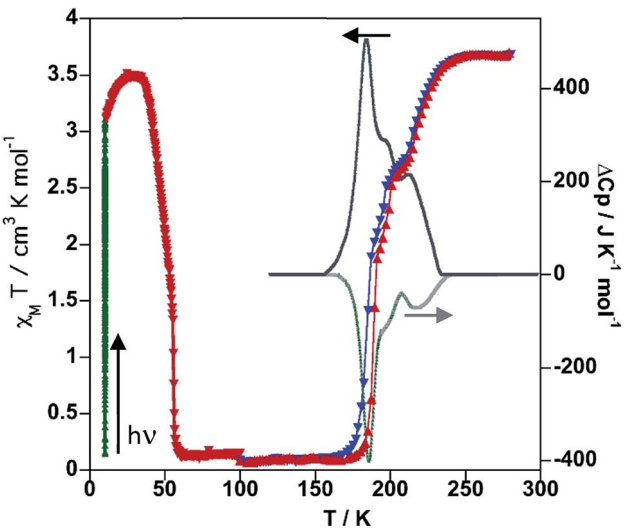

Fig. 3 Magnetic, photomagnetic and calorimetric properties of **1Fe@pyr**. Blue down triangles and red up triangles refer to cooling and heating modes, respectively. Green triangles show the increase of $\chi_M T$ upon irradiation at 10 K (LIESST effect), and red down triangles correspond to the heating from 10 K at 0.3 K min^{-1} to determine the T_{LIESST} temperature. Grey curves correspond to the anomalous variations of the molar specific heat C_p caused by the SCO for the cooling and heating modes.

Open Access Article. Published on 11 September 2018. Downloaded on 12/20/2019 3:04:47 PM.
This article is licensed under a Creative Commons Attribution-NonCommercial 3.0 Unported Licence.

The subsequent heating at 0.3 K min^{-1} in the dark shows an increase of $\chi_M T$, associated with the zero-field splitting of the S = 2 HS state of Fe^{II}, reaching a maximum value of 3.50 cm^3 K mol^{-1} in the temperature range 24–34 K, which suggests a quantitative population of the HS* state. Upon further heating the HS* relaxes back in two steps to the LS state with a characteristic $T_{LIESST} \approx 50$ K.[33]

The thermodynamic parameters obtained from differential scanning calorimetry were consistent with the $\chi_M T$ *vs.* T plot (grey lines in Fig. 3). The average enthalpy and entropy variations $\Delta H = 10.9$ kJ mol^{-1} and $\Delta S = 56$ J K^{-1} mol^{-1} are typical of Fe^{II} SCO compounds.

Single crystal UV-Vis spectra. 1Fe@pyr displays a reversible thermo-chromic change between pale-yellow (HS) and red (LS). Consequently, the SCO behaviour was monitored on a single crystal through UV-Vis absorption spectra in the temperature range 300–10 K (cooling and heating modes) with temperature scan rates of 1 and 5 K min^{-1} while recording the spectra every 1 and 5 min (see Fig. 4a, S3 and S4,† respectively). When cooling from 300 K to 10 K, the band centred at 800 nm associated with the HS state bleaches while a new band attributed to the LS state arises centred at 532 nm when cooling to 10 K. Considering the thickness of the crystal, 50 ± 1 μm, and a concentration of Fe of around 1.6 M, a typical value of ferrous spin crossover systems, an extinction coefficient, ε, equal to 7 and 125 M^{-1} cm^{-1} was found, respectively, for the 800 and 532 nm bands. These values are consistent with the d–d transitions $^5T_2 \rightarrow {}^5E$ and $^1A_1 \rightarrow {}^1T_1$ characteristic of the HS and LS states of Fe^{II}, respectively.

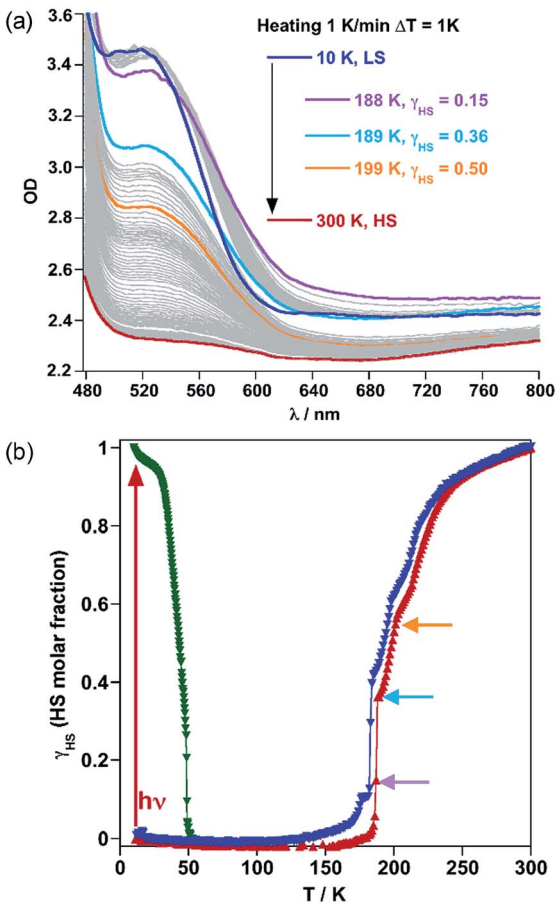

Fig. 4 SCO properties of **1Fe@pyr** monitored by using single crystal UV-Vis spectra: (a) temperature variable UV-Vis absorption spectrum in the cooling mode and (b) HS molar fraction of the thermal and light induced SCO.

Following the optical density difference between the maximum of the LS band at 532 nm and the tail of this band at 650 nm, the evolution of the HS molar fraction (γ_{HS}) with temperature was stablished by using Vergard's law (eqn (1)).

$$\gamma_{HS} = (OD_{LS} - OD_T)/(OD_{LS} - OD_{HS}), \quad (1)$$

where OD_{LS} is the optical density of the LS state, OD_{HS} is the optical density of the HS state at 300 K and OD_T is the optical density at a given temperature. The optical density (OD) is corrected from an eventual baseline jump or shift by taking the difference between the OD at 532 nm and the OD at 650 nm, where there is no noticeable absorption in the two states. The resulting SCO profile displays three main steps centred at 230, 195 and 184 K (Fig. 4b). Irradiation of the crystal with green light (λ = 532 nm) at 10 K quantitatively photo-generates the metastable HS* state. The thermal stability of HS* was examined following the spectra when heating the crystal in the dark at 0.3 K min^{-1} from 10 to 60 K (Fig. 4b and S5†). The thermal relaxation HS* → LS was characterized by a $T_{LIESST} = 45$ K. Both, thermal- and photo-induced SCO behaviours agree reasonably well with the complementary magnetic measurements.

Synergy between fluorescence and spin crossover

The crystal structure of **1Fe@pyr** reveals that the pyr guest molecules and bpben bridging ligands lie in an environment that is fully consistent to afford exciplex emission through π–π interactions.[34] Consistently with this, the excitation spectrum recorded at room temperature at 520 nm, shows a set of four different main bands, two of them highly resolved and centred at 254 and 332 nm. The other two bands are rather broad and centred at around 350 and 400 nm. Likewise, the emission spectrum of the sample has been recorded between 350 and 700 nm after excitation at 332 nm (Fig. S6†). The two characteristic bands of the monomer and excimer of pyrene are centred at 400 and 500 nm, respectively. In order to study the influence of the thermal spin transition on the luminescence properties, the sample was cooled down to 10 K at 5 K min^{-1} and the luminescence spectra were recorded in the cooling and heating modes (Fig. 5a and S7†). Upon cooling to 190 K from room temperature, the intensity of both peaks, excimer and monomer, slightly increases whereas with further cooling in the region of the spin transition at around 235–155 K the intensity of the monomer signal increases significantly concomitantly with the quenching of the excimer's signal (Fig. 5a). The thermal dependence of fluorescence for the non-SCO isostructural compound **1Zn@pyr** after excitation at 332 nm shows two main maxima centred at 439 and 484 nm (Fig. 5b), whose intensity does not change significantly in the 235–155 K interval where **1Fe@pyr** displays the SCO behaviour (see Fig. 5c). Clearly the spin transition properties of **1Fe@pyr** have a strong influence on the photoluminescence properties. This observation is

Open Access Article. Published on 11 September 2018. Downloaded on 12/20/2019 3:04:47 PM.
This article is licensed under a Creative Commons Attribution-NonCommercial 3.0 Unported Licence.

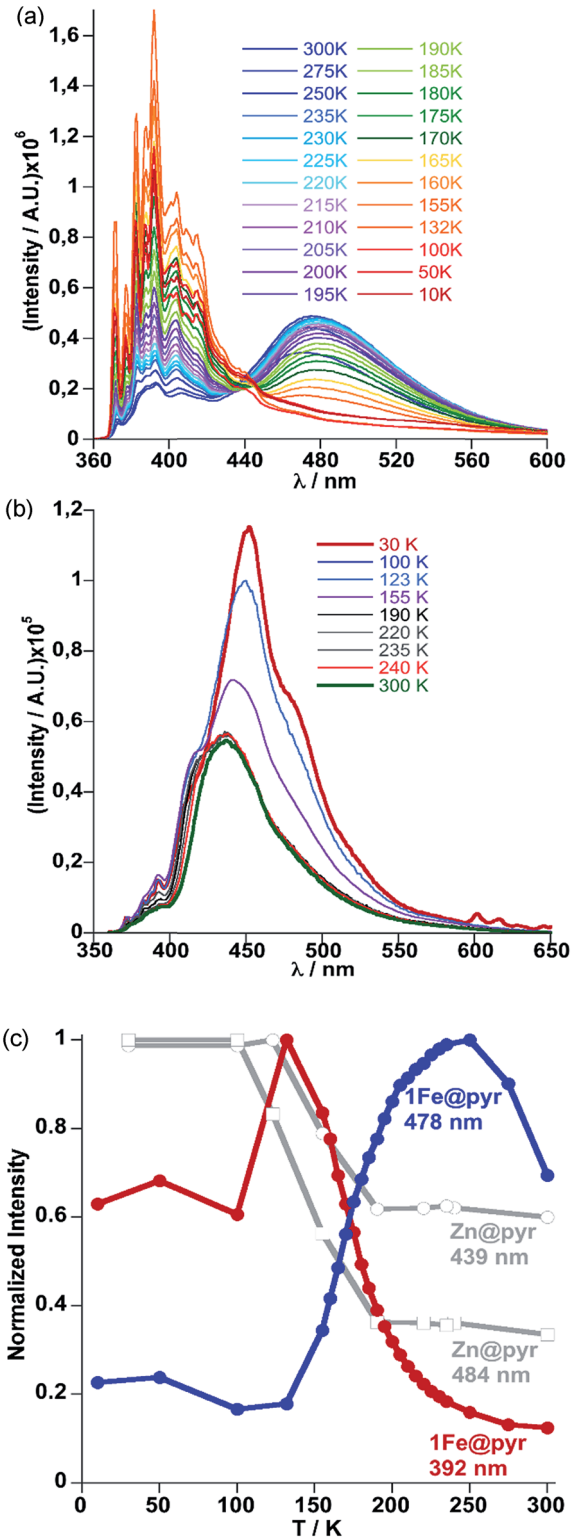

Fig. 5 (a) Evolution of fluorescence spectra with temperature upon cooling from 300 K to 10 K at 5 K min^{-1} for **1Fe@pyr**. (b) Evolution of the luminescence spectra with temperature upon cooling from 300 K to 10 K at 5 K min^{-1} for **1Zn@pyr**. (c) Thermal dependence of normalized intensity of the monomer and excimer signals at 392 nm (red) and 478 nm (blue) for **1Fe@pyr** and 439 nm and 484 nm (grey) for **1Zn@pyr**.

directly related to the absorption properties of the compound and the emission properties of the pyrene. The arising of the LS absorption band at 532 nm (Fig. 4a) upon cooling quenches the emission of the excimer signal of pyrene at 478 nm (Fig. 5a) due to the radiative energy transfer (emission–reabsorption) from the excited state of the pyrene to the MLCT-3d ($^1A_1 \rightarrow {}^1T_1$) band of the Fe^{II} complex in the LS state. The signal at 392 nm, that abruptly increases below the spin transition, overlaps with the MLCT-3d ($^1A_1 \rightarrow {}^1T_1$) transition band of the compound at any temperature. From the ratio between the intensity at 392 nm and 478 nm while heating and cooling at 5 K min^{-1} the thermal evolution of the normalized HS molar fraction $(\gamma_{HS})^{norm}$ has been obtained. The thermal spin transition stablished based on the luminescence properties of **1Fe@pyr** follows reasonably well the SCO profile obtained by absorption spectroscopy and magnetic measurements (Fig. 6). The differences observed, particularly at low temperatures, can be ascribed, on one hand, to the much more rapid temperature scan rate used for recording the SCO by luminescence and, on the other hand, to the difficulties to separate the increasing signal of the monomer emission from that of the exciplex as temperature decreases. In spite of this, the average equilibrium temperature at which $(\gamma_{HS})^{norm} = 0.5$, $T_{1/2} = 189.5$ K, centred in the middle of a hysteresis loop *ca.* 5 K wide, is virtually the same as that observed from magnetism and absorption spectroscopy. In a recent study, likely inspired by the complex $[Fe(abpt)_2(NCS)_2]$ with abpt = 4-amino-3,5-bis(pyridine-2-yl)-1,2,4-triazole,[35] pyrene was covalently coupled by condensation of 1-pyrenecarboxaldehyde with abpt to afford (pyrene-1-yl)-*N*-(3,5-di(pyridin-2-yl)-4*H*-1,2,4-triazol-4-yl)methanimine (L).[14] The resulting $[Fe(L)_2(NCS)_2]$ compound undergoes a SCO in the interval 200–350 K with $T_{1/2} = 267$ K. The pyrene moieties interact with each other defining four face-to-face π–π interactions (3.66–3.85 Å). The lack of exciplex emission well separated from the intrinsic emission of pyrene moieties precluded from delineating a neat correlation between the thermal SCO and fluorescence profiles in this compound. However, the obvious differences observed in the temperature dependence of fluorescence between $[Fe(L)_2(NCS)_2]$ and the free ligand L,

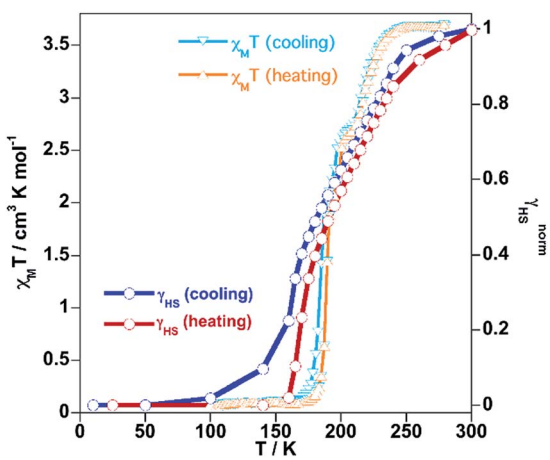

Fig. 6 Comparison of the SCO profiles obtained from magnetism and fluorescence for **1Fe@pyr**.

Open Access Article. Published on 11 September 2018. Downloaded on 12/20/2019 3:04:47 PM.
This article is licensed under a Creative Commons Attribution-NonCommercial 3.0 Unported Licence.

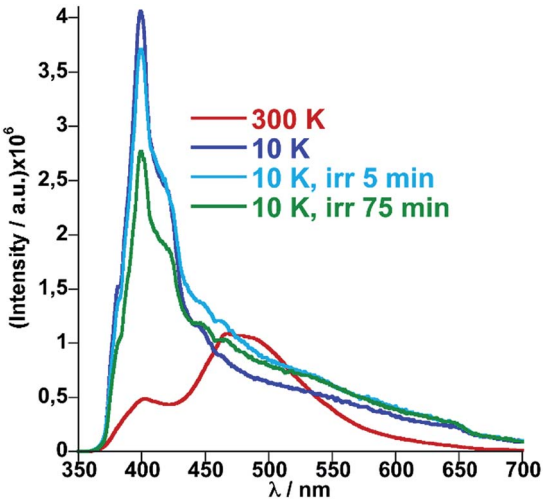

Fig. 7 Fluorescence spectra of **1Fe@pyr** at 10 K before and after irradiation at 520 nm.

associated with a resonance energy transfer process similar to that observed for **1Fe@pyr**, made possible to infer a clear influence of the SCO on the fluorescence. In particular, the partial population (*ca.* 21%) of the photo-generated HS* LIESST state of $[Fe(L)_2(NCS)_2]$ at 10 K also demonstrates this influence on the fluorescence.

Similarly, photo-excitation of the titular compound **1Fe@pyr** from LS to HS* (LIESST effect) has been preliminary followed by luminescence. In Fig. 7 the fluorescence spectra at 10 K before and after irradiation of the sample at 520 nm at two different irradiation times are compared. Interestingly, the fluorescence of the monomer decreases concomitantly with an increase of the excimer signal due to the excitation of the LS state into the metastable HS* state. In this sense, further analysis could be performed in order to study the cooperativity of the system thought LIESST and HS to LS relaxations at low temperature by taking advantage of the photoluminescence properties of pyrene.

Conclusions

In summary, we have successfully synthesized an unprecedented 3D Hofmann-type Fe^{II} SCO-CP functionalized with pyrene as a fluorescent guest. Strong π–π interactions between pyrene and the pillars of the **pcu** SCO framework result in exciplex emission. Both monomer and exciplex fluorescence are dependent on the spin state of the Fe^{II} nodes which in turn is controlled by temperature and light irradiation (LIESST effect), thereby resulting in ON–OFF switching of the luminescent signal. Implementing the prolific family of Hofmann-type SCO-MOFs with luminescence properties offers new opportunities for designing and probing devices at micro- and nano-scales for sensing and information processing. In this sense, incorporation of a luminescent source in the pillars of the framework is a further desired step. Our preliminary results in this direction are very promising and will be reported elsewhere in due course.

Conflicts of interest

There are no conflicts to declare.

Acknowledgements

This work was supported by the Spanish Ministerio de Economia y Competitividad (MINECO), FEDER (CTQ2013-46275-P and CTQ2016-78341-P), Unidad de Excelencia María de Maeztu (MDM-2015-0538), Generalitat Valenciana (PROMETEO/2016/147) and the Swiss National Science Foundation (Project number 200021-169033).

Notes and references

1 See for example:(*a*) *Spin Crossover in Transition Metal Compounds I-III. Top. Curr. Chem.*, P. Gütlich and H. A. Goodwin, 2004, vol. 233–235; (*b*) J. A. Real, A. B. Gaspar and M. C. Muñoz, *Dalton Trans.*, 2005, 2062; (*c*) A. Bousseksou, G. Molnár, L. Salmon and W. Nicolazzi, *Chem. Soc. Rev.*, 2011, **40**, 3313; (*d*) *Spin-crossover materials: properties and applications*, ed. M. A. Halcrow, John Wiley & Sons, 2013.

2 (*a*) M. Cavallini, I. Bergenti, S. Milita, J. C. Kengne, D. Gentili, G. Ruani, I. Salitros, V. Meded and M. Ruben, *Langmuir*, 2011, **27**, 4076; (*b*) P. N. Martinho, C. Rajnak and M. Ruben, in *Spin-Crossover Materials: Properties and Applications*, ed. M. A. Halcrow, Wiley, 2013, pp. 376–404; (*c*) G. Molnar, S. Rat, L. Salmon, W. Nicolazzi and A. Bousseksou, *Adv. Mater.*, 2018, **30**, 17003862.

3 H. J. Shepherd, C. M. Quintero, G. Molnar, L. Salmon and A. Bousseksou, in *Luminescent spin-crossover materials*, John Wiley & Sons Ltd., 2013, p. 347.

4 C. Piguet, E. Rivara-Minten, G. Bernardinelli, J.-C. Buenzli and G. Hopfgartner, *J. Chem. Soc., Dalton Trans.*, 1997, 421.

5 M. Matsuda, H. Isozaki and H. Tajima, *Thin Solid Films*, 2008, **517**, 1465.

6 L. Salmon, G. Molnár, D. Zitouni, C. Quintero, C. Bergaud, J.-C. Micheau and A. Bousseksou, *J. Mater. Chem.*, 2010, **20**, 5499.

7 S. Titos-Padilla, J. M. Herrera, X.-W. Chen, J. J. Delgado and E. Colacio, *Angew. Chem., Int. Ed.*, 2011, **50**, 3290.

8 C. M. Quintero, I. A. Gurals'kiy, L. Salmon, G. Molnar, C. Bergaud and A. Bousseksou, *J. Mater. Chem.*, 2012, **22**, 3745.

9 I. Suleimanov, O. Kraieva, J. Sánchez-Costa, I. O. Fritsky, G. Molnár, L. Salmon and A. Bousseksou, *J. Mater. Chem. C*, 2015, **3**, 5026.

10 I. Suleimanov, O. Kraieva, G. Molnár, L. Salmon and A. Bousseksou, *Chem. Commun.*, 2015, **51**, 15098.

11 M. Hasegawa, F. Renz, T. Hara, Y. Kikuchi, Y. Fukuda, J. Okubo, T. Hoshi and W. Linert, *Chem. Phys.*, 2002, **277**, 21.

12 H. Matzukizono, K. Kuroiwa and N. Kimikuza, *Chem. Lett.*, 2008, **37**, 446.

13 A. Santoro, L. J. Kershaw Cook, R. Kulmaczewski, S. A. Barrett, O. Cespedes and M. A. Halcrow, *Inorg. Chem.*, 2015, **54**, 682.

Open Access Article. Published on 11 September 2018. Downloaded on 12/20/2019 3:04:47 PM.
This article is licensed under a Creative Commons Attribution-NonCommercial 3.0 Unported Licence.

14 J.-L. Wang, Q. Liu, Y.-S. Meng, X. Liu, H. Zheng, Q. Shi, C.-Y. Duan and T. Liu, *Chem. Sci.*, 2018, **9**, 2892.
15 Y. Garcia, F. Robert, A. D. Naik, G. Zhou, B. Tinant, K. Robeyns, S. Michotte and L. Piraux, *J. Am. Chem. Soc.*, 2011, **133**, 15850.
16 B. Schafer, T. Bauer, I. Faus, J. A. Wolny, F. Dahms, O. Fuhr, S. Lebedkin, H.-C. Wille, K. Schlage, K. Chevalier, F. Rupp, R. Diller, V. Schünemann, M. M. Kappes and M. Ruben, *Dalton Trans.*, 2017, **46**, 2289.
17 C.-F. Wang, R.-F. Li, X.-Y. Chen, R.-J. Wei, L.-S. Zheng and J. Tao, *Angew. Chem., Int. Ed.*, 2015, **54**, 1574.
18 C. Lochenie, K. Schötz, F. Panzer, H. Kurz, B. Maier, F. Puchtler, S. Agarwal, A. Köhler and B. Weber, *J. Am. Chem. Soc.*, 2018, **140**, 700.
19 M. C. Muñoz and J. A. Real, *Coord. Chem. Rev.*, 2011, **255**, 2068.
20 Z.-P. Ni, J.-L. Liu, M. N. Hoque, W. Liu, J.-Y. Li, Y.-C. Chen and M. L. Tong, *Coord. Chem. Rev.*, 2017, **335**, 28.
21 V. Niel, J. M. Martínez-Agudo, M. C. Muñoz, A. B. Gaspar and J. A. Real, *Inorg. Chem.*, 2001, **40**, 3838.
22 A. Galet, A. B. Gaspar, M. C. Muñoz, G. V. Bukin, G. Levchenko and J. A. Real, *Adv. Mater.*, 2005, **17**, 2949.
23 (*a*) N. F. Sciortino, K. R. Scherl-Gruenwald, G. Chastanet, G. J. Halder, K. W. Chapman, J. F. Létard and C. J. Kepert, *Angew. Chem., Int. Ed.*, 2012, **51**, 10154; (*b*) M. J. Murphy, K. A. Zenere, F. Ragon, P. D. Southon, C. J. Kepert and S. M. Neville, *J. Am. Chem. Soc.*, 2017, **139**, 1330.
24 (*a*) M. Ohba, K. Yoneda, G. Agustí, M. C. Muñoz, A. B. Gaspar, J. A. Real, M. Yamasaki, H. Ando, Y. Nakao, S. Sakaki and S. Kitagawa, *Angew. Chem., Int. Ed.*, 2009, **48**, 4767; (*b*) G. Agustí, R. Ohtani, K. Yoneda, A. B. Gaspar, M. Ohba, J. F. Sánchez-Royo, M. C. Muñoz, S. Kitagawa and J. A. Real, *Angew. Chem., Int. Ed.*, 2009, **48**, 8944; (*c*) P. D. Southon, L. Liu, E. A. Fellows, D. J. Price, G. J. Halder, K. W. Chapman, B. Moubaraki, K. S. Murray, J. F. Létard and C. J. Kepert, *J. Am. Chem. Soc.*, 2009, **131**, 10998; (*d*) R. Ohtani, K. Yoneda, S. Furukawa, N. Horike, S. Kitagawa, A. B. Gaspar, M. C. Muñoz, J. A. Real and M. Ohba, *J. Am. Chem. Soc.*, 2011, **133**, 8600.
25 J. E. Clements, J. R. Price, S. M. Neville and C. J. Kepert, *Angew. Chem., Int. Ed.*, 2014, **53**, 10164.
26 V. Niel, A. L. Thompson, M. C. Muñoz, A. Galet, A. E. Goeta and J. A. Real, *Angew. Chem., Int. Ed.*, 2003, **42**, 3760.
27 (*a*) V. Meded, A. Bagrets, K. Fink, R. Chandrasekar, M. Ruben, F. Evers, A. Bernand-Mantel, J. S. Seldenthuis, A. Beukman and H. S. J. van der Zant, *Phys. Rev. B: Condens. Matter Mater. Phys.*, 2011, **83**, 245415; (*b*) F. Prins, M. Monrabal-Capilla, E. A. Osorio, E. Coronado and H. S. J. van der Zant, *Adv. Mater.*, 2011, **23**, 1545; (*c*) M. Cavallini, I. Bergenti, S. Milita, J. C. Kengne, D. Gentili, G. Ruani, I. Salitros, V. Meded and M. Ruben, *Langmuir*, 2011, **27**, 4076; (*d*) T. Miyamachi, M. Gruber, V. Davesne, M. Bowen, S. Boukari, L. Joly, F. Scheurer, G. Rogez, T. K. Yamada, P. Ohresser, E. Beaurepaire and W. Wulfhekel, *Nat. Commun.*, 2012, **3**, 938; (*e*) P. N. Martinho, C. Rajnak and M. Ruben, in *Spin-Crossover Materials: Properties and Applications*, ed. M. A. Halcrow, Wiley, 2013, p. 376 and references therein; (*f*) H. J. Shepherd, G. Molnár, W. Nicolazzi, L. Salmon and A. Bousseksou, *Eur. J. Inorg. Chem.*, 2013, 653; (*g*) A. Rotaru, J. Dugay, R. P. Tan, I. A. Guralskiy, L. Salmon, P. Demont, J. Carrey, G. Molnár, M. Respaud and A. Bousseksou, *Adv. Mater.*, 2013, **25**, 1745; (*h*) I. A. Gural'skiy, C. M. Quintero, J. Sánchez-Costa, P. Demont, G. Molnár, L. Salmon, H. J. Shepherd and A. Bousseksou, *J. Mater. Chem. C*, 2014, **2**, 2949; (*i*) A. C. Aragonés, D. Aravena, J. I. Cerdá, Z. Acís-Castillo, H. Li, J. A. Real, F. Sanz, J. Hihath, E. Ruiz and I. Díez-Pérez, *Nano Lett.*, 2016, **16**, 218.
28 (*a*) L. Piñeiro-López, M. Seredyuk, M. C. Muñoz and J. A. Real, *Chem. Commun.*, 2014, **50**, 1833; (*b*) L. Piñeiro-López, F. J. Valverde-Muñoz, M. Seredyuk, M. C. Muñoz, M. Haukka and J. A. Real, *Inorg. Chem.*, 2017, **56**, 7038.
29 J.-Y. Li, C.-T. He, Y.-C. Chen, Z.-M. Zhang, W. Liu, Z.-P. Ni and M. L. Tong, *J. Mater. Chem. C*, 2015, **3**, 7830.
30 (*a*) E. Trzop, D. Zhang, L. Piñeiro-Lopez, F. J. Valverde-Muñoz, M. C. Muñoz, L. Palatinus, L. Guerin, H. Cailleau, J. A. Real and E. Collet, *Angew. Chem., Int. Ed.*, 2016, **55**, 1; (*b*) J. E. Clements, J. R. Price, S. M. Neville and C. J. Kepert, *Angew. Chem., Int. Ed.*, 2016, **55**, 15105; (*c*) D. Zhang, E. Trzop, F. J. Valverde-Muñoz, L. Piñeiro-López, M. C. Muñoz, E. Collet and J. A. Real, *Cryst. Growth Des.*, 2017, **17**, 2736; (*d*) N. F. Sciortino, K. A. Zenere, M. E. Corrigan, G. J. Halder, G. Chastanet, J. F. Létard, C. J. Kepert and S. M. Neville, *Chem. Sci.*, 2017, **8**, 70; (*e*) M. J. Murphy, K. A. Zenere, F. Ragon, P. D. Southon, C. J. Kepert and S. M. Neville, *J. Am. Chem. Soc.*, 2017, **139**, 1330.
31 N. Ortega-Villar, M. C. Muñoz and J. A. Real, *Magnetochemistry*, 2016, **2**, 16.
32 S. Decurtins, P. Gütlich, P. C. Köhler, H. Spiering and A. Hauser, *Chem. Phys. Lett.*, 1984, **105**, 1.
33 J. F. Létard, P. Guionneau, L. Rabardel, J. A. K. Howard, A. Goeta, D. Chasseau and O. Kahn, *Inorg. Chem.*, 1998, **87**, 4432.
34 B. D. Wagner, G. J. McManus, B. Moulton and M. Zaworotko, *Chem. Commun.*, 2002, 2176.
35 (*a*) N. Moliner, A. B. Gaspar, M. C. Muñoz, S. Létard, J. F. Létard, X. Solans, R. Burriel, M. Castro, O. Kahn and J. A. Real, *Inorg. Chim. Acta*, 1999, **291**, 279; (*b*) A. B. Gaspar, M. C. Muñoz, N. Moliner, V. Ksenofontov, G. Levchenko, P. Gütlich and J. A. Real, *Monatsh. Chem.*, 2003, **134**, 285.

 This journal is © The Royal Society of Chemistry 2018

Journal of Materials Chemistry C

ROYAL SOCIETY OF CHEMISTRY

PAPER

View Article Online
View Journal | View Issue

Published on 19 December 2019. Downloaded by Universitat de València on 5/11/2021 3:01:49 PM.

Check for updates

Cite this: J. Mater. Chem. C, 2020, 8, 1623

Extrinsic *vs.* intrinsic luminescence and their interplay with spin crossover in 3D Hofmann-type coordination polymers†

Manuel Meneses-Sánchez,[a] Lucía Piñeiro-López,[a] Teresa Delgado,*[b] Carlos Bartual-Murgui,*[a] M. Carmen Muñoz,[c] Pradip Chakraborty[d] and José Antonio Real*[a]

Received 22nd November 2019,
Accepted 19th December 2019

DOI: 10.1039/c9tc06422b

rsc.li/materials-c

The research of new multifunctional materials, as those undergoing spin crossover (SCO) and luminescent properties, is extremely important in the development of further optical and electronic switching devices. As a new step towards this ambitious aim, the coupling of SCO and fluorescence is presented here following two main strategies: whether the fluorescent agent is integrated as a part of the main structure of a 3D SCO coordination polymer $\{Fe^{II}(bpan)[M^{I}(CN)_2]_2\}$ (bpan = bis(4-pyridyl)anthracene, M^{I} = Ag (**FebpanAg**), Au (**FebpanAu**)) or is a guest molecule inserted within the cavities of the 3D switchable framework $\{Fe^{II}(bpb)[M^{I}(CN)_2]_2\}\cdot$pyrene (bpb = bis(4-pyridyl)butadiyne, M^{I} = Ag (**FebpbAg·Pyr**), Au (**FebpbAu·Pyr**)). The magnetic, calorimetric, structural, UV-Vis absorption and fluorescent characterizations were performed confirming the occurrence of a SCO-fluorescence interplay in the studied compounds. Moreover, the relevance of the intrinsic or extrinsic nature of the luminescence on the efficiency of the interplay is discussed on the basis of the available information.

Introduction

The spin crossover (SCO) phenomena, exhaustively studied for Fe^{II} pseudo-octahedral complexes, deals with the reversible, detectable and controllable switching between the paramagnetic high-spin (HS) and the diamagnetic low-spin (LS) electronic configurations.[1–3] The HS ↔ LS transition can be achieved *via* an external perturbation (*i.e.* temperature or pressure change, light, an electric field or the adsorption/desorption of analytes) and is accompanied by substantial changes in optical, magnetic and structural properties. Therefore, the SCO event can be monitored by a wide range of different techniques such as magnetic susceptibility measurements, Mössbauer spectroscopy, UV-Vis-NIR absorption spectroscopy, X-ray diffraction, X-ray absorption or heat capacity measurements, among others. Due to their potential applications in electronics and/or opto-electronic devices,[4,5] these switchable compounds have attracted much attention in the realms of materials physics and chemistry.

Modulation of luminescence by controlling the HS/LS population and/or, conversely, tracking the HS/LS population during the SCO behavior by measuring the relative intensity of the luminescence signal are appealing features that may facilitate the integration of a SCO system into a real device. Although the approach of combining SCO and luminescence in the same material dates from two decades ago, it has been only recently that this idea has entailed a significant number of studies. They are classified according to the way by which the fluorophore is integrated in the SCO material as: (i) doping agent (mechanophysical mixture);[6–9] (ii) decorative element of core–shell nanoparticles;[10–14] (iii) intrinsic part of the SCO structure;[15–25] and (iv) counterion.[26] With the exception of ref. 25 which deals with a 2D compound, the aforementioned luminescent SCO materials are based on Fe^{II} discrete mononuclear or binuclear complexes and 1D polymeric compounds derived from triazole ligand. In general, all these synthetic strategies successfully resulted in a more or less marked modulation of the luminescence triggered by the spin state change. Regarding the synergic mechanism, the spectral overlap between the luminophore (the sensitizer) and the SCO center (the acceptor) results in an emission–re-absorption process in which the latter acts as a quencher of the luminescence.[27] In this case, the mechanism can be easily explained by the superposition of the metal-to-ligand charge transfer (MLCT) band or spin-allowed

[a] Departamento de Química Inorgánica, Instituto de Ciencia Molecular (ICMol), Universidad de Valencia, Valencia, Spain. E-mail: carlos.bartual@uv.es, jose.a.real@uv.es
[b] Département de Chimie Physique, Université de Genève, Rue Ernest Ansermet, 30, 1211 Genève, Switzerland. E-mail: mariateresa.delgadoperez@unige.ch
[c] Departamento de Física Aplicada, Universitat Politècnica de València, Camino de Vera s/n, E-46022, Valencia, Spain
[d] Department of Chemistry, Indian Institute of Technology Kharagpur, Kharagpur-721302, India

† Electronic supplementary information (ESI) available: Synthesis and characterization of ligands and coordination polymers, experimental and instrumental details. CCDC 1965270–1965275. For ESI and crystallographic data in CIF or other electronic format see DOI: 10.1039/c9tc06422b

Published on 19 December 2019. Downloaded by Universitat de València on 5/11/2021 3:01:49 PM.

metal-centered d–d transitions ($^1A_1 \rightarrow {}^1T_1$, $^1A_1 \rightarrow {}^1T_2$) band observed in the LS state and the corresponding region of the emission fluorescent spectrum. However, if the distance between the sensitizer and the acceptor is shorter than 10 nm, as long as there is spectral overlap, non-radiative energy transfer can also take place.

The porous functionality offered by most of the 3D SCO Hofmann-type coordination polymers[28–31] represents an interesting platform, yet almost unexplored, to investigate the interplay between SCO and luminescence. As a first example utilizing this approach, we recently reported on the clathration of the pyrene (Pyr) fluorophore in the SCO framework $\{Fe^{II}(bpben)[Au^{I}(CN)_2]_2\}$ (bpben = 1,4-bis(4-pyridyl)benzene). This compound displays synergic thermo- and photo-modulation of the pyrene guest monomer and host–guest (bpben-pyrene) excimer fluorescence signals that reflects the parallel thermo- and photo-induced HS ↔ LS spin state change in the host framework.[32]

These interesting results encouraged us to explore new bifunctional porous $\{Fe^{II}(L)[M^{I}(CN)_2]_2\}$ (M^{I} = Ag, Au) 3D frameworks capable to combine SCO and luminescence in a synergistic way. As a new step in this direction, here we report on the synthesis and characterization of two unprecedented series of doubly interpenetrated Hofmann-type coordination polymers formulated as $\{Fe^{II}(bpb)[M^{I}(CN)_2]_2\}$·pyrene (bpb = bis(4-pyridyl)butadiyne, M^{I} = Ag (**FebpbAg·Pyr**), Au (**FebpbAu·Pyr**)) and $\{Fe^{II}(bpan)[M^{I}(CN)_2]_2\}$ (bpan = bis(4-pyridyl)anthracene, M^{I} = Ag (**FebpanAg**), Au (**FebpanAu**)) (Scheme 1). In the series based on the bpb bridging pillar ligand, luminescence is, similarly as in the aforementioned bpben system, an extrinsic property that stems from the pyrene guest molecule. In contrast, the series based on the anthracene-bearing bpan bridging ligand, represents the first example of a 3D Hofmann-type SCO coordination polymer with intrinsic luminescence.

Results and discussion

Synthesis

Single crystals of compounds $\{Fe^{II}(bpan)[M^{I}(CN)_2]_2\}$ (M^{I} = Ag (**FebpanAg**) or Au (**FebpanAu**)) were obtained using liquid-to-liquid diffusions from $Fe^{II}(BF_4)_2{\cdot}6H_2O$, $KM^{I}(CN)_2$ (M^{I} = Ag or Au) and bpan ligand in methanol-dichloromethane solutions. Same conditions were used for the synthesis of the zinc analogue complex **ZnbpanAu** albeit using $Zn^{II}(BF_4)_2{\cdot}6H_2O$ instead of the Fe^{II} salt. Similarly, crystals of $\{Fe^{II}(bpb)[M^{I}(CN)_2]_2\}$·Pyrene ($M^{I}$ = Ag (**FebpbAg·Pyr**) or Au (**FebpbAu·Pyr**)) were synthesized following similar liquid phase diffusion methodology but using saturated methanol solutions of the pyrene fluorophore (see Experimental section). Despite considerable efforts to obtain single crystals of the bpb Zn^{II} complex, the desired product was not formed.

Elemental analysis and powder X-ray diffraction (PXRD) measurements confirmed the high purity of the obtained polycrystalline samples (see Experimental section and Fig. S1, respectively, ESI†). Comparison of the PXRD spectra also reveals that the Au and Ag counterparts are isostructural in both series of complexes as the more intense peaks are well reproduced from one derivative to the other. Thermogravimetric analysis were performed for **FebpbAg·Pyr**/**FebpbAu·Pyr** and **FebpanAg**/**FebpanAu** clathrates confirming the presence of about 1 molecule of pyrene per Fe^{II} ion for the former and the absence of trapped solvent for the latter (Fig. S2, ESI†) in good agreement with the elemental analysis and structural data shown hereafter.

SCO properties

Magnetic and calorimetric studies. The temperature dependence of the $\chi_M T$ product (where χ_M is the molar susceptibility and T is the temperature) for compounds **FebpanAg**/**FebpanAu** and **FebpbAg·Pyr**/**FebpbAu·Pyr** is depicted in Fig. 1. In all cases, at room temperature, the value of $\chi_M T$ is about 3.2 cm^3 K mol^{-1} indicating that practically all the Fe^{II} centers are in the HS state (S = 2). Upon cooling, the $\chi_M T$ value of **FebpanAu**/**FebpanAg** remains almost constant until dropping abruptly at $T_{1/2}{\downarrow}^{1}$ = 242/222 K ($T_{1/2}$ = temperature at which the population of the HS and LS Fe^{II} ions is equal to 50%) reaching a value

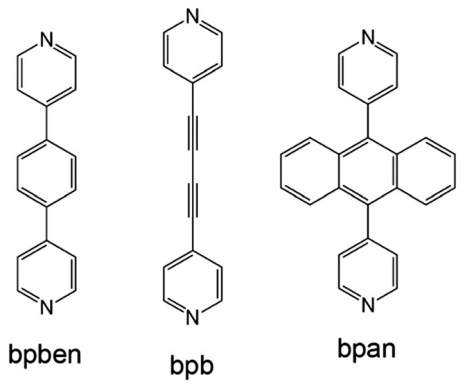

Scheme 1 Structure of the pillar ligands used in the study of synergies between SCO and luminescence in Hofmann-type coordination polymers.

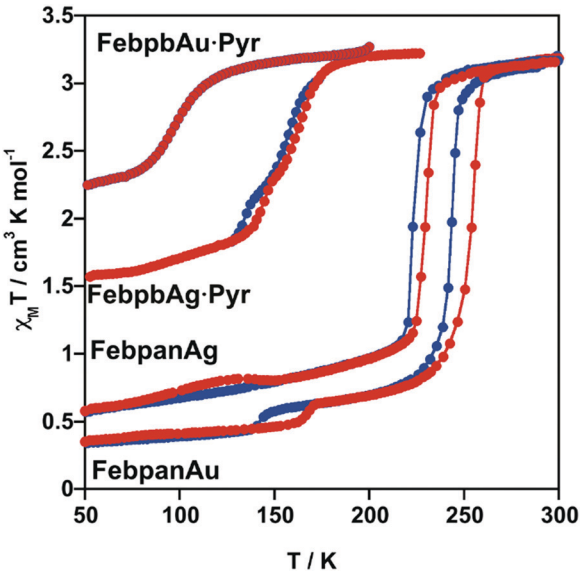

Fig. 1 $\chi_M T$ vs. T plots of compounds **FebpbAu·Pyr**, **FebpbAg·Pyr**, **FebpanAu** and **FebpanAg** (blue and red filled circles correspond to the cooling and heating modes, respectively).

 This journal is © The Royal Society of Chemistry 2020

Published on 19 December 2019. Downloaded by Universitat de València on 5/11/2021 3:01:49 PM.

ca. 0.70/1.09 cm^3 K mol^{-1} at 205 K. For **FebpanAu**, this $\chi_M T$ value remains almost constant upon cooling defining a plateau 65 K wide before undergoing a second small drop at $T_{1/2}\downarrow^2$ = 143 K reaching a value of 0.34 cm^3 K mol^{-1} at 50 K. Considering these variations of $\chi_M T$, *ca.* 80% and 10% of the Fe^{II} ions are involved in the spin state change in the first and the second step, respectively, whereas about 10% of the Fe^{II} centers remain as residual HS species at low temperature. In the heating mode, the $\chi_M T$ *vs.* T curve for **FebpanAu** does not match ($T_{1/2}\uparrow^2$ = 163 K and $T_{1/2}\uparrow^1$ = 252 K) with the cooling mode, thereby defining a hysteresis 10 K (first step) and 20 K (second step) wide.

Below 215 K, the magnetic behavior of **FebpanAg** slightly differs from that of the homologous Au derivative. After the first abrupt transition in the cooling mode, the $\chi_M T$ decreases gradually reaching a value of 0.6 cm^3 K mol^{-1} at 50 K. Whereas in the heating mode, a slight increase in the $\chi_M T$ increase is observed above 85 K and stabilized at 130 K ($\Delta\chi_M T$ = 0.2 cm^3 K mol^{-1}) defining an asymmetric hysteresis loop. At higher temperatures, an abrupt increase in $\chi_M T$ ($T_{1/2}\uparrow^1$ = 228 K) is observed resulting in a hysteresis loop 6 K wide.

Compound **FebpbAu·Pyr** presents a gradual and incomplete spin transition without hysteresis centered at $T_{1/2} \approx 100$ K with a remaining HS fraction of 72% at 50 K. Unlikely, the analogous compound **FebpbAg·Pyr** displays a gradual decrease of the $\chi_M T$ value with two steps associated with HS-to-LS transitions involving *ca.* 31% (from 180 to 150 K) and 15% (from 150 to 125 K) of the Fe^{II} ions, respectively. At 50 K, the value of $\chi_M T$ is 1.56 cm^3 K mol^{-1} showing that about 52% of the Fe^{II} ions remain in the HS state. The heating and cooling mode curves do not match thereby defining two hysteresis loops 4 K ($T_{1/2}\downarrow^1$ = 156 K, $T_{1/2}\uparrow^1$ = 160 K) and 7 K ($T_{1/2}\downarrow^2$ = 136 K, $T_{1/2}\uparrow^2$ = 143 K) wide. Repeating cycles on this sample shows very reproducible results (Fig. S3, ESI†).

The thermodynamic parameters associated with the SCO have been obtained from the differential scanning calorimetry (DSC) measurements for all samples except for **FebpbAu·Pyr** since its characteristic $T_{1/2}$ is out the temperature window of our calorimeter. The thermal dependence of the anomalous heat capacity variation (ΔC_p) for **FebpanAu**, **FebpanAg** and **FebpbAg·Pyr** is displayed in Fig. S4 (ESI†). The average enthalpy (ΔH) and entropy ($\Delta S = \Delta H/T_i$) variations as well as the average temperatures (T_i) of the maxima/minima of the ΔC_p *vs.* T plots are gathered in Table 1. The average T_i temperatures of the observed anomalies are consistent with those obtained from the magnetic measurements for the SCO. For **FebpanAu** and **FebpanAg**, the overall ΔH and ΔS values associated with the SCO are consistent with those reported for related 3D SCO Hofmann-type coordination polymers with cooperative SCO. For **FebpbAg·Pyr**, extrapolation of the HS ↔ LS transformation to 100% affords ΔH and ΔS values (*ca.* 8 kJ mol^{-1} and 54 J K^{-1} mol^{-1}) consistent with the gradual character of the thermal spin transition.

Table 1 Thermodynamic parameters obtained from DSC measurements

		$T_{1/2}^{av}$ (K)	ΔH_{av} (kJ mol^{-1})	ΔS_{av} (J K^{-1} mol^{-1})
FebpanAu	1st step	250.0	19.22	76.9
	2nd step	152.1	0.19	1.3
	Overall		19.41	78.2
FebpanAg	1st step	236.5	18.3	80.7
	2nd step	150.0[a]	0.6	4.2
	Overall		18.9	84.9
FebpbAg·Pyr	1st step	160.0	2.3[b]	16.3[b]
	2nd step	140.0	1.8[b]	10.5[b]
	Overall		4.1	26.8

[a] Only heating mode. [b] Evaluated for the 50% incomplete SCO.

Single crystal optical absorption spectroscopy. Fig. 2a and b display the thermal evolution of the optical absorption spectra for a single crystal of **FebpbAg·Pyr** and of **FebpanAu**, respectively, in the heating mode recorded at 5 K min^{-1} (see Fig. S5 for the cooling mode, ESI†). The thickness of both crystals was approximately 100 μm. In both cases, the tail of the very intense metal–ligand-charge-transfer (MLCT) band is observed between 450 and 800 nm at room temperature. Below 450 nm, the MLCT band saturates due to its high extinction coefficient. When both crystals are cooled down below the spin transition temperature, the $^1A_1 \rightarrow {}^1T_1$ d–d transition band ($\varepsilon_{530-550nm} \approx 50$ M^{-1} cm^{-1}) characteristic for the LS state of Fe^{II}, reaches a maximum at 10 K. The difference in optical density at 533/800 nm as well as 550/716 nm has been used for the silver and gold derivatives, respectively, to establish the thermal dependence of the HS molar fraction (γ_{HS}) through Vegard's law as stated elsewhere.[33] The γ_{HS} *vs.* T curves obtained for **FebpbAg·Pyr** or **FebpanAu** (Fig. 2c) match very well the SCO behaviors found *via* magnetic studies albeit higher spin transition temperatures have been observed ($T_{1/2}\downarrow^1$ = 158 K, $T_{1/2}\downarrow^2$ = 136 K and $T_{1/2}\uparrow^1$ = 161 K, $T_{1/2}\uparrow^2$ = 140 K for **FebpbAg·Pyr**; $T_{1/2}\downarrow$ = 242 K and $T_{1/2}\uparrow$ = 275 K for **FebpanAu**). The subtle difference in the SCO temperature may be attributed to the faster temperature scan rate employed for the single crystal optical absorption measurements (5 K min^{-1} *vs.* 1 K min^{-1}), that is, the real temperature of the sample may be lower than the nominal one during heating. In the case of **FebpbAg·Pyr**, the values of the HS fraction have been corrected by using the residual HS fraction obtained at low temperatures extracted from the χT *vs.* T curve. The size of the **FebpbAu·Pyr** and **FebpanAg** crystals was too small to record their absorption spectra individually. Therefore, dilution of the grinded crystals in KBr pellets and dispersion in mineral oil have been tried out but, as shown in Fig. S6 (ESI†), the quality of the optical absorption spectra is poor due to sample inhomogeneity.

Crystal structures

Structural data of **FebpanAu** were successfully recorded at 280, 200, and 120 K allowing to identify the structures at the different steps defined by the SCO curve. However, despite numerous attempts, we were not able to get good single crystals of the isostructural **FebpanAg** and **ZnbpanAu** thus preventing a complete analysis of their structures. The structures of complexes **FebpbAu·Pyr** and **FebpbAg·Pyr** were determined at 120 and 250/100 K, respectively. Tables S1 and S2 (ESI†) show the main crystallographic parameters obtained from the single crystal X-ray data of all studied compounds.

Published on 19 December 2019. Downloaded by Universitat de València on 5/11/2021 3:01:49 PM.

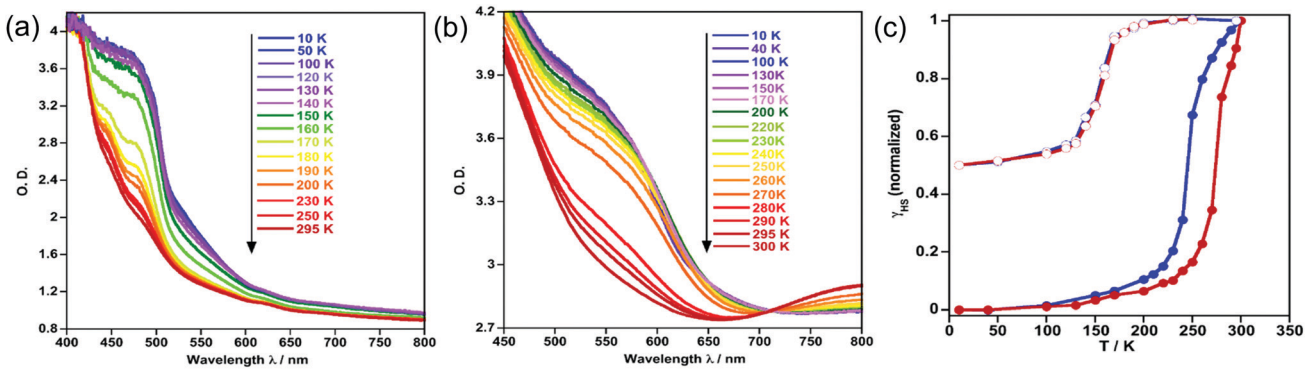

Fig. 2 Thermal dependence of single crystal absorption spectra during the thermal transition for **FebpbAg·Pyr** (a) and **FebpanAu** (b), and the corresponding HS fraction (γ_{HS}) *vs.* *T* curves obtained from the optical density difference at 533 and 800 nm for **FebpbAg·Pyr** (empty circles) and between 550 and 716 nm for **FebpanAu** (filled circles) (c).

Structure of FebpanAu. At 280 K, the structure of **FebpanAu** shows the monoclinic *P*2/*c* space group. It is constituted of two crystallographically non-equivalent pseudooctahedral $[Fe^{II}N_6]$ environments. The equatorial positions of the octahedrons are coordinated by four $[Au(CN)_2]^-$ groups which connect non-equivalent adjacent Fe^{II} centers (Fe1–Fe2–Fe1–...) building up 2D infinite $\{Fe_4[Au(CN)_2]_4\}_\infty$ sheets. The apical positions are occupied by two crystallographically distinct ditopic bpan ligands acting as pillars between adjacent sheets, thereby defining a 3D framework with primitive cubic unit (**pcu**) topology (Fig. 3). Each type of axial bpan ligand bridges one type of inequivalent Fe centers (Fe1 or Fe2) (Fig. 3). Although the NC–Au–CN moieties are essentially linear, the coordination bonds between the NC–Au–CN groups and the Fe^{II} ions form an angle strongly deviated from 180° (Fe1–N3–C15 = 165.78°; Fe1–N8–C34 = 158.97°; Fe2–N6–C32 = 163.69°; Fe2–N7–C33 = 164.78°), thereby conferring to the $\{Fe_4[Au(CN)_2]_4\}_\infty$ layers a corrugated shape. Indeed, if we consider the four NC–Au–CN groups radiating from Fe2, the four connected Fe1 sites are 1.029 Å below the equatorial plane Fe2N6N7N6N7. Consequently, the $\{Fe_4[Au(CN)_2]_4\}$ rhomboidal windows, whose Fe···Fe diagonals make 11.584 and 17.007 Å long, are slightly folded with respect to the short diagonal deviating 14.38° from planarity. The angles of the rhomboid are 68.099° and 110.579°. At 280 K, the Fe–N average distances, Fe1–N = 2.148 Å and Fe2–N = 2.157 Å, are typical of the Fe^{II} ions in the HS state in agreement with the magnetic data. The sum of the deviation from 90° of the twelve *cis* N–Fe–N bond angles (Σ) are 20.17° and 22.49° for Fe1 and Fe2 respectively.

The open nature of the framework favors the interpenetration of a second equivalent 3D structure, in such a way that each bpan ligand of one network passes exactly through the center of the $Fe_4[Au(CN)_2]_4$ rhomboids of the other.

The interpenetration is stabilized by aurophilic interactions (Au1···Au2 = 3.428 Å) (Fig. 4a and b). The anthracene moieties of the two independent bpan ligands display different orientations with respect to the plane defined by the atoms N1N2N3N3′(bpan1) around Fe1 and N4N5N6N6′(bpan2) around Fe2, being respectively 26.37° and 19.41°. The planes containing the pyridine rings asymmetrically bisect the equatorial angles N3Fe1N8 [pyridine containing N1 (51.41°) and N2 (67.66°)] and N6Fe2N7 [pyridine containing N4 (62.42°) and N5 (73.79°)]. Furthermore, the pyridine moieties are nearly orthogonal with respect to the anthracene fragment [bpan1: pyridine(N1) = 77.76°, pyridine(N2) = 94.03°;

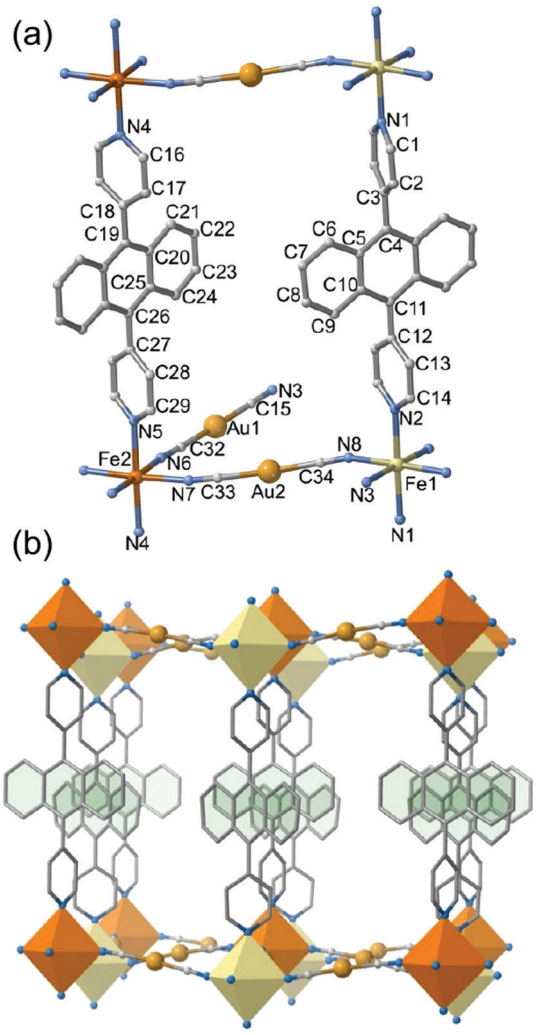

Fig. 3 (a) Representative fragment of the framework with the atom numbering of the asymmetric unit for **FebpanAu** at 280 K and (b) view of a single 3D network. Yellow and orange octahedrons correspond to Fe1 and Fe2, respectively.

 This journal is © The Royal Society of Chemistry 2020

Published on 19 December 2019. Downloaded by Universitat de València on 5/11/2021 3:01:49 PM.

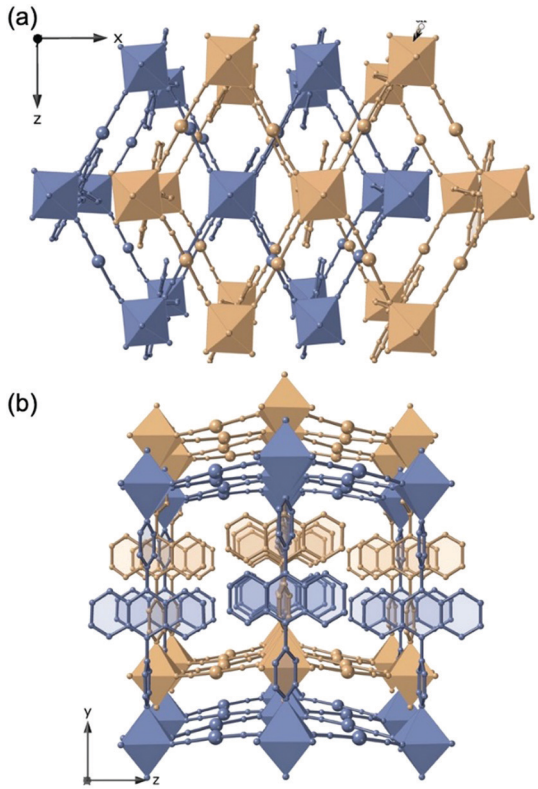

Fig. 4 Perspective views of the interpenetrated frameworks down to (a) [010] and (b) [100] directions for **FebpanAu** at 280 K.

bpan2: pyridine(N4) = 93.20° and pyridine(N5) = 81.84°] (see Fig. 3). This arrangement is adopted to minimize the inter- and intra-network repulsion between the hydrogen atoms of the anthracene groups. In addition, anthracene moieties from different networks display very weak π···π interactions with C···C contacts well above 4.1 Å (centroid–centroid distances of *ca.* 5.4 Å).

When cooling down to 200 K, the crystal color changes from pale-yellow to red indicating the occurrence of the spin transition, consistently with the magnetic and optical absorption measurements. Furthermore, the SCO is accompanied by a change of the space group from monoclinic *P*2/*c* to orthorhombic *Cmma*.

As a consequence of the symmetry breaking, the asymmetric unit now contains a unique octahedral Fe^{II} center, which is coordinated equatorially to four identical $[Au(CN)_2]^-$ groups and axially to only one crystallographically distinct bpan ligand. The average Fe–N bond length, equal to 1.954 Å, is 0.204 Å shorter than at 280 K, confirming that the HS ↔ LS transition is almost complete. Consistently, the angular distortion of the octahedron, Σ, decreases significantly to a value of 9.87° while the Fe–N–C(Au) angle increases up to 171.12° making the framework less distorted than in the monoclinic HS phase. Consequently, the two pyridine moieties are now practically coplanar and their planes bisect the N3–Fe–N3′ angles into two identical portions of 46.01°. In contrast, the anthracene group is disordered in two crystallographically equivalent orientations forming an angle of 31.42° to each other (Fig. S7a, ESI†). However, the average orientation is strictly orthogonal with respect to the pyridine groups. Furthermore, the constraining of the grid during the SCO process occurs in an anisotropic manner since the long Fe···Fe diagonal of the $\{Fe_4[Au(CN)_2]_4\}$ rhomboid decreases by 1.133 Å until 15.874(1) Å, while the short one increases by 0.736 Å up to 12.320(1) Å.[34] The Au–Au interactions between the two equivalent interpenetrated nets show a distance of 3.273 Å, 0.155 Å shorter with respect to the distance at 280 K.

When further cooling to 120 K, the structure undergoes a second crystallographic phase transition displaying the monoclinic *P*2/*n* space group. The structure is very similar to that at 200 K but it shows some important differences: (i) the average orientation of the anthracene groups, which are still disordered at 50% in two non-equivalent orientations (now rotated with respect to each other by 22.57°, Fig. S7b, ESI†), is no longer orthogonal to the pyridine rings defining angles of 73.28° (pyridineN1) and 77.17° (pyridineN2); (ii) the plane containing the two pyridine rings bisects the N3–Fe–N4 angles forming an angle of 54.56° with respect to the N1N3N2N3′ plane; (iii) the Fe–N average distance of 1.944 Å is slightly shorter (*ca.* 0.010 Å) than that at 200 K and reflects on the additional low-temperature step observed in the magnetic measurements; (iv) the aurophilic interactions are also stronger after this second phase transition showing a Au–Au distance value of 3.260 Å; and (v) the long/short Fe···Fe diagonal of the $\{Fe_4[Au(CN)_2]_4\}$ rhomboid slightly increases/decreases upon additional conversion to reach values of 15.914 and 12.298 Å, respectively.

Structure of FebpbM·Pyr (M = Ag, Au). FebpbM·Pyr (M = Ag, Au) are isostructural. Therefore, we will delineate in detail the structure of the Ag derivative at 250 and 100 K. The structure of the Au derivative was measured at 120 K where it remains in the HS state and is comparable with that of the Ag analogue at 250 K (see Table S2, ESI†).

FebpbAg·Pyr displays the triclinic $P\bar{1}$ space group at 250 and 100 K. Topologically, the structure of **FebpbAg·Pyr** is essentially the same as for **FebpanAu** discussed above. The most significant difference is that the corresponding $\{Fe_4[Ag(CN)_2]_4\}_\infty$ layers are pillared by the longer and much less bulky bpb bridging ligand forming a much open **pcu** framework (Fig. 5). The average Fe–N bond length and octahedral angular distortion Σ of the crystallographically unique Fe^{II} center are respectively, 2.180 Å and 18.37° at 250 K and 2.073 Å and 17.67° at 100 K. The equatorial Fe–N–C(Ag) bond angles, found in the range of 7.09–13.5° (250 K) and 6.66–10.61° (100 K), slightly deviate from the linearity. The moderate variation, 0.107 Å, of the average Fe–N bond length corresponds to the occurrence of a HS-to-LS conversion of 53.5%, which is in perfect agreement with the magnetic and optical data. The crystals change from yellow (HS)-to-dark orange (LS) when cooling from 250 K to 100 K.

As a consequence of its high void volume, this network is interpenetrated with a second equivalent structure as observed in Fig. 6a. Unlike the bpan pillar ligand in **FebpanAu**, the bpb ligands of one network passes slightly shifted from the center of the $\{Fe_4(Ag(CN)_2)_4\}$ rhomboids of the other network (Fig. 6b) thereby leaving wide channels for the intercalation of two crystallographically independent pyrene guest molecules within the generated pores. The two trapped pyrene guests are positioned face-to-face with respect to the pyridine coordinating groups of the bpb ligands, establishing a large number

Published on 19 December 2019. Downloaded by Universitat de València on 5/11/2021 3:01:49 PM.

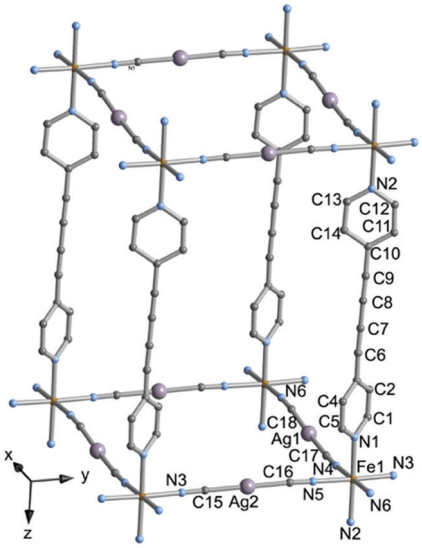

Fig. 5 Fragment of the **FebpbM·Pyr** (M = Ag, Au) framework emphasizing the atom numbering of the asymmetric unit.

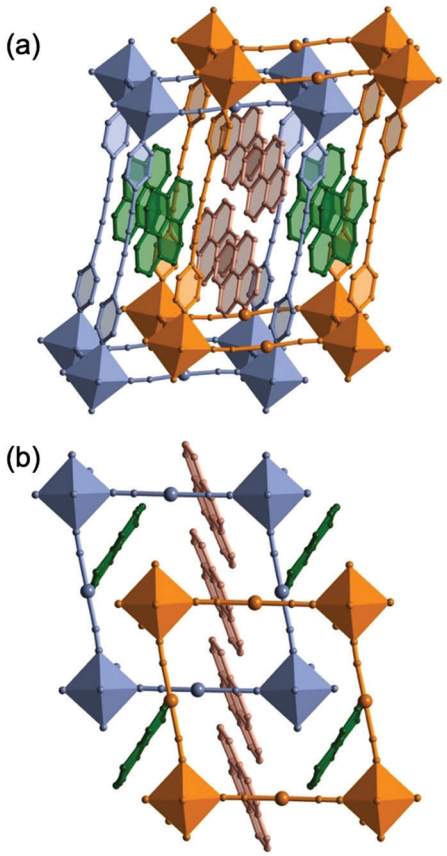

Fig. 6 (a) Side and (b) top views of a fragment of the **FebpbM·Pyr** (M = Ag, Au) structure showing the interpenetration of the two frameworks (blue/orange) and intercalation of the two crystallographically distinct pyrene molecules marked in color green (pyr1) and salmon (pyr2).

of π···π interactions (Fig. S8, ESI†). In one of the pyrene molecules, the π···π interactions are modified as a consequence of the spin state change (Table S3, ESI†).

Coupling between luminescence and SCO

The interplay between the two concurrent properties, *i.e.* luminescence and SCO, has been investigated for the dicyanoargentate derivatives **FebpbAg·Pyr** and **FebpanAg**. This choice was based on the fact that the dicyanoargentate counterpart of the bpb derivative displays a more complete SCO which takes place at higher temperature. Therefore, among **FebpanAg** and **FebpanAu**, the former was studied for comparison with **FebpbAg·Pyr**. The thermal evolution of the luminescence spectra has been followed for an ensemble of single crystals of the selected compounds. In the case of **FebpbAg·Pyr**, a very similar behavior to that described for the analogous compound $\{Fe^{II}(bpben)[(Au(CN)_2)_2]\}$@pyrene[32] has been found even though in the present case the transition is much more incomplete. As observed in Fig. 7a, two main contributions are present in the luminescence spectra at room temperature upon irradiation at 345 nm (see corresponding excitation spectra in Fig. S9a, ESI†). In the interval 350–450 nm, a multicomponent band, split into two main peaks, associated with the monomer form of pyrene is observed. From 450 to 700 nm a much broader and less defined band appears. This contribution is associated with the emission arising from the heterodimeric excimer formed by the pyrene molecules and the bpb bridging ligand due to strong π···π interactions established between them.[35] Upon cooling from room

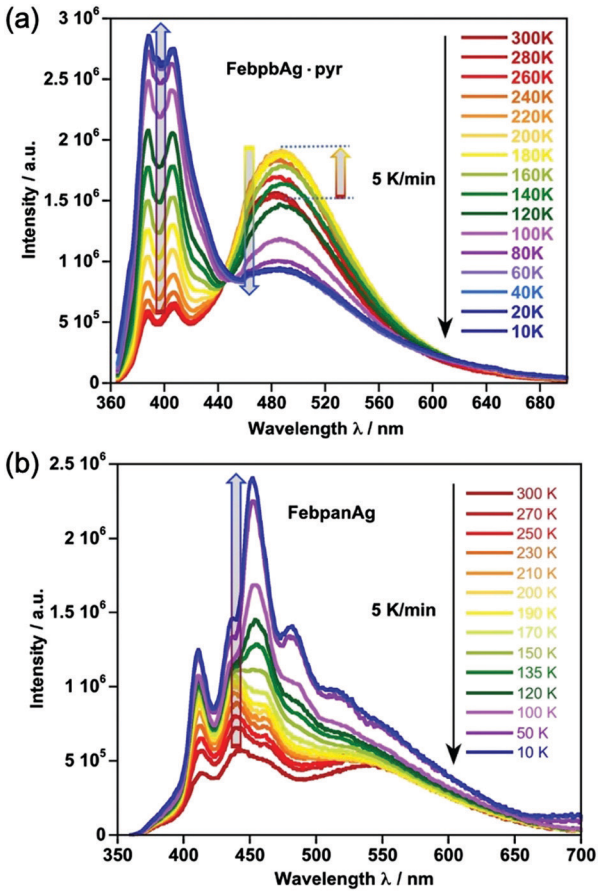

Fig. 7 Thermal evolution of the fluorescence of an ensemble of crystals of (a) **FebpbAg·Pyr** and (b) **FebpanAg** during cooling at 5 K min^{-1}.

 This journal is © The Royal Society of Chemistry 2020

Published on 19 December 2019. Downloaded by Universitat de València on 5/11/2021 3:01:49 PM.

temperature, the intensity of the monomer and excimer signals increases due to reduction of thermal quenching, that is, in the configurational coordinate model, the probability of finding a crossing point between the potential energy surfaces of the ground state and the higher energy excited states, populated at high temperatures, increases leading to non-radiative transitions.[27] However, at *ca.* 200 K, the intensity of the excimer signal is stabilized and, upon further cooling, it decreases abruptly whereas the intensity of the monomer band keeps on increasing. At 10 K, where $\gamma_{HS} \approx \gamma_{LS} \approx 0.5$, the monomer signal intensity reaches to a maximum in intensity and displays a highly defined doublet due to the reduction of vibrational degrees of freedom at such low temperatures, whereas the excimer signal is significantly quenched. This observation can be attributed to the overlap of the optical absorption spectra in the LS state and the excimer emission.

Fig. 7b shows the fluorescence emission of **FebpanAg** as a function of temperature (see corresponding excitation spectra in Fig. S9b, ESI†). At room temperature, irradiation at 345 nm induces the observation of two main contributions: a more resolved signal in the wave-length range 350–490 nm from the monomer and a broader and less defined band in the interval 490–700 nm from the excimer.[36–38] The fluorescence behavior of the anthracene excimer is usually characterized by a very short lifetime and makes difficult to detect it at room temperature albeit high pressure conditions in the crystalline state lead to its observation.[36] In the present case, the crystallinity of the sample and the rigidity of the lattice may contribute to the observation of the excimer signal from anthracene. Nonetheless, these interactions are less significant than in **FebpbAg·Pyr**, what would explain the lower intensity of the excimer signal in **FebpanAg** with respect to **FebpbAg·Pyr**. Upon cooling, both monomer and excimer signals increase in intensity. However, below 230 K, in correlation with the thermal spin transition of the complex, the excimer band undergoes some modifications in shape and seems to disappear upon further cooling whereas the intensity of the monomer signal increases giving rise to well-structured bands. As in the previous case, this behavior may be ascribed to the high optical absorption of the LS species within the range of the excimer emission.

In order to analyze in more detail the thermal dependence of the fluorescence for compound **FebpbAg·Pyr**, the intensities of the excimer and monomer signal were extracted from the corresponding spectra during cooling (Fig. 7a) and heating (Fig. S10a, ESI†) and plotted as a function of temperature (Fig. 8a and Fig. S10b, ESI†). The HS fraction, γ_{HS}, was calculated as the ratio between both signals and its thermal evolution is depicted in Fig. 8b. The resulting profile is consistent with the SCO observed from single crystal optical absorption spectroscopy although the thermal hysteresis is wider and the spin transition temperature is shifted towards lower temperatures. These discrepancies are likely related to differences in the temperature scanning rate used for each measurement method. Hence, as previously observed in $\{Fe^{II}(bpben)[(Au(CN)_2)_2]\}$@pyrene,[32] the modification of the luminescence behavior of pyrene has been demonstrated to be a sensitive technique to monitoring the SCO for compound **FebpbAg·Pyr**. In both cases, for the

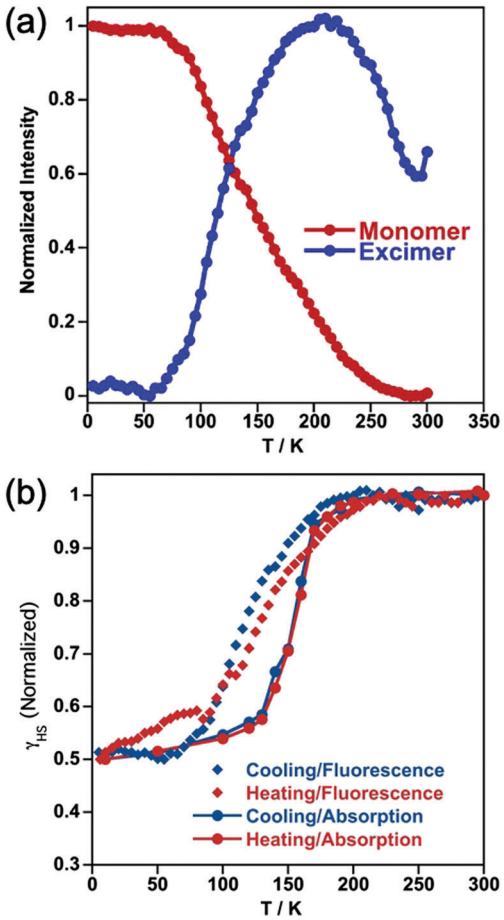

Fig. 8 (a) Thermal dependence of the monomer and excimer emission intensity of **FebpbAg·Pyr** in the cooling mode. (b) Comparison of the HS fraction, γ_{HS}, obtained from the ratio of the monomer emission over the excimer emission (filled diamonds) and from single crystal absorption spectroscopy (filled circles) in the heating and cooling modes at 5 K min^{-1}.

bpben- and bpb-containing compounds, the SCO observed through the thermal variation of the magnetic susceptibility can be accurately reproduced by the luminescence measurements (Fig. S11, ESI†).

Similarly, the thermal SCO of the intrinsically luminescent compound **FebpanAg** was also obtained by calculating γ_{HS} as the ratio of the excimer and the monomer signal. However, in this case the monomer signal was calculated as the average of the maximum intensity of the different observed peaks (see peaks from [1] to [5] in Fig. 9a (and Fig. S10c, ESI†) and the intensity *vs.* T plots for the cooling and heating modes in (Fig. S10b and d, respectively, ESI†). Although the resulting thermal dependence of the luminescence partially agrees with that obtained by magnetic susceptibility measurements (even the multi-step feature), the former displays a more gradual shape (Fig. 9c). These small differences can be ascribed to the faster temperature scan rates used for recording the thermal dependence of luminescence and the fact of exciting an ensemble of crystals. On the other hand, it is worth mentioning that the emission spectra of **FebpanAg** was obtained from exciting in the different structured-excitation bands with the origin of the different vibrational contributions between the ground and excited electronic states S_0 and S_1 (see excitation spectrum in Fig. S12a, ESI†)[39,40]

Published on 19 December 2019. Downloaded by Universitat de València on 5/11/2021 3:01:49 PM.

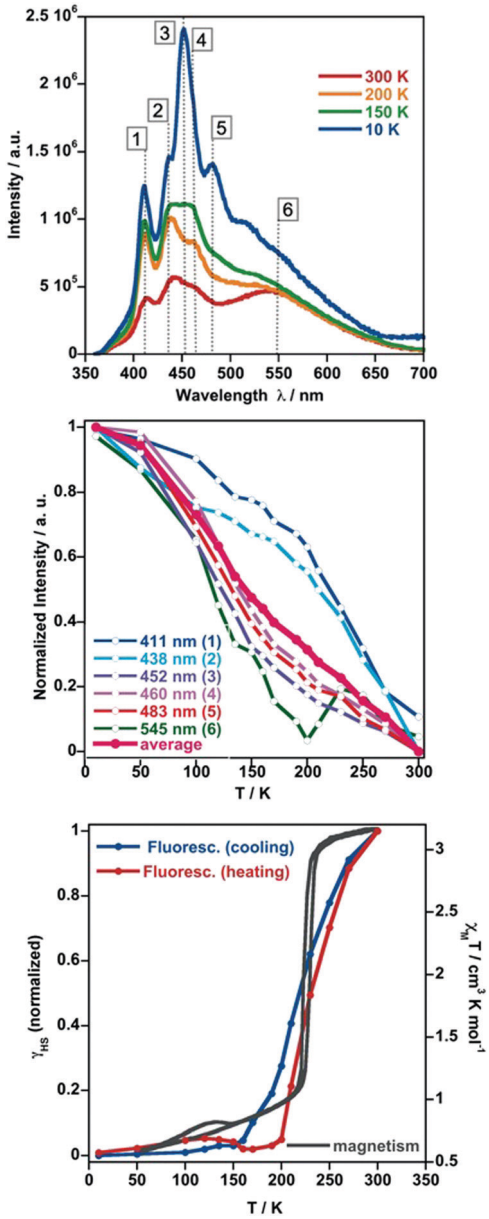

Fig. 9 Compound **FebpanAg**. Thermal evolution of: the monomer and excimer emission spectra (a); the different intensity maxima 1–6 (b); and the HS fraction (γ_{HS}) obtained from the ratio of the monomer emission over the excimer emission during the heating and cooling modes at 5 K min^{-1} (the results are compared with the thermal transition obtained by magnetism).

However, if one excites into the π–π* band of anthracene at approximately 260 nm, the emission is slightly different and in fact, when following the thermal evolution of the emission spectra the intensities of all peaks equally increase upon cooling, but the relative intensity of all the vibrational bands stays constant and the excimer signal is not present (see Fig. S12b and c for comparison, ESI†). Interestingly, other studies point to the same relative intensities and shape of the emission spectrum of anthracene regardless of whether the excitation is carried out at 280 or 360 nm.[41]

In order to verify whether the fluorescence-SCO synergy observed for **FebpbAg·Pyr** and **FebpanAg** also takes place in the corresponding **FebpbAu·Pyr** and **FebpanAu** analogues, their fluorescence spectra have been recorded at 300 K and at 80 K (see Fig. S13 containing a full characterization of the absorption, excitation and fluorescence spectra, ESI†). Whereas at 300 K the 100% of the Fe^{II} ions exhibit the HS state, at 80 K **FebpbAu·Pyr** and **FebpanAu** display 70%/30% and 0%/100% HS/LS state, respectively. Indeed, in the LS state, the intensities of the monomer signal increase significantly with respect to the excimer one, which exhibits once again a quench due to the strong optical absorption of the samples in the excimer region. Consistently, the excimer quenching is complete for the bpan derivative whereas it is partial for **FebpbAu·Pyr** confirming the incomplete character of its spin transition. Finally, the thermal dependence of the fluorescence spectra of the isostructural analogue **ZnbpanAu** has been recorded in the heating mode and, as expected, both monomer and excimer intensities increase at low temperatures since the Zn counterpart is not SCO-active (Fig. S14, ESI†).

Light induced spin state trapping (LIESST) experiments

First, LIESST effect studies were carried out for compounds **FebpbAg·Pyr** and **FebpanAu** *via* single crystal optical absorption since, as mentioned above, these are the samples from which big enough single crystals are obtained for absorption spectroscopy studies. The irradiation with a 532 nm laser for 10 minutes at 10 K revealed a LS-to-HS photoconversion of 100% for **FebpbAg·Pyr** and 80% for **FebpanAu** (Fig. S15a and d, respectively, ESI†). The temperature at which 50% of the photogenerated HS centers have relaxed to the LS state at a heating rate of 0.3 K min^{-1} is $T_{LIESST} \approx 43$ and 40 K for pyrene- and anthracene-containing SCO compounds, respectively (Fig. S15b and e, ESI†). These results have been confirmed by magnetic measurements (Fig. S16, ESI†). The photoswitching experiments were also followed by fluorescence spectroscopy for **FebpbAg·Pyr** and **FebpanAu**. In the case of **FebpbAg·Pyr**, as long as the temperature is not modified, the monomer signal remains stable upon irradiation whereas the excimer signal increases significantly evidencing the LS to HS conversion due to light stimulus (Fig. S15c, ESI†). In the case of **FebpanAu** no significant change occurs upon excitation at 532 nm and the excimer signal is not formed probably because the efficiency of LIESST effect is slightly lower than we previously observed by absorption spectroscopy (Fig. S15f, ESI†). Besides, as evidenced during the thermal transition, the excimer signal is observed only when γ_{HS} approaches 1.

Concluding remarks

This work has been undertaken as a new step in the study of the interplay between SCO and luminescence in 3D Hofmann-type coordination polymers. We have proposed two different approaches, one of them takes advantage of the porous nature of the framework to include a fluorescent guest, as recently reported for $\{Fe^{II}(bpben)[Au^{I}(CN)_2]_2\}\cdot$Pyr, in which luminescence is an extrinsic property of the framework. The other approach, for the first time, includes luminescence as an intrinsic function of the SCO

 This journal is © The Royal Society of Chemistry 2020

Published on 19 December 2019. Downloaded by Universitat de València on 5/11/2021 3:01:49 PM.

framework using a fluorescent bridging pillar ligand. In the first case we have chosen the bridging ligand bpb previously used in the synthesis of the coordination polymers $\{Fe^{II}(bpb)[M^{II}(CN)_4]\}\cdot G$ (M^{II} = Ni, Pd, Pt) and $\{Fe^{II}(bpb)[Ag^{I}(CN)_2]_2\}$.[42,43] The tetracyanometallate derivatives exhibit cooperative one- or two-step SCO behavior when two molecules of naphthalene or nitrobenzene (G) are docked inside the pores. However, the much longer dicyanoargentate ligand, facilitates a singular four-fold interpenetration of identical open frameworks, with **pcu** topology, even in presence of high concentrations of naphthalene or nitrobenzene guests. The inter-framework packing is so tight that does not leave room for guest molecules, thereby favoring strong elastic frustration[44] and, consequently, the occurrence of an incomplete SCO centered at *ca.* 130 K. In contrast, self-assembling of Fe^{II}, bpb and $[M^{I}(CN)_2]^-$ (M^{I} = Ag, Au) in presence of the much larger pyrene guest molecule favors the formation of a supramolecular isomer consisting of two-fold interpenetrated frameworks while the pyrene molecules are docked in the available spaces in a similar fashion as described for the bpben derivative. Despite the probable decongestion of the crystal packing in **FebpbM·Pyr** (M = Ag, Au), elastic frustration seems to remain since the SCO in both compounds is very incomplete and occurs at very low temperatures. Apparently, the interpenetration of the frameworks and the large number of host–guest $\pi\cdots\pi$ short-range interactions strongly influence the SCO behavior of this system. The lower SCO temperature observed for **FebpbAu·Pyr** compared to **FebpbAg·Pyr** is usually expected in Hofmann-type coordination polymers and is attributed to the slightly weaker ligand field induced by $[Au(CN)_2]^-$.[29]

Concerning the system **FebpanM** (M = Ag, Au), a reverse situation is observed with respect to the average critical temperatures above mentioned for the bpb derivatives. Both bpan derivatives undergo rather complete hysteretic SCO behaviors but, unexpectedly, the critical average temperature of the main transition is *ca.* 15 K lower for the Ag derivative. This suggests that, despite their isostructural nature, subtle effects of the crystal packing contribute to the effective ligand field experienced by the Fe^{II} center with a slightly larger destabilization of the LS state in case of the Ag derivative. Interestingly, both SCO behaviors can be classified as two-step transitions with very asymmetric steps. For example, compound **FebpanAu** presents a first step at high temperatures involving *ca.* 80% of the Fe^{II} centers and, separated by a large plateau *ca.* 70 K wide, and a second step occurs at lower temperatures involving *ca.* 10% of Fe^{II} centers. This behavior is associated with two consecutive symmetry breaking transformations. In addition to the expected structural changes associated with the coordination environment of Fe^{II}, the rotational freedom of the bulky anthracene group situated between the two coordinating pyridines of the bpan ligand seems to be in the origin of this singular behavior. Indeed, there is a clear correlation between the change in orientation of the anthracene groups, the change in crystallographic phase and the stabilization of the distinct HS/LS Fe^{II} fractions. In the HS state (280 K) the anthracene groups of the two crystallographically distinct bpan ligands are ordered. However, at 200 K after the first phase transition where *ca.* 80% of the Fe^{II} are LS, the structure features a unique bpan ligand but the anthracene displays positional disorder with two anthracene moieties distributed at 50% separated by 31.42°. One of the orientations practically matches that of the HS structure but the other is rotated 32.14° for the framework containing the Fe1 and 47.78° for the framework containing the Fe2 (see Fig. S7a, ESI†). At 120 K, the positional disorder remains but the angle between the two orientations is 22.57°. When comparing the position of the average planes of the two orientations defined by each anthracene at 120 and 200 K a subsequent rotation of 17.59° and 26.44° occurs (see Fig. S7b, ESI†). The latter reorientation is responsible for the additional symmetry breaking and small hysteretic spin state change at low temperature. Thus, throughout the HS ↔ LS transition, while the network shrinks, the anthracene moieties rotate most likely to minimize the interatomic repulsions. The SCO behavior of the isostructural silver derivative is perfectly comparable with that of the Au counterpart, although, the low temperature hysteretic spin transition is less pronounced in the Ag derivative, particularly in the cooling branch. This different behavior may be related to the higher flexibility of the $[Ag(CN)_2]^-$ bridge, and hence, to the larger adaptability to the steric constraints progressively generated by the anthracene groups while lowering the temperature.

As far as the SCO-fluorescence synergy is concerned, the excimer signal of **FebpbAg·Pyr** is strongly quenched upon cooling due to the strong absorption of the Fe^{II} in the LS state whereas it is maximum at room temperature when the HS state is fully populated. Besides, the relatively short-distances between pyrene molecule and Fe centers may favor non-radiative energy transfer between both species. Similar behavior has been recently reported for **FebpbenAu·Pyr**.[32] In the case of **FebpanAg**, radiative energy transfer occurs due to spectral overlap between the Fe^{II} and the anthracene molecules being minimum at room temperature when the excimer signal is observed due to the lower oscillator strength of the optical absorption transition of the Fe^{II} in the HS state. However, due to the longer distance between anthracene moiety and Fe^{II} atom in **FebpanAg** with respect to the distance between pyrene guest and Fe^{II} atom in **FebpbAg·Pyr**, non-radiative energy transfer is rather attributable to the latter compound resulting in a more obvious synergy. Besides, the $\pi\cdots\pi$ interactions operating between anthracene moieties in **FebpanAg** are much weaker than the frontal $\pi\cdots\pi$ interactions between pyrene and bpb bridging ligand in **FebpbAg·Pyr** giving rise to a weaker fluorescence signal of the excimer. This might be the reason why the synergy between the spin state and the luminescence is much more significant for **FebpbAg·Pyr** than for **FebpanAg**. Moreover, a third aspect to take into account is that the excimer signal in both **FebpbAg·Pyr** and **FebpanAg** could be partially affected by self-concentration quenching. However, the large Stokes shift between the monomer absorption and excimer emission signals make it rather unlikely.

Likewise, in the case of **FebpbAg·Pyr** the relative intensity of the excimer signal increases very significantly, with respect to that of the monomer, upon photoexcitation at low temperature (LIESST effect, λ^{irr} = 532 nm) due to the LS to HS photoconversion. This was previously observed for **FebpbenAu·Pyr**.[32] Hence, further experiments will be carried out in the future in

Published on 19 December 2019. Downloaded by Universitat de València on 5/11/2021 3:01:49 PM.

this respect to study the thermal dependence of the HS to LS relaxation after LIESST probed by fluorescence measurements. Comparison with analogous results obtained by absorption spectroscopy would provide a different approach to study the SCO-luminescence synergy.

The differences in the SCO-fluorescence coupling when considering either an intrinsic or an extrinsic luminescent 3D Hofmann-type compound is difficult to rationalize because even if the quantum yield of the luminophores are similar (0.36 and 0.32 for anthracene and pyrene respectively in cyclohexane)[45] and the oscillator strength of the acceptors are comparable, the synergy strongly depends on the geometry of the whole arrangement. In this sense, the extrinsic luminescence obtained through the insertion of different guest fluorescent molecules such as pyrene seems very promising due to the capacity of controlling the geometry and, in consequence, the guest–guest, guest–ligand and guest–Fe^{II} distances. Nonetheless, the nature of the energy transfer processes occurring based on the location of the luminophore and SCO centres within the structure plays a key role in the deep understanding of the parameters governing the SCO-luminescence synergy. In this sense, the change of the luminescence lifetimes and quantum yields of the luminophore depend upon incorporation into the Fe^{II} SCO 3D network. In addition, the comparison of results with the equivalent non-switchable material based on Zn^{II} would give an idea of the extent of non-radiative energy transfer involved in the synergy and of the importance of the lattice rigidity in the quantum yield values. In principle, stiffness is expected to prevent non-radiative decays hence leading to higher quantum yield.[27,46] Thus, further studies will be directed towards analysing the luminescence lifetime and the quantum yield of the studied compounds as a function of the spin fraction.

Conflicts of interest

There are no conflicts to declare.

Acknowledgements

Financial support from the Spanish Ministerio de Economía y Competitividad (MINECO) and FEDER funds (CTQ2016-78341-P and Unidad de Excelencia María de Maeztu MDM-2015-0538), the Generalitat Valenciana (PROMETEO/2016/147) and the Swiss National Science Foundation (Grant No 200020_152780). M. M.-S. thanks MINECO for a predoctoral FPI grant.

Notes and references

1 P. Gütlich, A. Hauser and H. Spiering, *Angew. Chem., Int. Ed. Engl.*, 1994, **33**, 2024–2054.
2 J. A. Real, A. B. Gaspar, V. Niel and M. C. Muñoz, *Coord. Chem. Rev.*, 2003, **236**, 121–141.
3 (*a*) P. Gütlich and G. Goodwin, *Top. Curr. Chem.*, 2004, **233**, 234–235; (*b*) J. A. Real, A. B. Gaspar and M. C. Muñoz, *Dalton Trans.*, 2005, 2062–2079; (*c*) *Spin-Crossover Materials: Properties and Applications*, ed. M. A. Halcrow, John Wiley & Sons Ltd, Chichester, 2013; (*d*) see special issue in Comptes Rendues "Spin crossover phenomenon" A. Bousseksou, *C. R. Chim.*, 2018, **21**, 1152–1169; (*e*) P. Gütlich, Y. Garcia and H. A. Goodwin, *Chem. Soc. Rev.*, 2000, **29**, 419–427.
4 J.-F. Létard, P. Guionneau and L. Goux-Capes, *Spin Crossover Transit. Met. Compd III*, 2004, **1**, 221–249.
5 A. Bousseksou, G. Molnár, L. Salmon and W. Nicolazzi, *Chem. Soc. Rev.*, 2011, **40**, 3313.
6 M. Matsuda, H. Isozaki and H. Tajima, *Thin Solid Films*, 2008, **517**, 1465–1467.
7 L. Salmon, G. Molnár, D. Zitouni, C. Quintero, C. Bergaud, J.-C. Micheau and A. Bousseksou, *J. Mater. Chem.*, 2010, **20**, 5499.
8 S. Bertazzo and K. Rezwan, *Langmuir*, 2010, **26**, 3364–3371.
9 C. M. Quintero, I. A. Gural'skiy, L. Salmon, G. Molnár, C. Bergaud and A. Bousseksou, *J. Mater. Chem.*, 2012, **22**, 3745.
10 I. Suleimanov, O. Kraieva, G. Molnar, L. Salmon and A. Bousseksou, *Chem. Commun.*, 2015, **51**, 15098–15101.
11 J. M. Herrera, S. Titos-Padilla, S. J. A. Pope, I. Berlanga, F. Zamora, J. J. Delgado, K. V. Kamenev, X. Wang, A. Prescimone, E. K. Brechin and E. Colacio, *J. Mater. Chem. C*, 2015, **3**, 7819–7829.
12 I. Suleimanov, O. Kraieva, G. Molnár, L. Salmon and A. Bousseksou, *Chem. Commun.*, 2015, **51**, 15098–15101.
13 I. Suleimanov, O. Kraieva, J. Sánchez Costa, I. O. Fritsky, G. Molnár, L. Salmon and A. Bousseksou, *J. Mater. Chem. C*, 2015, **3**, 5026–5032.
14 S. Titos-Padilla, J. M. Herrera, X.-W. Chen, J. J. Delgado and E. Colacio, *Angew. Chem., Int. Ed.*, 2011, **50**, 3290–3293.
15 B. Benaicha, K. Van Do, A. Yangui, N. Pittala, A. Lusson, M. Sy, G. Bouchez, H. Fourati, C. J. Gómez-García, S. Triki and K. Boukheddaden, *Chem. Sci.*, 2019, **10**, 6791–6798.
16 J. Yuan, S.-Q. Wu, M.-J. Liu, O. Sato and H.-Z. Kou, *J. Am. Chem. Soc.*, 2018, **140**, 9426–9433.
17 J.-L. Wang, Q. Liu, Y.-S. Meng, X. Liu, H. Zheng, Q. Shi, C.-Y. Duan and T. Liu, *Chem. Sci.*, 2018, **9**, 2892–2897.
18 C. Lochenie, K. Schö Tz, F. Panzer, H. Kurz, B. Maier, F. Puchtler, S. Agarwal, A. Kö and B. Weber, *J. Am. Chem. Soc.*, 2018, **140**, 700–709.
19 B. Schäfer, T. Bauer, I. Faus, J. A. Wolny, F. Dahms, O. Fuhr, S. Lebedkin, H.-C. Wille, K. Schlage, K. Chevalier, F. Rupp, R. Diller, V. Schünemann, M. M. Kappes and M. Ruben, *Dalton Trans.*, 2017, **46**, 2289–2302.
20 C.-F. Wang, R.-F. Li, X.-Y. Chen, R.-J. Wei, L.-S. Zheng and J. Tao, *Angew. Chem., Int. Ed.*, 2015, **54**, 1574–1577.
21 Y. Garcia, F.-O. Robert, A. D. Naik, G. Zhou, B. Tinant, K. Robeyns, S. Ebastien Michotte and L. Piraux, *J. Am. Chem. Soc.*, 2011, **133**(40), 15850–15853.
22 M. Hasegawa, F. Renz, T. Hara, Y. Kikuchi, Y. Fukuda, J. Okubo, T. Hoshi and W. Linert, *Chem. Phys.*, 2002, **277**, 21–30.
23 C. Piguet, E. Rivara-Minten, G. Bernardinelli, J.-C. G. Bünzli and G. Hopfgartner, *J. Am. Chem. Soc.*, 1997, 421–433.
24 C. Piguet, E. Rivara-Minten, G. Hopfgartner and J.-C. G. Bünzli, *Helv. Chim. Acta*, 1995, **78**, 1651–1672.
25 J.-Y. Ge, Z. Chen, L. Zhang, X. Liang, J. Su, M. Kurmoo and J.-L. Zuo, *Angew. Chem., Int. Ed.*, 2019, **58**, 8789–8793.

 This journal is © The Royal Society of Chemistry 2020

Published on 19 December 2019. Downloaded by Universitat de València on 5/11/2021 3:01:49 PM.

26 H. Matsukizono, K. Kuroiwa and N. Kimizuka, *Chem. Lett.*, 2008, **37**, 446–447.
27 H. J. Shepherd, C. M. Quintero, G. Molnár, L. Salmon and A. Bousseksou, *Spin-Crossover Materials*, John Wiley & Sons Ltd, Oxford, UK, 2013, pp. 347–373.
28 Y. Garcia, V. Niel, M. C. Muñoz and J. A. Real, *Top. Curr. Chem.*, 2004, **233**, 229–257.
29 M. C. Muñoz and J. A. Real, *Coord. Chem. Rev.*, 2011, **255**(17–18), 2068–2093.
30 R. Ohtani and S. Hayami, *Chem. – Eur. J*, 2017, **23**(10), 2236–2248.
31 Z.-P. Ni, J.-L. Liu, M. M. Hoque, W. Liu, J.-Y. Li, Y.-C. Chen and M.-L. Tong, *Coord. Chem. Rev.*, 2017, **335**, 28–43.
32 T. Delgado, M. Meneses-Sánchez, L. Piñeiro-López, C. Bartual-Murgui, M. C. Muñoz and J. A. Real, *Chem. Sci.*, 2018, **9**, 8446–8452.
33 L. Vegard, *Z. Kristallogr. – Cryst. Mater.*, 1928, **67**, 239–259.
34 B. R. Mullaney, L. Goux-Capes, D. J. Price, G. Chastanet, J. F. Létard and C. J. Kepert, *Nat. Commun.*, 2017, **8**, 1053.
35 M. A. Slifkin, *Nature*, 1963, **200**, 766–767.
36 M. Sugino, Y. Araki, K. Hatanaka, I. Hisaki, M. Miyata and N. Tohnai, *Cryst. Growth Des.*, 2013, **13**, 4986–4992.
37 R. Akatsuka, A. Momotake, Y. Shinohara, Y. Kanna, T. Sato, M. Moriyama, K. Takahashi, Y. Nishimura and T. Arai, *J. Photochem. Photobiol., A*, 2011, **223**, 1–5.
38 C. Tang, X. Zhu, Y. Song, W. Liu, Q. Yang, Z. Lv and Y. Yang, *J. Photochem. Photobiol., A*, 2019, **376**, 263–268.
39 H. G. O. Becker, *J. Prakt. Chem./Chem.-Ztg.*, 1980, **322**, 704.
40 J. C. Lindon, G. E. Tranter and D. W. Koppenaal, *Encyclopedia of spectroscopy and spectrometry*, Academic Press, Oxford, 3rd edn, 2017, pp. 636–653.
41 T. Z. Janosi, J. Korppi-Tommola, Z. Csok, L. Kollar, P. Myllyperkio and J. Erostyak, *J. Spectrosc.*, 2014, **2014**, 1–8.
42 L. Piñeiro-López, M. Seredyuk, M. C. Muñoz and J. A. Real, *Chem. Commun.*, 2014, **50**, 1833–1835.
43 L. Piñeiro-López, F. J. Valverde-Muñoz, M. Seredyuk, M. C. Muñoz, M. Haukka and J. A. Real, *Inorg. Chem.*, 2017, **56**, 7038–7047.
44 M. Paez-Espejo, M. Sy and K. Boukheddaden, *J. Am. Chem. Soc.*, 2016, **138**, 3202–3210.
45 Oregon Medical Laser Center.org, https://omlc.org/.
46 A. S. Marfunin, *Spectroscopy, Luminescence and Radiation Centers in Minerals*, Springer-Verlag, Berlin, Germany, 1979, p. 352.

Inorganic Chemistry

pubs.acs.org/IC

Featured Article

Enhanced Interplay between Host−Guest and Spin-Crossover Properties through the Introduction of an N Heteroatom in 2D Hofmann Clathrates

Manuel Meneses-Sánchez, Rubén Turo-Cortés, Carlos Bartual-Murgui,* Iván da Silva, M. Carmen Muñoz, and José Antonio Real*

Cite This: *Inorg. Chem.* 2021, 60, 11866−11877

Read Online

ACCESS | Metrics & More | Article Recommendations | Supporting Information

ABSTRACT: Controlled modulation of the spin-crossover (SCO) behavior through the sorption−desorption of invited molecules is an extensively exploited topic because of its potential applications in molecular sensing. For this purpose, understanding the mechanisms by which the spin-switching properties are altered by guest molecules is of paramount importance. Here, we show an experimental approach revealing a direct probe of how the interplay between SCO and host−guest chemistry is noticeably activated by chemically tuning the host structure. Thus, the axial ligand 4-phenylpyridine (4-PhPy) in the 2D Hofmann clathrates $\{Fe(4\text{-PhPy})_2[M(CN)_4]\}$ (**PhPyM**; M = Pt, Pd) is replaced by 2,4-bipyridine (2,4-Bipy), resulting in the isomorphous compounds $\{Fe(2,4\text{-Bipy})_2[M(CN)_4]\}$ (**BipyM**; M = Pt, Pd), which basically differ from the former in that they have a noncoordinated N heteroatom in the ancillary aromatic substituent, i.e., 2-pyridyl instead of phenyl. Our chemical, magnetic, calorimetric, and structural characterizations demonstrate that this subtle chemical composition change provokes outstanding modifications not only in the capability to adsorb small guests as water or methanol but also in the extent to which these guests affect the SCO characteristics.

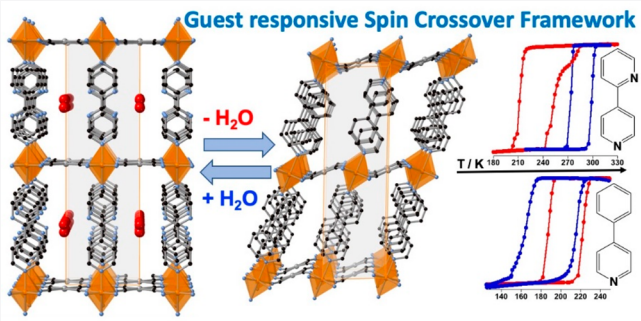

■ INTRODUCTION

The spin-crossover (SCO) behavior is essentially a molecular phenomenon exhibited by some octahedral transition-metal complexes with electronic configurations $3d^4$−$3d^7$ that involves the reversible, controllable, and detectable switching between the low-spin (LS) and high-spin (HS) states.[1,2] This switchable behavior has predominantly been studied for hexacoordinated $\{Fe^{II}N_6\}$ $3d^6$ complexes because a large number of common N-donor ligands accomplish the necessary condition; i.e., the energy balance between the ligand-field strength and the interelectronic repulsion is of the order of magnitude of k_BT.[3−5] The HS ↔ LS switching can be triggered by a series of external stimuli (temperature, pressure, light, guest analytes, etc.), implicating remarkable variations of the optical, structural, magnetic, and electric properties. Interestingly, this external perturbation−physical signal change coupling, together with the possibility of obtaining nanometric architectures,[6] is the basis for potential applications of SCO materials in areas of chemical sensing, switching devices, display, or information storage.[7−10] However, from an application-perspective point of view, the SCO requires, in general, a high degree of cooperativity within the crystalline network. Cooperativity stems from long-range elastic interactions between the SCO centers in such a way that the spin-state change is efficiently transmitted within the material.[3] Hence, cooperative thermally driven SCO materials may exhibit abrupt or even hysteretic γ_{HS} versus T curves (γ_{HS} = HS-state molar fraction), giving way to bistable properties. In the last 2 decades, chemists have made many efforts in order to achieve strong bistable SCO compounds. To do so, the synthesis of extended 1−3D coordination polymers (CPs), in which the SCO centers are connected by coordination/covalent bonds, has been one of the main synthetic strategies.[11,12]

Fe^{II} Hofmann-type CPs (Fe^{II}-HCPs) have been one the most investigated classes of CPs within the SCO community. From the vast family of reported Fe^{II}-HCPs, those frameworks presenting the general formula $\{Fe^{II}(L)_x[M^{II}(CN)_4]\}$ (x = 2 or 1 for 2D or 3D systems, respectively) are constituted of bimetallic layers where the Fe^{II} ions are connected through $[M^{II}(CN)_4]^{2-}$ anions (M = Pt, Pd, Ni).[13,14] The cyanome-

Received: June 25, 2021
Published: August 4, 2021

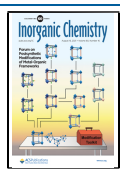

Downloaded via UNIV DE VALENCIA on October 25, 2021 at 10:51:33 (UTC).
See https://pubs.acs.org/sharingguidelines for options on how to legitimately share published articles.

ACS Publications © 2021 American Chemical Society

https://doi.org/10.1021/acs.inorgchem.1c01925
Inorg. Chem. 2021, 60, 11866−11877

tallate-based layers are stacked in such a way that the organic axial ligands (L; typically substituted pyridines or triazole-based ligands) either are monodentate and interdigitated in the case of 2D networks or act as bis-monodentate bridges between adjacent layers for 3D derivatives. One of the reasons explaining the strong interest raised by Fe^{II}-HCPs in the last years lies in the intrinsic porosity (or guest-induced porosity) offered by their networks and the possibility of decorating their pores through chemical functionalization. This feature, which has been studied mainly for 3D systems because of their permanent porosity, permits the uptake of a high variety of guest molecules, which, in turn, are capable of modulating the SCO properties of the HCP.[15,16] The mechanism by which the SCO is modulated through a guest molecule depends on the nature of the interactions established between the host framework and adsorbed molecule. For example, trapped bulky guests in the 3D Fe^{II}-HCP $\{Fe(Pz)[Pt(CN)_4]\}$ (Pz = pyrazine) generate steric hindrance, tending to stabilize the HS state.[17] Conversely, other specific host−guest interactions operating in the same framework lead to stabilization of the LS state, likely due to indirect modification of the ligand-field strength of the Fe^{II} center.

Because of their interdigitated nature and therefore the lack of porosity, guest effect studies on 2D Fe^{II}-HCP SCO systems are scarce and rather limited to the inclusion of small guest molecules such as water (H_2O) or ethanol (EtOH). Often, the presence of these guests provokes elastic frustration, namely, the hindering of the metal−organic framework's natural expansion−contraction during the HS ↔ LS transition, which usually is reflected on a decrease of the SCO temperature and/or multistepped SCO behavior.[18−27] An increase of the SCO temperature upon H_2O adsorption was only observed in compound $\{Fe(thtrz)_2[Pd(CN)_4]\}$ and attributed to modification of the ligand-field strength of Fe^{II} via host−guest interactions.[18] Recently, SCO modulation of the flexible 2D Fe^{II}-HCP $\{Fe(5\text{-}NH_2Pym)_2[M^{II}(CN)_4]\}$ (5-NH_2Pym = 5-aminopyrimidine; M^{II} = Pt, Pd) mediated by the adsorption of H_2O, methanol (MeOH), or EtOH was reported and justified by both electronic and steric effects operating between the protic guest molecules and 5-NH_2Pym axial ligands.[28] A similar guest effect was found in the related family of 2D porous compounds$\{Fe^{II}(NCS)_2(L)_2\}$·guest [L = 1,2-bis(4′-pyridyl)ethene (tvp),[29] 4,4′-azopyridine (azpy),[30] 2,3-bis(4′-pyridyl)-2,3-butanediol (bpbd),[31,32] 1,2-bis(4′-pyridyl)-1,2-ethanediol (bped),[33] 1,2-bis(4′pyridyl)ethane (bpe);[34] guest = acetonitrile, acetone, MeOH, EtOH, and 1-propanol], whose modifications of the SCO temperature and hysteresis width were related to specific host−guest interactions involving the L bridging ligand. All of these results indicate that functionalization of the host framework is crucial not only to promoting the binding of the guest molecule to the host framework but also to modifying through this interaction the SCO characteristics in a controlled manner.

Aiming at providing new insights regarding the influence of host−guest interactions over the SCO behavior, here we report on a comparative study of two closely related series of 2D Fe^{II}-HCPs generically formulated as $\{Fe^{II}(L)_2[M^{II}(CN)_4]\cdot nG$, with L = 4-phenylpyridine (4-PhPy) or 2,4-bipyridine (2,4-Bipy) (Scheme 1), M^{II} = Pd or Pt, and G = H_2O and/or MeOH. Both series differ from each other by the presence or absence of a peripheral noncoordinated N heteroatom in the ancillary aromatic ring (phenyl or 2-pyridine). Although the SCO properties of the unsolvated 4-PhPy derivatives were investigated in a precedent work,[35] their structures and foreseeable structural changes stemming from the presence/absence of guests as well as their correlation with the SCO properties have remained unknown so far. Consequently, here we analyze the structural, magnetic, and guest adsorption properties of the unsolvated and solvated forms of both series of compounds. Our results show the following: (i) from ab initio X-ray structural determinations, the unsolvated $\{Fe^{II}(4\text{-}PhPy)_2[M^{II}(CN)_4]$ (**PhPyM**; M = Pd, Pt) and $\{Fe^{II}(2,4\text{-}Bipy)_2[M^{II}(CN)_4]$ (**BipyM**; M = Pd, Pt) forms are isostructural; (ii) the presence of the N heteroatom in **BipyM** enhances considerably its sensing properties with respect to those of **PhPyM** because of the generation of stronger intermolecular interactions with the adsorbed guest molecules; (iii) single-crystal analyses of the corresponding solvated forms for both series of compounds show the occurrence of noticeable structural modifications, which, in turn, have a remarkable impact over the SCO behavior.

Scheme 1. Ligands Employed in This Work: 4-PhPy and 2,4-Bipy

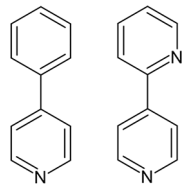

■ EXPERIMENTAL SECTION

Synthesis. The 4-PhPy and 2,4-Bipy ligands are commercially available and were purchased from Acros Organics and Apollo Scientific, respectively.

Single crystals of **PhPyM·*x*MeOH·*y*H_2O** (M = Pd, Pt) were obtained by slow diffusion techniques. A solution of $Fe(BF_4)_2\cdot 6H_2O$ (33.8 mg, 0.1 mmol) and the 4-PhPy ligand (31.0 mg, 0.2 mmol) in 2 mL of H_2O/MeOH (2:1) was placed in one side of an H-shaped vessel, whereas a solution of $K_2[M(CN)_4]$ [M = Pd (28.9 mg, 0.1 mmol), Pt (43.1 mg, 0.1 mmol)] in 2 mL of H_2O was placed in the other side. Finally, the vessel was filled with a mixture of H_2O/MeOH (1:1) and sealed with parafilm. Yellow square-plate single crystals were obtained in 1 week with a yield of ca. 50%. Anal. Calcd for **PhPyPt** [$C_{26}H_{18}FeN_6Pt$ (665.4)]: C, 46.93; H, 2.73; N, 12.63. Found: C, 46.24; H, 2.81; N, 12.42. Anal. Calcd for **PhPyPd** [$C_{26}H_{18}FeN_6Pd$ (576.7)]: C, 54.15; H, 3.15; N, 14.57. Found: C, 53.23; H, 3.26; N, 14.31.

Single crystals of **BipyM·H_2O** (M = Pd, Pt) were obtained by slow diffusion techniques. A solution of $Fe(BF_4)_2\cdot 6H_2O$ (33.8 mg, 0.1 mmol) and the 2,4-Bipy ligand (31.2 mg, 0.2 mmol) in 2 mL of H_2O/MeOH (3:1) was placed in one side of a H-shaped vessel, whereas a solution of $K_2M(CN)_4$ [M = Pd (28.9 mg, 0.1 mmol), Pt (43.1 mg, 0.1 mmol)] in 2 mL of H_2O was placed in the other side. Finally, the vessel was filled with a mixture of H_2O/MeOH (1:1) and sealed with parafilm. Yellow square-plate single crystals were obtained in 1 week with a yield ca. 50%. Anal. Calcd for **BipyPt·H_2O** [$C_{24}H_{18}FeN_8OPt$ (685.4)]: C, 42.06; H, 2.65; N, 16.35. Found: C, 41.88; H, 2.51; N, 16.48. Anal. Calcd for **BipyPd·H_2O** [$C_{24}H_{18}FeN_8OPd$ (596.7)]: C, 48.31; H, 3.04; N, 18.78. Found: C, 48.49; H, 2.92; N, 19.02.

Physical Measurements. *Magnetic Measurements.* Variable-temperature magnetic susceptibility data were recorded with a Quantum Design MPMS2 SQUID magnetometer equipped with a 7 T magnet, operating at 1 T and at temperatures 50−400 K using a scan rate of 2 K min^{-1}. Experimental susceptibilities were corrected for diamagnetism of the constituent atoms using Pascal's constants.

https://doi.org/10.1021/acs.inorgchem.1c01925
Inorg. Chem. 2021, 60, 11866−11877

Calorimetric measurements were performed using a Mettler Toledo DSC 821e differential scanning calorimeter. Low temperatures were obtained with an aluminum block attached to the sample holder, refrigerated with a flow of liquid nitrogen, and stabilized at a temperature of 110 K. The sample holder was kept in a drybox under a flow of dry nitrogen gas to avoid H_2O condensation. The measurements were carried out using around 15 mg of a microcrystalline sample sealed in aluminum pans with a mechanical crimp. Temperature and heat-flow calibrations were made with standard samples of indium by using its melting transition (429.6 K; 28.45 J g^{-1}). An overall accuracy of ±0.2 K in the temperature and ±2% in the heat capacity is estimated. The uncertainty increases for determination of the anomalous enthalpy and entropy due to the subtraction of an unknown baseline.

Single-Crystal X-ray Diffraction. Single-crystal X-ray diffraction data were collected on an Oxford Diffraction Supernova diffractometer using graphite-monochromated Mo Kα radiation (λ = 0.71073 Å). A multiscan absorption correction was performed. The structures were solved by direct methods using *SHELXS-2014* and refined by full-matrix least squares on F^2 using *SHELXL-2014*.[36] Non-H atoms were refined anisotropically, and H atoms were placed in calculated positions refined using idealized geometries (riding model) and assigned to fixed isotropic displacement parameters. All details can be found in CCDC 2090594 (**BipyPt·H_2O**_120 K), 2090595 (**BipyPd·H_2O**), 2090596 (**PhPyPd·MeOH·0.5H_2O**), 2090599 (**BipyPt·H_2O·MeOH**), 2090600 (**PhPyPd·MeOH·0.5H_2O**), and 2090601 (**BipyPt·H_2O**_283 K), which contain the supplementary crystallographic data for this paper.

Powder X-ray Diffraction (PXRD). Measurements were performed on a PANalytical Empyrean powder X-ray diffractometer (monochromatic Cu Kα radiation) in capillary measurement mode. Because of the spontaneous rehydration of **BipyPt** and **BipyPd**, these samples were prepared by heating the hydrated forms into open capillaries inside an oven at 120 °C for 1 h and rapidly sealing them to keep air from entering. Crystal structures of compounds **PhPyM** and **BipyM** were solved ab initio using the *Topas Academic v6* program (http://www.topas-academic.net/). Very similar monoclinic unit cell parameters were found for both cases, and the atomic positions of the Pt and Fe atoms were located using the charge-flipping method.[37] Subsequent difference Fourier maps showed the missing electron densities for the cyanide and organic ligand, which were located at the expected positions (using the corresponding solvated crystal structures as description models). The final Rietveld[38] refinements, which showed excellent agreement between the calculated and experimental patterns, included restraints on the Pt/Fe−cyanide and Fe−organic ligand distances; the organic ligand was described by applying a semirigid body description. All details can be found in CCDC 2090597 (**PhPyPt**) and 2090598 (**BipyPt**).

Elemental Analyses. C, H, and N analyses were performed with a CE Instruments EA 1110 CHNS elemental analyzer.

Thermogravimetric analysis (TGA) experiments were carried out with a TA Instruments TGA550 device equipped with a Pt/Rh oven (T_{max} = 1000 °C). The time-dependent TGA experiments were performed by connecting the TGA apparatus to a flow mass controller. Thus, humid air was passed at room pressure and a temperature of 30 °C and driven into the TGA chamber, where a previously desolvated sample of **BipyPt** or **BipyPd** was mounted in a Pt pan.

■ RESULTS

Synthesis and Chemical Characterization. Single crystals of **PhPyM·*x*MeOH·*y*H_2O** and **BipyM·H_2O** (M = Pt, Pd) were grown by liquid−liquid slow diffusion using H-shaped tubes containing, on the one side, a H_2O/MeOH solution of a Fe^{II}-4-PhPy or -2,4-Bipy mixture and, on the other side, an aqueous solution of the corresponding $[M(CN)_4]^{2-}$ potassium salt (see the Experimental Section for more details).

PXRD (Figure S1) and magnetic measurements (vide infra) of pristine crystals of **PhPyM·*x*MeOH·*y*H_2O** soaked in the mother liquor indicate that the synthesis method affords an imprecise mixture of solvates with x and y in the intervals 0−1 and 0−0.5, respectively. Only the crystal structure of the majority component of these solvates was successfully identified and presents the formula **PhPyM·MeOH·0.5H_2O**. Once removed from the mother liquor, crystals of **PhPyM·*x*MeOH·*y*H_2O** spontaneously desorb most of the guest molecules, provoking a total loss of crystallinity. This was confirmed by elemental analysis, PXRD, TGA (see the Experimental Section and Figures S1 and S2), and magnetic measurements (vide infra). Indeed, according to TGA, only an equivalent weight of 0.2−0.4 molecules of H_2O remains in the dried samples at ambient conditions. Besides, solvent-free **PhPyM** derivatives are easily obtained from a thermal treatment at 400 K for 10 min. In view of the changes detected in the PXRD patterns upon solvent desorption (Figure S1), the loss of guest molecules is accompanied by relevant structural changes.

It is worth noting that **PhPyM** does not readsorb H_2O from air moisture. This was deduced from TGA measurements performed on desorbed **PhPyM** samples exposed to air for several days, which showed no mass loss up to 530 K when the structures start to decompose (Figure S2).

Chemical characterization of **BipyM·H_2O** (M = Pt, Pd) shows that the guest H_2O molecule is retained within the structure once the samples are removed from the mother liquor and exposed at ambient conditions (see elemental analysis, PXRD patterns, and TGA measurements in the Experimental Section and Figures S3 and S4, respectively). Nonetheless, according to the TGA measurements (Figure S4), the H_2O molecule can be easily desorbed with gentle heating above 300 K, giving rise to the dehydrated **BipyM** counterparts. Similar to that observed in **PhPyM**, H_2O desorption provokes relevant structural modifications in view of the differences detected from the PXRD patterns of the solvated and desolvated compounds (Figure S3).

TGA studies show, in contrast to that observed for **PhPyM**, that both **BipyPt** and **BipyPd** are capable of gradually readsorbing one molecule of H_2O per Fe^{II} ion from air moisture. Indeed, the H_2O readsorption monitored in situ by

Scheme 2. Adsorption and Desorption Processes Observed for Compounds PhPyM·*x*MeOH·*y*H_2O and BipyM·H_2O upon Different Treatments

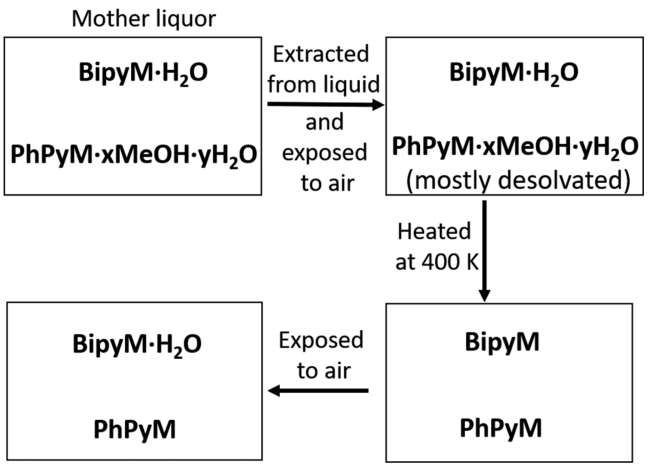

https://doi.org/10.1021/acs.inorgchem.1c01925
Inorg. Chem. 2021, 60, 11866−11877

TGA reveals that **BipyM** recovers the original monohydrated phase in less than 1 h (see Scheme 2 and Figure S5). Importantly, the close similarity between the PXRD patterns of compounds **PhPyM** and **BipyM** (Figure S6) points out that the corresponding desorbed phases are isostructural.

Magnetic Characterization. *SCO Properties of **PhPyM·xMeOH·yH$_2$O** and **BipyM·H$_2$O** (M = Pt, Pd).* Figure 1 displays the thermal dependence of $\chi_M T$ (where χ_M is the molar magnetic susceptibility and T is the temperature) for **PhPyM·*x*MeOH·*y*H$_2$O** and **BipyM·H$_2$O** and for their respective complete desolvated forms ($\chi_M T$ vs T plots of the partially desolvated **PhPyM·*x*MeOH·*y*H$_2$O** forms are shown in Figure S7). In order to monitor the SCO behavior of the pristine solvated forms and considering their propensity to lose the included solvent molecules, the magnetic properties were measured soaked in their mother liquor (open circles in Figure 1a,b). At 240 K, $\chi_M T$ is ca. 3.5 cm^3 K mol^{-1} for compound **PhPyPt·*x*MeOH·*y*H$_2$O**, which is assignable to a fully HS (S = 2) Fe^{II} ion (Figure 1a). This value remains practically constant within the temperature range 240−50 K, proving that this compound does not exhibit SCO properties. Similarly, compound **PhPyPd·*x*MeOH·*y*H$_2$O** shows a $\chi_M T$ value of 3.5 cm^3 K mol^{-1} between 300 and 170 K (Figure 1b). However, below this temperature, $\chi_M T$ decreases abruptly by 0.5 cm^3 K mol^{-1} ($T^{\downarrow}_{1/2}$ = 164 K), denoting the occurrence of a HS-to-LS transition involving ca. 14% of the Fe^{II} centers. In the heating mode, the $\chi_M T$ versus T plot does not match the cooling mode, with the latter being more gradual and shifted to higher temperatures ($T^{\uparrow}_{1/2}$ = 185 K), thereby defining an asymmetric hysteresis loop with $T_{1/2}$ = 174.5 K and ΔT = 21 K [$T^{\downarrow}_{1/2}/T^{\uparrow}_{1/2}$ are the equilibrium temperatures at which 50% of the SCO-active Fe^{II} ions have changed from spin state during the cooling/heating modes, $T_{1/2} = (T^{\uparrow}_{1/2} + T^{\downarrow}_{1/2})/2$, and ΔT is the hysteresis width $T^{\uparrow}_{1/2} - T^{\downarrow}_{1/2}$].

As was already mentioned, removing crystals of **PhPyM·*x*MeOH·*y*H$_2$O** (M = Pt, Pd) from their mother liquor provokes instantaneous loss of most of the guest molecules (Figure S2), causing important modifications in the magnetic properties of both the Pt and Pd derivatives. Indeed, the SCO of both air-dried samples defines an almost complete and asymmetric hysteresis loop characterized by a double step in the cooling mode ($T^{\downarrow 1}_{1/2}$ = 202 K and $T^{\downarrow 2}_{1/2}$ = 180 K for Pt; $T^{\downarrow 1}_{1/2}$ = 182 K and $T^{\downarrow 2}_{1/2}$ = 163 K for Pd) and a single step in the heating mode ($T^{\uparrow}_{1/2}$ = 218 K, ΔT^1 = 16 K, and ΔT^2 = 38 K for Pt; $T^{\uparrow}_{1/2}$ = 200 K, ΔT^1 = 18 K, and ΔT^2 = 37 K for Pt) (Figure S7). The subsequent treatment at 400 K for 1 h leads to the completely desorbed forms **PhPyPt** and **PhPyPd**, which exhibit abrupt, complete, and hysteretic one-step spin transitions with $T_{1/2}/\Delta T$ of 204/36 K and 185/29 K, respectively (filled circles in Figure 1a,b). These curves were perfectly reproduced for the same samples several days after exposure to ambient conditions (Figure S8), confirming, in good agreement with the TGA studies (Figure S2), that these compounds are not prone to readsorb H$_2$O from air moisture.

Freshly prepared soaked crystals of **BipyM·H$_2$O** (M = Pt, Pd) exhibit abrupt, complete, and hysteretic spin transitions centered at room temperature with $T_{1/2}/\Delta T$ of 286.5/25 K and 282.5/35 K, respectively (open circles in Figure 1c,d). According to the TGA data (Figure S4), the H$_2$O molecule included in **BipyPt·H$_2$O** and **BipyPd·H$_2$O** is retained at $T \leq$ 300 K in contact with air. Consequently, to ensure the retention of H$_2$O and considering the dry atmosphere and vacuum conditions of the SQUID chamber, the magnetic properties of the air-dried samples were checked first in the temperature sequence 290−220 K in order to compare them with those of the soaked samples. As expected, the SCO curves recorded upon cooling [$T^{\downarrow}_{1/2}$ = 272 K (Pt) and 273 K (Pd); Figure S9] are close to those obtained for the crystals soaked in the mother liquor [275 K (Pt) and 266 K (Pd)], confirming

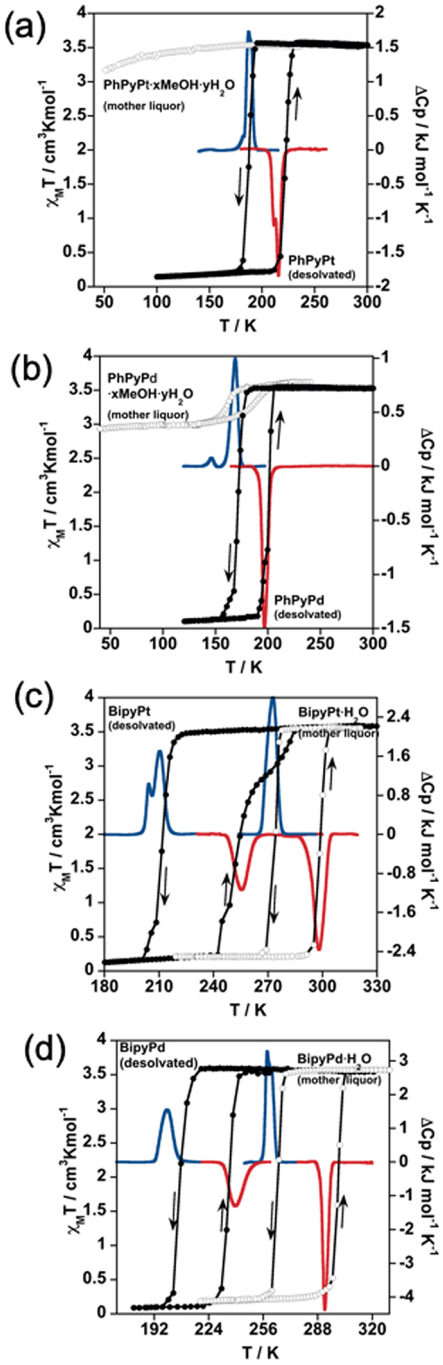

Figure 1. Thermal dependence of $\chi_M T$ for: (i) **PhPyM·*x*MeOH·*y*H$_2$O** [M = Pt (a), Pd (b)] measured in the mother liquor (open circles) and after treatment at 400 K for 1 h (filled circles) and (ii) **BipyM·H$_2$O** [M = Pt (c), Pd (d)] measured in the mother liquor (open circles) and after treatment at 400 K for 1 h (filled circles). Calorimetric measurements in the cooling (blue curves) and heating (red curves) modes of the desolvated counterparts of **PhPyPt** (a), **PhPyPd** (b), **BipyPt** (c), and **BipyPd** (d) and the hydrated air-dried products of **BipyPt·H$_2$O** (c) and **BipyPd·H$_2$O** (d).

https://doi.org/10.1021/acs.inorgchem.1c01925
Inorg. Chem. 2021, 60, 11866−11877

that the H_2O molecule persists within the structure at ambient conditions. In order to analyze the heating branch, $\chi_M T$ was measured in the temperature range 220−320 K, obtaining $T_{1/2}^{\uparrow}$ values of 303 K (Pt) and 293 K (Pd). The resulting SCO curves are very similar to those of the soaked samples (Figure S9), suggesting that, although the solvates can be subjected to dehydration during the process of heating above 300 K, either the effective desolvation must be very small or it does not affect the $T_{1/2}^{\uparrow}$ value. When compounds **BipyPt·H$_2$O/BipyPd·H$_2$O** are heated at 400 K for 1 h inside the SQUID magnetometer, the H_2O molecule is totally evacuated, affording the desorbed counterparts **BipyPt/BipyPd**. The dehydrated derivatives also display strongly cooperative SCO behaviors (filled circles in Figure 1c,d) but dramatically downshifted in temperature by 54 K (Pt) and 61.5 K (Pd) with respect to their corresponding hydrated counterparts. Nevertheless, the hysteresis widths are overall maintained (ΔT = 41/28 K for **BipyPt/BipyPd**). In good agreement with the TGA measurements, the room temperature centered SCO curves of the original monohydrated derivatives are completely recovered when the desorbed samples are exposed to air for ca. 1 h (Figure S10).

In order to investigate the capability of the unsolvated samples to reinclude MeOH or H_2O molecules in the structure and to assess the degree of reversibility of the magnetic behavior described above, the desolvated **PhPyM** and **BipyM** derivatives were dispersed in MeOH or H_2O for several hours. In order to evaluate the eventual structural changes associated with the adsorption processes, PXRD patterns were performed for the solids immersed in the corresponding solvents (Figures S11 and S12). The results show the occurrence of important modifications in the patterns of both **PhPyM** and **BipyM** when they are soaked in MeOH. In particular, the shift of the 002 peak centered around 7.6° toward lower 2θ values reflects an increase in separation between two consecutive bimetallic layers as a consequence of inclusion of the MeOH molecule. Besides, whereas noticeable modifications of the patterns of **BipyM** soaked in H_2O confirm the adsorption of H_2O in this network, patterns of **PhPyM** are virtually unchanged in H_2O, indicating a negligible amount of adsorbed H_2O. The $\chi_M T$ versus T curves of the soaked crystals (Figures 2 and S13 for Pt and Pd derivatives, respectively) clearly reveal that the adsorption of MeOH stabilizes the HS state at all temperatures for the four compounds (black curves in Figures 2 and S13). In contrast, the adsorption of H_2O in **PhPyM** and **BipyM** provokes opposite effects on their respective spin transitions. For **PhPyM**, the average $T_{1/2}$ values slightly decrease from 204 to 190 K (M = Pt) and from 185 to 180 K (M = Pd), and the hysteresis width ΔT increases from 35 to 51 K (M = Pt) and from 29 to 36 K (M = Pd). For **BipyM**, their $T_{1/2}$ values increase considerably from 238 to 281.5 K (M = Pt) and from 221 to 282 K (M = Pd), while ΔT decreases from 32 to 23 K (M = Pt) and remains unchanged for M = Pd. Importantly, magnetic (Figure S14) and TGA (Figure S15) characterizations performed for compounds **PhPyM·*x*solv** (solv = H_2O, MeOH) and **BipyM·*x*MeOH** a few minutes after removing them from the corresponding solvent clearly suggest the occurrence of rapid desorption of the guest molecules, a fact that avoids a proper estimation of x. In contrast, as aforementioned, the air-dried samples of **BipyM·H$_2$O** (M = Pt^{II}, Pd^{II}) maintain the H_2O molecule per Fe^{II} ion of the initial as-synthesized hydrated framework.

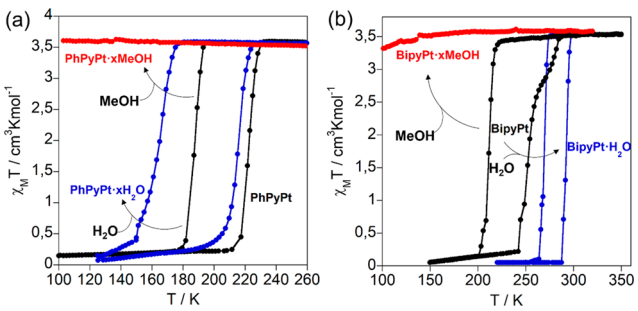

Figure 2. SCO properties of (a) **PhPyPt** and (b) **BipyPt** before (black curves) and after adsorption of H_2O (blue curves) and MeOH (red curves).

Included H$_2$O-Dependent SCO in BipyPt·*x*H$_2$O (*x* = 0−1). The marked difference observed between the SCO temperatures of the dehydrated (x = 0) and hydrated (x = 1) counterparts in the **BipyM·*x*H$_2$O** systems (Figure 2b) encouraged us to investigate the SCO profiles of some intermediate degrees of hydration. Even if we were unable to estimate the exact amount of H_2O for these intermediate hydrates, we managed to get hydration degrees from x = 1 to 0 by the sequential controlled heating of a pristine hydrated sample of **BipyPt·H$_2$O** inside the SQUID magnetometer. First, a fresh **BipyPt·H$_2$O** sample was measured in the 290−180−305 K temperature sequence, obtaining the expected SCO behavior of the completely hydrated framework (Figure 3a). Then, the solid was heated up to 305 K for 10 min and the thermal variation of χ_MT subsequently registered in the 305−180−320 K temperature range. The resulting curve shows the split of the SCO in two defined steps with $T_{1/2}^{\downarrow 1}/T_{1/2}^{\uparrow 1}$ = 278/298 K and $T_{1/2}^{\downarrow 2}/T_{1/2}^{\uparrow 2}$ = 220/264 K, which are reminiscent of the SCO behaviors of the completely hydrated and dehydrated compounds, respectively (Figure 3b). After that, the sample was heated at 320 K for 10 min followed by monitoring of the $\chi_M T$ values with the 320−180−320 K temperature range. Surprisingly, the SCO curve registered after this thermal treatment exhibits an outstanding hysteresis loop with a ΔT value of 84 K and values of $T_{1/2}^{\downarrow}$ and $T_{1/2}^{\uparrow}$ of 208 and 292 K, respectively (Figure 3c). Hence, whereas $T_{1/2}^{\downarrow}$ is comparable to that of the dehydrated compound, $T_{1/2}^{\uparrow}$ is very similar to that of the hydrated counterpart. Afterward, the sample was heated again at 320 K and measured within the same temperature range, observing an exclusive modification of the heating branch, which reflects the apparition of two steps ($T_{1/2}^{\uparrow 2}$ = 256 K and $T_{1/2}^{\uparrow 1}$ = 286 K), therefore delineating an asymmetric hysteresis loop (Figure 3d). Finally, subsequent treatment at 400 K led to the above-mentioned SCO behavior of the dehydrated compound (Figure 3e).

Calorimetric Measurements. Differential scanning calorimetry analysis was performed in order to confirm the SCO behaviors obtained by the SQUID measurements. The calorimetry data of desolvated **PhPyPt**, **PhPyPd**, **BipyPt**, and **BipyPd** and hydrated **BipyPt·H$_2$O** and **BipyPd·H$_2$O** compounds were conducted with a scan rate of 10 K min^{-1} in the cooling and heating modes, obtaining the corresponding ΔC_p versus T curves displayed in Figure 1. The $T_{1/2}$ and ΔT values extracted from these curves (Table 1) are in very good accord with the magnetic data. The slight discrepancies obtained (notably in the $T_{1/2}^{\downarrow}$ values) are related to the different scan rates used for the different techniques. Furthermore, the double peaks observed for some of the

https://doi.org/10.1021/acs.inorgchem.1c01925
Inorg. Chem. 2021, 60, 11866−11877

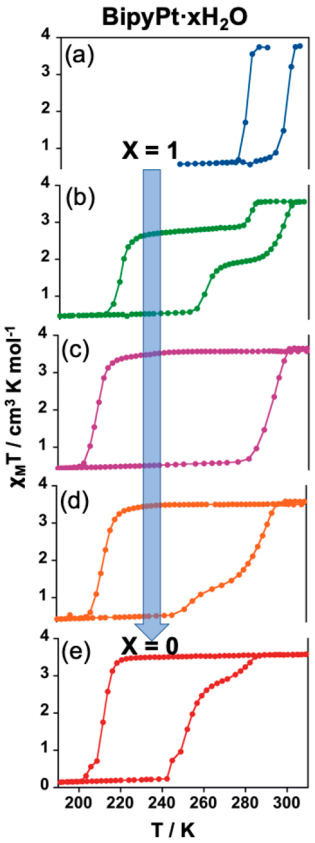

Figure 3. Evolution of the SCO properties of **BipyPt·xH$_2$O** from the (a) fully hydrated (x = 1) to the (e) completely dehydrated (x = 0) derivatives. $\chi_M T$ versus T curves displayed in parts b−d were obtained by the in situ sequential heating of the original hydrated sample (see the text).

samples reflect subtle changes of the slope of the γ_{HS} vs T curve during the HS−LS transformation and usually are associated with structural rearrangements concomitant with the spin transition. The estimated average ΔH and ΔS variations involved in the spin-state changes (Table 1) are comparable with those observed for cooperative SCO of related 2D Hofmann-type clathrates.[11−13] The $\Delta C_p(T)$ curve of an intermediate hydrated state was also registered after gentle heating of compound **BipyPt·H$_2$O** inside the calorimeter device. As a result, the cooling and heating ΔC_p versus T curves reflect a double-step SCO consistent with that observed in the magnetic study (Figure S16). The average ΔH (kJ mol^{-1})/ΔS (J mol^{-1} K^{-1}) values associated with the first and second steps are 6.565/28.484 and 7.058/24.626, respectively.

Crystal Structures. Crystal structures of **PhPyM·MeOH·0.5H$_2$O** (M = Pt, Pd) were successfully obtained at 120 K (HS), while that of **BipyPt·H$_2$O** was measured at 283 K (HS) and 120 K (LS). However, the structure of **BipyPd·H$_2$O** was analyzed only at 120 K (LS) because these crystals rapidly lose their crystallinity when measured above 280 K. Furthermore, the structure of compound **BipyPt·H$_2$O·MeOH**, obtained by soaking crystals of **BipyPt·H$_2$O** in pure MeOH for several days, was determined at 120 K (HS). The crystal structures of the unsolvated **PhPyPt** and **BipyPt** counterparts were solved at 298 K (HS) from ab initio methods using the *Topas Academic v6* program through the treatment and Rietveld refinement of the corresponding PXRD patterns (see the Experimental Section for more details). Relevant crystallographic data for all compounds are gathered in Tables S1−S3, while the corresponding significant metal-to-ligand bond lengths, angles, and intermolecular interactions are given in Tables S4−S6, respectively. Rietveld plots are given in Figure S17 for the final refinements.

*Structure of **PhPyM·MeOH·0.5H$_2$O** (M = Pt, Pd).* At 120 K, the crystal structures of **PhPyM·MeOH·0.5H$_2$O** (M = Pt, Pd) were determined in the orthorhombic *Imma* space group. They consist of a crystallographic unique type of octahedral {FeN$_6$} site coordinated equatorially by four N atoms belonging to four equivalent square-planar [M(CN)$_4$]$^{2-}$ units, which bridge four other equivalent Fe^{II} centers, forming bimetallic {Fe^{II}[M^{II}(CN)$_4$]}$_n$ layers. The axial positions are occupied by two equivalent terminal 4-phenylpyridine ligands (Figure 4a), thereby completing the 2D framework. At 120 K, the average Fe−N bond length is 2.179 and 2.181 Å for Pt and Pd derivatives, respectively, reflecting that, even at low temperature, the Fe^{II} ions are in the HS state, in good agreement with the magnetic data and the yellow color of the crystals. The {Fe^{II}(4-PhPy)$_2$[M^{II}(CN)$_4$]}$_n$ layers are pillared in such a way that the axial 4-PhPy ligands of adjacent layers are interdigitated, establishing π−π stacking interactions where the centroid-to-centroid distances of the face-to-face aromatic rings are 3.720 Å (M^{II} = Pt) and 3.740 Å (M^{II} = Pd) (Figure S18a). Moreover, one molecule of MeOH and a half molecule of H$_2$O per unit cell are hosted within the interlayer hydrophobic space, inducing a tilt of the [FeN$_6$] octahedra and a slight corrugation of the bimetallic {Fe^{II}[M^{II}(CN)$_4$]}$_n$ planes (Figure 4b). Indeed, the [Fe(N$_{eq}$)$_4$] equatorial plane of the [FeN$_6$] octahedron defines average angles of 8.6° (M^{II} = Pt) and 9.1° (M^{II} = Pd) with the square-planar units [M^{II}(CN)$_4$]$^{2-}$, thereby generating by symmetry two inequivalent channels between the interdigitated layers. Whereas one of

Table 1. Thermodynamic Parameters Extracted from the Magnetic and Calorimetric Measurements

	magnetism		calorimetry			
compound	$T_{1/2}$ (K)	ΔT (K)	$T_{1/2}$ (K)	ΔT (K)	ΔH (kJ mol^{-1})	ΔS (J mol^{-1} K^{-1})
BipyPt	238	32	233	44	13.23	63.31
BipyPt·H$_2$O	286.5	25	285	24	17.99	63.22
BipyPd	221	28	219.5	39	12.90	59.15
BipyPd·H$_2$O	282.5	35	273.5	37	16.57	61.75
PhPyPt·xMeOH·yH$_2$O	no SCO					
PhPyPt	204	36	201.5	29	10.29	47.98
PhPyPd·xMeOH·yH$_2$O	174.5 (incomplete)	21				
PhPyPd	185	29	181	28.5	11.41	57.09

https://doi.org/10.1021/acs.inorgchem.1c01925
Inorg. Chem. 2021, 60, 11866−11877

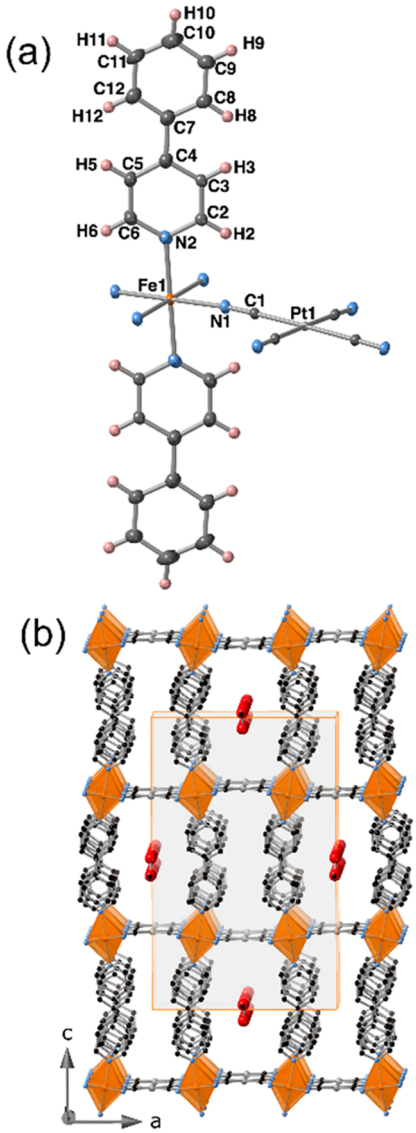

Figure 4. (a) ORTEP representation of the Fe^{II} environment displayed by **PhPyM·MeOH·0.5H_2O** (M = Pt, Pd). (Atoms are represented at 50% probability). (b) Fragment of the 2D networks formed by four stacked layers showing the channels where the solvent molecules are located in **PhPyM·MeOH·0.5H_2O**.

these channels does not contain any guest due to the small void left by the neighboring 4-PhPy ligands, the other is wide enough to host the solvent molecules. These guest molecules are distributed along the channel in such a way that they define a plane that is stabilized through hydrogen bonds and situated at 2.6 Å with respect to the aromatic H atoms of the 4-PhPy ligand.

*Structure of **BipyM·H_2O** (M = Pt, Pd).* At 120 K, the crystal structures of **BipyM·H_2O** present the orthorhombic *Cmmm* space group. The structure consists of a unique octahedral $\{FeN_6\}$ site coordinated by four equivalent square-planar $[M(CN)_4]^{2-}$ bridging ligands in the equatorial positions and by the 4-substituted pyridine N atom of two equivalent terminal 2,4-bipy ligands in the axial positions (Figure 5a). It is worth noting that atoms N3 and C6 are disordered by symmetry and have been modeled with an occupancy of 0.5 in each position. Conversely to the 4-Phpy-based compounds, the average Fe−N distances are 1.953 and 1.958 Å for **BipyPt·H_2O** and **BipyPd·H_2O**, respectively, indicating that the Fe^{II} ion is in the LS state, in good agreement with the magnetic data and the red color of the crystals. Furthermore, the $\{Fe^{II}[M^{II}(CN)_4]\}_n$ layers are strictly planar (Figure 6a), in contrast to that observed for **PhPyM·MeOH·0.5H_2O**. As a result of their higher structural homogeneity, only one type of channel is generated between the interdigitated bimetallic layers where one molecule of H_2O is hosted, occupying discrete positions and interacting via moderate hydrogen bonds with the N3 heterocyclic atom of the 2,4-bipy ligand (O1···N3 intermolecular distance of 2.953 Å for Pt and 3.000 Å for Pd). Moreover, the pillared layers are stabilized by $\pi-\pi$ interactions established between the pyridine moieties of the interdigitated 2,4-bipy ligands with centroid-to-centroid distances of 3.665 and 3.671 Å for **BipyPt·H_2O** and **BipyPd·H_2O**, respectively (Figure S18b). In good agreement with the magnetic data, crystals of **BipyPt·H_2O** become yellow upon heating, evidencing the occurrence of a LS-to-HS transition. This was confirmed by analysis of the structure at 283 K, which is basically the same as that at 120 K but exhibiting, as the main difference, an increase of 0.206 Å in the Fe−N average distance.

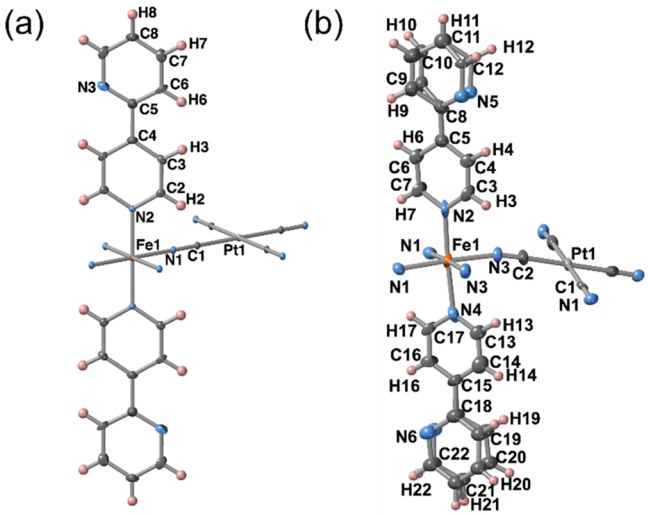

Figure 5. ORTEP representations of the Fe^{II} environment displayed by (a) **BipyPt·H_2O** and (b) **BipyPt·H_2O·MeOH**. Atoms are represented at 50% probability.

*Structure of **BipyPt·H_2O·MeOH**.* When crystals of **BipyPt·H_2O** are immersed in pure MeOH for several days, they adsorb one molecule of MeOH, leading to compound **BipyPt·H_2O·MeOH**. The MeOH uptake is accompanied by a single-crystal-to-single-crystal transformation from the orthorhombic *Cmmm* space group to the orthorhombic *Pnma* space group. This loss of symmetry is reflected in the apparition of two nonequivalent 2,4-Bipy ligands as well as two distinct types of equatorial coordinating N atoms (N1 and N3). Furthermore, the entry of MeOH induces the occurrence of a positional disorder on the noncoordinated pyridine of the 2,4-bipy ligand (Figure 5b). At 120 K, crystals of **BipyPt·H_2O·MeOH** are yellow and consist, analogously to **BipyPt·H_2O**, of a layered structure. However, in contrast with the monohydrated phase, the bimetallic layers are considerably corrugated likely provoked by inclusion of the molecule of MeOH, which distorts the 2D network (Figure 6b). This corrugation is reflected on the angles of 6.54° and 23.01° defined between the $[Fe(N_{eq})_4]$ equatorial plane of the $[FeN_6]$ octahedron and

https://doi.org/10.1021/acs.inorgchem.1c01925
Inorg. Chem. 2021, 60, 11866−11877

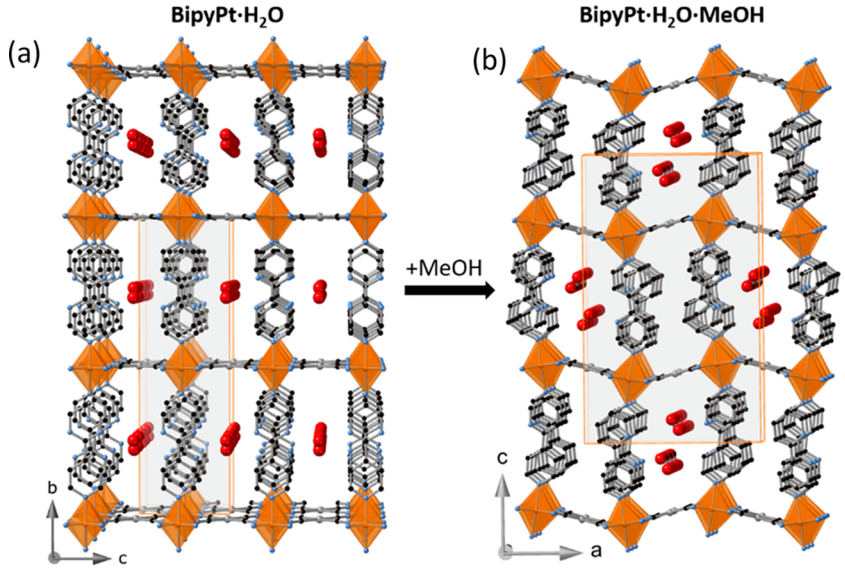

Figure 6. Structural modifications observed on the (a) **BipyPt·H_2O** (isostructutal to **BipyPd·H_2O**) network upon MeOH adsorption and the corresponding transformation in (b) **BipyPt·H_2O·MeOH**. The two disordered positions of the noncoordinated pyridine are shown for compound **BipyPt·H_2O·MeOH**.

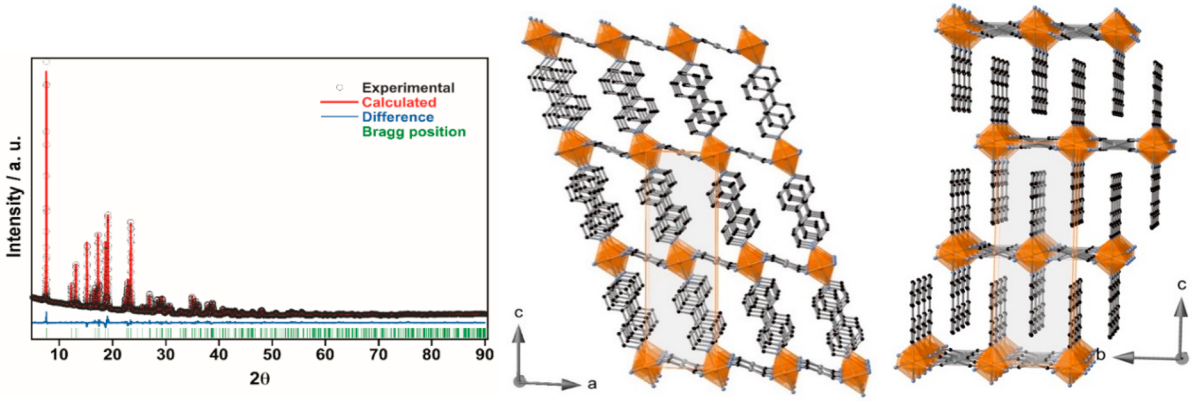

Figure 7. Rietveld fitting of the experimental XRPD pattern for **PhPyPt** (left) (for **BipyPt**, see Figure S17). Views along the *b* (middle) and *a* (right) axes of a fragment of the desolvated **PhPyPt** framework.

the adjacent square-planar units $[Pt^{II}(CN)_4]^{2-}$. The guest MeOH molecules are accommodated along the channels generated between the protruding interdigitated 2,4-bipy axial ligands of consecutive layers, where one molecule of H_2O has also been detected. Both guests establish hydrogen-bonding interactions (N−O distances in the 2.8−3.3 Å range) with the noncoordinated N heteroatom of the axial 2,4-bipy ligand. The Fe−N average distance is 2.160 Å, which indicates that the structure is blocked at the HS state even at 120 K.

*Structures of **BipyPt** and **PhPyPt**.* The solvent-free **BipyPt** and **PhPyPt** compounds are isostructural and adopt the monoclinic *I*2/*m* space group at 298 K. The Fe^{II} ion lies in an inversion center with average Fe−N bond lengths of 2.167 and 2.168 Å for **BipyPt** and **PhPyPt**, respectively, which are consistent with the HS state of the Fe^{II} site. Analogously to the corresponding solvated forms, the structure is composed of an infinite stack of bimetallic $\{Fe(L)_2[Pt(CN)_4]\}$ layers. However, at variance with the previously described structures, the layers of unsolvated forms are strongly corrugated (Figure 7). Indeed, the angle defined by the average equatorial planes $[Fe(N_{eq})_4]$ and $[Pt(CN)_4]^{2-}$ is around 38° for both derivatives. This corrugation induces a marked tilt of the axial ligands with respect to the mean plane defined by the Fe^{II}-M^{II} bimetallic layer favoring a considerably more dense and efficient packing between layers in such a manner that no solvent-accessible channels are present within the structures.

■ DISCUSSION

The main objective of this work was to evaluate the affinity toward adsorption of hydrophilic guests in two equivalent series of 2D Hofmann-type $\{Fe^{II}(L)_2[M^{II}(CN)_4]\}$ (M^{II} = Pt^{II}, Pd^{II}) CPs based on the axial ligands L = 4-PhPy (**PhPyM**) and 2,4-Bipy (**BipyM**) and to assess the structural effects induced by adsorption/desorption of the guest and its consequences on the SCO properties. Both series of 2D frameworks essentially differ in the presence/absence of an extra N heteroatom and consequently in the distinct hydrophobicity of the interlayer spaces generated between the interdigitated 2,4-Bipy and 4-PhPy ligands.

Solvent Affinity and Structural Rearrangements. The different capabilities of compounds **PhPyM** and **BipyM** for retaining MeOH or H_2O can be rationalized by analyzing the

https://doi.org/10.1021/acs.inorgchem.1c01925
Inorg. Chem. 2021, 60, 11866−11877

structures of the corresponding solvates. For example, in the **PhPyM·MeOH·0.5H_2O** and **BipyM·H_2O·MeOH** clathrates, the interactions of the MeOH molecules with the host framework are rather repulsive because of the steric requirements created by the methyl group of the MeOH molecule. As a result, the interdigitated 4-PhPy or 2,4-bipy ligands are tilted, maximizing the host−guest distances and forcing the aperture of channels in the interlayer space to facilitate the inclusion of MeOH. However, on the basis of the magnetic behavior (Figures 2 and S13) and PXRD (Figure S11), these distorted structures are adopted when the crystals are soaked in MeOH, but they are not stable once exposed to air, thereby losing the guest molecules and reverting to the desorbed **PhPyM** and **BipyM** phases. In contrast, the H_2O molecules located between adjacent layers in **BipyM·H_2O** occupy discrete positions in such a way that they establish hydrogen bonds with the N heteroatom of the noncoordinating pyridine of the 2,4-bipy ligand. As a result of this hydrogen bonding, the H_2O molecule remains attached to the host framework unless a heating treatment is applied. The H_2O molecules are situated at the center of the square windows defined by four neighboring interdigitated 2,4-bipy ligands and the equatorial CN^- groups. Hence, their presence does not suppose any steric repulsion over the host network, promoting a very regular, ordered, and stable structure reminiscent of those of the analogues 2D-Hofmann compounds {Fe(pyrimidine)$_2$[M(CN)$_4$]}·$x$$H_2O$ (**PymM**)[39] and {Fe(pyridazine)$_2$[M(CN)$_4$]·$x$$H_2O$} (**PdzM**).[24]

Whereas desorbed compounds **PhPyM** are not capable of recovering H_2O from humid air, compounds **BipyM** exhibit a strong affinity to H_2O, readsorbing it spontaneously within a few minutes. It is important to stress that this marked difference cannot be ascribed to structural factors because both unsolvated forms are isostructural and isomorphous; consequently, the interstitial space generated within the interdigitated axial ligands of two consecutive layers is similar in both series of compounds. Indeed, the presence of the N heteroatom in **BipyM** is the driving force responsible for its high affinity toward H_2O, which is sequestered by the host framework, triggering a crystal transformation. Thus, crystals convert from the desorbed phase **BipyM** (monoclinic *C*) to the monohydrated phase **BipyM·H_2O** (orthorhombic *C*), inducing a large "wine-rack"-like transformation to accommodate the H_2O molecules. These marked structural changes are unprecedented within the family of 2D Hofmann-type frameworks, which show the ability to recover H_2O from humidity.[18,19,21,28,39] The H_2O affinity of the unsolvated **BipyM** system strongly contrasts with that exhibited by the related compounds {Fe(pyrimidine)$_2$[M(CN)$_4$]} (M = Pt, Pd), which also display an available uncoordinated N atom in the axial pyrimidine ligands. In their monohydrated forms, the H_2O molecule seems more labile, exhibiting full (M = Pt) and partial (M = Pd) spontaneous desorption. However, only the Pt derivative can recover half of the H_2O molecule, while the Pd derivative does not show H_2O adsorption in contact with air. This smaller affinity for H_2O may be related to the much smaller interlayer distance and likely larger rigidity exhibited by the pyrimidine derivatives, which prevent the framework from hosting the H_2O molecules.

The lack of structural modifications observed from the PXRD patterns upon soaking **PhPyM** in H_2O (Figure S11) suggests a minimal adsorption of this guest. This observation is likely due to the hydrophobic nature of the intralayer cavities in these derivatives. In contrast, the PXRD patterns for these derivatives immersed in MeOH (Figure S11) denote remarkable changes in their structure, suggesting a greater tolerance toward MeOH adsorption, a fact that is likely due to the stronger affinity of MeOH to hydrophobic voids.[40]

Nature of the Axial Ligand and Its Influence on the SCO. Although here we contribute to a detailed structural study and guest-dependent SCO experiments for compounds **PhPyPt** and **PhPyPd**, their magnetic behavior in the unsolvated form was already reported[35] and successfully reproduced in this work. The formal replacement of 4-PhPy with 2,4-Bipy as the axial ligand in the 2D Hofmann-type {Fe(L)$_2$[M(CN)$_4$]} series provokes remarkable changes in the SCO behavior. As far as the isostructural unsolvated forms are concerned, the average $T_{1/2}$ temperatures of the 2,4-Bipy derivatives are 38 K (M = Pt) and 44 K (M = Pd) larger than those of the 4-Phpy counterparts. Without excluding the possible influence of subtle structural effects, this marked difference should be mainly ascribed to the electronic effects induced by the peripheral 4-pyridyl or 4-phenyl groups on the coplanar coordinating pyridine ring. In this respect, although similar coordinating capabilities are expected for both ligands, the slightly larger electronegativity of 2,4-Bipy associated with the presence of the noncoordinating pyridine group, on the one hand, makes the N lone pair of the coordinating pyridine group less diffuse, thereby decreasing its σ-donor character but, on the other hand, simultaneously increases the π-acceptor character of 2,4-bipy, with the resulting effect being an increase of the ligand-field strength and, hence, the $T_{1/2}$ values for the **BipyM** derivatives.

Guest-Dependent SCO Behavior. Concerning the solvated forms, the changes observed in the SCO reflect the ability of the framework to include the guest molecules and the resulting host−guest interplay. For example, the **PhPyM** derivatives soaked in H_2O exhibit SCO behaviors centered at temperatures only slightly smaller (5 K for M = Pd and 14 K for M = Pt) than the ones observed for the unsolvated counterparts (note that only $T_{1/2}^{\downarrow}$ is reduced, whereas $T_{1/2}^{\uparrow}$ is not modified). This suggests that the amount of adsorbed H_2O is very small, prompting a slight stabilization of the HS via elastic frustration. In contrast, the **BipyM** derivatives soaked in H_2O essentially recover the original SCO of the as-synthesized samples. It is worth mentioning that the $T_{1/2}$ values of the **BipyM·H_2O** solvates are in the range of 50−60 K higher than those of their unsolvated counterparts. This important stabilization of the LS state shifting $T_{1/2}$ near room temperature must be facilitated by the highly regular orthorhombic *Cmmm* structure adopted by **BipyM·H_2O**, which favors the lack of elastic frustration. The increase of $T_{1/2}$ with the adsorption of H_2O is relatively common in 3D Hofmann-type compounds and has been associated with structural changes produced upon the hydration process and/or the host−guest interactions (i.e., hydrogen bonding) between H_2O and the ligands surrounding the Fe^{II} ion.[15] However, a $T_{1/2}$ increase mediated by H_2O adsorption is rare in 2D Hofmann structures. This is the case of compound {Fe(thtrz)$_2$[Pd(CN)$_4$]}, for which a difference of 40 K between the empty and monohydrated derivatives was also explained by host−guest interactions influencing the Fe^{II} environment.[19] Conversely, the majority of the reported 2D-layered Hofmann structures present an increase of $T_{1/2}$ upon dehydration, which has been mainly justified by a reduction of the elastic frustration. In the present case, inclusion of the H_2O

https://doi.org/10.1021/acs.inorgchem.1c01925
Inorg. Chem. 2021, 60, 11866−11877

molecule not only is not a source of steric hindrance but also is responsible for the $T_{1/2}$ upshift until attaining the room temperature range. Importantly, whatever the degree of solvation, examples of 2D Hofmann frameworks presenting hysteretic SCO properties centered around room temperature are still scarce[18,24] and are needed for future applications.

The progressive and controlled desorption of H_2O in **BipyM·H$_2$O** to afford **BipyM** is accompanied by a reduction in $T_{1/2}$ and the occurrence of a crystallographic transformation from the orthorhombic *Cmmm* to the monoclinic *I*2/*m* space group. The latter defines a less regular network, which is reflected in an important increase of corrugation in the bimetallic layers. Interestingly, this decrease in T_c does not seem to be homogeneous with the sample showing intermediate dehydrated phases, whose SCO behaviors suggest the presence of mixtures of pure hydrated and dehydrated species. However, interestingly, the evolution of this dehydration process gives rise to an intermediate phase that displays a huge square-shaped hysteresis loop 84 K, which clearly suggests the presence of a homogeneous genuine phase instead the overlap of two distinct phases. The presence of such an intermediate state was detected through sophisticated single-crystal X-ray diffraction analysis in the mononuclear system $[Fe(bpp)(H_2L)](ClO_4)_2{\cdot}1.5C_3H_6O$ [bpp = 2,6-bis-(pyrazol-3-yl)pyridine; H_2L = 2,6-bis[5-(2-methoxyphenyl)-pyrazol-3-yl]pyridine; C_3H_6O = acetone].[41]

The introduction of MeOH in both the **PhPyM** and **BipyM** frameworks induces deactivation of the SCO. Indeed, the magnetic measurements of these compounds soaked in liquid MeOH yield paramagnetic curves. This result is consistent with the structures of **PhPyM·MeOH·0.5H$_2$O** and **BipyPt·MeOH·H$_2$O**, where the Fe^{II} ions are HS at all temperatures. As mentioned above, the adsorption of MeOH implicates important structural changes in the host framework, i.e., the adjacent axial ligand 2,4-Bipy (or 4-PhPy) of a layer tilt in opposite directions, opening channels along which the MeOH is accommodated. These structural changes generate short intermolecular contacts featuring steric repulsions, i.e., those established between the methylene H atoms of MeOH and the aromatic H atoms of the coordinating pyridine. Likely, this steric factor is responsible for the elastic frustration that involves stabilization of the HS state. Along this line, the small fraction of SCO-active Fe^{II} ions observed for crystals of **FePhPy·*x*MeOH·*y*H$_2$O** (Figure 1b) soaked in the mother liquor is likely due to the existence of MeOH-free phases containing H_2O or exhibiting complete absence of solvent. Indeed, the presence of this SCO-active phase was detected by PXRD (Figure S1).

■ CONCLUSIONS

In summary, guest-dependent structural and SCO properties of the isomorphous 2D Hofmann CPs $\{Fe(4\text{-}PhPy)_2[M(CN)_4]\}$ (**PhPyM**) and $\{Fe(2,4\text{-}Bipy)_2[M(CN)_4]\}$ (**BipyM**) (M = Pd, Pt) were characterized and compared. Our results indicate that, although the sole difference between both families of compounds stems from the presence/absence of a non-coordinated N heteroatom within the interlayer space, this subtle difference in the chemical composition deeply impacts not only the adsorption capability of the clathrate but also the degree to which the SCO is modulated upon guest uptake. Thus, whereas the adsorption of H_2O in **BipyM** is rapid and spontaneous at ambient conditions, it occurs to a very low extent for **PhPyM**, even when soaked in H_2O. The driving force of the higher H_2O affinity of the former is necessarily ascribed to the hydrogen bonds established between H_2O and the noncoordinated N heteroatom. These interactions induce the opening of interlayer channels along which the H_2O molecules are accommodated, leading to regular and homogeneous layered structures. The uptake of H_2O in **BipyM** provokes a remarkable increase of the SCO temperatures (by 50−60 K), shifting the wide hysteresis loops at around room temperature. This SCO shift has been correlated with a combination of structural and electronic factors. In contrast, the small amount of H_2O adsorbed by **PhPyM** marginally influences the SCO temperature, likely due to subtle elastic frustration effects. Besides, although MeOH molecules are efficiently absorbed in solution by both series of compounds leading to distorted layered networks, steric repulsions between the MeOH molecules and host network are behind its rapid desorption under an ambient atmosphere. This steric factor also provides elastic frustration to the system because the SCO properties of both families of compounds are deactivated when soaked in MeOH. This comparative study sheds light on how fine-tuning the host framework greatly modifies the coupling of host−guest and SCO properties and contributes to paving the way toward the application of these materials as chemical sensors.

■ ASSOCIATED CONTENT

Supporting Information

The Supporting Information is available free of charge at https://pubs.acs.org/doi/10.1021/acs.inorgchem.1c01925.

Crystallographic details, additional structural views and PXRD patterns, Rietveld refinement plots, TGA data, and additional magnetic measurements (PDF)

Accession Codes

CCDC 2090594−2090601 contain the supplementary crystallographic data for this paper. These data can be obtained free of charge via www.ccdc.cam.ac.uk/data_request/cif, or by emailing data_request@ccdc.cam.ac.uk, or by contacting The Cambridge Crystallographic Data Centre, 12 Union Road, Cambridge CB2 1EZ, UK; fax: +44 1223 336033.

■ AUTHOR INFORMATION

Corresponding Authors

Carlos Bartual-Murgui − *Instituto de Ciencia Molecular and Departamento de Química Inorgánica, Universidad de Valencia, Paterna, València E-46980, Spain;* orcid.org/0000-0003-1547-8018; Email: Carlos.bartual@uv.es

José Antonio Real − *Instituto de Ciencia Molecular and Departamento de Química Inorgánica, Universidad de Valencia, Paterna, València E-46980, Spain;* orcid.org/0000-0002-2302-561X; Email: jose.a.real@uv.es

Authors

Manuel Meneses-Sánchez − *Instituto de Ciencia Molecular and Departamento de Química Inorgánica, Universidad de Valencia, Paterna, València E-46980, Spain*

Rubén Turo-Cortés − *Instituto de Ciencia Molecular and Departamento de Química Inorgánica, Universidad de Valencia, Paterna, València E-46980, Spain*

Iván da Silva − *ISIS Neutron Facility, STFC Rutherford Appleton Laboratory, Chilton, Oxfordshire OX11 0QX, U.K.;* orcid.org/0000-0002-4472-9675

M. Carmen Muñoz − *Departamento de Física Aplicada, Universitat Politècnica de València, Valencia 46022, Spain;* orcid.org/0000-0003-2630-3897

Complete contact information is available at: https://pubs.acs.org/10.1021/acs.inorgchem.1c01925

Notes

The authors declare no competing financial interest.

■ ACKNOWLEDGMENTS

This work was supported by the Spanish Ministerio de Ciencia e Innovación (MICINN) and FEDER funds (Grant PID2019-106147GB-I00), Unidad de Excelencia María de Maeztu (Grants MDM2015-0538-18-2 and CEX2019-000919-M), and EU Framework FET-OPEN project COSMICS (Grant Agreement 766726). R.T.-C. and M.M.-S. thank the MICINN for a predoctoral grant.

■ REFERENCES

(1) König, E. Nature and dynamics of the spin-state interconversion in metal complexes. *Struct. Bonding (Berlin, Ger.)* **1991**, *76*, 51.

(2) Gütlich, P., Goodwin, G., Eds. Spin crossover in transition metal compound I−III. *Topics in Current Chemistry*; Springer, 2004; pp 233−235.

(3) Gütlich, P.; Hauser, A.; Spiering, H. Thermal and Optical Switching of Iron(II) Complexes. *Angew. Chem., Int. Ed. Engl.* **1994**, *33*, 2024−2054.

(4) Gütlich, P.; Garcia, Y.; Goodwin, H. A. Spin crossover phenomena in Fe(ii) complexes. *Chem. Soc. Rev.* **2000**, *29*, 419−427.

(5) See the special issue "Spin Crossover Phenomenon": Wolny, J. A.; Schunemann, V.; Nemeth, Z.; Vanko, G. Spectroscopic techniques to characterize the spin state: Vibrational, optical, Mössbauer, NMR, and X-ray spectroscopy. *C. R. Chim.* **2018**, *21*, 1152−1169.

(6) Kahn, O.; Martinez, J. Spin-Transition Polymers: From Molecular Materials Toward Memory Devices. *Science* **1998**, *279*, 44.

(7) Halcrow, M. A. *Spin-Crossover Materials: Properties and Applications*; Wiley: West Sussex, U.K., 2013.

(8) Létard, J.-F.; Guionneau, P.; Goux-Capes, L. Towards spin crossover applications. *Top. Curr. Chem.* **2004**, *235*, 221−249.

(9) Bousseksou, A.; Molnár, G.; Salmon, L.; Nicolazzi, W. Molecular spin crossover phenomenon: recent achievements and prospects. *Chem. Soc. Rev.* **2011**, *40*, 3313.

(10) Molnár, G.; Rat, S.; Salmon, L.; Nicolazzi, W.; Bousseksou, A. Spin Crossover Nanomaterials: From Fundamental Concepts to Devices. *Adv. Mater.* **2018**, *30*, 1703862−23.

(11) Real, J. A.; Gaspar, A. B.; Niel, V.; Muñoz, M. C. Communication between Iron(II) Building Blocks in Cooperative Spin Transition Phenomena. *Coord. Chem. Rev.* **2003**, *236*, 121−141.

(12) Garcia, Y.; Niel, V.; Muñoz, M. C.; Real, J. A. Spin Crossover in 1D, 2D and 3D Polymeric Fe(II) Networks. *Top. Curr. Chem.* **2004**, *233*, 229−257.

(13) Muñoz, M. C.; Real, J. A. Thermo-, Piezo-, Photo- and Chemo-Switchable Spin Crossover Iron(II)-Metallocyanate Based Coordination Polymers. *Coord. Chem. Rev.* **2011**, *255*, 2068−2093.

(14) Kucheriv, O. I.; Fritsky, I. O.; Gural'skiy, I. A. Spin crossover in FeII cyanometallic frameworks. *Inorg. Chim. Acta* **2021**, *521*, 120303.

(15) Ohtani, R.; Hayami, S. Guest-Dependent Spin-Transition Behavior of Porous Coordination Polymers. *Chem. - Eur. J.* **2017**, *23*, 2236−2248.

(16) Ni, Z. P.; Liu, J. L.; Hoque, M. N.; Liu, W.; Li, J. Y.; Chen, Y. C.; Tong, M. L. Recent Advances in Guest Effects on Spin-Crossover Behavior in Hofmann-Type Metal-Organic Frameworks. *Coord. Chem. Rev.* **2017**, *335*, 28−43.

(17) Ohba, M.; Yoneda, K.; Agustí, G.; Munoz, M. C.; Gaspar, A. B.; Real, J. A.; Yamasaki, M.; Ando, H.; Nakao, Y.; Sakaki, S.; Kitagawa, S. Bidirectional chemo-switching of spin state in a microporous framework. *Angew. Chem., Int. Ed.* **2009**, *48*, 4767.

(18) Zenere, K. A.; Duyker, S. G.; Trzop, E.; Collet, E.; Chan, B.; Doheny, P. W.; Kepert, C. J.; Neville, S. M. Increasing spin crossover cooperativity in 2D Hofmann-type materials with guest molecule removal. *Chem. Sci.* **2018**, *9*, 5623−5629.

(19) Sciortino, N. F.; Ragon, F.; Klein, Y. M.; Housecroft, C. E.; Davies, C. G.; Jameson, G. N. L.; Chastanet, G.; Neville, S. M. Guest-Responsive Elastic Frustration "On−Off" Switching in Flexible, Two-Dimensional Spin Crossover Frameworks. *Inorg. Chem.* **2018**, *57*, 11068−11076.

(20) Milin, E.; Patinec, V.; Triki, S.; Bendeif, E.-E.; Pillet, S.; Marchivie, M.; Chastanet, G.; Boukheddaden, K. Elastic Frustration Triggering Photoinduced Hidden Hysteresis and Multistability in a Two-Dimensional Photoswitchable Hofmann-Like Spin-Crossover Metal−Organic Framework. *Inorg. Chem.* **2016**, *55*, 11652−11661.

(21) Sciortino, N. F.; Ragon, F.; Zenere, K. A.; Southon, P. D.; Halder, G. J.; Chapman, K. W.; Piñeiro-Lopez, L.; Real, J. A.; Kepert, C. J.; Neville, S. M. Exploiting Pressure To Induce a "Guest-Blocked" Spin Transition in a Framework Material. *Inorg. Chem.* **2016**, *55*, 10490−10498.

(22) Brennan, A. T.; Zenere, K. A.; Kepert, C. J.; Clegg, J. K.; Neville, S. M. Three Distinct Spin-Crossover Pathways in Halogen-Appended 2D Hofmann Frameworks. *Inorg. Chem.* **2021**, *60* (6), 3871−3878.

(23) Brennan, A. T.; Zenere, K. A.; Brand, H. E. A.; Price, J. R.; Bhadbhade, M. M.; Turner, G. F.; Moggach, S. A.; Valverde-Muñoz, F. J.; Real, J. A.; Clegg, J. K.; Kepert, C. J.; Neville, S. M. Guest Removal and External Pressure Variation Induce Spin Crossover in Halogen-Functionalized 2-D Hofmann Frameworks. *Inorg. Chem.* **2020**, *59* (19), 14296−14305.

(24) Gural'skiy, I. A.; Shylin, S. I.; Ksenofontov, V.; Tremel, W. Pyridazine-Supported Polymeric Cyanometallates with Spin Transitions. *Eur. J. Inorg. Chem.* **2019**, *2019*, 4532−4537.

(25) Sciortino, N. F.; Zenere, K. A.; Corrigan, M. E.; Halder, G. J.; Chastanet, G.; Létard, J.-F.; Kepert, C. J.; Neville, S. M. Four-step iron(ii) spin state cascade driven by antagonistic solid state interactions. *Chem. Sci.* **2017**, *8*, 701.

(26) Murphy, M. J.; Zenere, K. A.; Ragon, F.; Southon, P. D.; Kepert, C. J.; Neville, S. M. Guest Programmable Multistep Spin Crossover in a Porous 2-D Hofmann-Type Material. *J. Am. Chem. Soc.* **2017**, *139*, 1330−1335.

(27) Klein, Y. M.; Sciortino, N. F.; Ragon, F.; Housecroft, C. E.; Kepert, C. J.; Neville, S. M. Spin crossover intermediate plateau stabilization in a flexible 2-D Hofmann-type coordination polymer. *Chem. Commun.* **2014**, *50*, 3838−3840.

(28) Turo-Cortés, R.; Bartual-Murgui, C.; Castells-Gil, J.; Muñoz, M. C.; Martí-Gastaldo, C.; Real, J. A. Reversible guest-induced gate-opening with multiplex spin crossover responses in two-dimensional Hofmann clathrates. *Chem. Sci.* **2020**, *11*, 11224−11234.

(29) Real, J. A.; Andres, E.; Muñoz, M. C.; Julve, M.; Granier, T.; Bousseksou, A.; Varret, F. Spin Crossover in a Catenane Supramolecular System. *Science* **1995**, *268*, 265.

(30) Halder, G. J. Guest-Dependent Spin Crossover in a Nanoporous Molecular Framework Material. *Science* **2002**, *298*, 1762.

(31) Neville, S. M.; Moubaraki, B.; Murray, K. S.; Kepert, C. J. A Thermal Spin Transition in a Nanoporous Iron(II) Coordination Framework Material. *Angew. Chem., Int. Ed.* **2007**, *46*, 2059.

(32) Neville, S. M.; Halder, G. J.; Chapman, K. W.; Duriska, M. B.; Moubaraki, B.; Murray, K. S.; Kepert, C. J. Guest Tunable Structure and Spin Crossover Properties in a Nanoporous Coordination Framework Material. *J. Am. Chem. Soc.* **2009**, *131*, 12106−12108.

(33) Halder, G. J.; Chapman, K. W.; Neville, S. M.; Moubaraki, B.; Murray, K. S.; Létard, J.-F.; Kepert, C. J. Elucidating the Mechanism of a Two-Step Spin Transition in a Nanoporous Metal−Organic Framework. *J. Am. Chem. Soc.* **2008**, *130*, 17552.

(34) Neville, S. M.; Halder, G. J.; Chapman, K. W.; Duriska, M. B.; Southon, D.; Cashion, J. D.; Létard, J.-F.; Moubaraki, B.; Murray, K. S.; Kepert, C. J. Single-Crystal to Single-Crystal Structural Transformation and Photomagnetic Properties of a Porous Iron(II) Spin-Crossover Framework. *J. Am. Chem. Soc.* **2008**, *130*, 2869.

(35) Seredyuk, M.; Gaspar, A. B.; Ksenofontov, V.; Verdaguer, M.; Villain, F.; Gütlich, P. Thermal- and Light-Induced Spin Crossover in Novel 2D Fe(II) Metalorganic Frameworks {Fe(4-PhPy)$_2$[M^{II}(CN)$_x$]$_y$}·sH$_2$O: Spectroscopic, Structural, and Magnetic Studies. *Inorg. Chem.* **2009**, *48*, 6130−6141.

(36) (a) Sheldrick, G. M. *Acta Crystallogr., Sect. A: Found. Crystallogr.* **2008**, *64*, 112. (b) Sheldrick, G. M. *SHELXL-2014*; University of Göttingen, 2014.

(37) Oszlányi, G.; Sütő, A. Ab initio structure solution by charge flipping. *Acta Crystallogr., Sect. A: Found. Crystallogr.* **2004**, *60*, 134−141.

(38) Rietveld, H. M. A profile refinement method for nuclear and magnetic structures. *J. Appl. Crystallogr.* **1969**, *2*, 65−71.

(39) Bartual-Murgui, C.; Rubio-Giménez, V.; Meneses-Sánchez, M.; Valverde-Muñoz, F. J.; Tatay, S.; Martí-Gastaldo, C.; Muñoz, M. C.; Real, J. A. Epitaxial Thin-Film vs Single Crystal Growth of 2D Hofmann-Type Iron(II) Materials: A Comparative Assessment of their Bi-Stable Spin Crossover Properties. *ACS Appl. Mater. Interfaces* **2020**, *12* (26), 29461−29472.

(40) Gounder, R.; Davis, M. E. Beyond shape selective catalysis with zeolites: Hydrophobic void spaces in zeolites enable catalysis in liquid water. *AIChE J.* **2013**, *59*, 3349−3358.

(41) Aromí, G.; Beavers, M.; Sánchez Costa, J.; Craig, G. A.; Mínguez Espallargas, G.; Orera, A.; Roubeau, O. Snapshots of a solid-state transformation: coexistence of three phases trapped in one crystal. *Chem. Sci.* **2016**, *7*, 2907−2915.

https://doi.org/10.1021/acs.inorgchem.1c01925
Inorg. Chem. 2021, 60, 11866−11877